Tunable Dirac Polaritons in Cavity-Embedded Metasurfaces

Charlie-Ray Mann

Department of Physics and Astronomy
University of Exeter

A thesis submitted for the degree of
Doctor of Philosophy in Physics

Supervisors: Eros Mariani & William L. Barnes

April 2021

Declaration

Tunable Dirac Polaritons in Cavity-Embedded Metasurfaces.

Submitted by Charlie-Ray Mann, to the University of Exeter as a thesis for the degree of Doctor of Philosophy in Physics, April 2021.

This thesis is available for Library use on the understanding that it is copyright material and that no quotation from the thesis may be published without proper acknowledgement.

I certify that all material in this thesis which is not my own work has been identified and that any material that has previously been submitted and approved for the award of a degree by this or any other University has been acknowledged.

C-R Mann

Charlie-Ray Mann
April 2021

“A great deal of my work is just playing with equations and seeing what they give.”

Paul Dirac

Acknowledgements

Eros, I consider myself incredibly lucky to have had you as a supervisor, a mentor, and a friend over the last few years – you are a wonderful human being. I vividly remember the meeting where you encouraged me to do a PhD and you said "you'll be dropped in the middle of the ocean and you'll either sink or swim" – I hope I didn't sink. I am extremely grateful that you gave me the freedom and autonomy to explore and develop my own ideas, which has been an invaluable experience for me. I will always fondly remember the endless espresso-fuelled rewrites of the papers, the expensive steaks and rum, and the fact that you taught a Cornish boy proper English grammar. More importantly, you have always believed in my abilities even when I didn't, and you have always provided me with so many opportunities. You even brought me croissants and coffee when I laid in hospital. Thank you for everything, Eros, I consider you a true friend.

I am also very grateful to my second supervisor, Bill. You were the first physicist that I ever encountered on my first day as an undergraduate at Exeter, and I remember you saying that "doing physics is very different to studying physics" – this always stuck with me and definitely steered me towards a PhD even in those early days. Your enthusiasm has always been extremely infectious, and I always enjoyed our back-to-basics sessions. Sorry for not sticking with the fabrication of nanoparticle arrays at the beginning of the PhD – I probably would have been terrible at experiments anyway!

Towards the end of my PhD I also had the great privilege of collaborating with Simon Horsley. Thank you for always being so generous with your time to discuss physics and explain complex ideas in such an elegant and illuminating way. I was always astounded by your seemingly boundless knowledge of physics and mathematics. Undoubtedly, it was your brilliant course on wave physics that convinced me to reinterpret all of my results using a Green's function formalism!

I would also like to give a special mention to Peter Winlove, Gyaneshwar Srivastava, Pete Vukusic and Andrey Shytov who have inspired me during my time at Exeter.

Over the last few years, I have met many other fantastic people that have made this PhD experience so memorable. Thanks to Craig Tollerton for all the highly competitive squash games (I think you probably won 55-54 in the end, or thereabouts), to Joseph Beadle, Josh Hamilton and Miguel Camacho for all the joyful coffee breaks, and to all the crew on the third floor for creating an enjoyable office environment; Tom Sturges, Tom McDermott, Iori Thomas, Hai-Yao Deng, Angus Laurenson, Andy Wild, Jamie Le Signe and many others.

A special thanks goes to Tom Collier for all the beers down the pub, the political discussions, the many travel shenanigans, and for turning our office into an overgrown vegetable patch (though the chilli chutney was beautiful). You are a truly lovely man and I wish you and Laëtitia all the best in your new chapter together.

During my PhD I also had the great pleasure of supervising some brilliant Masters students: Daniel Bosworth, Andy Wild, Jordan Meadows, Henry Wang, Angus Crookes, Adam Chaou, Joshua Mitchell Cole and Isiah Rudkin-Crawford. I know that many of you have gone on to start your own PhD journey and I sincerely wish you all the best in whatever the future brings you.

I would also like to express my gratitude to everyone involved in the CDT who created such an interesting and engaging PhD experience. I am particularly indebted to Anja Roeding for supporting me through difficult periods of ill-health, and always being there to lend an ear. You have such a calming influence and a wonderful ability to relieve stress and anxiety in any situation.

To my family, you really are an odd bunch, but I love you all. Mum and Dad, thanks for always encouraging me to fulfill my potential as a child, whether that be in sport or academic work (I'm sorry that I chose physics over rugby in the end!). Stevie, Gavin and Clare, thanks for all the laughter, memories and support over the years.

Finally, to my darling Amy. Although you are quite terrible at maths and physics, you really should be a co-author of this thesis because none of this was possible without you. When we fell in love all those years ago at school, I knew you were going to change the course of my life forever. I didn't come from an academic background and I found the idea of university quite intimidating, but you encouraged me to follow my passion. You stayed by my side every step of the way, you always gave me the confidence to explore beyond my comfort zone, and you have always been there to put your arms around me when things are not going so well. Most importantly, you make me smile and laugh every single day, especially when you try to mimic my presentations without having a clue what a Dirac point is (even after reading my thesis). Amy, you have made me happier than I ever thought I could be and I love you so very much. I cannot wait to start the new chapter of our lives together.

"Physics isn't the most important thing. Love is"

Richard Feynman

Thesis abstract

The physics of graphene has been aptly described as “QED in a pencil trace” because the low-energy electrons behave like massless Dirac fermions – these exhibit pseudo-relativistic phenomena that were once thought to be exclusive to the realm of high-energy physics. Inspired by the rise of graphene, in this thesis we theoretically explore a range of novel phenomena that can emerge in 2D hexagonal metasurfaces composed of subwavelength arrays of dipole emitters/antennas. These metasurfaces exhibit Dirac polaritons whose properties are not solely determined by the intrinsic structure of the emitters and the metasurface geometry; in fact, their properties are also inextricably tied to the local photonic environment. Exploiting this hybrid light-matter nature of the Dirac polaritons, we unveil that one can dramatically alter their fundamental properties by structuring the photonic environment via a cavity waveguide.

First, we show that a honeycomb metasurface is not merely a simple analog of graphene, despite sharing the same underlying lattice structure. In particular, the metasurface exhibits two distinct species of massless Dirac polaritons, type-I and type-II, where the latter emerge from a non-trivial winding in the light-matter interaction. Moreover, by varying the cavity width one can induce the multi-merging of the type-I and type-II Dirac points and the subsequent annihilation of the type-II Dirac points. Consequently, we unveil a morphing between a linear and a quadratic spectrum which is accompanied by a change in the topological winding number and an inversion of the chirality.

Unfortunately, because the polaritons are neutral particles they do not experience a Lorentz force when subjected to a real magnetic field. Despite this fundamental drawback, we show that one can generate a pseudo-magnetic field for the polaritons by straining the honeycomb metasurface. Interestingly, by varying the cavity width one can tune the strength of the pseudo-magnetic field and even switch it off entirely without modifying the strain configuration. This enables one to emulate phenomena such as Landau quantization, where varying the cavity width can induce a collapse and revival of the polariton Landau levels.

Finally, we show that one can generate non-trivial Berry curvature in momentum space by breaking the inversion symmetry of a kagome metasurface. Crucially, the geometrical and topological properties of the polaritons are not fixed by the symmetry-breaking perturbation but also depend qualitatively on the local photonic environment in which the dipoles are embedded. Specifically, we show that one can invert the valley-Chern numbers and thus switch the chirality of the polariton valley-Hall edge states by varying the cavity width.

Table of contents

List of figures

1

Introduction

Niels Bohr: *“What are you working on Mr. Dirac?”*

Paul Dirac: *“I’m trying to take the square-root of something.”*

Soon after this curious exchange at the 5th Solvay conference in 1927, Paul Dirac published his famous relativistic wave equation for the electron that now bears his name – the Dirac equation [1]. Guided almost entirely by mathematical beauty, Dirac was able to reconcile two fundamental pillars of theoretical physics, quantum mechanics and special relativity. From this unification emerged a natural explanation of the spin-1/2 angular momentum of the electron, without any ad-hoc assumptions. More striking, perhaps, was his outlandish prediction of anti-particles and the fact that matter itself could fleet in and out of existence, for which there was no empirical evidence at the time [2, 3]. Paul Dirac fundamentally altered our understanding of nature, which led to him being duly awarded the Nobel Prize for physics in 1933 and, despite the passing of many years, the Dirac equation remains a cornerstone of the standard model of particle physics.

In recent years, the Dirac equation has experienced somewhat of a renaissance within the unlikely field of condensed-matter physics. One would be forgiven for assuming that Dirac’s relativistic description of the electron is only relevant for high-energy physics, and that Schrodinger’s non-relativistic theory is entirely sufficient to describe the low-energy physics of condensed-matter systems – the electrons certainly do not scoot around near the speed of light. In fact, materials are extremely complex environments where electrons interact with seemingly impenetrable lattices of atoms that are often plagued with defects and disorder. As Wolfgang Pauli once famously remarked: “Festkörperphysik ist eine Schmutzphysik”, that is “solid-state physics is the physics of dirt”. Nevertheless, physicists have discovered a rapidly expanding catalog of condensed-matter systems whose low-energy quasiparticles are effectively governed by a Dirac-like Hamiltonian – a novel class of systems called Dirac materials [4].

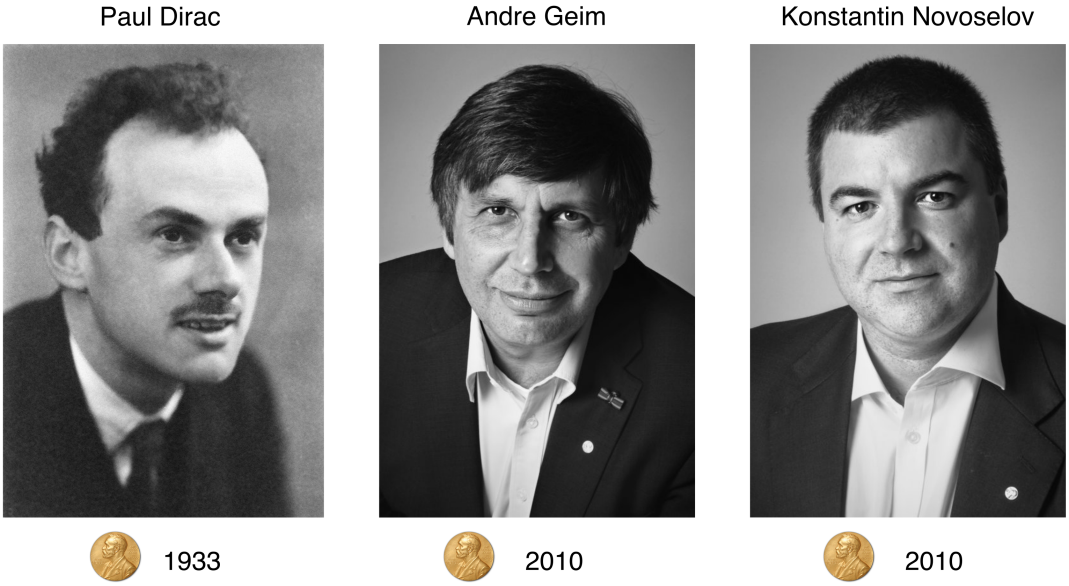

Figure 1.1 | Influential Nobel Prize winners. Paul Dirac (left [104]) was awarded the 1933 Nobel Prize in physics along with Erwin Schrödinger "for the discovery of new productive forms of atomic theory". Andre Geim (middle [105]) and Konstantin Novoselov (right [106]) were jointly awarded the 2010 Nobel Prize in physics "for groundbreaking experiments regarding the two-dimensional material graphene".

Undoubtedly, the most celebrated and intensely studied Dirac material is graphene: a two-dimensional (2D) monolayer of carbon atoms arranged in a honeycomb lattice [5]. The underlying symmetries conspire to rid the electrons of their effective mass, giving rise to linearly dispersing conduction and valence bands that touch at singular points in the Brillouin zone [6] – the so-called Dirac points. Consequently, the electrons in graphene behave like massless Dirac fermions which are effectively described by a massless Dirac Hamiltonian in (2+1)-dimensions [7], and thus exhibit pseudo-relativistic phenomena – it has quite aptly been described as "QED in a pencil trace" [8]. While its unique band structure had been known for decades [6], graphene was presumed to be thermodynamically unstable in the free state; it was generally viewed as a purely "academic material" [9] that was principally used as a starting point to study other carbon allotropes such as bulk graphite and carbon nanotubes.

However, after another round of their "Friday night experiments" at the University of Manchester, Andre Geim and Konstantin Novoselov successfully isolated monolayer graphene in 2004 by mechanically exfoliating bulk graphite [10]. This remarkable discovery, for which they were awarded the Nobel prize for physics in 2010, sparked a flurry of research that is still throwing up surprises till this very day. Any lab in possession of a pencil and scotch tape can explore pseudo-relativistic physics in simple table-top experiments without having to pay the hefty price of a particle accelerator – an academic material no more.

The most iconic example is the Klein paradox [11–14], which refers to the bizarre prediction that ultra-relativistic electrons would pass through extremely large potential barriers with unit probability if it far exceeds the rest energy of the electron [11]. This phenomenon has evaded experimental observation in high-energy physics because it is only relevant in a few exotic scenarios such as collisions of ultra-heavy ions [15, 16] and particle-antiparticle pair creation during black hole evaporation [17]. Yet, it turns out to underpin many of the remarkable transport properties of graphene and renders it impossible to confine the massless Dirac fermions using conventional electrostatic barriers [18].

Among a wealth of interesting phenomena in graphene, arguably the most spectacular is that elastic strain deformations of the graphene membrane generate a fictitious gauge field for the electrons [19–21]. Therefore, by judiciously engineering inhomogeneous strain patterns one can generate pseudo-magnetic fields that can mimic some of the properties of real ones [22–26]. For example, enormous pseudo-magnetic fields upwards of 300 tesla were first observed in graphene nanobubbles [27], far greater than that which can be achieved with real magnetic fields in a normal laboratory setting. Remarkably, scanning tunnelling spectroscopy measurements revealed that the electronic spectrum was reconstructed into a series of quantized Landau levels, despite the absence of a real magnetic field [27].

Interestingly, long before graphene was experimentally realized it also played a pivotal role in developing the field of topological insulators – these are systems which are characterized by an insulating bulk but have gapless edge states [28]. While the integer quantum Hall effect was the first topological phase of matter to be discovered in 1980 [29], it was generally believed to be a rather special case since it required large magnetic fields to induce Landau quantization. This naive view was overturned by Duncan Haldane who, in 1988, revealed that time-reversal symmetry breaking was the key ingredient for topological order [30]. To demonstrate this, he proposed an ingenious toy model that included a staggered magnetic flux through a graphene membrane with a vanishing net magnetic field. This perturbation gaps out the Dirac points and turns graphene into a Chern insulator which exhibits the quantum anomalous Hall effect [30]. The Chern insulator is characterized by an integer topological invariant known as the Chern number which, according to the bulk-boundary correspondence, predicts the number of chiral edge states at the boundary which are topologically protected against backscattering from disorder.

The next major theoretical advance came in 2005 from Charles Kane and Eugene Mele who showed that topological order could emerge even in the presence of time-reversal symmetry [31]. Specifically, they demonstrated that spin-orbit coupling could gap out the Dirac cones, turning graphene into a topological insulator which exhibits the quantum spin-Hall effect. This topological insulator is characterized by a $\mathbb{Z}_2$ topological invariant [32], which gives rise to a pair of spin-polarized chiral edge states that propagate in opposite directions and are robust against defects that cannot flip the spin (i.e., non-magnetic defects).

In analogy with spin, graphene also boasts an additional valley degree of freedom which labels energetically degenerate but inequivalent Dirac points at well-separated momenta in the Brillouin zone. If one gaps out the Dirac points by breaking inversion symmetry then one obtains an insulator which exhibits interesting valley-contrasting physics such as the valley-Hall effect [33–35]. While, strictly speaking, a valley-Hall insulator is topologically trivial it can be classified according to non-trivial valley-Chern numbers. If one then forms a domain wall between two valley-Hall insulators with opposite valley-Chern numbers then there is an associated bulk-boundary correspondence; the change in valley-Chern number across the interface predicts the number of valley-polarized chiral edge states that are robust against disorder that does not mix the two valleys [36–43].

It is important to stress that the emergence of Dirac points in the electronic spectrum of graphene is by no means an accident, and certainly not restricted to the specific physics of graphene; in fact, their existence is a direct manifestation of the underlying symmetries. This realization inspired an extensive quest to emulate some of these fascinating properties in a myriad of artificial Dirac systems [44–60], including ultracold atoms loaded into optical lattices [57] and carbon monoxide molecules deposited on a copper substrate [56]. Within the realm of photonics, graphene-related physics has been successfully simulated in honeycomb arrays of dielectric waveguides [60], microwave resonators [58], and semiconductor micropillars [59]. In these systems the evanescent coupling between lattice sites enables photons to effectively hop between neighbouring sites, thereby directly emulating the tight-binding physics of graphene.

One of the major attractions of these graphene simulators is that one can leverage the exquisite control over the lattice parameters to explore Dirac-related physics in regimes that are difficult, or even impossible to achieve in graphene itself. For example, a transition to a gapped insulating phase via the strain-induced merging and annihilation of the Dirac points attracted considerable theoretical attention as a possible mechanism to pinch off current in bulk graphene [61–64]. However, to date, this tantalizing transition has evaded experimental observation due to the very large strains required [62], but it has been observed in photonic graphene systems where it is relatively simple to imprint any arbitrary strain configuration into the lattice design [65–67]. Similarly, it remains extremely challenging to engineer the in-plane strain configurations in a graphene membrane that generate a uniform pseudo-magnetic field over a large area. However, they can be easily engineered in photonic lattices which provides a novel way of manipulating light [68–70].

Furthermore, given that photons are inert to real magnetic fields they do not undergo Landau quantization and, as a result, there is no direct analog of the quantum Hall effect for photons. Even so, pioneering theoretical work from Haldane and Raghu in 2005 demonstrated that topological protection could indeed be afforded to photons [71, 72], sparking the burgeoning field of topological photonics [73–75]. Shortly after, the first photonic analog of the Chern insulator was experimentally realized at microwave frequencies by applying an external magnetic field across a gyromagnetic photonic crystal [76]. However, with an eye on exploiting topological protection in photonic devices, the challenges involved in breaking time-reversal symmetry motivated the quest for passive topological photonic systems that preserve time-reversal symmetry.

Unfortunately, there is no photonic analog of the $\mathbb{Z}_2$ topological insulator because it relies on Kramer's theorem for fermions with half-integer spin which photons do not possess. Nevertheless, there have been many proposals for emulating the quantum spin-hall phase in photonic systems by engineering a variety of pseudo-spin degrees of freedom. These systems exhibit pseudo-spin polarized edge states with varying degrees of topological protection depending on the type of disorder which mixes the pseudo-spins [77–81]. In contrast, the valley degree of freedom is independent of the underlying particle statistics and emerges naturally in hexagonal lattices. Therefore, the photonic analog of the valley-Hall insulator can be easily induced by breaking certain lattice symmetries [82], and has been successfully realized across the electromagnetic spectrum at microwave [83–85], terahertz [86, 87], and optical [88–92] frequencies. Because these systems do not rely on magnetic fields or external driving to break time-reversal symmetry they hold great promise for revolutionizing future photonic devices.

1.1 Motivation of this thesis

Given the flexibility offered by photonic analogs of graphene, it is interesting to ask if one can modify the fundamental properties of the massless Dirac quasiparticles while preserving the underlying symmetries. It is evident that the symmetries place strict constraints on the effective Hamiltonian. In particular, the presence of time-reversal symmetry ($\mathcal{T}$) and spatial inversion symmetry ($\mathcal{I}$) locally stabilizes the Dirac points [93], preventing a gap from opening up, while the three-fold rotational symmetry ($\mathcal{C}_3$) pins the Dirac points to the

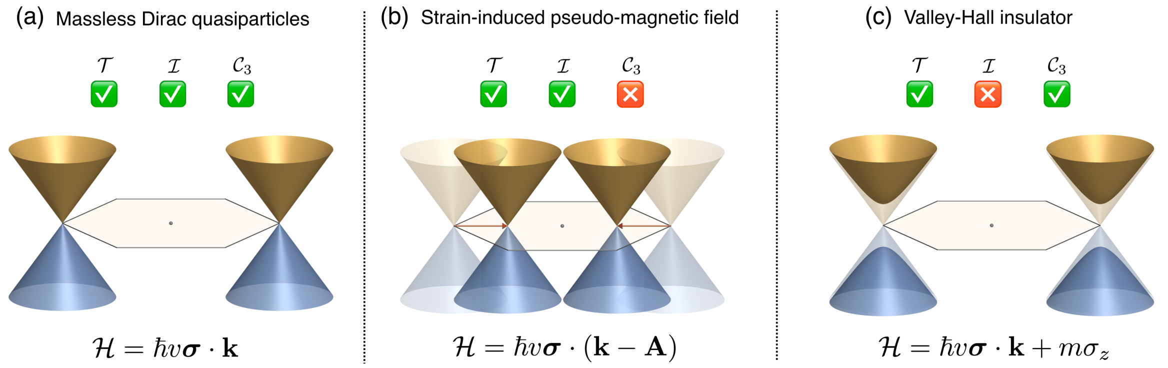

Figure 1.2 | Dirac physics in two-dimensions. (a) The combination of $\mathcal{T}$ and $\mathcal{I}$ symmetry locally stabilizes the Dirac points while the $\mathcal{C}_3$ symmetry pins them to the high-symmetry points. Consequently, the quasiparticles are effectively described by a 2D massless Dirac Hamiltonian with Dirac velocity v. (b) Straining the lattice breaks the $\mathcal{C}_3$ symmetry which decouples the Dirac points from the high-symmetry points, and the shift of the Dirac cone is described by a pseudo-vector potential $\mathbf{A}$. By judiciously engineering an inhomogeneous strain pattern one can generate a uniform pseudo-magnetic field. (c) Breaking the $\mathcal{I}$ symmetry generates a mass m in the effective Hamiltonian which gaps out the Dirac points, giving rise to a valley-Hall insulator that exhibits interesting valley-contrasting physics. While the symmetries constrain the form of the effective Hamiltonian in all three scenarios, they cannot tell us anything about the value of the Hamiltonian parameters such as the Dirac velocity, pseudo-vector potential and Dirac mass – these depend sensitively on the details of the system which, in principle, can be tuned.

high-symmetry points in the Brillouin zone as schematically shown in figure 1.2(a). However, the symmetries cannot tell us anything about the parameters in the Hamiltonian as these depend sensitively on the details of the system.

To leading order in momentum, the only parameter that enters the massless Dirac Hamiltonian is the Dirac velocity. Since the photonic graphene systems are intentionally designed to emulate the tight-binding physics of graphene, the Dirac velocity is predominantly determined by the nearest-neighbour interaction strength. However, the underlying symmetries do not preclude the existence of other Dirac points in the spectrum, nor do they protect the massless nature of the Dirac quasiparticles. Unfortunately, there is usually little room to modify the nature of the interactions between lattice sites, and consequently there exists no mechanism to qualitatively tune the Hamiltonian parameters while preserving the underlying symmetries.

A similar lack of tunability persists for the strain-induced pseudo-magnetic fields in photonic graphene systems. While real magnetic fields that are applied across samples in a lab can be tuned by varying external parameters, the pseudo-magnetic fields are usually determined solely by the strain configuration. To change the pseudo-magnetic field one has to precisely reconfigure the entire strain pattern – this is difficult, if not impossible to do and therefore one needs to fabricate an entirely new structure with a different strain pattern each time [68]. While, in principle, one could envisage engineering a photonic lattice on a flexible substrate, it would remain challenging to generate the required strain distribution across the sample with a controllable amplitude by applying external forces.

This drawback motivated us to ask whether it is possible to tune the pseudo-magnetic field without modifying the strain configuration at all. More interestingly, is it possible to switch the pseudo-magnetic field off without removing the strain? Straining the lattice breaks the $\mathcal{C}_3$ symmetry which permits a pseudo-vector potential term to appear in the Dirac Hamiltonian – this shifts the Dirac cone in momentum space away from the high-symmetry points as shown in figure 1.2(b). While the symmetries dictate the dependence of the pseudo-vector potential on the strain tensor [21], they cannot tell us anything about its magnitude for a given strain configuration. While it is almost inevitable that straining the lattice will generate a pseudo-vector potential, nothing in principle precludes us from tuning it to zero, there just exists no mechanism to do so in photonic graphene systems.

Furthermore, while the topological phase of a photonic Chern insulator can be changed by switching the direction of the applied magnetic field, the phase of the photonic valley-Hall insulator is determined by the symmetry-breaking perturbation that is usually imprinted into the lattice design. To deterministically change the valley-Chern numbers one needs to somehow invert the symmetry-breaking perturbation. However, it is usually difficult, if not impossible to reconfigure every unit cell in the photonic lattice after it has been fabricated, and therefore the valley-Hall edge states are usually forced to propagate in a fixed direction. This raises an interesting question: is it possible to induce topological transitions without inverting the symmetry-breaking perturbation? While breaking the inversion symmetry generates a mass term in the Dirac Hamiltonian that gaps out the Dirac points as depicted in figure 1.2(c), the value of the Dirac mass depends sensitively on the details of the system. Fundamentally, nothing prevents us from tuning the Dirac mass to zero and inverting the valley-Chern numbers via some other mechanism, without restoring the symmetry.

1.2 Outline of this thesis

What happens if we replace each carbon atom in graphene with a dipole emitter or antenna? Does the metasurface inherit some of the properties of graphene? Is this just another photonic analog of graphene? In this thesis, we explore these questions by considering 2D hexagonal metasurfaces composed of subwavelength arrays of interacting dipoles. We do not specialize to any particular system because we envisage that the essential physics could be realized in a variety of experimental set-ups, ranging from microwave metasurfaces composed of classical antennas to arrays of quantum emitters. These metasurfaces hybridize with the surrounding photons giving rise to mixed light-matter polaritons which are evanescently bound to the lattice. In stark contrast to the photonic analogs of graphene, the emitters do not simply interact only with their nearest-neighbours; in fact, the photons can mediate long-range dipole-dipole interactions whose strength oscillates with separation distance, thereby going beyond the paradigm of conventional tight-binding physics.

As one might expect, the underlying symmetries of the hexagonal metasurfaces endow the polaritons with Dirac-like properties – we refer to these as Dirac polaritons. However, due to the hybrid nature of the Dirac polaritons, their properties are not determined solely by the intrinsic structure of the emitters and the geometry of the metasurface; they are also inextricably linked to the local photonic environment in which the dipoles are embedded. Exploiting this, we show that one can modify the fundamental properties of the Dirac polaritons by structuring the surrounding photonic environment via an enclosing cavity waveguide.

Since the pioneering work by Edwin Purcell [94], it is well known that a cavity can either enhance or inhibit the spontaneous decay rate of an emitter because it modifies the availability and properties of the photonic modes that the emitter can couple to [95–99]. More importantly for this work, it follows that one can qualitatively modify the nature of the dipole-dipole interactions between emitters by varying the cavity width. Utilizing this mechanism, one can qualitatively tune the parameters in the effective Dirac polariton Hamiltonian without modifying the lattice geometry. Therefore, while intense efforts are devoted to designing photonic systems that emulate tight-binding models, this work hints at a rich landscape of physics emerging from non-trivial long-range interactions that are prevalent in electromagnetic systems.

The outline of this thesis is as follows:

Chapter 2: In this introductory chapter we provide a brief overview of some of the most interesting graphene-related physics. Using a simple tight-binding model we derive the massless Dirac Hamiltonian that describes the low-energy quasiparticles in graphene, and we show how this gives rise to Klein tunnelling and a pseudo-relativistic Landau level spectrum. Furthermore, we will unveil what constraints the underlying symmetries place on the form of the Hamiltonian, and we will proceed to see how breaking these symmetries leads to interesting phenomena. Specifically, we will show that straining the lattice gives rise to a pseudo-vector potential which can be judiciously engineered to generate a pseudo-magnetic field. For large uniform strains we show that one can induce the merging and annihilation of the Dirac points resulting in a trivial insulator. Finally, we will introduce two different models of non-trivial insulators that arise from gapping out the Dirac points: the Haldane model which breaks $\mathcal{T}$ symmetry and the Semenoff model which breaks $\mathcal{I}$ symmetry. The Haldane model represents a topological insulator with a non-zero Chern number and therefore supports unidirectional chiral edge states. In contrast, the Semenoff model represents a valley-Hall insulator with non-trivial valley-Chern numbers and thus exhibits valley-polarized chiral edge states along certain domain walls.

Chapter 3: In this technical chapter we lay the theoretical foundations that will be used as a starting point throughout the rest of the thesis. We begin by deriving the longitudinal and transverse components of the cavity Green's function which encode the Coulomb and photon-mediated interactions between the dipoles, respectively. Using a simple square metasurface as a concrete example, we develop a self-consistent coupled-dipole theory using the Green's function formalism, which can be used to describe the collective dynamics of dipoles embedded inside a cavity waveguide. Moreover, focusing on transverse dipolar excitations, we show how one can modify the nature of the dipole-dipole interactions by varying the cavity width. For relatively large cavity widths the short-range Coulomb interactions dominate the physics near the corners of the Brillouin zone due to the subwavelength spacing of the metasurface. However, for relatively small cavity widths the Coulomb interactions become suppressed due to the screening effect of the cavity, while the long-range photon-mediated interactions become dominant as the strength of the light-matter coupling is increased.

Chapter 4: In this chapter we explore the nature of the polaritons supported by a cavity-embedded honeycomb metasurface. Despite its superficial similarity with graphene, we show that the metasurface supports two distinct species of massless Dirac polaritons: type-I and type-II. The latter, more exotic class are characterized by critically tilted Dirac cones and have no counterpart in the standard model as they strongly break Lorentz invariance. While the deterministic type-I Dirac points are enforced by the symmetry, and are the analogs of the ones found in graphene, the type-II Dirac points are accidental and emerge from a non-trivial winding in the light-matter interaction; consequently, their existence depends critically on the nature of the dipole-dipole interactions. By varying the cavity width we show that one can manipulate the location of the type-II Dirac points in the Brillouin zone which leads to multiple phase transitions, including the multi-merging of type-I and type-II Dirac points and the subsequent annihilation of type-II Dirac points.

This chapter presents original research that was published as follows:

[100] Mann, C.-R., Sturges, T. J., Weick, G., Barnes, W. L. & Mariani, E. Manipulating type-I and type-II Dirac polaritons in cavity-embedded honeycomb metasurfaces. *Nature Communications* **9,** 2194 (2018).

Author contributions: C.-R.M. performed the theoretical calculations and wrote the manuscript; T.J.S. contributed to the theoretical calculations; E.M. and G.W. initially conceived the idea; E.M. and W.L.B. supervised the project. All authors commented on the manuscript.

Chapter 5: In this penultimate chapter we show that one can generate a pseudo-magnetic field for the massless Dirac polaritons by straining the honeycomb metasurface. Without altering the strain pattern, we unveil how one can tune the pseudo-magnetic field by modifying the photonic environment via an enclosing cavity waveguide. In fact, there exists a critical cavity width where the pseudo-magnetic field is completely switched off for any strain configuration. Consequently, for small strains one can generate a Lorentz-like force that deflects polariton wavepackets into effective cyclotron orbits whose radius can be controlled via the cavity width. For larger strains one can induce Landau quantization of the polariton cyclotron orbits, where modifying the cavity width can give rise to a collapse and revival of the polariton Landau levels.

This chapter presents original research that was published as follows:

[101] Mann, C.-R., Horsley, S. A. R. & Mariani, E. Tunable pseudo-magnetic fields for polaritons in strained metasurfaces. *Nature Photonics* **14**, 669-674 (2020).

Author contributions: C.-R.M. conceived the idea, developed the theory, performed the calculations and wrote the manuscript; S.A.R.H. contributed to the theoretical understanding; E.M. contributed to the theoretical understanding and supervised the project. All authors commented on the manuscript.

Chapter 6: In this final chapter we show how one can induce the valley-Hall phase for polaritons supported by a metasurface composed of identical dipoles. Specifically, we consider a kagome metasurface which exhibits deterministic Dirac points, and we proceed to gap them out by expanding/shrinking the distance between the dipoles within each unit cell which breaks the $\mathcal{I}$ symmetry. Crucially, the geometrical and topological properties of the polaritons are not solely determined by the symmetry-breaking perturbation but also depend critically on the surrounding photonic environment. By modifying the nature of the dipole-dipole interactions via the cavity width, we show that one can tune the Dirac mass and make it vanish at a critical cavity width, despite the broken $\mathcal{I}$ symmetry. Consequently, we demonstrate that one can invert the valley-Chern numbers and thus switch the chirality of the polariton valley-Hall edge states by modifying only the cavity width.

This chapter presents original research that has been submitted for publication as follows:

[102] Mann, C.-R., & Mariani, E. Topological transitions induced by cavity-mediated interactions in photonic metasurfaces. *arXiv:2010.01636* (2020).

Author contributions: C.-R.M. conceived the idea, developed the theory, performed the calculations and wrote the manuscript; E.M. contributed to the theoretical understanding and supervised the project. All authors commented on the manuscript.

Other publications not discussed in this thesis:

[103] Lamowski, S. , Mann, C.-R., Hellbach, F., Mariani, E., Weick, G. & Pauly, F. Plasmon polaritons in cubic lattices of spherical metallic nanoparticles. *Physical Review B* **97**, 125409 (2018).

2

Dirac physics in two-dimensions

DIRAC materials have built a bridge between the realm of high-energy physics and condensed-matter physics, enabling the exploration of pseudo-relativistic phenomena in simple table-top experiments. In this chapter we present a brief overview of some interesting physics related to the most celebrated Dirac material: graphene. We begin by introducing Dirac's relativistic equation for the electron in (3+1)-dimensions, and we show how the low-energy quasiparticles in graphene are effectively described by a massless Dirac Hamiltonian in (2+1)-dimensions. Furthermore, we demonstrate that the Dirac points correspond to topological defects in momentum space which are characterized by topological winding numbers, and we will unveil the symmetries that stabilize their existence. Then we will proceed to show how breaking these symmetries can give rise to intriguing phenomena. First, we demonstrate how inhomogeneous strain deformations can generate a pseudo-magnetic field, and we reveal how large uniform strains can induce the merging and annihilation of the Dirac points. Finally, we will introduce two different models of non-trivial insulators that exhibit interesting geometrical and topological properties and emerge from gapping out the Dirac points: the Haldane model and the Semenoff model.

2.1 Dirac's relativistic equation for the electron

Paul Dirac was a peculiar man whose mind was not constrained by empirical observations, but was almost entirely guided by the beauty of mathematical equations. In 1928, a few years after graduating from the University of Bristol with a degree in electrical engineering, Dirac published his relativistic theory of the electron [1]; one of the greatest achievements in the history of theoretical physics which challenged our intuition about the very nature of matter itself. As the result of his masterful leap of human imagination, Dirac was able to explain the origin of the electron's intrinsic spin-1/2 angular momentum and predict the existence of anti-particles – an extraordinary consequence of reconciling relativity and quantum mechanics.

To understand what motivated Dirac to develop his theory, it is natural to begin with the non-relativistic wave equation for a free electron

$$\mathrm{i}\hbar \frac{\partial \Psi_{\mathrm{S}}}{\partial t} = -\frac{\hbar^2}{2m}\nabla^2 \Psi_{\mathrm{S}}\,, \tag{2.1}$$

which was proposed by Erwin Schrödinger a couple years earlier in 1926 [107–112]. One can build this wave equation from the non-relativistic energy-momentum relation $E = |\mathbf{p}|^2/2m$ (where E is the energy, $\mathbf{p}$ is the momentum and m is the mass) by promoting the classical variables to operators via the identification $\mathbf{p} \to -\mathrm{i}\hbar\boldsymbol{\nabla}$ and $E \to \mathrm{i}\hbar\partial_t$, where $\hbar$ is the reduced Planck constant and $\boldsymbol{\nabla} = [\,\partial_x\,,\,\partial_y\,,\,\partial_z\,]$. These operators act on a complex scalar wavefunction Ψ_{S} which is interpreted as a probability amplitude, and its square modulus as a probability density.

In relativity theory, space and time are inextricably linked, and therefore a relativistic generalization of Schrödinger's equation demands that space and time derivatives must enter symmetrically. In 1927, Oskar Klein [113] and Walter Gordon [114] first attempted to reconcile relativity and quantum mechanics by promoting Einstein's energy-momentum relation $E^2 = c^2|\mathbf{p}|^2 + m^2c^4$ to a wave equation

$$\frac{1}{c^2}\frac{\partial^2 \Psi_{\mathrm{KG}}}{\partial t^2} = \left(\nabla^2 - \frac{m^2c^2}{\hbar^2}\right)\Psi_{\mathrm{KG}}\,, \tag{2.2}$$

where c is the speed of light. Unfortunately, while the Klein-Gordon equation is Lorentz-invariant, it was plagued with difficulties; in particular, the probability density was no longer positive definite which meant that the relativistic scalar Ψ_{KG} could no longer be legitimately interpreted as a probability amplitude as in Schrödinger's theory. At the time, this was a seemingly fundamental flaw which saw the Klein-Gordon equation abandoned as a plausible single-particle description of a relativistic electron.

To resolve this dilemma, Dirac sought after an equation that was first order in both space and time, thereby obtaining a Lorentz-invariant theory that gave positive-definite probability densities. Loosely speaking, he attempted to take the square-root of the Klein-Gordon equation by postulating a first-order wave equation of the form [1]

$$\mathrm{i}\hbar\frac{\partial\Psi_{\mathrm{D}}}{\partial t} = \Big(- \mathrm{i}\hbar c\boldsymbol{\alpha}\cdot\boldsymbol{\nabla} + \alpha_0 mc^2\Big)\Psi_{\mathrm{D}}\,, \tag{2.3}$$

where $\boldsymbol{\alpha} = [\,\alpha_1\,,\,\alpha_2\,,\,\alpha_3\,]$ and α_i $(i = 0,1,2,3)$ are some mathematical objects to be unveiled. The strict requirement of consistency with the Klein-Gordon equation places significant conditions on the algebraic properties of the α_i objects; that is, they must be involutory and anticommute with one another

$$\alpha_i^2 = \mathbb{1}\,, \quad \{\,\alpha_i\,,\,\alpha_j\,\} = 2\delta_{ij}\mathbb{1}\,, \tag{2.4}$$

where $\mathbb{1}$ is the identity element and δ_{ij} is the Kronecker delta function. While ordinary numbers obviously fail to meet these requirements, Dirac immediately realised that the 2×2 Pauli spin matrices

$$\sigma_x = \begin{bmatrix} 0 & 1 \\ 1 & 0 \end{bmatrix}, \quad \sigma_y = \begin{bmatrix} 0 & -\mathrm{i} \\ \mathrm{i} & 0 \end{bmatrix}, \quad \sigma_z = \begin{bmatrix} 1 & 0 \\ 0 & -1 \end{bmatrix}, \tag{2.5}$$

satisfied this anticommuting algebra – the first tantalizing glimpse that the union of quantum mechanics and relativity naturally endows the electron with an intrinsic spin-1/2 angular momentum.

However, there only exists three Pauli matrices, while four are needed to satisfy all of the conditions in (3+1)-dimensions. Consequently, Dirac was compelled to use 4×4 matrices which he constructed from the Pauli matrices

$$\alpha_x = \begin{bmatrix} 0 & \sigma_x \\ \sigma_x & 0 \end{bmatrix}, \quad \alpha_y = \begin{bmatrix} 0 & \sigma_y \\ \sigma_y & 0 \end{bmatrix}, \quad \alpha_z = \begin{bmatrix} 0 & \sigma_z \\ \sigma_z & 0 \end{bmatrix}, \quad \alpha_0 = \begin{bmatrix} \mathbb{1}_2 & 0 \\ 0 & -\mathbb{1}_2 \end{bmatrix}, \tag{2.6}$$

where $\mathbb{1}_2$ is the 2×2 identity matrix, with the immediate implication that the electron wavefunction Ψ_{D} could no longer be a scalar, but rather a 4-component spinor. Crucially, the low-energy limit of Dirac's relativistic equation recovered Pauli's phenomenological theory of the electron [115], which explained the necessity of a 2-component wavefunction to account for its spin-1/2 angular momentum and correctly predicted the magnetic moment with the anomalous gyromagnetic ratio – a remarkable achievement in its own right.

But what do the other two components correspond to in the full relativistic theory? This extra doubling gives rise to solutions with negative energies – a serious difficulty which Dirac was not immediately able to remedy. While negative energies can be simply disregarded in a classical theory on the grounds of being unphysical, Dirac knew that they posed a more fundamental problem in a quantum theory since perturbations could induce transitions from the positive-energy states to negative-energy states. However, Dirac later proposed a radical solution that empty space was, in fact, not very empty at all, but was filled entirely with negative-energy electrons – the so-called *Dirac sea* – which stabilized the vacuum by virtue of Pauli's exclusion principle [2]. From this, he further hypothesized the existence of an anti-electron which he viewed as a hole in the Dirac sea, and predicted that matter itself could fleet in and out of existence [3]:

> *"A hole, if there were one, would be a new kind of particle, unknown to experimental physics, having the same mass and opposite charge of the electron. We may call such a particle an anti-electron. We should not expect to find any of them in nature, on account of their rapid rate of recombination with electrons, but if they could be produced experimentally in high vacuum they would be quite stable and amenable to observation."*

Indeed, this was a very bold prediction because, at the time, there was no empirical evidence to suggest the existence of anti-particles. Yet, only a couple years later in 1932, Carl Anderson observed anomalous cosmic-ray tracks through a cloud chamber that matched the mass-to-charge ratio of an electron, but were bent in opposite direction due to their positive charge [116] – this was unambiguous evidence of Dirac's anti-electron which Anderson dubbed the positron. Subsequently, both Dirac and Anderson were duly awarded the Nobel Prize for physics in 1933 and 1936, respectively.

2.2 Graphene

It is entirely reasonable to suspect that Dirac's relativistic description of the electron plays little role in condensed-matter physics; after all, one is usually interested in energy scales much smaller than the rest energy of the electron. However, materials can provide a very complex environment – a renormalized vacuum, if you like – where the emergent electronic quasiparticles can exhibit drastically different properties from their free space counterparts. For example, many readers will be familiar with conventional band theory where the quasi-

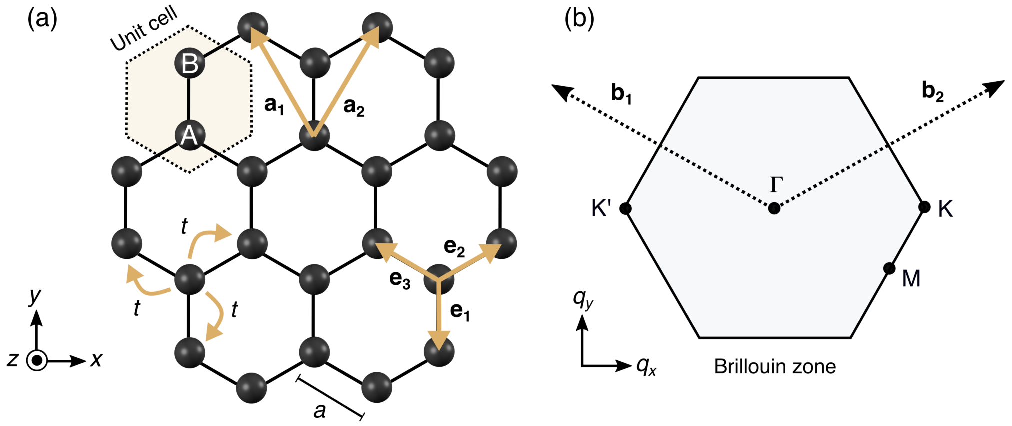

Figure 2.1 | Crystallographic structure of monolayer graphene. (a) Schematic of monolayer graphene which is composed of two inequivalent hexagonal sublattices of carbon atoms which we label A and B. The primitive lattice vectors are $\mathbf{a}_1$ and $\mathbf{a}_2$, while the three nearest-neighbour vectors are $\mathbf{e}_1$, $\mathbf{e}_2$ and $\mathbf{e}_3$, and a is the carbon-carbon distance. The essential electronic properties of graphene can be captured with a simple tight-binding model where t is the nearest-neighbour hopping parameter. (b) Corresponding first Brillouin zone in momentum space where the high-symmetry points are labelled and $\mathbf{b}_1$ and $\mathbf{b}_2$ are the primitive reciprocal lattice vectors.

particles can be described by a Schrödinger equation with a renormalized effective mass, which can even take negative values. In Dirac materials, we have a more exotic scenario where the quasiparticles are governed by a pseudo-relativistic Dirac equation.

The most intensely studied Dirac material is graphene, which is a crystalline allotrope of carbon consisting of a monolayer of atoms arranged in a 2D honeycomb array as schematically depicted in figure 2.1(a). This structure results from the sp^2 hybridization of the $2s$, $2p_x$ and $2p_y$ orbitals which form in-plane covalent σ-bonds between the neighbouring carbon atoms. The remaining $2p_z$ orbitals, which are oriented perpendicular to the graphene membrane, hybridize to form half filled π-bands which are responsible for most of the remarkable electronic properties exhibited by graphene.

Its unusual gapless spectrum was first calculated by Philip Wallace in 1947 [6], though principally serving as a starting point to understand the properties of bulk graphite. While graphene was a thriving theoretical toy model that was used to explore relativistic quantum electrodynamics in (2+1)-dimensions [7, 30], this atomically-thin 2D structure was presumed to be thermodynamically unstable until it was unexpectedly discovered by Andre Geim and Konstantin Novoselov in 2004 [10]. Graphene immediately assumed a celebrity-like status and its discovery was awarded the Nobel Prize only 6 years later, demonstrating the profound impact it has had on material science and condensed-matter physics.

2.2.1 Tight-binding model

The crystallographic structure of graphene is not a Bravais lattice. Instead, the carbon atoms are located at periodic positions $\mathbf{R}_{\mathrm{A}} = \mathbf{R} + \mathbf{d}_{\mathrm{A}}$ and $\mathbf{R}_{\mathrm{B}} = \mathbf{R} + \mathbf{d}_{\mathrm{B}}$, which form two inequivalent hexagonal sublattices that we label A and B, respectively. Here, the basis vectors

$$\mathbf{d}_{\mathrm{A}} = \frac{a}{2}\Big[\,0\,,\,-1\,\Big]\,, \quad \mathbf{d}_{\mathrm{B}} = \frac{a}{2}\Big[\,0\,,\,1\,\Big]\,, \tag{2.7}$$

locate the positions of the carbon atoms within the unit cell, where $a \approx 1.42$Å is the carbon-carbon separation distance. Furthermore, $\mathbf{R} = l_1\mathbf{a}_1 + l_2\mathbf{a}_2$ represent the set of lattice translation vectors describing the underlying hexagonal Bravais lattice, where $l_1, l_2 \in \mathbb{Z}$ are integers, and

$$\mathbf{a}_1 = \frac{\sqrt{3}a}{2}\Big[\,-1\,,\,\sqrt{3}\,\Big]\,, \quad \mathbf{a}_2 = \frac{\sqrt{3}a}{2}\Big[\,1\,,\,\sqrt{3}\,\Big]\,, \tag{2.8}$$

are the primitive lattice vectors. The corresponding set of reciprocal lattice vectors are $\mathbf{g} = n_1\mathbf{b}_1 + n_2\mathbf{b}_2$, where $n_1, n_2 \in \mathbb{Z}$ are integers, and

$$\mathbf{b}_1 = \frac{2\pi}{3a}\Big[\,-\sqrt{3}\,,\,1\,\Big]\,, \quad \mathbf{b}_2 = \frac{2\pi}{3a}\Big[\,\sqrt{3}\,,\,1\,\Big]\,, \tag{2.9}$$

are the primitive reciprocal lattice vectors which define the Brillouin zone shown in figure 2.1(b).

The essential electronic properties of graphene are captured by a single-orbital, spinless tight-binding model which, in the language of second quantization, reads

$$H = -t\sum_{\mathbf{R}_{\mathrm{B}}}\sum_{n=1}^{3} b^{\dagger}_{\mathbf{R}_{\mathrm{B}}} a_{\mathbf{R}_{\mathrm{B}}+\mathbf{e}_n} + \text{H.c.}\ . \tag{2.10}$$

Here, $a^{\dagger}_{\mathbf{R}_{\mathrm{A}}}$ and $b^{\dagger}_{\mathbf{R}_{\mathrm{B}}}$ create electrons in the $2p_z$ orbitals located at $\mathbf{R}_{\mathrm{A}}$ and $\mathbf{R}_{\mathrm{B}}$ on the A and B sublattices, respectively. Note, for convenience we have set the on-site energy of the $2p_z$ orbitals to zero. Furthermore, $t \approx 3$eV is the nearest-neighbour hopping parameter that determines the energy scale of the bands, and

$$\mathbf{e}_1 = a\Big[\,0\,,\,-1\,\Big]\,, \quad \mathbf{e}_2 = \frac{a}{2}\Big[\,\sqrt{3}\,,\,1\,\Big]\,, \quad \mathbf{e}_3 = \frac{a}{2}\Big[\,-\sqrt{3}\,,\,1\,\Big]\,, \tag{2.11}$$

are the nearest-neighbour vectors that connect the inequivalent sublattices.

We can exploit the discrete translational symmetry of the lattice by introducing the Fourier transform of the operators

$$a^\dagger(\mathbf{q}) = \frac{\sqrt{\mathcal{A}}}{2\pi}\sum_{\mathbf{R}_\mathrm{A}} a^\dagger_{\mathbf{R}_\mathrm{A}} \mathrm{e}^{\mathrm{i}\mathbf{q}\cdot\mathbf{R}_\mathrm{A}}\,, \quad b^\dagger(\mathbf{q}) = \frac{\sqrt{\mathcal{A}}}{2\pi}\sum_{\mathbf{R}_\mathrm{B}} b^\dagger_{\mathbf{R}_\mathrm{B}} \mathrm{e}^{\mathrm{i}\mathbf{q}\cdot\mathbf{R}_\mathrm{B}}\,, \tag{2.12}$$

which create Bloch functions that extend over the A and B sublattices, respectively. Here, $\mathbf{q} = [\, q_x\,,\, q_y\,]$ is the 2D Bloch wavevector that is restricted to the first Brillouin zone shown in figure 2.1(b), and $\mathcal{A} = 3\sqrt{3}a^2/2$ is the area of the unit cell shown in figure 2.1(a). Using equation (2.12) we can block diagonalize the tight-binding Hamiltonian in momentum space which can be written in matrix form as

$$H = \iint\limits_{\mathrm{BZ}} \mathrm{d}^2\mathbf{q}\, \psi^\dagger(\mathbf{q})\mathcal{H}(\mathbf{q})\psi(\mathbf{q})\,, \tag{2.13}$$

where $\psi^\dagger(\mathbf{q}) = [\, a^\dagger(\mathbf{q})\,,\, b^\dagger(\mathbf{q})\,]$ is a spinor operator. The corresponding 2×2 single-particle Bloch Hamiltonian in the sublattice space reads

$$\mathcal{H}(\mathbf{q}) = \begin{bmatrix} 0 & f(\mathbf{q}) \\ f^*(\mathbf{q}) & 0 \end{bmatrix}\,, \tag{2.14}$$

where the off-diagonal matrix elements are given by

$$f(\mathbf{q}) = -t\sum_{n=1}^{3} \mathrm{e}^{-\mathrm{i}\mathbf{q}\cdot\mathbf{e}_n}\,. \tag{2.15}$$

Equation (2.14) can easily be diagonalized to yield the spectrum of the electronic bands

$$E_\lambda(\mathbf{q}) = \lambda|f(\mathbf{q})|\,, \tag{2.16}$$

where $\lambda = \pm$ labels the valence ($\lambda = -$) and conduction ($\lambda = +$) bands. The corresponding spinor eigenstates

$$|\psi_\lambda(\mathbf{q})\rangle = \frac{1}{\sqrt{2}}\begin{bmatrix} 1 \\ \lambda\mathrm{e}^{\mathrm{i}\varphi(\mathbf{q})} \end{bmatrix} \tag{2.17}$$

encode an emergent pseudo-spin degree of freedom, where the two components describe the relative amplitude and phase of the wavefunction on the two inequivalent sublattices. We can

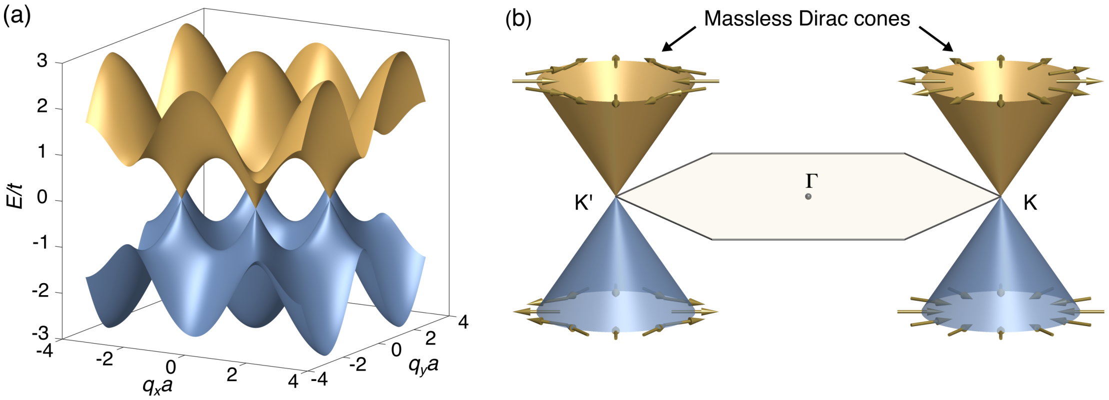

Figure 2.2 | Pseudo-relativistic spectrum of graphene. (a) Electronic band structure of monolayer graphene obtained with a nearest-neighbour tight-binding model. The conduction and valence bands coalesce at the high-symmetry K/K' points in the Brillouin zone which are called the Dirac points. (b) Within the vicinity of the Dirac points, the bands disperse linearly forming massless Dirac cones that are effectively described by a 2D massless Dirac Hamiltonian. The massless Dirac fermions are chiral because their pseudo-spin (gold arrows) is inextricably linked to the their momentum. For example, in the K valley the pseudo-spin is locked parallel/antiparallel to the momentum in the upper/lower bands. This chirality is responsible for many of graphene's remarkable electronic properties.

therefore represent the spinor eigenstates by a pseudo-spin vector on the Bloch sphere

$$\mathbf{S}_\lambda(\mathbf{q}) = \langle\psi_\lambda(\mathbf{q})|\,\boldsymbol{\sigma}\,|\psi_\lambda(\mathbf{q})\rangle = \lambda\,[\,\cos\varphi(\mathbf{q})\,,\,\sin\varphi(\mathbf{q})\,,\,0\,]\,, \tag{2.18}$$

where $\boldsymbol{\sigma} = [\,\sigma_x\,,\,\sigma_y\,,\,\sigma_z\,]$ is the vector of Pauli matrices and the azimuthal angle is given by

$$\varphi(\mathbf{q}) = \arg[f^*(\mathbf{q})]\,. \tag{2.19}$$

In figure 2.2(a) we show the electronic band structure within the nearest-neighbour approximation. The most notable feature is that the conduction and valence bands are degenerate at the corners of the Brillouin zone which are the so-called Dirac points. While it may appear that there are six unique Dirac points, only two of these are inequivalent since the others are related by reciprocal lattice vectors and thus correspond to the same states. In what follows we will focus on the inequivalent Dirac points located at

$$\tau\mathbf{K} = \tau\left[\frac{4\pi}{3\sqrt{3}a}\,,\,0\right]\,, \tag{2.20}$$

where $\tau = \pm$ is the valley index that corresponds to the high-symmetry K ($\tau = +$) and K' ($\tau = -$) points.

2.2.2 Emergent Dirac physics

In pristine graphene the two bands are half filled and therefore the Fermi energy resides exactly at the Dirac points. To elucidate the nature of the electronic quasiparticles near the Fermi energy we can derive an effective Hamiltonian that captures the essential physics within the vicinity of the Dirac points. To do this we expand the matrix elements in equation (2.15) near the K/K' points to leading order in $\mathbf{k} = \mathbf{q} - \tau\mathbf{K}$ which yields

$$f_\tau(\mathbf{k}) \simeq \hbar v_\mathrm{F}(\tau k_x - \mathrm{i}k_y)\,, \tag{2.21}$$

where $v_\mathrm{F} = 3ta/2\hbar$ is the Fermi velocity. Therefore, we can write the effective Hamiltonian near the Fermi energy as

$$H_\mathrm{eff} = \sum_{\tau=\pm} \iint \mathrm{d}^2\mathbf{k}\, \psi_\tau^\dagger(\mathbf{k})\mathcal{H}_\tau(\mathbf{k})\psi_\tau(\mathbf{k})\,, \tag{2.22}$$

where $\psi_\tau^\dagger(\mathbf{k}) = [\, a_\tau^\dagger(\mathbf{k})\,,\, b_\tau^\dagger(\mathbf{k})\,]$ is the spinor operator in each valley. Furthermore, the effective single-particle Hamiltonian for the K valley reads

$$\mathcal{H}_+(\mathbf{k}) = \hbar v_\mathrm{F}\begin{bmatrix} 0 & k_x - \mathrm{i}k_y \\ k_x + \mathrm{i}k_y & 0 \end{bmatrix} = \hbar v_\mathrm{F}\boldsymbol{\sigma}\cdot\mathbf{k}\,, \tag{2.23}$$

while the effective single-particle Hamiltonian for the K' valley reads

$$\mathcal{H}_-(\mathbf{k}) = \hbar v_\mathrm{F}\begin{bmatrix} 0 & -k_x - \mathrm{i}k_y \\ -k_x + \mathrm{i}k_y & 0 \end{bmatrix} = -\hbar v_\mathrm{F}\boldsymbol{\sigma}^*\cdot\mathbf{k}\,. \tag{2.24}$$

We can see that the low-energy quasiparticles within each valley are effectively described by a pseudo-relativistic Dirac Hamiltonian. Since the electrons in graphene exist within an effective (2+1)-dimensional space, the effective Hamiltonians in equation (2.23) and equation (2.24) are spanned by the 2×2 Pauli matrices which satisfy the anticommuting algebra $\{\sigma_i\,,\,\sigma_j\} = 2\delta_{ij}\mathbb{1}_2$ – we do not require the 4×4 Dirac matrices that are needed in (3+1)-dimensions. Furthermore, the matrix structure of the Hamiltonian does not originate from the real spin of the electron (which we have neglected in our treatment), but emerges from the presence of the two inequivalent sublattices which endow the electrons with a pseudo-spin degree of freedom – the Pauli matrices act within this sublattice space. Crucially, the third Pauli matrix σ_z does not appear in the Hamiltonian. Therefore, the electronic quasiparticles behave like massless Dirac fermions which exhibit a pseudo-relativistic linear spectrum near the K/K' points

$$E_\lambda(\mathbf{k}) = \lambda\hbar v_\mathrm{F}|\mathbf{k}|\,, \tag{2.25}$$

as depicted in figure 2.2(b) – these are referred to as massless Dirac cones.

As a result, the massless Dirac fermions exhibit a kind of chirality where the pseudo-spin is inextricably linked to the momentum. To see this, we can obtain the spinor eigenstates of the effective Hamiltonian within each valley which read

$$|\psi_{\tau\lambda}(\mathbf{k})\rangle = \frac{1}{\sqrt{2}}\begin{bmatrix} 1 \\ \tau\lambda \mathrm{e}^{\mathrm{i}\tau\phi_\mathbf{k}} \end{bmatrix}, \tag{2.26}$$

and the corresponding pseudo-spin vector is

$$\mathbf{S}_{\tau\lambda}(\mathbf{k}) = \langle\psi_{\tau\lambda}(\mathbf{k})|\,\boldsymbol{\sigma}\,|\psi_{\tau\lambda}(\mathbf{k})\rangle = \tau\lambda\,[\,\cos(\tau\phi_\mathbf{k})\,,\,\sin(\tau\phi_\mathbf{k})\,,\,0\,]\,, \tag{2.27}$$

where $\phi_\mathbf{k} = \arctan(k_y/k_x)$. For the K valley, the energy eigenstates are simultaneous eigenstates of the chirality operator

$$\boldsymbol{\sigma}\cdot\hat{\mathbf{k}}\,|\psi_{+\lambda}(\mathbf{k})\rangle = \lambda\,|\psi_{+\lambda}(\mathbf{k})\rangle\,, \tag{2.28}$$

where the pseudo-spin vector is locked parallel/antiparallel to the momentum in the upper/lower band as depicted in figure 2.2(b). For the K' valley, the energy eigenstates are simultaneous eigenstates of a more generalized chirality operator

$$\boldsymbol{\sigma}^*\cdot\hat{\mathbf{k}}\,|\psi_{-\lambda}(\mathbf{k})\rangle = -\lambda\,|\psi_{-\lambda}(\mathbf{k})\rangle\,, \tag{2.29}$$

where the pseudo-spin winds in the opposite direction to the momentum as depicted in figure 2.2(b). This chiral nature of the massless Dirac fermions gives rise to many of graphene's remarkable properties, some of which we will discuss in the following sections.

2.2.3 Pseudo-relativistic Klein tunnelling

The quantum tunnelling of a massive Schrödinger particle through a finite potential barrier is a typical exercise that every physics student encounters in an elementary quantum mechanics course [117–119]. The wavefunction becomes evanescent in the classically forbidden region, leading to a finite probability for the particle to tunnel through the barrier which is exponentially suppressed as the barrier width and height is increased.

However, in 1929, Oskar Klein applied Dirac's new relativistic equation to the same scattering problem and revealed a very counter-intuitive result: as the potential barrier is increased beyond the rest energy of the electron the transmission probability tends to unity [11]. This exotic prediction, which is often dubbed the Klein paradox [13, 14], caused a lot of confusion at the time. Shortly after in 1931, Fritz Sauter replaced Klein's infinitely sharp barrier with a more realistic linearly-varying potential and showed that the tunnelling probability is exponentially suppressed [12], as one might expect from the non-relativistic case. Consequently, the Klein tunnelling phenomenon requires very sharp barriers with a potential drop on the order of the electron rest energy ($\sim mc^2$) over a Compton wavelength ($\sim \hbar/mc$); this has rendered Klein's Gerdanken experiment relevant only in a few exotic scenarios within the realm of high-energy physics, such as collisions of ultra-heavy ions [15, 16] and particle-antiparticle pair creation during black hole evaporation [17].

Enter graphene. It's quite remarkable that such an elusive high-energy phenomenon would have any relevance in a condensed-matter system, yet it plays an key role in the electronic transport properties of graphene [18]. Let us consider a scenario where the massless Dirac fermions in graphene are incident upon a potential barrier which is translationally invariant along the y-direction $V = V(x)$. We assume that the potential barrier is smooth on the scale of the lattice constant so that intervalley scattering is negligible. Consequently, the valleys are decoupled and in what follows we will focus on the K valley where the effective Hamiltonian in real space reads

$$\mathcal{H}_+ = -\mathrm{i}\hbar v_\mathrm{F}\boldsymbol{\sigma}\cdot\boldsymbol{\nabla} + V(x)\mathbb{1}_2\,, \tag{2.30}$$

where we have used the replacement $\mathbf{k} \rightarrow -\mathrm{i}\boldsymbol{\nabla} = -\mathrm{i}[\,\partial_x\,,\,\partial_y\,]$. The effective Hamiltonian acts on the spinor envelope wavefunction $\psi(\mathbf{r}) = [\,\psi_\mathrm{A}(\mathbf{r})\,,\,\psi_\mathrm{B}(\mathbf{r})\,]$, where $\psi_\mathrm{A}(\mathbf{r})/\psi_\mathrm{B}(\mathbf{r})$ describes the component on the A/B sublattice. Note, we have also assumed that the potential is diagonal in the sublattice space, which is consistent with the approximation that it varies slowly on the scale of the lattice constant. Finally, for simplicity we assume that the potential is sharp on the scale of the Fermi wavelength $\lambda_\mathrm{F} = 2\pi/k_\mathrm{F}$, where $k_\mathrm{F} = E_\mathrm{F}/\hbar v_\mathrm{F}$ is the Fermi wavevector and $E_\mathrm{F} > 0$ is the Fermi energy that we take to be positive. This allows us to approximate the potential barrier as a piece-wise constant function

$$V(x) = V_0\Theta(x)\Theta(w-x)\,, \tag{2.31}$$

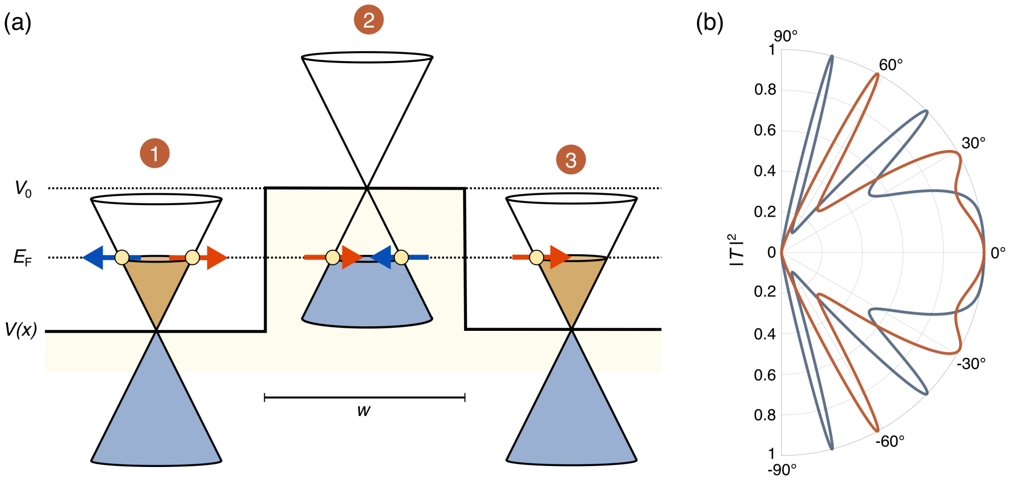

Figure 2.3 | Pseudo-relativistic Klein tunnelling in graphene. (a) Schematic of a npn-junction modelled as a square potential barrier of height V_0 and width w. We also depict the spectrum of the massless Dirac fermions in regions 1-3 which are incident from the left and the Fermi energy is positive $E_{\mathrm{F}} > 0$. The pseudo-spin vectors are depicted by red and blue arrows for the states that can take part in the scattering process at normal incidence, where we have neglected intervalley scattering and considered only the K valley. (b) Transmission probability at all incident angles through a barrier of height $V_0 = 3E_{\mathrm{F}}$ (blue line) and $V_0 = 3.3E_{\mathrm{F}}$ (red line). Due to the chirality of the massless Dirac fermions, backscattering is suppressed because a smooth potential cannot flip the pseudo-spin. Consequently, we observe perfect transmission through the barrier at normal incidence which is independent of the barrier height and width. Results obtained with $k_{\mathrm{F}} = 0.2/a$ and $w = 4\lambda_{\mathrm{F}}$.

where $\Theta(x)$ is the Heaviside step function and w is the width of the barrier. Furthermore, we specialize to the case where $V_0 > E_{\mathrm{F}}$ such that the barrier forms a npn-junction as schematically depicted in figure 2.3(a).

To solve this tunnelling problem we simply need to match the appropriate eigenstates at the interface using the relevant boundary conditions. The spinor envelope wavefunction in region 1 is given by

$$\psi_1(\mathbf{r}) = \frac{1}{\sqrt{2}} \begin{bmatrix} 1 \\ \mathrm{e}^{\mathrm{i}\phi_1} \end{bmatrix} \mathrm{e}^{\mathrm{i}(k_x x + k_y y)} + \frac{R}{\sqrt{2}} \begin{bmatrix} 1 \\ \mathrm{e}^{\mathrm{i}(\pi - \phi_1)} \end{bmatrix} \mathrm{e}^{\mathrm{i}(-k_x x + k_y y)} , \tag{2.32}$$

where the first term represents the incident wavefunction at an angle of incidence ϕ_1 with respect to the x-axis, and $k_x = k_{\mathrm{F}} \cos\phi_1$ and $k_y = k_{\mathrm{F}} \sin\phi_1$ are the corresponding wavevector components. The second term represents the reflected wavefunction, where R is the unknown reflection coefficient. In region 2, which is inside the barrier, the spinor envelope wavefunction reads

$$\psi_2(\mathbf{r}) = \frac{A_1}{\sqrt{2}} \begin{bmatrix} 1 \\ -\mathrm{e}^{\mathrm{i}\phi_2} \end{bmatrix} \mathrm{e}^{\mathrm{i}(k'_x x + k_y y)} + \frac{A_2}{\sqrt{2}} \begin{bmatrix} 1 \\ -\mathrm{e}^{\mathrm{i}(\pi - \phi_2)} \end{bmatrix} \mathrm{e}^{\mathrm{i}(-k'_x x + k_y y)} , \tag{2.33}$$

where the first term represents the refracted wave through the first interface and the second term represents the reflected wave from the second interface with unknown coefficients A_1 and A_2, respectively. Note, since the potential barrier is translationally invariant along the y-direction, the transverse component of the wavevector k_y will be preserved in each region. Therefore, $k'_x = \sqrt{k'^2_{\mathrm{F}} - k_y^2}$ where $k'_{\mathrm{F}} = k_{\mathrm{F}}(V_0/E_{\mathrm{F}} - 1)$ is the modified Fermi wavelength in the barrier region, and $\phi_2 = \arctan(k_y/k'_x)$ is the refraction angle. Finally, in region 3 the spinor envelope wavefunction reads

$$\psi_3(\mathbf{r}) = \frac{T}{\sqrt{2}} \begin{bmatrix} 1 \\ \mathrm{e}^{\mathrm{i}\phi_1} \end{bmatrix} \mathrm{e}^{\mathrm{i}(k_x x + k_y y)}\,, \tag{2.34}$$

where T is the unknown transmission coefficient.

As the Dirac Hamiltonian is first order in spatial derivatives we only require the continuity of the spinor wavefunction at the interfaces [18]

$$\psi_1(\mathbf{r})\bigg|_{x=0} = \psi_2(\mathbf{r})\bigg|_{x=0}\,, \quad \psi_2(\mathbf{r})\bigg|_{x=w} = \psi_3(\mathbf{r})\bigg|_{x=w}\,, \tag{2.35}$$

from which one can deduce the transmission coefficient

$$T = \frac{\mathrm{e}^{-\mathrm{i}k_x w} \cos\phi_1 \cos\phi_2}{\cos(k'_x w)\cos\phi_1\cos\phi_2 + \mathrm{i}\sin(k'_x w)(1 + \sin\phi_1 \sin\phi_2)}\,. \tag{2.36}$$

In figure 2.3(b) we plot the transmission probability $|T|^2$ at all incident angles for barrier heights of $V_0 = 3E_{\mathrm{F}}$ (blue line) and $V_0 = 3.3E_{\mathrm{F}}$ (red line), where we have used $k_{\mathrm{F}} = 0.2/a$ and $w = 4\lambda_{\mathrm{F}}$. While we can observe Fabry-Pérot-like resonances at oblique angles of incidence, these are strongly suppressed for smoother potential barriers [120]. The most striking result is at normal incidence ($\phi_1 = 0$), where the massless Dirac particles are perfectly transmitted through the barrier. Furthermore, unlike the Klein tunnelling phenomena for relativistic electrons, in graphene this perfect transmission at normal incidence persists for any barrier shape due to the massless nature of the Dirac fermions – there is no energy gap where the wavefunction becomes evanescent inside the barrier (see appendix A.1 for more details).

This absence of backscattering can also be shown by considering the elastic scattering from a smooth impurity potential $V(\mathbf{r})$. Within the first order Born approximation, the scattering probability reads

$$P(\Delta\phi) \propto |\,\langle\psi_{+\lambda}(\mathbf{k}')|\,V(\mathbf{r})\mathbb{1}_2\,|\psi_{+\lambda}(\mathbf{k})\rangle\,|^2 \propto |\tilde{V}(\mathbf{k}' - \mathbf{k})|^2 \cos\frac{\Delta\phi}{2}\,, \tag{2.37}$$

where $\tilde{V}(\mathbf{k}-\mathbf{k}')$ is the Fourier transform of the impurity potential and $\Delta\phi = \phi_{\mathbf{k}} - \phi_{\mathbf{k}'}$ is the angle between $\mathbf{k}$ and $\mathbf{k}'$. The first term is the usual result of the Born approximation, while the second term is called the chirality factor [121] and is given by the scalar product of the initial and final spinors. For the special case $\mathbf{k} \to -\mathbf{k}$ the matrix element vanishes identically, resulting in the complete suppression of backscattering – this has been shown to hold true to all orders in the scattering potential [122]. Another intuitive way to see this is to note that the chirality of the massless Dirac fermions means that the pseudo-spin is locked to the momentum. Therefore, any backscattering must be accompanied by a pseudo-spin flip, which is impossible if the potential varies smoothly on the scale of the lattice constant.

Signatures of the Klein tunnelling phenomenon have indeed been observed in transport experiments on graphene devices that incorporate electrostatic barriers [123–125]. In fact, it poses serious difficulties for electronic devices that require the charge transport to be switched off on demand, because conventional confinement strategies that exploit potential barriers fail spectacularly. However, it could also pave the way for novel graphene-based electronic devices with new functionality. For example, electrons passing through a np-junction exhibit negative refraction [126–128], in analogy with how light passes through a left-handed metamaterial with a negative refractive index [129, 130]. Furthermore, it has been proposed that one could exploit this for Veselago lensing of electrons [128].

2.2.4 Pseudo-relativistic Landau levels

The unexpected discovery of the integer quantum Hall effect by Klaus von Klitzing in 1980 [29], for which he was awarded the Nobel Prize in 1985, resulted in a paradigmatic shift within condensed-matter physics. This novel phase of matter did not fit into Landau's classification scheme based on spontaneous symmetry breaking, but required a different principal based on the notion of topological order. The quantum Hall effect arises when a 2D electron gas is subjected to a strong perpendicular magnetic field at sufficiently low temperatures, and it manifests as remarkably flat plateaus in the Hall conductivity that occur at integer multiples of e^2/h:

$$\sigma_{xy} = \frac{ge^2}{h}\nu\,, \qquad \nu = 0, \pm 1, \pm 2, \pm 3, \dots \tag{2.38}$$

Here, e is the electric charge, h is the Plank's constant, and $g = 2$ is the degeneracy factor that accounts for the two-fold spin degree of freedom. With improving sample quality over the years, the quantization is now observed up to a remarkable precision of about 1 part in 10^9 [131]. In the enthusiastic words of Ady Stern [132]:

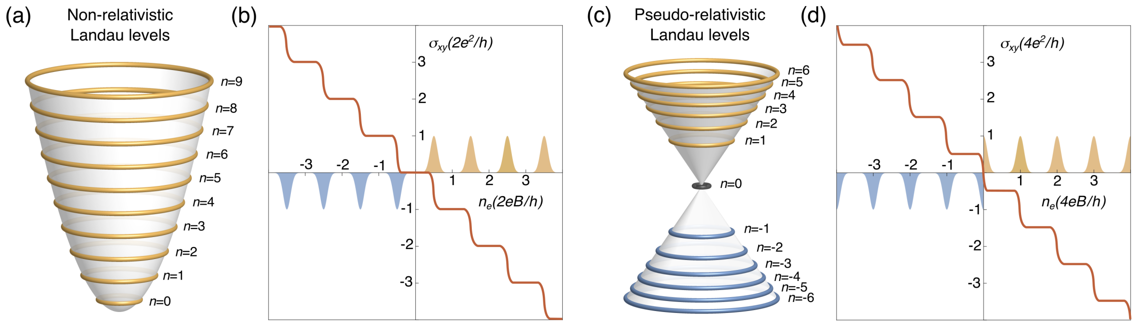

Figure 2.4 | Pseudo-relativistic Landau levels and the unconventional quantum Hall effect. (a) Landau level spectrum exhibited by a non-relativistic electron gas when subjected to a large magnetic field. (b) Schematic of the conventional quantum hall effect which manifests as a series of plateaus in the Hall conductivity at integer multiples of ge^2/h (red line), where $g = 2$ due to the spin degeneracy. The disorder-broadened Landau levels are also schematically depicted for the electrons (orange) and holes (blue). (c) Pseudo-relativistic Landau level spectrum exhibited by the massless Dirac fermions in graphene. (d) Schematic of the unconventional quantum Hall effect exhibited by graphene. Due to the anomalous zero-energy Landau level ($n = 0$) that is equally shared between the electrons and holes, the plateaus in the Hall conductivity occur at half-odd-integer multiples of ge^2/h, where $g = 4$ due to the spin and valley degeneracy.

“When we say it does not change, we mean it does not change. When we say it is a straight line, we mean it is the straightest line that you have ever seen. Think about it. It is independent of details, such as the material used, the shape of the sample, the name of the experimentalist, or the day of the week. Would you imagine that from such a dirty looking sample, the ratio of two fundamental constants of the universe would emerge? I have to say before going into details: this is so beautiful.”

An essential ingredient for the emergence of the quantum Hall effect is Landau quantization where the continuous spectrum becomes quantized into Landau levels [133]

$$E_n = \hbar\omega_{\mathrm{c}}\left(n + \frac{1}{2}\right), \qquad n = 0, 1, 2, 3, \ldots \tag{2.39}$$

as shown in figure 2.4(a). This equidistant ladder of discrete energy levels is due to the underlying quadratic dispersion of the non-relativistic electrons. The cyclotron frequency $\omega_{\mathrm{c}} = eB/m$ determines the size of the gap between the Landau levels which scales linearly with the magnetic field strength B, where m is the effective mass. Furthermore, each Landau level is macroscopically degenerate where the number of states per unit area is $n_B = gB/\phi_0$, with $\phi_0 = h/e$ being the magnetic flux quantum.

Robert Laughlin beautifully argued that the quantized Hall conductance is a direct consequence of gauge invariance and the existence of a mobility gap [134], while Bertrand Halperin emphasized the existence of chiral edge states which carry the current and do not become localized in the presence of disorder [135]. Heuristically, these chiral edge states may be understood from a semi-classical perspective as stemming from skipping cyclotron orbits at the boundary. On the other hand, in a series of remarkable papers, David Thouless and others [136–140] showed that the global geometric properties of the filled bulk eigenstates can be characterized by an integer topological invariant, known as the TKNN invariant or Chern number, which precisely determines the quantized Hall conductance – we will discuss the Chern number in more detail in section 2.4.1. The link between these two viewpoints remained unclear until Yasuhiro Hatsugai rigorously established a bulk-boundary correspondence [141, 142], where he showed that the Chern number of the filled bands determines the number of chiral edge states which contribute to the transport.

Rather ironically, the fact that the perfect plateaus exist over a wide range of parameters is due to the presence of moderate disorder within the sample. The disorder broadens the Landau levels and creates a reservoir of localized bulk states where the Fermi energy can be pinned without modifying the transport characteristics as the electron density n_e is varied – even Wolfgang Pauli would have been impressed by the importance of dirt. The precise distribution of the microscopic impurities is unimportant as this can be viewed as continuous deformations of the system which cannot change the topological invariant, as long as the disorder is not strong enough to collapse the bulk gap. Therefore, the Hall conductance exhibits plateaus when the Fermi energy falls between Landau levels, and jumps by an amount of ge^2/h when the Fermi energy crosses each Landau level as schematically depicted in figure 2.4(b).

To see how the story is modified in graphene we can employ the Peierls substitution into the effective Dirac Hamiltonian for each valley

$$\mathcal{H}_+ = v_{\mathrm{F}}\boldsymbol{\sigma}\cdot\left[-\mathrm{i}\hbar\boldsymbol{\nabla}+e\mathbf{A}(\mathbf{r})\right] , \quad \mathcal{H}_- = -v_{\mathrm{F}}\boldsymbol{\sigma}^*\cdot\left[-\mathrm{i}\hbar\boldsymbol{\nabla}+e\mathbf{A}(\mathbf{r})\right] , \tag{2.40}$$

where $\mathbf{A}$ is the magnetic vector potential that determines the magnetic field $\mathbf{B} = \boldsymbol{\nabla}\times\mathbf{A}$. This approximation is valid as long as the magnetic field strength is sufficiently small so that the corresponding magnetic length $l_B = \sqrt{\hbar/eB}$ in much larger than the lattice spacing $l_B \gg a$. We can find the Landau level spectrum exactly using a purely algebraic approach, which is similar to the algebraic solution of the harmonic oscillator. First we introduce the mechanical momentum operators

$$\mathit{\Pi}_x = -\mathrm{i}\hbar\partial_x + eA_x , \quad \mathit{\Pi}_y = -\mathrm{i}\hbar\partial_y + eA_y , \tag{2.41}$$

which satisfy the commutation relations $[\mathit{\Pi}_y\,,\,\mathit{\Pi}_x] = \mathrm{i}\hbar eB$, and from these we can construct creation and annihilation operators

$$c = \frac{1}{\sqrt{2\hbar eB}}(\mathit{\Pi}_x - \mathrm{i}\mathit{\Pi}_y)\,, \quad c^\dagger = \frac{1}{\sqrt{2\hbar eB}}(\mathit{\Pi}_x + \mathrm{i}\mathit{\Pi}_y)\,, \tag{2.42}$$

which satisfy the usual harmonic oscillator commutation relations $[\,c\,,\,c^\dagger\,] = 1$. In terms of these new operators, the effective Hamiltonian for each valley can be written as

$$\mathcal{H}_+ = \sqrt{2\hbar eBv_\mathrm{F}^2}\begin{bmatrix} 0 & c \\ c^\dagger & 0 \end{bmatrix}\,, \quad \mathcal{H}_- = -\sqrt{2\hbar eBv_\mathrm{F}^2}\begin{bmatrix} 0 & c^\dagger \\ c & 0 \end{bmatrix}\,. \tag{2.43}$$

The corresponding eigenstates can then be constructed from the eigenstates of the number operator $c^\dagger c\,\big||n|\big\rangle = |n|\,\big||n|\big\rangle$, where $n \in \mathbb{Z}$ is an integer that will be interpreted as the Landau level index. For $n \neq 0$ the eigenstates read

$$\big|\psi_+^n\big\rangle = \frac{1}{\sqrt{2}}\begin{bmatrix} \mathrm{sgn}(n)\,\big||n|-1\big\rangle \\ \big||n|\big\rangle \end{bmatrix}\,, \quad \big|\psi_-^n\big\rangle = \frac{1}{\sqrt{2}}\begin{bmatrix} \big||n|\big\rangle \\ -\,\mathrm{sgn}(n)\,\big||n|-1\big\rangle \end{bmatrix}\,, \tag{2.44}$$

while for $n = 0$ the eigenstates are

$$\big|\psi_+^0\big\rangle = \begin{bmatrix} 0 \\ |0\rangle \end{bmatrix}\,, \quad \big|\psi_-^0\big\rangle = \begin{bmatrix} |0\rangle \\ 0 \end{bmatrix}\,. \tag{2.45}$$

These eigenstates can be easily verified by applying the Hamiltonian operators and the corresponding quantized Landau level spectrum is given by [30, 143, 144]

$$E_n = \mathrm{sgn}(n)\hbar\omega_\mathrm{c}\sqrt{|n|}\,, \qquad n = 0, \pm1, \pm2, \pm3, \ldots \tag{2.46}$$

where $\omega_\mathrm{c} = \sqrt{2eBv_\mathrm{F}^2/\hbar}$. This pseudo-relativistic spectrum, which is shown in figure 2.4(c), stands in sharp contrast to the conventional Landau level spectrum exhibited by non-relativistic electrons. In particular, the Landau levels scale with the squareroot of the Landau index and magnetic field strength due to the linear spectrum of the massless Dirac fermions – this has been directly verified by measuring cyclotron resonances in infrared transmission experiments [145, 146] and by measuring tunneling current in scanning tunneling spectroscopy experiments [147, 148]. Moreover, due to the chirality of the massless Dirac fermions, graphene exhibits a zero-energy Landau level ($n = 0$) that is independent of the magnetic field and is half filled at $n_e = 0$. This anomaly is responsible for the unconventional quantum

Hall effect in graphene where, as schematically depicted in figure 2.4(d), the plateaus in the Hall conductivity occur at half-odd-integer multiples of ge^2/h [144, 149]:

$$\sigma_{xy} = \frac{ge^2}{h}\nu\,, \qquad \nu = \pm 1/2, \pm 3/2, \pm 5/2, \ldots \tag{2.47}$$

Here, the degeneracy factor is $g = 4$ due to presence of both spin and valley degrees of freedom. This unusual series of plateaus has been directly observed in graphene [150, 151] providing conclusive evidence of the pseudo-relativistic nature of the charge carriers.

2.2.5 Topological stability of the Dirac points

Given that we used a very minimal tight-binding model to describe the electronic properties of graphene, it is important to ask how stable the Dirac points are to perturbations, and to understand what underlying symmetries protect their existence. Furthermore, it is important to understand how robust the properties of the massless Dirac fermions are. For example: what happens if we make the hopping parameters anisotropic? What if we add long-range hopping between distant neighbours? What if we change the on-site energies of the A and B sublattices? Will the Dirac fermions remain massless? Is the chirality fixed?

To answer these questions, let us assume the most general form of a two-band Hamiltonian

$$\mathcal{H}(\mathbf{q}) = \begin{bmatrix} d_0(\mathbf{q}) + d_z(\mathbf{q}) & d_x(\mathbf{q}) - \mathrm{i}d_y(\mathbf{q}) \\ d_x(\mathbf{q}) + \mathrm{i}d_y(\mathbf{q}) & d_0(\mathbf{q}) - d_z(\mathbf{q}) \end{bmatrix} = d_0(\mathbf{q})\mathbb{1}_2 + \boldsymbol{\sigma}\cdot\mathbf{d}(\mathbf{q})\,, \tag{2.48}$$

with

$$\mathbf{d}(\mathbf{q}) = [\,d_x(\mathbf{q})\,,\, d_y(\mathbf{q})\,,\, d_z(\mathbf{q})\,]\,, \tag{2.49}$$

where $d_i(\mathbf{q}) \in \mathbb{R}$ are real functions ($i = 0, x, y, z$). The spectrum of the Hamiltonian is

$$E_\lambda(\mathbf{q}) = d_0(\mathbf{q}) + \lambda|\mathbf{d}(\mathbf{q})| = d_0(\mathbf{q}) + \lambda\sqrt{d_x^2(\mathbf{q}) + d_y^2(\mathbf{q}) + d_z^2(\mathbf{q})}\,, \tag{2.50}$$

and we can represent the corresponding spinor eigenstates by a pseudo-spin vector on the Bloch sphere which is given by

$$\mathbf{S}_\lambda(\mathbf{q}) = \lambda\hat{\mathbf{d}}(\mathbf{q}) = \frac{\lambda}{|\mathbf{d}(\mathbf{q})|}\,[\,d_x(\mathbf{q})\,,\, d_y(\mathbf{q})\,,\, d_z(\mathbf{q})\,]\;. \tag{2.51}$$

Note, while the diagonal term $d_0(\mathbf{q})$ modifies the spectrum (and can dramatically affect the properties), it does not affect the spinor eigenstates and plays no role in determining the stability of the Dirac points.

According to the von Neumann–Wigner theorem [152], in order to have an accidental degeneracy that is not by virtue of any symmetries we need to tune three parameters. This is because a degeneracy requires the three coefficients of the anticommuting Pauli matrices to vanish simultaneously

$$d_x(\mathbf{q}) = 0\,, \qquad d_y(\mathbf{q}) = 0\,, \qquad d_z(\mathbf{q}) = 0\,. \tag{2.52}$$

Unfortunately, in two dimensions we only have two momentum variables $\mathbf{q} = [\,q_x\,,\,q_y\,]$ that are naturally varied throughout the Brillouin zone; therefore, band degeneracies are generally unstable in two dimensions and they require fine tuning of the system parameters.

We can understand this lack of stability from a topological viewpoint. If we consider a closed contour $\mathit{\Gamma}$ in the Brillouin zone where the bands are gapped – that is, any band degeneracies either lie inside or outside the contour – then $\mathbf{q} \to \hat{\mathbf{d}}(\mathbf{q})$ defines a map from a circle $\mathbb{S}^1$ to the Bloch sphere $\mathbb{S}^2$. Since the fundamental group of the sphere is trivial $\pi_1(\mathbb{S}^2) = 0$ (all loops on a sphere can be contracted to a point), there exists no topological invariant that can protect band crossings in two dimensions. Consequently, there exists arbitrarily small perturbations that can gap out the Dirac points.

However, the presence of symmetries can impose constraints on the Hamiltonian which can stabilize the presence of Dirac points in two dimensions. For graphene, the relevant symmetries are spatial inversion $\mathcal{I} : [x\,,\,y] \to [-x\,,\,-y]$ and time-reversal $\mathcal{T} : t \to -t$ [93]. The honeycomb lattice exhibits $\mathcal{I}$ symmetry with respect to the centre of the carbon-carbon bonds and the hexagons, and since the operation exchanges the two sublattices it is therefore represented by the unitary operator $\mathcal{U}_{\mathcal{I}} = \sigma_x$. Furthermore, $\mathcal{I}$ also sends $\mathbf{q} \to -\mathbf{q}$ and thus imposes the following constraint on the Bloch Hamiltonian

$$\mathcal{I} : \quad \mathcal{U}_{\mathcal{I}} \mathcal{H}(\mathbf{q}) \mathcal{U}_{\mathcal{I}}^{-1} = \sigma_x \mathcal{H}(\mathbf{q}) \sigma_x = \mathcal{H}(-\mathbf{q})\,, \tag{2.53}$$

which is satisfied if

$$d_0(\mathbf{q}) = d_0(-\mathbf{q})\,, \quad d_x(\mathbf{q}) = d_x(-\mathbf{q})\,, \quad -d_y(\mathbf{q}) = d_y(-\mathbf{q})\,, \quad -d_z(\mathbf{q}) = d_z(-\mathbf{q})\,. \tag{2.54}$$

Moreover, $\mathcal{T}$ does not affect the sublattices and is therefore represented by the anti-unitary operator $\mathcal{U}_{\mathcal{T}} = \mathcal{K}$ which represents complex conjugation. Furthermore, $\mathcal{T}$ also sends $\mathbf{q} \to -\mathbf{q}$ and thus imposes the following constraint on the Bloch Hamiltonian

$$\mathcal{T} : \quad \mathcal{U}_{\mathcal{T}} \mathcal{H}(\mathbf{q}) \mathcal{U}_{\mathcal{T}}^{-1} = \mathcal{H}^*(\mathbf{q}) = \mathcal{H}(-\mathbf{q})\,, \tag{2.55}$$

which is satisfied if

$$d_0(\mathbf{q}) = d_0(-\mathbf{q})\,, \quad d_x(\mathbf{q}) = d_x(-\mathbf{q})\,, \quad -d_y(\mathbf{q}) = d_y(-\mathbf{q})\,, \quad d_z(\mathbf{q}) = d_z(-\mathbf{q})\,. \tag{2.56}$$

It is evident that neither $\mathcal{I}$ or $\mathcal{T}$ symmetry can individually stabilize the Dirac points because they relate the Hamiltonians at $\mathbf{q}$ and $-\mathbf{q}$, and therefore they do not impose a constraint on the form of the Hamiltonian at a general momentum. However, the product of $\mathcal{I}$ and $\mathcal{T}$ symmetry imposes the following constraint

$$\mathcal{I}\mathcal{T}: \qquad (\mathcal{U}_\mathcal{I}\mathcal{U}_\mathcal{T})\mathcal{H}(\mathbf{q})(\mathcal{U}_\mathcal{I}\mathcal{U}_\mathcal{T})^{-1} = \sigma_x\mathcal{H}^*(\mathbf{q})\sigma_x = \mathcal{H}(\mathbf{q})\,, \tag{2.57}$$

which is satisfied if

$$d_0(\mathbf{q}) = d_0(\mathbf{q})\,, \quad d_x(\mathbf{q}) = d_x(\mathbf{q})\,, \quad d_y(\mathbf{q}) = d_y(\mathbf{q})\,, \quad -d_z(\mathbf{q}) = d_z(\mathbf{q})\,. \tag{2.58}$$

Consequently, the presence of $\mathcal{I}\mathcal{T}$ symmetry enforces the σ_z term in the Hamiltonian to vanish identically

$$d_z(\mathbf{q}) = 0\,. \tag{2.59}$$

Therefore, it is now possible to have stable Dirac points without any fine tuning of the system parameters since we only have two conditions to fulfill which depend on two momentum variables that are varied throughout the Brillouin zone.

From the viewpoint of topology, we note that when $\mathcal{I}\mathcal{T}$ symmetry is present then the tip of the pseudo-spin vector is restricted to the equatorial plane of the Bloch sphere which we can write as

$$\mathbf{S}_\lambda(\mathbf{q}) = \lambda\hat{\mathbf{d}}(\mathbf{q}) = \lambda\left[\,\cos\varphi(\mathbf{q})\,, \,\sin\varphi(\mathbf{q})\,, \,0\,\right]\,, \tag{2.60}$$

where the azimuthal angle is given by

$$\varphi(\mathbf{q}) = \arg[d_x(\mathbf{q}) + \mathrm{i}d_y(\mathbf{q})]\,. \tag{2.61}$$

If we again consider a closed contour $\mathit{\Gamma}$ in Brillouin zone where the bands are gapped, then $\mathbf{q} \to \hat{\mathbf{d}}(\mathbf{q})$ defines a map from a circle $\mathbb{S}^1$ to the equatorial plane of the Bloch sphere $\mathbb{S}^1$. Crucially, the fundamental group of the circle is non-trivial $\pi_1(\mathbb{S}^1) = \mathbb{Z}$, and the corresponding symmetry-protected topological invariant of the map is the pseudo-spin winding number

$$W = \oint_{\mathit{\Gamma}} \frac{\mathrm{d}\mathbf{q}}{2\pi} \cdot \boldsymbol{\nabla}_\mathbf{q}\,\varphi(\mathbf{q}) \in \mathbb{Z}\,, \tag{2.62}$$

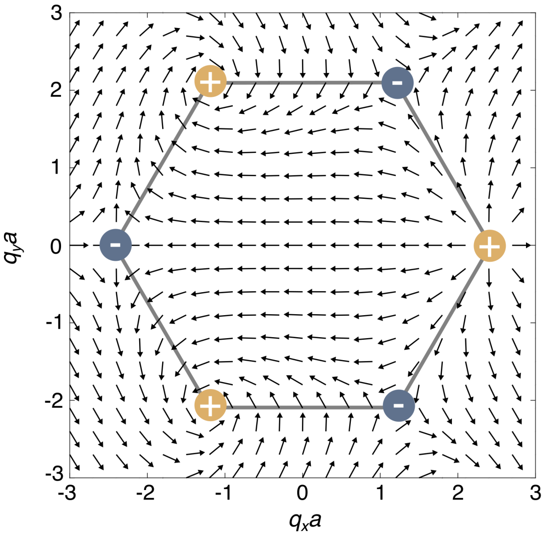

Figure 2.5 | Dirac points as topological defects in momentum space. Pseudo-spin field in momentum space corresponding to the conduction band in graphene. The Dirac points coincide with vortices in the pseudo-spin field which are located at the high-symmetry K/K' points. These are topological defects which are stabilized by the presence of $\mathcal{T}$ and $\mathcal{I}$ symmetry. We label them according to their topological winding numbers, where the Dirac point at the K point corresponds to a vortex with a topological charge of $+1$ (yellow circles), while the Dirac point at the K' point corresponds to an antivortex with a topological charge of -1 (blue circles).

where $\boldsymbol{\nabla}_{\mathbf{q}} = [\,\partial_{q_x}\,,\,\partial_{q_y}\,]$. This integer counts the number of rotations that the pseudo-spin vector undergoes as one traverses the closed path Γ in the anticlockwise direction – it does not depend on the precise details of the chosen contour and it can only change by an integer amount if the band gap closes on the contour. Note, for an arbitrary path the winding number cannot tell you how many Dirac points lie inside the contour; it can only tell you the total sum of the individual topological charges associated with the enclosed Dirac points.

In figure 2.5 we plot the pseudo-spin field in momentum space for the conduction band of graphene using equation (2.18). We observe that the Dirac points correspond to vortices in the pseudo-spin field; that is, they are topological defects in momentum space. The topological charges of the two inequivalent Dirac points can be calculated by considering a small circular contour Γ_τ that encloses each Dirac point, and using the effective Hamiltonian for each valley we obtain

$$W(\tau\mathbf{K}) = \oint_{\Gamma_\tau} \frac{\mathrm{d}\mathbf{k}}{2\pi} \cdot \boldsymbol{\nabla}_{\mathbf{k}} \, \arg\left(\tau k_x + \mathrm{i}k_y\right) = \oint_{\Gamma_\tau} \frac{\mathrm{d}\mathbf{k}}{2\pi} \cdot \boldsymbol{\nabla}_{\mathbf{k}} \, \left[\tau\phi_{\mathbf{k}}\right] = \tau \,. \qquad (2.63)$$

Therefore, the Dirac point in the K valley corresponds to a vortex with topological charge $+1$, where the pseudo-spin winds once in the anticlockwise direction, while the Dirac point in the

K' valley corresponds to an anti-vortex with topological charge -1, where the pseudo-spin winds once in the clockwise direction.

This vorticity that is associated with the Dirac points renders them locally stable. Any small perturbation that preserves $\mathcal{IT}$ symmetry cannot open a gap, it can only shift the location of the Dirac points. However, given that the two Dirac points carry opposite topological charges, they are not globally stable since a large perturbation could merge them together and annihilate them – we will discuss this scenario in more detail in section 2.3.2. Moreover, if we break $\mathcal{I}$ or $\mathcal{T}$ symmetry then we can gap out the Dirac points which gives rise to an insulator with interesting geometrical and topological properties – we will discuss these scenarios in more detail in section 2.4.

2.2.6 Symmetry constraints on the effective Hamiltonian

Next we will analyze the constraints imposed on the form of the effective Hamiltonian by the C_{3v} little point group of the K/K' points – this is the subgroup of the full C_{6v} honeycomb point group that leaves the K/K' points invariant modulo a reciprocal lattice vector. Note, while the little group at a generic wavevector is trivial, strict constraints are imposed on the small wavevector expansion within the vicinity of the high-symmetry points [21]. In what follows we will focus on the K point, since the effective Hamiltonian near the K' point is related by $\mathcal{T}$ symmetry (and $\mathcal{I}$ symmetry). Let us assume a general two-band Hamiltonian

$$\mathcal{H}_+(\mathbf{k}) = \begin{bmatrix} d_0(\mathbf{k}) & d_x(\mathbf{k}) - \mathrm{i}d_y(\mathbf{k}) \\ d_x(\mathbf{k}) + \mathrm{i}d_y(\mathbf{k}) & d_0(\mathbf{k}) \end{bmatrix} = d_0(\mathbf{k})\mathbb{1}_2 + \boldsymbol{\sigma}\cdot\mathbf{d}(\mathbf{k})\,, \tag{2.64}$$

with

$$\mathbf{d}(\mathbf{k}) = [\,d_x(\mathbf{k})\,,\, d_y(\mathbf{k})\,]\,, \tag{2.65}$$

where $d_i(\mathbf{k}) \in \mathbb{R}$ are real functions ($i = 0, x, y$) and $\mathbf{k} = \mathbf{q} - \mathbf{K}$ represents the wavevector measured from the K point.

The C_{3v} little point group is generated by $\{\,\mathcal{C}_3\,,\,\mathcal{M}_y\,\}$, where $\mathcal{C}_3$ represents an anticlockwise rotation by $2\pi/3$ about the z-axis and $\mathcal{M}_y : [\,x\,,y\,] \to [\,x\,,\,-y\,]$ represents a mirror reflection in the xz-plane. If we set the rotation centre to be a site located on the A sublattice then the unitary operator representing the rotation reads

$$\mathcal{U}_{\mathcal{C}_3} = \begin{bmatrix} 1 & 0 \\ 0 & \Omega \end{bmatrix}\,, \tag{2.66}$$

where $\Omega \equiv \mathrm{e}^{\mathrm{i}\frac{2\pi}{3}}$, which leads to the following constraint on the effective Hamiltonian

$$\mathcal{C}_3 : \quad \mathcal{U}_{\mathcal{C}_3}\mathcal{H}_+(\pi, \pi^*)\mathcal{U}_{\mathcal{C}_3}^{-1} = \mathcal{H}_+(\Omega\pi, \Omega^*\pi^*)\,. \tag{2.67}$$

For convenience, here we have introduced the complex representation of the wavevector $\pi = k_x + \mathrm{i}k_y$ and its complex conjugate $\pi^* = k_x - \mathrm{i}k_y$, because they transform simply under rotations as $\mathcal{C}_3\pi = \Omega\pi$ and $\mathcal{C}_3\pi^* = \Omega^*\pi^*$, respectively. The constraint given by equation (2.67) implies that the diagonal terms must satisfy

$$d_0(\pi, \pi^*) = d_0(\Omega\pi, \Omega^*\pi^*)\,, \tag{2.68}$$

and the off-diagonal terms must satisfy

$$[d_x(\pi, \pi^*) + \mathrm{i}d_y(\pi, \pi^*)]\Omega = d_x(\Omega\pi, \Omega^*\pi^*) + \mathrm{i}d_y(\Omega\pi, \Omega^*\pi^*)\,. \tag{2.69}$$

If we include up to quadratic terms in the wavevector expansion, then equation (2.68) is solved by

$$d_0(\mathbf{k}) = c_1 + c_2\pi\pi^* = c_1 + c_2(k_x^2 + k_y^2)\,, \tag{2.70}$$

where $c_1, c_2 \in \mathbb{R}$ are real constants, and equation (2.69) is solved by

$$d_x(\mathbf{k}) + \mathrm{i}d_y(\mathbf{k}) = c_3\pi + c_4\pi^{*2} = c_3(k_x + \mathrm{i}k_y) + c_4(k_x^2 - k_y^2 - 2\mathrm{i}k_xk_y)\,, \tag{2.71}$$

where $c_3, c_4 \in \mathbb{C}$ are complex constants in general.

Finally, the $\mathcal{M}_y$ symmetry planes bisect the carbon-carbon bonds and the operation exchanges the two sublattices – therefore, it is represented by the unitary operator $\mathcal{U}_{\mathcal{M}_y} = \sigma_x$. Moreover, it also sends $k_y \to -k_y$ which leads to the following constraint on the effective Hamiltonian

$$\mathcal{M}_y : \quad \mathcal{U}_{\mathcal{M}_y}\mathcal{H}_+(\mathbf{k})\mathcal{U}_{\mathcal{M}_y}^{-1} = \sigma_x\mathcal{H}_+(k_x\,,\,k_y)\sigma_x = \mathcal{H}_+(k_x\,,\,-k_y)\,, \tag{2.72}$$

which is satisfied if

$$d_0(k_x\,,\,k_y) = d_0(k_x\,,\,-k_y)\,,\ d_x(k_x\,,\,k_y) = d_x(k_x\,,\,-k_y)\,,\ -d_y(k_x\,,\,k_y) = d_y(k_x\,,\,-k_y)\,. \tag{2.73}$$

These conditions impose no further constraints on the general form of the Hamiltonian, but they enforce the coefficients in equation (2.71) to be real $c_3, c_4 \in \mathbb{R}$. However, from equation (2.72) and equation (2.67) one can show that the combination of $\mathcal{M}_y$ and $\mathcal{C}_3$ symmetries also enforce the σ_z term to vanish, even in the absence of $\mathcal{I}$ symmetry.

Putting all these constraints together, the most general form of the effective Hamiltonian near the K point up to quadratic order in $\mathbf{k}$ reads

$$\mathcal{H}_+(\mathbf{k}) = \Big[c_1 + c_2(k_x^2 + k_y^2)\Big]\mathbb{1}_2 + \Big[c_3 k_x + c_4(k_x^2 - k_y^2)\Big]\sigma_x + \Big[c_3 k_y - 2c_4 k_x k_y\Big]\sigma_y\,. \tag{2.74}$$

If we retain only the off-diagonal terms that are linear in $\mathbf{k}$, then this is equivalent to the effective Dirac Hamiltonian that we found for graphene in equation (2.23). Note, if we had continued the expansion of equation (2.21) to higher order in $\mathbf{k}$ then we would have also obtained the quadratic off-diagonal terms in equation (2.74). However, these terms are much smaller than the linear terms for $|\mathbf{k}|a \ll 1$ and therefore they just give rise to trigonal warping of the band structure [5]. Furthermore, the diagonal terms in equation (2.74) would arise if we included next-nearest-neighbour hopping, but they are also very small and thus only weakly break the electron-hole symmetry [5].

From equation (2.71) we can see that the $\mathcal{C}_3$ symmetry forces the off-diagonal terms in the Hamiltonian to vanish at the K point. Therefore, we have established that we can add arbitrary, long-range hopping to the tight-binding model (or any other perturbation) and the Dirac points will remain robust at the K/K' points, as long as they respect $\mathcal{T}$, $\mathcal{I}$ and $\mathcal{C}_3$ symmetry. However, this begs the question: are the fundamental properties of the massless Dirac fermions also robust? While the symmetry constrains the form of the Hamiltonian, the parameters depend sensitively on the details of the system which can have a dramatic effect on the properties of the corresponding quasiparticles.

To highlight this, we could contrive a set of hopping parameters within a toy model such that the linear terms vanish and only the quadratic off-diagonal terms survive. In this extreme case, the effective Hamiltonian near the K/K' points would read

$$\mathcal{H}_\tau(\mathbf{k}) = c_4 \begin{bmatrix} 0 & (\tau k_x + \mathrm{i}k_y)^2 \\ (\tau k_x - \mathrm{i}k_y)^2 & 0 \end{bmatrix}, \tag{2.75}$$

which is equivalent to the effective Hamiltonian that describes the dominant properties of the low-energy quasiparticles in AB-stacked bilayer graphene [153]. The Hamiltonian can be easily diagonalized to yield a quadratic spectrum

$$E_\lambda(\mathbf{k}) = \lambda c_4 |\mathbf{k}|^2\,, \tag{2.76}$$

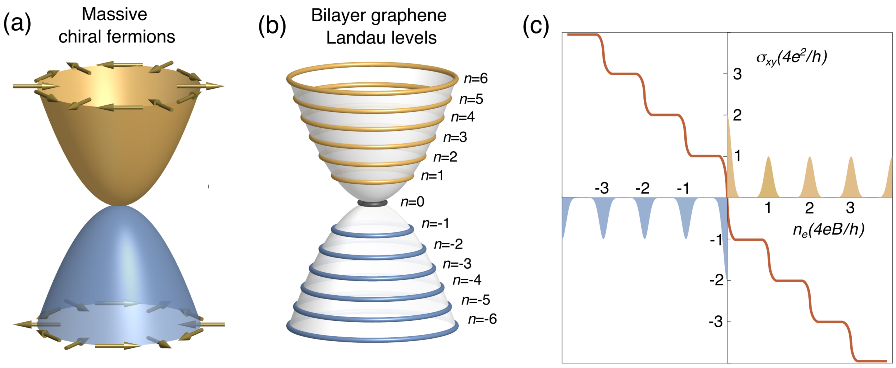

Figure 2.6 | Massive chiral fermions in bilayer graphene. (a) Quadratic spectrum of the massive chiral fermions near the K point, where the pseudo-spin winds twice around the hybrid Dirac point. (b) Landau level spectrum exhibited by the massive chiral fermions where the zero-energy Landau level ($n = 0$) has twice the degeneracy of the other Landau levels due to the doubling of the winding number. (c) Schematic of the unconventional quantum Hall effect exhibited by bilayer graphene where the plateaus in the Hall conductivity occur at integer multiples of ge^2/h, where $g = 4$ due to the spin and valley degeneracy. This is reminiscent of the conventional case, but the plateau at $n_e = 0$ is missing due to the degeneracy doubling of the zero-energy Landau level.

as depicted in figure 2.6(a), and the corresponding eigenstates read

$$|\psi_{\tau\lambda}(\mathbf{k})\rangle = \frac{1}{\sqrt{2}} \begin{bmatrix} 1 \\ \tau\lambda \mathrm{e}^{-\mathrm{i}2\tau\phi_{\mathbf{k}}} \end{bmatrix} . \tag{2.77}$$

While the quasiparticles are no longer massless, the spectrum is still gapless but with quadratic band degeneracies at the K/K' points that are characterized by higher-order topological charges

$$W(\tau\mathbf{K}) = \oint_{\Gamma_\tau} \frac{\mathrm{d}\mathbf{k}}{2\pi} \cdot \boldsymbol{\nabla}_{\mathbf{k}} \arg\left[(\tau k_x - \mathrm{i}k_y)^2\right] = \oint_{\Gamma_\tau} \frac{\mathrm{d}\mathbf{k}}{2\pi} \cdot \boldsymbol{\nabla}_{\mathbf{k}} \left[-2\tau\phi_{\mathbf{k}}\right] = -2\tau\,. \tag{2.78}$$

Consequently, the pseudo-spin

$$\mathbf{S}_{\tau\lambda}(\mathbf{k}) = \tau\lambda\left[\,\cos(-2\tau\phi_{\mathbf{k}})\,,\,\sin(-2\tau\phi_{\mathbf{k}})\,,\,0\,\right]\,, \tag{2.79}$$

winds twice around the quadratic band degeneracies as schematically shown in figure 2.6(a). We refer to these as hybrid Dirac points because they split into multiple Dirac points under small perturbations of the Hamiltonian.

This modified dispersion and pseudo-spin winding number means that bilayer graphene exhibits qualitatively different properties compared to graphene [154]. For example, if we consider elastic scattering from a smooth impurity potential $V(\mathbf{r})$, as we did in section 2.2.3, then within the first Born approximation the scattering probability is

$$P(\Delta\phi) \propto |\left\langle\psi_{\tau\lambda}(\mathbf{k}')\right| V(\mathbf{r})\mathbb{1}_2 \left|\psi_{\tau\lambda}(\mathbf{k})\right\rangle|^2 \propto |\tilde{V}(\mathbf{k}'-\mathbf{k})|^2 \cos\Delta\phi\,. \tag{2.80}$$

In stark contrast to graphene, here the chirality factor is maximum for backscattering $\mathbf{k} \to -\mathbf{k}$ because the pseudo-spins point in the same direction. As a result, it has been shown that bilayer graphene exhibits perfect reflection (anti-Klein tunnelling) when normally incident on a npn-barrier [18].

Moreover, the corresponding Landau level spectrum in the presence of a large magnetic field reads [153]

$$E_n = \mathrm{sgn}(n)\hbar\omega_\mathrm{c}\sqrt{|n|(|n|+1)}\,, \qquad n = 0, \pm 1, \pm 2, \pm 3, \ldots \tag{2.81}$$

as schematically shown in figure 2.6(b), where $\omega_\mathrm{c} = eB/m$ and $m \propto 1/c_4$ is the effective mass. Crucially, the doubling of the winding number doubles the degeneracy of the zero-energy Landau level ($n = 0$) where the corresponding eigenstates are

$$\left|\psi_+^{0,0}\right\rangle = \begin{bmatrix} 0 \\ |0\rangle \end{bmatrix}, \quad \left|\psi_+^{0,1}\right\rangle = \begin{bmatrix} 0 \\ |1\rangle \end{bmatrix}, \quad \left|\psi_-^{0,0}\right\rangle = \begin{bmatrix} |0\rangle \\ 0 \end{bmatrix}, \quad \left|\psi_-^{0,1}\right\rangle = \begin{bmatrix} |1\rangle \\ 0 \end{bmatrix}. \tag{2.82}$$

Therefore, bilayer graphene exhibits another distinct type of quantum Hall effect, where the plateaus in the Hall conductivity occur at integer multiples of ge^2/h [153]:

$$\sigma_{xy} = \frac{ge^2}{h}\nu\,, \qquad \nu = \pm 1, \pm 2, \pm 3, \ldots \tag{2.83}$$

where $g = 4$ due to the spin and valley degrees of freedom. This scenario, which is schematically shown in figure 2.6(c), resembles the conventional quantum Hall effect for a non-relativistic electron gas, which one may expect given the quadratic dispersion. However, the plateau at $n_e = 0$ is missing due to the degeneracy doubling of the zero-energy Landau level and this results in a larger step of $8e^2/h$ which has been observed experimentally [155].

2.3 Strained graphene

Unfortunately, there currently exists no mechanism to tune the hopping parameters in graphene while preserving the symmetries, and therefore the properties of the massless Dirac quasiparticles are fixed by the rigid lattice structure. However, elastic deformations of the graphene membrane can change the orientation and length of the carbon-carbon bonds which, in turn, can modify the hopping parameters and give rise to interesting physics – this is the essence of the tantalizing concept known as strain-engineering [62, 156]. Straining the lattice breaks the $\mathcal{C}_3$ symmetry which means the Dirac points are no longer pinned to the high-symmetry points and the Dirac cones can shift in momentum space. To capture the essential physics related to strain we will explore the generalized tight-binding Hamiltonian

$$H = -\sum_{\mathbf{R}_\mathrm{B}} \sum_{n=1}^{3} t_n b^\dagger_{\mathbf{R}_\mathrm{B}} a_{\mathbf{R}_\mathrm{B}+\mathbf{e}_n} + \mathrm{H.c.}\ , \tag{2.84}$$

where the hopping parameters t_n can vary along the three nearest-neighbour bonds. However, for simplicity, we will assume that the carbon atoms remain located at their original unstrained positions.

2.3.1 Strain-induced pseudo-magnetic field

First we will restrict our attention to very small deformations of the membrane and discuss one of the most striking consequences of the Dirac-like spectrum in graphene: the emergence of strain-induced pseudo-magnetic fields. The lattice deformation shifts the carbon atoms to new positions

$$\bar{\mathbf{R}}_\mathrm{A} = \mathbf{R}_\mathrm{A} + \mathbf{u}(\mathbf{R}_\mathrm{A})\,, \quad \bar{\mathbf{R}}_\mathrm{B} = \mathbf{R}_\mathrm{B} + \mathbf{u}(\mathbf{R}_\mathrm{B})\,, \tag{2.85}$$

where we have introduced the in-plane displacement field

$$\mathbf{u}(\mathbf{r}) = [\, u_x(\mathbf{r})\,,\, u_y(\mathbf{r})\,] \tag{2.86}$$

which characterizes the strain configuration. We will assume that the displacement field varies slowly on the scale of the lattice constant and derive an effective theory that is valid to leading order in the linear strain tensor

$$\varepsilon_{ij} = \frac{1}{2}\left(\frac{\partial u_i}{\partial r_j} + \frac{\partial u_j}{\partial r_i}\right)\,, \qquad i,j = x,y\,. \tag{2.87}$$

Moreover, for simplicity, we will initially consider uniform strain where the strain tensor is constant across the lattice, and we will generalize to non-uniform strain later.

As a result of the lattice deformation, the nearest-neighbour vectors change according to

$$\bar{\mathbf{e}}_n \simeq \mathbf{e}_n + \boldsymbol{\nabla} u \cdot \mathbf{e}_n\,, \tag{2.88}$$

where $\boldsymbol{\nabla} u_{ij} = \partial u_j / \partial r_i$ is the displacement gradient tensor. We will assume that the hopping parameter has an exponential dependence on the bond length [62] and therefore, to leading order in strain, the modified hopping parameters read

$$t_n = t\mathrm{e}^{-\beta\left(\frac{|\bar{\mathbf{e}}_n|}{a}-1\right)} \simeq t\left(1 - \frac{\beta}{a^2} e_n^i e_n^j \varepsilon_{ij}\right), \tag{2.89}$$

where $\beta \approx 3$. As stated above, we are only interested in the effects arising from the change in hopping parameters and not the geometric effects emerging from the lattice distortion. Therefore, after Fourier transforming equation (2.84) we obtain the following Bloch Hamiltonian

$$\mathcal{H}(\mathbf{q}) = \begin{bmatrix} 0 & h(\mathbf{q}) \\ h^*(\mathbf{q}) & 0 \end{bmatrix}, \tag{2.90}$$

where the off-diagonal matrix elements are given by

$$h(\mathbf{q}) = -t \sum_{n=1}^{3} \left(1 - \frac{\beta}{a^2} e_n^i e_n^j \varepsilon_{ij}\right) \mathrm{e}^{-\mathrm{i}\mathbf{q}\cdot\mathbf{e}_n} . \tag{2.91}$$

If we expand equation (2.90) to leading order in $\mathbf{k} = \mathbf{q} - \tau\mathbf{K}$ then we obtain the following effective Hamiltonian near the K/K' points

$$\mathcal{H}_+(\mathbf{k}) = \hbar v_{\mathrm{F}} \boldsymbol{\sigma} \cdot (\mathbf{k} - \mathbf{A}), \quad \mathcal{H}_-(\mathbf{k}) = -\hbar v_{\mathrm{F}} \boldsymbol{\sigma}^* \cdot (\mathbf{k} + \mathbf{A}), \tag{2.92}$$

where the strain gives rise to a pseudo-vector potential that reads

$$\mathbf{A} = \frac{\beta}{2a} [\, \varepsilon_{xx} - \varepsilon_{yy} \, , \, -2\varepsilon_{xy} \,] \, . \tag{2.93}$$

This effective gauge field describes how the Dirac cones shifts in momentum space due to the applied strain. Note, since $\mathcal{T}$ symmetry is preserved the Dirac cones in the inequivalent valleys shift in opposite directions as schematically shown in figure 2.7. Furthermore, it is important to stress that the dependence of the pseudo-vector potential on the strain tensor is constrained by the symmetries of the unstrained lattice [21].

Treating inhomogeneous strain is more subtle since the translational symmetry of the lattice is broken and therefore the tight-binding model cannot be block diagonalized in momentum space. However, if we assume that the strain varies slowly on the scale of the lattice constant, then the effective Hamiltonian in real space is given by the replacement

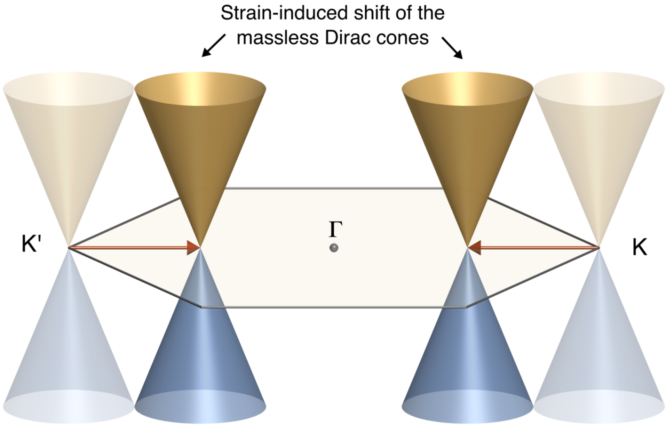

Figure 2.7 | Strain-induced pseudo-vector potential. Applying uniform strain to the graphene membrane renders the hopping parameters anisotropic which breaks $\mathcal{C}_3$ symmetry but preserves $\mathcal{I}$ and $\mathcal{T}$ symmetry. As a result, the massless Dirac cones in different valleys shift away from the high-symmetry points in opposite directions, thereby mimicking the effect of a gauge field. By judiciously engineering an inhomogeneous strain pattern one can generate a pseudo-magnetic field which has opposite signs in the two valleys by virtue of $\mathcal{T}$ symmetry.

$\mathbf{k} \to -\mathrm{i}\boldsymbol{\nabla}$ and $\varepsilon_{ij} \to \varepsilon_{ij}(\mathbf{r})$, which leads to

$$\mathcal{H}_+ = \hbar v_\mathrm{F}\boldsymbol{\sigma}\cdot[-\mathrm{i}\boldsymbol{\nabla} - \mathbf{A}(\mathbf{r})]\,, \quad \mathcal{H}_- = -\hbar v_\mathrm{F}\boldsymbol{\sigma}^*\cdot[-\mathrm{i}\boldsymbol{\nabla} + \mathbf{A}(\mathbf{r})]\,. \tag{2.94}$$

Consequently, electrons propagating through an inhomogeneously strained graphene membrane experience a pseudo-magnetic field given by

$$\mathbf{B}_\tau = \tau\boldsymbol{\nabla}\times\mathbf{A}\,, \tag{2.95}$$

which can mimic some of the properties of real ones; it can generate a Lorentz-like force [25], lead to Aharonov-Bohm interferences [26] and induce Landau quantization [22]. However, in stark contrast to a real magnetic field, the applied strain does not break $\mathcal{T}$ symmetry and therefore the pseudo-magnetic field has opposite signs in the two valleys.

Very soon after the theoretical prediction, enormous pseudo-magnetic fields upwards of 300 tesla were experimentally observed in graphene nanobubbles, where scanning tunnelling spectroscopy measurements revealed that the electronic spectrum was reconstructed into a series of quantized Landau levels [27]. Despite this tantalizing prospect and wealth of theoretical investigations [22–26, 157–160], a controllable way to engineer the in-plane strain configurations that are required to generate uniform pseudo-magnetic fields over a large area [22, 23] still remains elusive. Thus far, experimental studies have been predominantly restricted to localized deformations of the graphene membrane with non-planar morphology

[27, 161–164]. However, this problem is completely circumvented in artificial systems where one can simply imprint any arbitrary strain pattern into the lattice design [68–70, 165]. In fact, these pseudo-magnetic fields have attracted a growing interest in recent years because they present a novel way of manipulating neutral particles and classical waves which are completely inert to real magnetic fields [68–70, 165–172].

2.3.2 Strain-induced merging and annihilation of the Dirac points

In the previous section we showed that the Dirac points are locally stable if one introduces small perturbations that break the $\mathcal{C}_3$ symmetry – they just shift in momentum space away from the K/K' points. The natural question is: what happens for large perturbations? For a moment, let us consider the extreme anisotropic case where $t_1 \gg t_2, t_3$. Here the system essentially consists of a set of isolated dimers described by the Hamiltonian $\mathcal{H} = -t_1\sigma_x$, which has a fully gapped spectrum $E_\lambda = \lambda t_1$ with no remnants of the Dirac points – what happened here?

To elucidate the nature of this transition we will consider the special case of uniform strain where only one hopping parameter is modified $t_1 = t'$, while the others are kept constant $t_2 = t_3 = t$. By Fourier transforming equation (2.84) to momentum space we obtain the Bloch Hamiltonian

$$\mathcal{H}(\mathbf{q}) = \begin{bmatrix} 0 & g(\mathbf{q}) \\ g^*(\mathbf{q}) & 0 \end{bmatrix} , \tag{2.96}$$

where the off-diagonal elements are given by

$$g(\mathbf{q}) = -(t'\mathrm{e}^{-\mathrm{i}\mathbf{q}\cdot\mathbf{e}_1} + t\mathrm{e}^{-\mathrm{i}\mathbf{q}\cdot\mathbf{e}_2} + t\mathrm{e}^{-\mathrm{i}\mathbf{q}\cdot\mathbf{e}_3}) \, . \tag{2.97}$$

The spectrum of the Hamiltonian reads

$$E_\lambda(\mathbf{q}) = \lambda|g(\mathbf{q})| \, , \tag{2.98}$$

and the corresponding eigenstates can be represented by the pseudo-spin vector

$$\mathbf{S}_\lambda(\mathbf{q}) = \lambda \, [\, \cos\varphi(\mathbf{q}) \, , \, \sin\varphi(\mathbf{q}) \, , \, 0 \,] \, , \tag{2.99}$$

where the azimuthal angle is given by

$$\varphi(\mathbf{q}) = \arg[g^*(\mathbf{q})] \, . \tag{2.100}$$

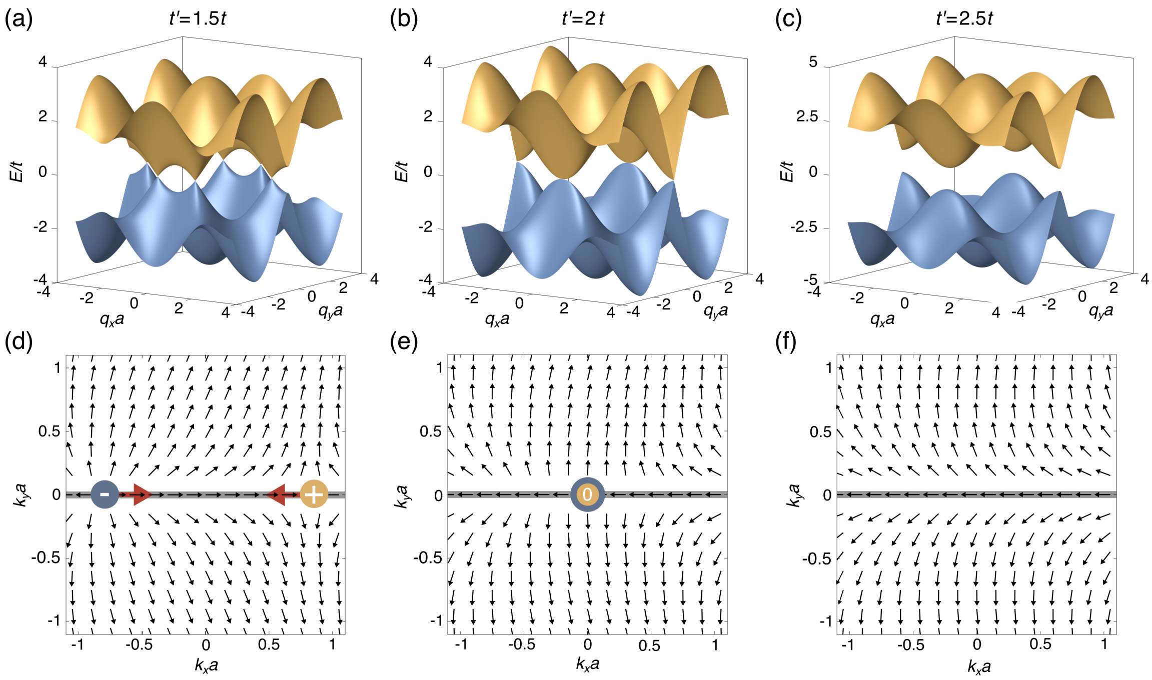

Figure 2.8 | Strain-induced merging and annihilation of the Dirac points. (a)-(c) Electronic band structure for the anisotropic tight-binding model with $t' = 1.5t$, $t' = 2t$ and $t' = 2.5t$, respectively. (d)-(f) Corresponding pseudo-spin fields near the M point, where the Dirac points (vortices) are labelled according to their topological winding numbers. For $t < t' < 2t$, the Dirac points shift away from the K/K' points due to the broken $\mathcal{C}_3$ symmetry, and they migrate towards the M point as the anisotropy of the hopping parameters is increased (red arrows). At the critical value $t' = 2t$, the two Dirac points with opposite topological charges merge together at the M point, forming a semi-Dirac point with zero topological charge. As the anisotropy is increased further $t' > 2t$, the Dirac points annihilate one another and the spectrum becomes gapped, resulting in a transition from a semi-metal phase to an insulator phase.

In figures 2.8(a)-(c) we plot the spectrum for $t' = 1.5t$, $t' = 2t$ and $t' = 2.5t$, respectively. For the regime $t < t' < 2t$ we can see that the Dirac points shift away from the K/K' points and migrate towards the M point as the anisotropy is increased. This migration continues until a critical value $t' = 2t$ where the two inequivalent Dirac points merge together at the M point, and then the spectrum becomes fully gapped as the anisotropy is increased further $t' > 2t$. Therefore, increasing the anisotropy of the hopping parameters drives a transition from a semi-metallic phase to an insulating phase [61–64].

To explore the nature of this transition further, we can derive an effective Hamiltonian near one of the M points which we chose to be located at $\mathbf{M} = [\,2\pi/3a\,,\,0\,]$. By expanding equation (2.96) to leading order in $\mathbf{k} = \mathbf{q} - \mathbf{M}$ we obtain [63, 64]

$$\mathcal{H}_{\mathrm{M}}(\mathbf{k}) = (\mathit{\Delta}_{\mathrm{M}} - t_{\mathrm{M}} k_x^2)\sigma_x + v_{\mathrm{M}} k_y \sigma_y\,, \tag{2.101}$$

and the corresponding spectrum reads

$$E_\lambda(\mathbf{k}) = \lambda\sqrt{(\mathit{\Delta}_\mathrm{M} - t_\mathrm{M}k_x^2)^2 + v_\mathrm{M}^2 k_y^2}\,, \tag{2.102}$$

where $\mathit{\Delta}_\mathrm{M} = 2t - t'$, $t_\mathrm{M} = 3a^2t/4$ and $v_\mathrm{M} = a(t + t')$. Note that equation (2.101) is consistent with the general form of the Hamiltonian which we have derived using symmetry analysis in appendix A.2.

For the regime $t < t' < 2t$, we can see from equation (2.102) that there exists two Dirac points located along the $\mathrm{K}/\mathrm{K}' \to \mathrm{M}$ lines at

$$\mathbf{k}_\mathrm{M}^\pm = \pm\sqrt{\frac{\mathit{\Delta}_\mathrm{M}}{t_\mathrm{M}}}\big[\,1\,,\,0\,\big]\,. \tag{2.103}$$

If we expand equation (2.101) to leading order in $\mathbf{k}' = \mathbf{k} - \mathbf{k}_\mathrm{M}^\pm$ then we obtain the effective Hamiltonian within the vicinity of the two Dirac points

$$\mathcal{H}_\mathrm{M}^\pm(\mathbf{k}') = \mp\frac{t_\mathrm{M}}{\mathit{\Delta}_\mathrm{M}}k'_x\sigma_x + v_\mathrm{M}k'_y\sigma_y\,. \tag{2.104}$$

This is a generalized massless Dirac Hamiltonian where the spectrum

$$E_\lambda(\mathbf{k}') = \lambda\sqrt{\frac{t_\mathrm{M}^2}{\mathit{\Delta}_\mathrm{M}^2}k_x'^2 + v_\mathrm{M}^2 k_y'^2} \tag{2.105}$$

is anisotropic with different group velocities along the k_x and k_y directions due to the broken $\mathcal{C}_3$ symmetry. Moreover, from the Hamiltonian in equation (2.104) one can show that the Dirac points have opposite topological charges, which can also be inferred from the pseudo-spin field shown in figure 2.8(d).

At the critical anisotropy $t' = 2t$, the two Dirac points merge together as the gap parameter vanishes $\mathit{\Delta}_\mathrm{M} = 0$, and the effective Hamiltonian near the M point reads

$$\mathcal{H}_\mathrm{M}(\mathbf{k}) = -t_\mathrm{M}k_x^2\sigma_x + v_\mathrm{M}k_y\sigma_y\,. \tag{2.106}$$

The corresponding spectrum

$$E_\lambda(\mathbf{k}) = \lambda\sqrt{t_\mathrm{M}^2 k_x^4 + v_\mathrm{M}^2 k_y^2} \tag{2.107}$$

is highly anisotropic with a linear dispersion along the k_y direction and a quadratic dispersion along the k_x direction – this critical band degeneracy has been aptly dubbed a semi-Dirac point [173]. Moreover, one can easily check that the corresponding topological winding number vanishes

$$W(\mathbf{M}) = -\oint_{\Gamma} \frac{\mathrm{d}\mathbf{k}}{2\pi} \cdot \boldsymbol{\nabla}_{\mathbf{k}} \arctan\left(\frac{v_{\mathrm{M}} k_y}{t_{\mathrm{M}} k_x^2}\right) = 0\,, \tag{2.108}$$

which can also be seen directly in the pseudo-spin field shown in figure 2.8(e) – this is required since the topological charge must be preserved through the merging transition. Note that the semi-Dirac nature of this band degeneracy is required because a Hamiltonian that is linear in both Pauli matrices would necessarily exhibit vorticity [174]. Unlike the Dirac points, this lack of a topological charge renders the semi-Dirac point susceptible to a gap-opening perturbation. This is precisely what we observe when the anisotropy is increased further $t' > 2t$, where a global gap opens up and the vorticity in the pseudo-spin field vanishes as shown in figure 2.8(f).

Since it is notoriously difficult to confine massless Dirac fermions using conventional electrostatic barriers by virtue of the Klein tunnelling phenomenon, this tantalizing prospect of engineering a bulk gap via strain attracted considerable theoretical interest [62]. However, since the Dirac points are well separated in momentum space, it has been predicted that one needs to engineer very large strains of about 20% in order to induce this transition in graphene [62]; consequently, it has evaded experimental observation to date. In contrast, this merging transition has been observed in photonic graphene systems [65–67] where it is relatively simple to engineer the required anisotropy.

2.4 Dirac mass generation

In this final part, we will explore what happens when we gap out the Dirac points. To generate a mass term we have to introduce a perturbation that anticommutes with the massless Dirac Hamiltonian. The only remaining Pauli matrix is σ_z and we have shown in section 2.2.5 that this term vanishes in the presence of both $\mathcal{T}$ and $\mathcal{I}$ symmetry. Therefore, in order to generate a mass for the Dirac fermions and turn graphene into an insulator, one (or both) of these symmetries has to be broken. Unlike the insulating phase that arises from the merging and annihilation of the Dirac points, these insulators have very interesting geometrical and topological properties that depend qualitatively on which symmetry is broken. Before we introduce two different models of non-trivial insulators, in the next section we will provide a very brief overview of some important concepts relating to the geometrical and topological properties of Bloch bands in two dimensions.

2.4.1 Geometry and topology of Bloch bands in two dimensions

Topology is a branch of mathematics that is concerned with global properties of various objects that are preserved under continuous deformations. Naturally, one can then group objects into equivalence classes according to a topological invariant that takes integer values. The canonical example is the number of holes in a 2D orientable surface known as the genus; a sphere is topologically distinct from a torus because you cannot deform one into the other without tearing a hole or gluing two parts together. At first glance, this rather abstract field of study appears to be of little relevance to electrons propagating through periodic crystals. For a long time electronic materials were coarsely classified as metals or insulators, based primarily on the nature of the energy bands and the position of the Fermi level. This naive view changed dramatically with the discovery of the quantum Hall effect [29], whose topological origin was unveiled by David Thouless and others [134–142] which eventually paved the way for the thriving field of topological insulators [28].

One of the central questions underpinning the field is: given two Hamiltonians that describe two different gapped insulators, when are they essentially equivalent? To answer this, one seeks to classify the Hamiltonians by establishing an integer topological invariant that characterizes the global geometric properties of the eigenstates. The two Hamiltonians are then said to be topologically inequivalent if they have a different value of the topological invariant; one system cannot be continuously transformed into the another without closing the bulk energy gap. In what follows we will limit our discussion to 2D systems and a minimal two-band Hamiltonian of the form

$$\mathcal{H}(\mathbf{q}) = \begin{bmatrix} d_z(\mathbf{q}) & d_x(\mathbf{q}) - \mathrm{i}d_y(\mathbf{q}) \\ d_x(\mathbf{q}) + \mathrm{i}d_y(\mathbf{q}) & -d_z(\mathbf{q}) \end{bmatrix} = \boldsymbol{\sigma} \cdot \mathbf{d}(\mathbf{q}) \,, \tag{2.109}$$

where we have neglected the term proportional to the identity as it does not modify the topology of the bands.

Within topological band theory, the Berry phase plays a central role [138]. In this context, the Berry phase is a geometric phase that is acquired by a Bloch state when it is adiabatically transported around a closed path $\varGamma$ in the Brillouin zone

$$\gamma(\varGamma) = \oint_{\varGamma} \mathrm{d}\mathbf{q} \cdot \boldsymbol{\mathcal{A}}_{\lambda}(\mathbf{q}) \,, \tag{2.110}$$

where we have introduced the Berry connection of the λ band

$$\boldsymbol{\mathcal{A}}_\lambda(\mathbf{q}) = \mathrm{i}\,\langle\psi_\lambda(\mathbf{q})|\,\boldsymbol{\nabla}_{\mathbf{q}}\,|\psi_\lambda(\mathbf{q})\rangle\ . \tag{2.111}$$

This is analogous to the vector potential in electromagnetism but in momentum space, and it is a gauge-dependent quantity; under the gauge transformation

$$|\psi_\lambda(\mathbf{q})\rangle \to |\psi'_\lambda(\mathbf{q})\rangle = \mathrm{e}^{\mathrm{i}\zeta(\mathbf{q})}\,|\psi_\lambda(\mathbf{q})\rangle\ , \tag{2.112}$$

where $\zeta(\mathbf{q})$ is a continuous real function, the Berry connection transforms as

$$\boldsymbol{\mathcal{A}}_\lambda(\mathbf{q}) \to \boldsymbol{\mathcal{A}}'_\lambda(\mathbf{q}) = \boldsymbol{\mathcal{A}}_\lambda(\mathbf{q}) - \boldsymbol{\nabla}_{\mathbf{q}}\zeta(\mathbf{q})\,. \tag{2.113}$$

What about the Berry phase, is it a gauge-invariant quantity or can it be gauged away? In order for the eigenstates to remain single valued, we also require $\mathrm{e}^{\mathrm{i}\zeta(\mathbf{q})}$ to be single valued. Consequently, at the start and end of a closed contour the gauge function can only differ by an integer multiple of 2π, and the corresponding Berry phase transforms as

$$\gamma(\mathit{\Gamma}) \to \gamma'(\mathit{\Gamma}) = \gamma(\mathit{\Gamma}) + 2m\pi\,, \tag{2.114}$$

where $m \in \mathbb{Z}$ is an integer. Therefore, the Berry phase is indeed a gauge-invariant quantity modulo 2π.

We can continue the analogy with electromagnetism by invoking Stokes' theorem which allows us to write the Berry phase as

$$\gamma(\mathit{\Gamma}) = \iint\limits_{S_{\mathit{\Gamma}}} \mathrm{d}^2\mathbf{q}\,\mathcal{F}_\lambda(\mathbf{q})\,, \tag{2.115}$$

where $S_{\mathit{\Gamma}}$ is the surface enclosed by the contour $\mathit{\Gamma}$. Here we have introduced the Berry curvature of the λ band

$$\mathcal{F}_\lambda(\mathbf{q}) = \frac{\partial}{\partial q_x}\mathcal{A}^y_\lambda(\mathbf{q}) - \frac{\partial}{\partial q_y}\mathcal{A}^x_\lambda(\mathbf{q})\,, \tag{2.116}$$

which is analogous to the magnetic field in momentum space – it is a gauge-invariant quantity that describes the local geometric properties of the Bloch states. In its present form it contains derivatives of the eigenstates which is a nuisance if one wants to numerically compute the Berry curvature. It is therefore useful to transform it into a manifestly gauge-invariant form, which for the two band-model reads

$$\mathcal{F}_\lambda(\mathbf{q}) = \mathrm{i}\frac{\langle\psi_\lambda(\mathbf{q})|\frac{\partial}{\partial q_x}\mathcal{H}(\mathbf{q})|\psi_{\lambda'}(\mathbf{q})\rangle\langle\psi_{\lambda'}(\mathbf{q})|\frac{\partial}{\partial q_y}\mathcal{H}(\mathbf{q})|\psi_\lambda(\mathbf{q})\rangle}{[E_{\lambda'}(\mathbf{q}) - E_\lambda(\mathbf{q})]^2} + \text{c.c.}\ . \tag{2.117}$$

We have seen in section 2.2.5 and section 2.2.6 that the symmetries of the system place strict constraints on the form of the Hamiltonian. Similarly, the symmetries also place strict constraints on the form of the Berry curvature. In particular, it is simple to show that the presence of $\mathcal{T}$ symmetry imposes that the Berry curvature must be an odd function of $\mathbf{q}$

$$\mathcal{T}:\ \mathcal{F}_\lambda(\mathbf{q}) = -\mathcal{F}_\lambda(-\mathbf{q})\,, \tag{2.118}$$

while $\mathcal{I}$ symmetry constrains the Berry curvature to be an even function of $\mathbf{q}$

$$\mathcal{I}:\ \mathcal{F}_\lambda(\mathbf{q}) = \mathcal{F}_\lambda(-\mathbf{q})\,. \tag{2.119}$$

Consequently, in the presence of both $\mathcal{T}$ and $\mathcal{I}$ symmetry the Berry curvature must vanish everywhere

$$\mathcal{IT}:\ \mathcal{F}_\lambda(\mathbf{q}) = 0\,. \tag{2.120}$$

However, from equation (2.117) we can see that the Berry curvature is ill-defined at band degeneracies where the adiabatic theorem breaks down. Moreover, using the eigenstates of the effective Dirac Hamiltonian in equation (2.26) one can easily show that massless Dirac fermions acquire a non-trivial Berry phase of $\pm\pi$ when adiabatically transported around a Dirac point. This result is independent of the path and therefore the Dirac points must be singular sources of $\pm\pi$ Berry flux, and the corresponding Berry curvature can only be unlocked if one lifts the degeneracy by breaking $\mathcal{T}$ or $\mathcal{I}$ symmetry.

If the bands are fully gapped then we can define an integer topological invariant for each band known as the Chern number, which is defined as the integral of the Berry curvature over the entire Brillouin zone [136]

$$C_\lambda = \frac{1}{2\pi}\iint\limits_{\mathrm{BZ}} \mathrm{d}^2\mathbf{q}\,\mathcal{F}_\lambda(\mathbf{q}) \in \mathbb{Z}\,. \tag{2.121}$$

Evidently, a minimum requirement for a band to exhibit a non-zero Chern number is for $\mathcal{T}$ symmetry to be broken by virtue of the constraint given by equation (2.118). If we use the explicit form of the two-band Hamiltonian in equation (2.109) then we can re-express the

Berry curvature as

$$\mathcal{F}_\lambda(\mathbf{q}) = -\frac{\lambda}{2}\left(\frac{\partial\hat{\mathbf{d}}}{\partial q_x} \times \frac{\partial\hat{\mathbf{d}}}{\partial q_y}\right) \cdot \hat{\mathbf{d}}\,, \tag{2.122}$$

which provides us with a simple geometrical interpretation of the Chern number. If the spectrum is fully gapped then $\mathbf{q} \to \hat{\mathbf{d}}(\mathbf{q})$ defines a map from the Brillouin zone $\mathbb{T}^2$ to the Bloch sphere $\mathbb{S}^2$. The Chern number is equivalent to the wrapping number of this map which counts the number of times the surface traced out by $\hat{\mathbf{d}}$ wraps around the Bloch sphere as the momentum is varied over the entire Brillouin zone. This topological invariant is therefore robust against continuous variations of the Hamiltonian parameters, and can only change abruptly by an integer amount if the spectral gap closes and reopens. Band insulators that have a vanishing Chern number are called trivial since they can be smoothly deformed into a trivial atomic insulator without closing the spectral gap. In contrast, topological insulators with non-zero Chern numbers are referred to as Chern insulators.

At first glance, it may seem contradictory that the Chern number does not vanish identically. If we naively invoke Stokes' theorem then we can write the Chern number as a line integral of the Berry connection over the boundary of the Brillouin zone. However, the Brillouin zone is a closed manifold which does not have a boundary, and therefore if the Berry connection is well defined over the whole Brillouin zone then the resulting integral vanishes. Consequently, a non-zero Chern number represents an obstruction to finding a global gauge that is continuous and single valued over the entire Brillouin zone [140].

We can illustrate this clearly using the two-band Hamiltonian where the eigenstates can be expressed as

$$|\psi_-^{(1)}(\mathbf{q})\rangle = \begin{bmatrix} \sin(\theta/2)\mathrm{e}^{-\mathrm{i}\varphi} \\ -\cos(\theta/2) \end{bmatrix}, \quad |\psi_+^{(1)}(\mathbf{q})\rangle = \begin{bmatrix} \cos(\theta/2) \\ \sin(\theta/2)\,\mathrm{e}^{\mathrm{i}\varphi} \end{bmatrix}, \tag{2.123}$$

for the lower and upper band, respectively. Here the spherical angles parametrizing the vector $\hat{\mathbf{d}}(\mathbf{q})$ read

$$\varphi(\mathbf{q}) = \arctan\left[\frac{d_y(\mathbf{q})}{d_x(\mathbf{q})}\right], \quad \theta(\mathbf{q}) = \arccos\left[\frac{d_z(\mathbf{q})}{|\mathbf{d}(\mathbf{q})|}\right]. \tag{2.124}$$

One should note that this choice of the spinor eigenstates is not unique as they are only defined up to a global phase. For the gauge that we have chosen in equation (2.123) the eigenstates are well defined everywhere except for when $\hat{\mathbf{d}}(\mathbf{q})$ points to the south pole ($\theta = \pi$) where they have an ill-defined phase. Alternatively, we could chose a different gauge related by the transformation

$$|\psi_\lambda^{(2)}(\mathbf{q})\rangle = \mathrm{e}^{-\mathrm{i}\lambda\varphi(\mathbf{q})}\, |\psi_\lambda^{(1)}(\mathbf{q})\rangle \ , \tag{2.125}$$

where the eigenstates now read

$$|\psi_-^{(2)}(\mathbf{q})\rangle = \begin{bmatrix} \sin(\theta/2) \\ -\cos(\theta/2)\mathrm{e}^{\mathrm{i}\varphi} \end{bmatrix} , \quad |\psi_+^{(2)}(\mathbf{q})\rangle = \begin{bmatrix} \cos(\theta/2)\mathrm{e}^{-\mathrm{i}\varphi} \\ \sin(\theta/2) \end{bmatrix} . \tag{2.126}$$

While this gauge is now well defined at the south pole ($\theta = \pi$), it is ill-defined at the north pole ($\theta = 0$) – we cannot remove the problematic point, we can only shift its position. Consequently, if $\hat{\mathbf{d}}(\mathbf{q})$ wraps the entire Bloch sphere, as it does for a Chern insulator, one cannot find a gauge that is well defined everywhere throughout the entire Brillouin zone.

Furthermore, we can show that this obstruction leads to an integer-valued Chern number and another practical way of calculating it. For the majority of the Brillouin zone let us choose the first gauge defined by equation (2.123), and let $\mathbf{q}_i^{\mathrm{s}}$ ($i = 1, 2, \dots$) denote the positions in the Brillouin zone where $\hat{\mathbf{d}}(\mathbf{q})$ reaches the south pole. We can then define a set of small patches that enclose the obstructions [140, 141]

$$\mathbb{R}_{\mathrm{s}}^{\epsilon} = \Big\{ \mathbf{q} \in \mathbb{T}^2 \ : \ |\mathbf{q} - \mathbf{q}_i^{\mathrm{s}}| < \epsilon \, , \, \theta(\mathbf{q}_i^{\mathrm{s}}) = \pi \Big\} \, , \tag{2.127}$$

and inside these regions we adopt the second gauge given by equation (2.126). The corresponding Berry connection within these patches is given by the gauge transformation

$$\boldsymbol{\mathcal{A}}_\lambda^{(2)}(\mathbf{q}) = \boldsymbol{\mathcal{A}}_\lambda^{(1)}(\mathbf{q}) + \lambda \boldsymbol{\nabla}\varphi(\mathbf{q}) \, . \tag{2.128}$$

Now that the phase is uniquely determined over the entire Brillouin zone, we can apply Stokes' theorem to the separate regions which allows us to express the Chern number as [140, 141]

$$C_\lambda = \frac{1}{2\pi} \oint_{\partial\mathbb{R}_{\mathrm{s}}^{\epsilon}} \mathrm{d}\mathbf{q} \cdot \Big[\boldsymbol{\mathcal{A}}_\lambda^{(2)}(\mathbf{q}) - \boldsymbol{\mathcal{A}}_\lambda^{(1)}(\mathbf{q}) \Big] = \frac{\lambda}{2\pi} \oint_{\partial\mathbb{R}_{\mathrm{s}}^{\epsilon}} \mathrm{d}\mathbf{q} \cdot \boldsymbol{\nabla}_{\mathbf{q}}\varphi(\mathbf{q}) = \lambda \sum_i W(\mathbf{q}_i^{\mathrm{s}}) \, , \tag{2.129}$$

where $\partial\mathbb{R}_{\mathrm{s}}^{\epsilon}$ represents the boundary of $\mathbb{R}_{\mathrm{s}}^{\epsilon}$. From equation (2.129) we can see that the Chern number is given by the sum of the topological winding numbers associated with the vortices in the azimuthal phase $\varphi(\mathbf{q})$ located at $\mathbf{q}_i^{\mathrm{s}}$ – this shows that the Chern number can only assume integer values. If we repeat the preceding analysis while switching the role of the two gauges, then we can express the above formula in a more symmetric form

$$C_\lambda = -\frac{\lambda}{2}\sum_i W(\mathbf{q}_i)\,\mathrm{sgn}[d_z(\mathbf{q}_i)]\,, \tag{2.130}$$

where $\mathbf{q}_i$ denote the locations where $\hat{\mathbf{d}}(\mathbf{q})$ reaches either the south and north pole. Equation (2.130) provides us with a convenient way of calculating the Chern number for a two-band model without having to numerically integrate the Berry curvature.

2.4.2 Haldane insulator

Shortly after the discovery of the quantum Hall effect, Duncan Haldane realized that $\mathcal{T}$ symmetry breaking was the essential ingredient for a quantized Hall conductance and not the formation of Landau levels due to a macroscopic magnetic field. In 1988, he devised an ingenious toy model to illustrate this [30], which contributed to him being duly decorated with the Nobel Prize in 2016. Specifically, he used the simple tight-binding model of graphene and introduced a periodic pattern of magnetic flux with the full symmetry of the lattice, but with zero net magnetic flux piercing through each unit cell [30]. Within the framework of a tight-binding model, these fluxes do not modify the nearest-neighbour hopping parameters because all the corresponding closed paths encircle complete unit cells. However, if we now include next-nearest-neighbour hopping then the hopping parameter becomes complex $t'\mathrm{e}^{\pm\mathrm{i}\vartheta}$, where t' is the hopping amplitude and ϑ is the Aharonov-Bohm phase acquired along the hopping path due to the local magnetic flux. The sign depends on the direction of the hop, and in figure 2.9(a) the dotted arrows show the hopping directions associated with a positive sign.

This model is described by the Hamiltonian $H_\mathrm{H} = H + \Delta H_\mathrm{H}$, where H is the nearest-neighbour tight-binding Hamiltonian of pristine graphene given by equation (2.10). The new term that Haldane introduced reads

$$\Delta H_\mathrm{H} = t'\mathrm{e}^{\mathrm{i}\vartheta}\sum_{\mathbf{R}_\mathrm{A}}\sum_{j=1}^{3} a^\dagger_{\mathbf{R}_\mathrm{A}} a_{\mathbf{R}_\mathrm{A}+\boldsymbol{\delta}_j} + t'\mathrm{e}^{-\mathrm{i}\vartheta}\sum_{j=1}^{3}\sum_{\mathbf{R}_\mathrm{B}} b^\dagger_{\mathbf{R}_\mathrm{B}} b_{\mathbf{R}_\mathrm{B}+\boldsymbol{\delta}_j} + \mathrm{H.c.}\,, \tag{2.131}$$

where the vectors $\boldsymbol{\delta}_1 = \mathbf{e}_2 - \mathbf{e}_3$, $\boldsymbol{\delta}_2 = \mathbf{e}_3 - \mathbf{e}_1$ and $\boldsymbol{\delta}_3 = \mathbf{e}_1 - \mathbf{e}_2$ connect next-nearest-neighbour sites. Importantly, the added magnetic flux preserves the translational symmetry of the lattice, and therefore the electron states retain their usual Bloch character. We note that Haldane also considered staggered on-site energies in his model but we reserve this for a separate discussion in section 2.4.4

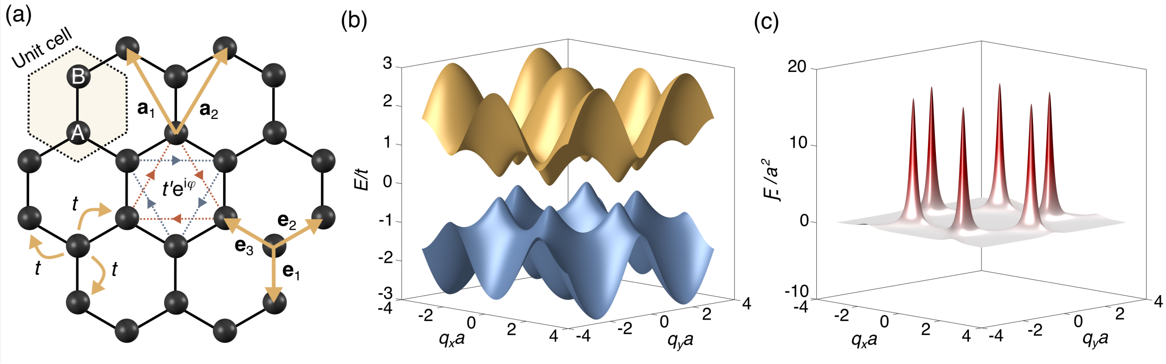

Figure 2.9 | Haldane insulator. (a) Schematic of the Haldane model, which is the graphene tight-binding model with additional complex next-nearest-neighbour hopping. The blue/red arrows show the hopping directions associated with a positive phase $t'\mathrm{e}^{\mathrm{i}\varphi}$. Physically, this model corresponds to introducing periodic magnetic flux with the full symmetry of the lattice, but with zero net magnetic flux through each unit cell. (b) Spectrum of the Haldane Hamiltonian with $\vartheta = \pi/2$ and $t' = 0.05t$. The magnetic flux breaks $\mathcal{T}$ symmetry which gaps out the Dirac points, giving rise to a bulk insulator at half filling. (c) Berry curvature for the valence band which is an even function of $\mathbf{q}$ by virtue of $\mathcal{I}$ symmetry and is positive throughout the Brillouin zone. For this model the Chern number is $C_- = +1$, while for $\vartheta \to -\vartheta$ the Berry curvature becomes negative and one obtains $C_- = -1$.

We can Fourier transform the Haldane Hamiltonian to momentum space where the Bloch Hamiltonian reads $\mathcal{H}_\mathrm{H}(\mathbf{q}) = \mathcal{H}(\mathbf{q}) + \Delta\mathcal{H}_\mathrm{H}(\mathbf{q})$. Here $\mathcal{H}(\mathbf{q})$ is given by equation (2.14) and the new Haldane term reads

$$\Delta\mathcal{H}_\mathrm{H}(\mathbf{q}) = d_0(\mathbf{q})\mathbb{1}_2 + d_z(\mathbf{q})\sigma_z \,, \tag{2.132}$$

where

$$d_0(\mathbf{q}) = 2t'\cos\vartheta \sum_{j=1}^{3} \cos(\mathbf{q}\cdot\boldsymbol{\delta}_j) \,, \quad d_z(\mathbf{q}) = -2t'\sin\vartheta \sum_{j=1}^{3} \sin(\mathbf{q}\cdot\boldsymbol{\delta}_j) \,. \tag{2.133}$$

According to equation (2.54) $\mathcal{I}$ symmetry is preserved, while according to equation (2.56) $\mathcal{T}$ symmetry is broken which gives rise to a σ_z term in the Hamiltonian.

In figure 2.9(b) we plot the spectrum of the Haldane model

$$E_\lambda(\mathbf{q}) = d_0(\mathbf{q}) + \lambda\sqrt{|f(\mathbf{q})|^2 + d_z^2(\mathbf{q})} \tag{2.134}$$

for $\vartheta = \pi/2$ and $t' = 0.05t$. Since $\mathcal{T}$ symmetry is broken for these parameters, the spectrum is fully gapped and therefore the Haldane Hamiltonian describes an insulator at half filling. As the spectrum alone cannot tell us anything about the topology of the system, in figure 2.9(c) we plot the corresponding Berry curvature for the valence band using equation (2.117), which is an even function of $\mathbf{q}$ by virtue of $\mathcal{I}$ symmetry. Notably, the Berry curvature is positive throughout the whole Brillouin zone, while it is negative if we switch the sign of the phase $\vartheta \to -\vartheta$. Consequently, if one directly computes the integral in equation (2.121) one finds that the Haldane model represents a topological insulator with a Chern number of $C_- = \pm 1$.

We can see this in a more intuitive way by analysing the obstructions. Since the $\mathcal{T}$ symmetry-breaking term in the Haldane Hamiltonian does not modify the σ_x and σ_y terms, the only place where $\hat{\mathbf{d}}(\mathbf{q})$ can visit the poles is at the K/K' points (i.e., where the off-diagonal terms vanish). Therefore, it is useful to derive the effective Hamiltonian near the K/K' points which read

$$\mathcal{H}_+(\mathbf{k}) = E_0 \mathbb{1}_2 + \hbar v_\mathrm{F} \boldsymbol{\sigma} \cdot \mathbf{k} + m_+ \sigma_z \,, \quad \mathcal{H}_-(\mathbf{k}) = E_0 \mathbb{1}_2 - \hbar v_\mathrm{F} \boldsymbol{\sigma}^* \cdot \mathbf{k} + m_- \sigma_z \,, \tag{2.135}$$

where

$$E_0 = -3t' \cos\vartheta \,, \quad m_\tau = \tau 3\sqrt{3} t' \sin\vartheta \,. \tag{2.136}$$

Apart from a global energy shift E_0, the Haldane fermions are described by a massive Dirac Hamiltonian with a gapped Dirac cone spectrum

$$E_\lambda(\mathbf{k}) = E_0 + \lambda \sqrt{\hbar^2 v_\mathrm{F}^2 |\mathbf{k}|^2 + m_\tau^2} \,. \tag{2.137}$$

Crucially, while the spectrum in each valley is identical, the Haldane mass m_τ has opposite signs for the two valleys and therefore $\hat{\mathbf{d}}(\mathbf{q})$ visits both poles of the Bloch sphere. From equation (2.130) we can easily deduce the Chern number of the valence band

$$C_- = \frac{1}{2} \sum_\tau W(\tau \mathbf{K}) \, \mathrm{sgn}[d_z(\tau \mathbf{K})] = \frac{1}{2} [\mathrm{sgn}(m_+) - \mathrm{sgn}(m_-)] = \mathrm{sgn}(m_+) \,, \tag{2.138}$$

which is precisely what we obtain if we directly integrate the Berry curvature.

2.4.3 Topological chiral edge states

One of the most important manifestations of non-trivial topology in the bulk is the emergence of gapless edge states at the boundary. Heuristically, we can understand this as follows: if we consider an interface between two topologically distinct insulators then the band gap must close somewhere along the interface in order for the topological invariant to change. The corresponding Hall conductance [136]

$$\sigma_{xy} = \frac{e^2}{h} \sum_n C_n \tag{2.139}$$

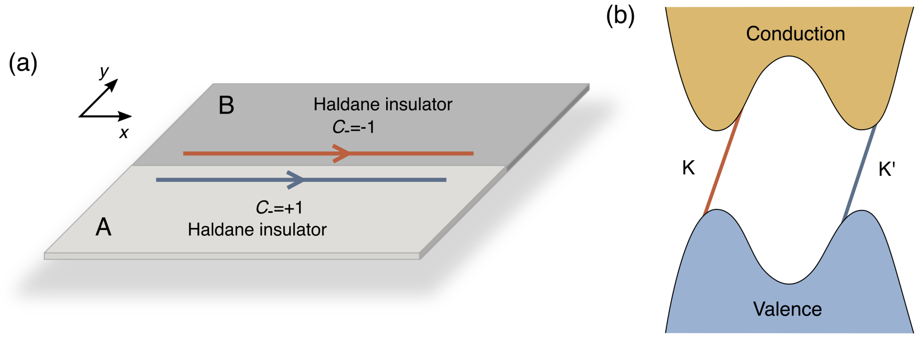

Figure 2.10 | Topological chiral edge states. (a) Schematic of a domain wall interface between two topologically distinct insulators, where region A is a Haldane insulator with $C_- = +1$ and region B is a Haldane insulator with $C_- = -1$. (b) Schematic of the interface spectrum. The bulk spectrum is gapped and identical in both regions but there exists chiral edge states that traverse the bulk gap and are exponentially localized at the interface. Since $\mathcal{T}$ symmetry is broken, these chiral edge states propagate in the same direction and are thus topologically protected against backscattering because there are no states available to transport current in the opposite direction.

is determined by the sum of the Chern numbers of the occupied bulk bands which, via the bulk-boundary correspondence, determines the number of chiral edge states at the boundary with the vacuum that contribute to the transport. Moreover, because $\mathcal{T}$ symmetry is broken these topological edge states only propagate in one direction around the boundary and are therefore insensitive to disorder – they cannot be backscattered because there are no states available to transport current in the opposite direction.

To illustrate this bulk-boundary correspondence, let us consider an interface between two topologically distinct Haldane insulators as schematically depicted in figure 2.9(a). To describe the full physics at a microscopic level, one should use the full tight-binding model and interpolate the parameters across the interface. Here we will just focus on the essential physics which can be captured by the effective Dirac Hamiltonian [28]

$$\mathcal{H}_\tau = -\mathrm{i}\hbar v_\mathrm{F}(\tau\sigma_x\partial_x + \sigma_y\partial_y) + m_\tau(y)\sigma_z\,. \tag{2.140}$$

We model the interface as a spatially varying mass along the y-direction

$$m_\tau(y) = \begin{cases} +\tau m_\mathrm{H}, & \text{for } y < 0 \\ -\tau m_\mathrm{H}, & \text{for } y > 0 \end{cases} \tag{2.141}$$

and we have neglected the irrelevant energy shift E_0. While the bulk spectrum in each region is identical, they have opposite Chern numbers as the mass within each valley changes sign across the interface.

We can exploit the translational invariance along the x-direction by writing the spinor envelope wavefunction as $\psi_\tau(\mathbf{r}) = \psi_\tau(y)\mathrm{e}^{\mathrm{i}k_x x}$. First, we will try to find a zero-energy state for $k_x = 0$ which is a solution to the following equation

$$-\mathrm{i}\hbar v_\mathrm{F}\sigma_y\partial_y\psi_\tau(y) + m_\tau(y)\sigma_z\psi_\tau(y) = 0 \quad \rightarrow \quad \partial_y\psi_\tau(y) = \frac{m_\tau(y)}{\hbar v_\mathrm{F}}\sigma_x\psi_\tau(y)\,. \tag{2.142}$$

We want to obtain physical solutions where the wavefunction is bounded and normalizable, which means that it must be an eigenstate of σ_x with an eigenvalue of $\tau\,\mathrm{sgn}(m_\mathrm{H})$. Therefore, the solution within each valley is a Jackiw-Rebbi-like [175] mode

$$\psi_\tau(y) \propto \begin{bmatrix} 1 \\ \tau\,\mathrm{sgn}(m_\mathrm{H}) \end{bmatrix} \mathrm{e}^{-\frac{|m_\mathrm{H}|}{\hbar v_\mathrm{F}}|y|}\,, \tag{2.143}$$

which is exponentially localized at the interface. To find the solution for finite k_x one simply has to note that $\psi_\tau(y)$ is also an eigenstate of σ_y with eigenvalue $\mathrm{i}\tau\,\mathrm{sgn}(m_\mathrm{H})$, and therefore the full solution reads

$$\psi_\tau(\mathbf{r}) \propto \begin{bmatrix} 1 \\ \tau\,\mathrm{sgn}(m_\mathrm{H}) \end{bmatrix} \mathrm{e}^{-\frac{|m_\mathrm{H}|}{\hbar v_\mathrm{F}}|y|}\mathrm{e}^{\mathrm{i}k_x x}\,. \tag{2.144}$$

To find the corresponding spectrum of the edge states we can act on the wavefunction with the effective Hamiltonian which yields

$$E_\tau(k_x) = \mathrm{sgn}(m_\mathrm{H})\hbar v_\mathrm{F} k_x\,. \tag{2.145}$$

Therefore, each valley supports a chiral edge state which propagate in the same direction as schematically depicted in figure 2.9(b). This is consistent with the more general bulk-boundary correspondence which says that the number of chiral edge states is determined by the change in Chern number across the interface – here we have $\Delta C_- = C_-^\mathrm{B} - C_-^\mathrm{A} = 2$. Moreover, we note that $\mathrm{sgn}(\Delta C_-)$ determines the chirality of the edge states (i.e., their propagation direction).

While the quantum Hall effect was the first realization of a Chern insulator phase, the quantum anomalous Hall effect was first realized in magnetically doped topological insulator films [176], and more recently in an intrinsic magnetic topological insulator [177] and twisted bilayer graphene aligned on boron nitride [178]. Furthermore, the photonic analog of the Chern insulator was first realized at microwave frequencies by applying an external magnetic field across a gyromagnetic photonic crystal which exploits magneto-optical effects in ferrite rods [76]. More recently it has been realized at optical frequencies by applying a magnetic field across a polariton micropillar lattice which exploits the Zeeman splitting of excitons [179]. We also note that one can break $\mathcal{T}$ symmetry by temporally modulating the system parameters [180–182], where the effective Floquet Hamiltonian can be characterized by non-trivial Chern numbers. Using this mechanism the Haldane model has been effectively emulated in artificial graphene systems including cold atom arrays [183] and photonic waveguide arrays [184].

2.4.4 Semenoff insulator

A few years before Haldane proposed his model of the Chern insulator, Gordon Semenoff introduced another type of insulator based on graphene [7]. Specifically, he introduced staggered on-site energies on the two sublattices as depicted in figure 2.11(a), which breaks $\mathcal{I}$ symmetry while preserving $\mathcal{T}$ symmetry. The system is described by the Hamiltonian $H_\mathrm{S} = H + \Delta H_\mathrm{S}$, where H is the Hamiltonian of pristine graphene given by equation (2.10) and the new term reads

$$\Delta H_\mathrm{S} = E_\mathrm{A} \sum_{\mathbf{R}_\mathrm{A}} a^\dagger_{\mathbf{R}_\mathrm{A}} a_{\mathbf{R}_\mathrm{A}} + E_\mathrm{B} \sum_{\mathbf{R}_\mathrm{B}} b^\dagger_{\mathbf{R}_\mathrm{B}} b_{\mathbf{R}_\mathrm{B}} \,. \tag{2.146}$$

Here, $E_\mathrm{A}/E_\mathrm{B}$ is the on-site energy of the sites located on the A/B sublattice. This model is naturally realized in hexagonal boron nitride which has the same crystal structure as graphene but with different atomic species residing on the two sublattices – however, the band gap is very large and the Dirac-like physics is somewhat washed away. Alternatively, this model can be realized by fabricating graphene on a boron nitride substrate which presents a sublattice-specific potential landscape if the crystallographic axes are aligned [35]. Furthermore, similar physics also emerges in transition metal dichalcogenides although the crystal structure is somewhat more complicated [185].

We can Fourier transform the Semenoff Hamiltonian to momentum space where the Bloch Hamiltonian reads $\mathcal{H}_\mathrm{S}(\mathbf{q}) = \mathcal{H}(\mathbf{q}) + \Delta\mathcal{H}_\mathrm{S}(\mathbf{q})$. Here $\mathcal{H}(\mathbf{q})$ is given by equation (2.14) and the new term reads

$$\Delta\mathcal{H}_\mathrm{S} = E_0 \mathbb{1}_2 + m\sigma_z \,, \tag{2.147}$$

where the diagonal term is given by the average on-site energy $E_0 = (E_\mathrm{A} + E_\mathrm{B})/2$ which we will set to zero. The mass term is momentum-independent and given by the difference in on-site energies

$$m = \frac{1}{2}(E_\mathrm{A} - E_\mathrm{B}) \,. \tag{2.148}$$

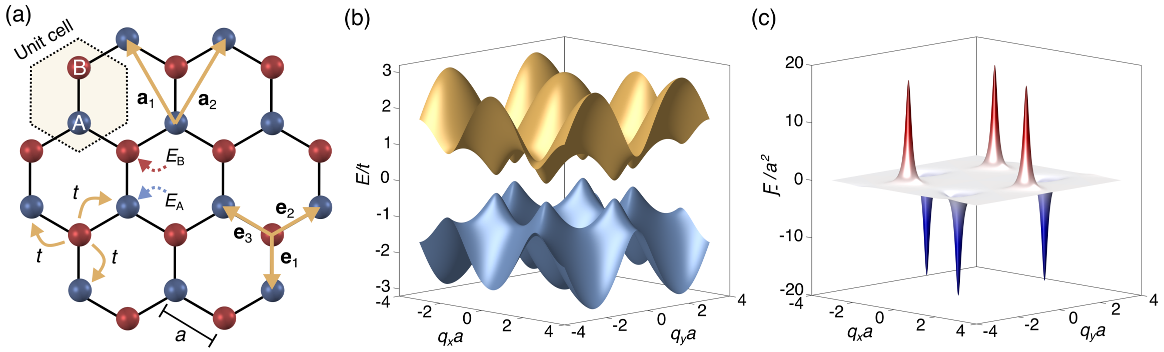

Figure 2.11 | Semenoff insulator. (a) Schematic of the Semenoff model, which is the graphene tight-binding model with staggered onsite energies $E_\mathrm{A} \neq E_\mathrm{B}$ on the two inequivalent sublattices. (b) Spectrum of the Semenoff Hamiltonian with $m = 0.25t$. The staggered onsite energies break $\mathcal{I}$ symmetry which gaps out the Dirac points, giving rise to a bulk insulator at half filling. (c) Corresponding Berry curvature for the valence band which is an odd function of $\mathbf{q}$ by virtue of $\mathcal{T}$ symmetry. Consequently, the Chern number vanishes and thus the Semenoff model represents a trivial insulator. However, for small perturbations, the Berry curvature is strongly localized near the two valleys which gives rise to non-trivial valley-Chern numbers $C_-^\tau = \tau\,\mathrm{sgn}(m)/2$. Reversing the symmetry-breaking perturbation ($m \to -m$) inverts the sign of the valley-Chern numbers $C_-^\tau = -\tau\,\mathrm{sgn}(m)/2$.

In figure 2.11(b) we show the spectrum on the Semenoff Hamiltonian

$$E_\lambda(\mathbf{q}) = \lambda\sqrt{|f(\mathbf{q})| + m^2} \tag{2.149}$$

for $m = 0.25t$ which is fully gapped and therefore corresponds to an insulator at half filling.

In figure 2.11(c) we plot the corresponding Berry curvature for the valence band, which is an odd function of $\mathbf{q}$ by virtue of $\mathcal{T}$ symmetry. Consequently, in stark contrast to the Haldane insulator, this model represents a trivial insulator with a vanishing Chern number. This is evident if one considers the limit $|m| \gg t$ where the states are entirely localized on one of the two sublattices. Therefore, the Semenoff insulator can be adiabatically transformed into a trivial atomic insulator without closing the gap; but is it really that trivial? The answer is a definitive no. While the total Berry curvature vanishes, for small perturbations the Berry curvature is strongly localized near the K/K' points, which can give rise to very interesting valley-contrasting physics [33–35, 185–187].

We can capture the essential physics by linearizing the Hamiltonian near the K/K' points which read

$$\mathcal{H}_+(\mathbf{k}) = \hbar v_\mathrm{F}\boldsymbol{\sigma}\cdot\mathbf{k} + m_+\sigma_z \quad , \quad \mathcal{H}_-(\mathbf{k}) = -\hbar v_\mathrm{F}\boldsymbol{\sigma}^*\cdot\mathbf{k} + m_-\sigma_z\,, \tag{2.150}$$

where $m_+ = m_- = m$. As expected, the Semenoff fermions are effectively described by a massive Dirac Hamiltonian with a gapped Dirac cone spectrum

$$E_\lambda(\mathbf{k}) = \lambda\sqrt{\hbar^2 v_\mathrm{F}^2|\mathbf{k}|^2 + m_\tau^2}\,, \tag{2.151}$$

which is similar to the low-energy spectrum of the Haldane insulator. However, the Semenoff mass has the same sign in both valleys, and therefore $\hat{\mathbf{d}}(\mathbf{q})$ only ever visits the north (south) pole of the Bloch sphere if $m > 0$ ($m < 0$). In other words, it does not wrap the Bloch sphere and therefore one can define a smooth gauge over the entire Brillouin zone. Consequently, the Chern number must vanish which can also be seen from equation (2.130) which gives

$$C_- = \frac{1}{2}\sum_\tau W(\tau\mathbf{K})\,\mathrm{sgn}[d_z(\tau\mathbf{K})] = \frac{1}{2}[\mathrm{sgn}(m_+) - \mathrm{sgn}(m_-)] = 0\,. \tag{2.152}$$

Using the effective Dirac Hamiltonians in equation (2.150) we can calculate a simple analytical expression for the effective Berry curvature

$$\mathcal{F}_\lambda^\tau(\mathbf{k}) = -\tau\lambda\frac{\hbar^2 v_\mathrm{F}^2 m}{2(\hbar^2 v_\mathrm{F}^2|\mathbf{k}|^2 + m^2)^{3/2}}\,, \tag{2.153}$$

which, as expected, has opposite signs in the two valleys. Within the regime of semiclassical dynamics, the Berry curvature acts as an effective magnetic field in momentum space which can generate a Lorentz-like force. This drives electrons within different valleys to opposite transverse edges when subjected to an in-plane electric field, which is the origin of the valley-Hall effect [33–35, 185–187].

Furthermore, if we integrate the effective Berry curvature for each valley then we obtain the so-called valley-Chern numbers

$$C_\lambda^\tau = \frac{1}{2\pi}\iint\limits_{\mathbb{R}^2} \mathrm{d}^2\mathbf{k}\,\mathcal{F}_\lambda^\tau(\mathbf{k}) = -\tau\lambda\,\mathrm{sgn}(m)\frac{1}{2}\,, \tag{2.154}$$

which assume half-integer values $\pm 1/2$. At first sight, this seems to be in contradiction with the definition of the Chern number which always assumes an integer value. However, the integral in equation (2.154) is not over a closed manifold (i.e., the Brillouin zone) but is over the entire real domain $\mathbf{k} \in \mathbb{R}^2$, and therefore it is not restricted to integer values. Strictly speaking, the value of $\pm 1/2$ is an artefact of the Dirac approximation. For large perturbations the Berry curvature becomes increasingly dispersed throughout the Brillouin zone and the contributions from each valley cancel – in the limit $|m| \gg |t|$ the Berry curvature vanishes.

Consequently, the valley-Chern numbers are only well defined when the Berry curvature is localized near the valleys. Furthermore, the sum of the valley-Chern numbers is equal to the Chern number $C_\lambda = C_\lambda^+ + C_\lambda^- = 0$ which vanishes, as required by $\mathcal{T}$ symmetry. The question is: do the non-trivial valley-Chern numbers have any physical consequence on the boundary of the system?

2.4.5 Valley-Hall edge states

While the valley-Chern numbers imply that the geometrical properties of the eigenstates are non-trivial, they are not topological invariants. However, if one considers a domain wall between two insulators that have opposite valley-Chern numbers, then one can establish a new topological invariant and bulk-boundary correspondence: the change in valley-Chern number across the interface predicts the number of valley-polarized chiral edge states that populate the interface [36–41]. Since $\mathcal{T}$ symmetry is preserved, the valley-Hall edge states within each valley propagate in opposite directions in analogy with the quantum spin-Hall insulator [31].

To illustrate this, let us consider a domain wall between two distinct Semenoff insulators as schematically depicted in figure 2.12(a), where the staggered on-site energies are reversed across the interface [37]. To highlight the essential physics we will use the same procedure as outlined in section 2.4.3. In particular, we can model the interface using the effective Dirac Hamiltonian in equation (2.140), where the spatially-varying mass is now given by

$$m_\tau(y) = \begin{cases} +m_\mathrm{S}, & \text{for } y < 0 \\ -m_\mathrm{S}, & \text{for } y > 0 \end{cases} \tag{2.155}$$

While the bulk spectrum is identical in both regions, they have opposite valley-Chern numbers as the mass changes sign across the interface.

As before, we can exploit the translational invariance along the x-direction by writing the wavefunction as $\psi_\tau(\mathbf{r}) = \psi_\tau(y)\mathrm{e}^{\mathrm{i}k_x x}$, where the zero-energy eigenstates with $k_x = 0$ are the solutions to equation (2.142). In order for the wavefunctions to be bounded and normalizable, they must be eigenstates of σ_x with eigenvalue $\mathrm{sgn}(m_\mathrm{S})$. Therefore, after restoring the parallel wavevector, the envelope wavefunction of the valley-Hall edge states read

$$\psi_\tau(\mathbf{r}) \propto \begin{bmatrix} 1 \\ \mathrm{sgn}(m_\mathrm{S}) \end{bmatrix} \mathrm{e}^{-\frac{|m_\mathrm{S}|}{\hbar v_\mathrm{F}}|y|}\mathrm{e}^{\mathrm{i}k_x x}\,, \tag{2.156}$$

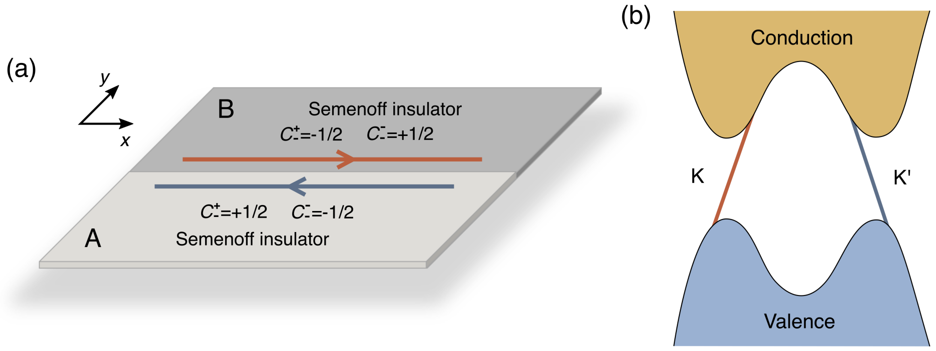

Figure 2.12 | Topological valley-Hall edge states. (a) Schematic of a domain wall interface between two distinct valley-Hall insulators, where region A is a Semenoff insulator with $C_-^\tau = \tau$ and region B is a Semenoff insulator with $C_-^\tau = -\tau$. (b) Schematic of the interface spectrum. The bulk spectrum is gapped and identical in both regions, but each valley exhibits a chiral edge state which traverses the bulk gap and is exponentially localized at the interface. Since $\mathcal{T}$ symmetry is preserved, these valley-Hall edge states propagate in opposite directions and are robust against backscattering from disorder that does not strongly mix the valleys.

and their spectrum is given by

$$E_\tau(k_x) = \tau\,\mathrm{sgn}(m_\mathrm{S})\hbar v_\mathrm{F} k_x\,. \tag{2.157}$$

Consequently, each valley supports a chiral edge state which propagate in opposite directions as schematically depicted in figure 2.12(b) – this is consistent with the bulk-boundary correspondence since $\Delta C_-^\tau = \tau$.

It should be stressed that these valley-Hall edge states do not boast the same topological protection as the chiral edge states associated with the Chern insulator, where the latter exist along any interface and are protected against backscattering from arbitrary disorder. In contrast, the valley-Hall edge states are only well defined along certain inclinations where the valley projections on the edge Brillouin zone are well separated in momentum space. Moreover, they are only robust against backscattering from disorder that does not strongly mix the valleys.

To date, these valley-Hall edge states have evaded observation in graphene, but they have been experimentally observed in bilayer graphene [42, 43]. Moreover since the valley-Hall insulator phase can easily be induced by breaking simple lattice symmetries, it has been successfully realized in a wide variety of photonic systems across the electromagnetic spectrum [83–92] and in many other artificial lattices [188–192]. The major advantage of these systems is that one does not require magnetic fields or external driving to break $\mathcal{T}$ symmetry, which is a strict requirement for the Chern insulator.

2.5 Conclusion

In this introductory chapter we have provided a brief overview of some of the most interesting aspects of graphene-related physics. In particular, we have shown that the low-energy quasiparticles are effectively described by a massless Dirac Hamiltonian, and thus exhibit pseudo-relativistic phenomena such as Klein tunnelling. We have demonstrated that the Dirac points are locally stabilized by the presence of $\mathcal{T}$ and $\mathcal{I}$ symmetry, while the $\mathcal{C}_3$ symmetry of the honeycomb lattice pins them to the high-symmetry points. Furthermore, we have highlighted that interesting physics can emerge by systematically breaking these symmetries. In particular, straining the lattice breaks the $\mathcal{C}_3$ symmetry which gives rise to a pseudo-vector potential in the Hamiltonian, which can be engineered to generate a pseudo-magnetic field. Moreover, applying large uniform strain can induce the merging and annihilation of the Dirac points, resulting in a transition from a semi-metal phase to a trivial insulator phase. Finally, we have shown that breaking $\mathcal{T}$ and $\mathcal{I}$ symmetry gaps out the Dirac cones which gives rise to interesting insulators with non-trivial geometrical and topological properties. The former results in a Chern insulator which supports unidirectional chiral edge states, while the latter results in a valley-Hall insulator which supports counter-propagating valley-Hall edge states along certain domain wall interfaces.

3

Light-matter interactions inside a cavity waveguide

Metamaterials have transformed our ability to manipulate waves. By engineering the way light interacts with matter on a subwavelength scale one can control light in ways that are impossible to achieve with natural materials. Taking inspiration from graphene physics, in the following chapters we will explore a range of interesting phenomena that can emerge in 2D hexagonal metasurfaces composed of a subwavelength arrays dipoles embedded inside a cavity waveguide. In this chapter we will build the theoretical foundations that will be used as the starting point throughout the rest of the thesis. Specifically, we will develop a self-consistent coupled-dipole theory using a Green's function formalism, which can describe the collective dynamics of dipoles embedded inside a cavity waveguide. Using a simple square metasurface as a concrete example, we will demonstrate how this theory can be used to derive the dispersion of the cavity polaritons supported by a periodic array of dipoles. Furthermore, we will highlight how one can modify the nature of the dipole-dipole interactions, and thus the properties of the polaritons, by varying only the cavity width.

3.1 Introduction

The radiative properties of emitters and antennas are not fixed characteristics that are determined solely by their intrinsic structure; they are also inextricably linked to the local photonic environment in which they are embedded. Probably the most well known example is the Purcell effect [94], where spontaneous emission rates can be enhanced or inhibited by placing an emitter within a structured photonic environment, e.g., above a mirror [193–196], inside a cavity [95–99] or inside a photonic crystal [197–201]. Moreover, their properties can be drastically altered when other emitters/antennas are within close proximity due to collective interactions which lead to frequency shifts and modified decay rates [202–207]. Even richer scenarios can emerge in ordered 1D arrays and 2D metasurfaces, which have been extensively explored in classical systems [208–216] and more recently in the quantum domain [217–226]. In particular, for subwavelength arrays, the collective interactions result in subradiant polariton excitations that are decoupled from free space photons and can thus be exploited for guiding electromagnetic energy.

It is evident that the properties of these hybrid polaritons can be tailored by modifying the underlying geometry of the lattice. Therefore, taking inspiration from the physics of graphene, in the following chapters we will consider 2D hexagonal metasurfaces which endow the polaritons with Dirac-like properties. However, the local photonic environment also plays a fundamental role since it determines the availability and properties of the photonic modes that mediate interactions between the emitters [227–232].

To illustrate this, consider the special case where there are no resonant photonic modes that the emitter can couple to (e.g., deep inside the band gap of a photonic crystal). Here the electromagnetic field would decay evanescently from the emitter; only in this special case would a lattice of emitters essentially emulate tight-binding physics. However, in the general case, there are many resonant photonic modes available (e.g., in free space) and the coherent dipole-dipole interactions become long-range and oscillate with separation distance – the interaction strength does not simply decrease monotonically with separation distance. Therefore, the intuition acquired from tight-binding models tends to break down as one typically needs to include all the interactions between all pairs of emitters to capture the essential physics.

Exploiting this unique property of the emitters, we will consider a scenario where the metasurfaces are embedded inside a cavity waveguide comprised of two perfect mirrors. Moreover, we focus solely on the transverse polaritons where the dipole moments are oriented normal to the plane of the lattice; for this case, there always exists resonant cavity modes that the dipoles can couple to. For relatively large cavity widths the properties of the Dirac polaritons are dominated by the near-field Coulomb interactions due to the subwavelength spacing of the metasurfaces. However, as the cavity width is reduced, the Coulomb interactions become suppressed due to the screening effect of the cavity waveguide. In stark contrast, the long-range photon-mediated interactions become increasingly dominant as the light-matter interaction strength is increased. Using this mechanism to modify the dipolar coupling, we will unveil a range of interesting phenomena that are impossible to achieve in photonic systems that emulate the tight-binding physics of graphene.

In this chapter we will lay the theoretical foundations that will be used as a starting point throughout the rest of this thesis. We will not specialize to any particular system as we are interested in the general physics that could potentially be realized in a variety of experimental set-ups across the electromagnetic spectrum. These could range from classical metasurfaces composed of microwave antennas to quantum metasurfaces composed of atom-like emitters – though our classical analysis will only be applicable in the single-excitation subspace [233]. We begin by deriving the longitudinal and transverse components of the cavity Green's function which encode the Coulomb and photon-mediated interactions, respectively. Using the cavity Green's function, we will then develop a self-consistent coupled-dipole theory that enables one to describe the collective dynamics of an array of dipoles embedded inside a cavity waveguide and calculate the dispersion of the cavity polaritons.

3.2 Maxwell's equations in the Coulomb gauge

In the frequency domain, Maxwell's equations read [234]

$$\boldsymbol{\nabla}\cdot\mathbf{E}(\mathbf{r},\omega)=\frac{1}{\epsilon_0}\rho(\mathbf{r},\omega)\,, \tag{3.1}$$

$$\boldsymbol{\nabla}\cdot\mathbf{B}(\mathbf{r},\omega)=0\,, \tag{3.2}$$

$$\boldsymbol{\nabla}\times\mathbf{E}(\mathbf{r},\omega)=\mathrm{i}\omega\mathbf{B}(\mathbf{r},\omega)\,, \tag{3.3}$$

$$\boldsymbol{\nabla}\times\mathbf{B}(\mathbf{r},\omega)=-\mathrm{i}\mu_0\epsilon_0\omega\mathbf{E}(\mathbf{r},\omega)+\mu_0\mathbf{J}(\mathbf{r},\omega)\,, \tag{3.4}$$

where $\mathbf{E}(\mathbf{r},\omega)$ is the electric field, $\mathbf{B}(\mathbf{r},\omega)$ is the magnetic field, $\rho(\mathbf{r},\omega)$ is the charge density, $\mathbf{J}(\mathbf{r},\omega)$ is the current density, ϵ_0 is the permittivity of free space, and μ_0 is the permeability of free space. We can automatically satisfy the homogeneous Maxwell's equations by expressing the electric and magnetic fields as

$$\mathbf{E}(\mathbf{r},\omega) = \mathrm{i}\omega\mathbf{A}(\mathbf{r},\omega) - \boldsymbol{\nabla}\phi(\mathbf{r},\omega)\,, \qquad \mathbf{B}(\mathbf{r},\omega) = \boldsymbol{\nabla}\times\mathbf{A}(\mathbf{r},\omega)\,, \tag{3.5}$$

where we have introduced two auxiliary fields; the scalar potential $\phi(\mathbf{r},\omega)$ and the vector potential $\mathbf{A}(\mathbf{r},\omega)$. However, the choice of potentials is not unique since the electric and magnetic fields (and therefore Maxwell's equations) are manifestly invariant under the following gauge transformation

$$\begin{aligned} \mathbf{A}(\mathbf{r},\omega) &\to \mathbf{A}'(\mathbf{r},\omega) = \mathbf{A}(\mathbf{r},\omega) + \boldsymbol{\nabla}\chi(\mathbf{r},\omega) \\ \phi(\mathbf{r},\omega) &\to \phi'(\mathbf{r},\omega) = \phi(\mathbf{r},\omega) + \mathrm{i}\omega\chi(\mathbf{r},\omega) \end{aligned} \tag{3.6}$$

where $\chi(\mathbf{r},\omega)$ is an arbitrary scalar field [235]. In what follows, we will remove this redundancy by choosing a gauge that is useful for describing the metasurfaces.

According to the Helmholtz theorem, we may decompose the electric field as

$$\mathbf{E}(\mathbf{r},\omega) = \mathbf{E}_{\parallel}(\mathbf{r},\omega) + \mathbf{E}_{\perp}(\mathbf{r},\omega)\,, \tag{3.7}$$

where $\mathbf{E}_{\parallel}(\mathbf{r},\omega)$ is the longitudinal (irrotational) component and $\mathbf{E}_{\perp}(\mathbf{r},\omega)$ is the transverse (solenoidal) component which satisfy the following conditions

$$\boldsymbol{\nabla}\times\mathbf{E}_{\parallel}(\mathbf{r},\omega) = 0\,, \qquad \boldsymbol{\nabla}\cdot\mathbf{E}_{\perp}(\mathbf{r},\omega) = 0\,. \tag{3.8}$$

In contrast, the magnetic field is a purely transverse field since its divergence vanishes according to equation (3.2). Moreover, it is evident from equation (3.6) that the transverse component of the vector potential $\mathbf{A}_{\perp}(\mathbf{r},\omega)$ is a gauge invariant quantity; therefore, the gauge transformation amounts to a redistribution of the longitudinal electric field between the scalar and vector potentials.

In what follows we will work in the Coulomb gauge where the vector potential is chosen to be a purely transverse field whose divergence is zero

$$\boldsymbol{\nabla}\cdot\mathbf{A}(\mathbf{r},\omega) = 0\,, \qquad \mathbf{A}(\mathbf{r},\omega) = \mathbf{A}_{\perp}(\mathbf{r},\omega)\,. \tag{3.9}$$

The advantage of the Coulomb gauge is that it separates the static and dynamical aspects of a system [236], where the longitudinal component of the electric field is entirely described by the scalar potential

$$\mathbf{E}_{\parallel}(\mathbf{r},\omega) = -\boldsymbol{\nabla}\phi(\mathbf{r},\omega)\,, \tag{3.10}$$

while the transverse component is entirely described by the vector potential

$$\mathbf{E}_{\perp}(\mathbf{r},\omega) = \mathrm{i}\omega\mathbf{A}(\mathbf{r},\omega)\,. \tag{3.11}$$

If we substitute equation (3.10) into equation (3.1) then we find that the scalar potential satisfies Poisson's equation

$$\nabla^2\phi(\mathbf{r},\omega) = -\frac{1}{\epsilon_0}\rho(\mathbf{r},\omega)\,, \tag{3.12}$$

and thus corresponds to the Coulomb potential generated by an instantaneous charge distribution. Furthermore, if we substitute equation (3.4) into the curl of equation (3.3), then from equation (3.11) we find that the vector potential satisfies the following equation

$$\nabla^2\mathbf{A}(\mathbf{r},\omega) + k_\omega^2\mathbf{A}(\mathbf{r},\omega) = -\mathrm{i}\epsilon_0\mu_0\omega\boldsymbol{\nabla}\phi(\mathbf{r},\omega) - \mu_0\mathbf{J}(\mathbf{r},\omega)\,, \tag{3.13}$$

where we have defined $k_\omega = \omega/c$. Given that the vector potential is a purely transverse field in the Coulomb gauge, the right hand side of equation (3.13) ought to be transverse as well. To see this, we can substitute equation (3.1) into the divergence of equation (3.4) to obtain the continuity equation

$$\mathrm{i}\omega\rho(\mathbf{r},\omega) = \boldsymbol{\nabla}\cdot\mathbf{J}_{\parallel}(\mathbf{r},\omega)\,. \tag{3.14}$$

Finally, using equation (3.10) we can eliminate the longitudinal components on the right hand side of equation (3.13) to obtain

$$\nabla^2\mathbf{A}(\mathbf{r},\omega) + k_\omega^2\mathbf{A}(\mathbf{r},\omega) = -\mu_0\mathbf{J}_{\perp}(\mathbf{r},\omega)\,, \tag{3.15}$$

where the source is just the transverse component of the current density [235].

Since the scalar potential responds instantaneously to changes in the charge distribution, we can infer from equation (3.10) that the longitudinal electric field propagates with infinite speed which, at first glance, appears to violate causality – however, it must be stressed that only the total electric field has any physical meaning. It can be shown that the vector potential, and therefore the transverse electric field, also has a non-retarded component which conspires to exactly cancel the non-retarded contribution from the scalar potential, yielding a fully retarded and causal electric field [237].

3.3 Dyadic Green's function for a cavity waveguide

The total electric field generated by an arbitrary current source can be expressed in terms of an integral equation

$$\mathbf{E}(\mathbf{r},\omega) = -\frac{1}{\mathrm{i}\epsilon_0\omega\mathcal{V}} \iiint\limits_{V} \mathrm{d}^3\mathbf{r}'\, \overleftrightarrow{\mathbf{G}}(\mathbf{r},\mathbf{r}',\omega)\cdot\mathbf{J}(\mathbf{r}',\omega)\ , \tag{3.16}$$

where the integration volume V encloses the source and $\overleftrightarrow{\mathbf{G}}(\mathbf{r},\mathbf{r}',\omega)$ is the dyadic Green's function [238]. Note, in equation (3.16) we have introduced the factor $\mathcal{V}$ which has units of volume in order to render the Green's function dimensionless – its explicit form will be conveniently chosen later to simplify equations. If we specialize to the case of a point dipole source located at $\mathbf{r}_0$ whose current density is

$$\mathbf{J}(\mathbf{r},\omega) = -\mathrm{i}\omega\mathbf{p}(\omega)\delta(\mathbf{r}-\mathbf{r}_0)\,, \tag{3.17}$$

where $\mathbf{p}(\omega)$ is the corresponding dipole moment and $\delta(\mathbf{r}-\mathbf{r}_0)$ is the Dirac delta function, then equation (3.16) gives

$$\mathbf{E}(\mathbf{r},\omega) = \frac{1}{\epsilon_0\mathcal{V}}\overleftrightarrow{\mathbf{G}}(\mathbf{r},\mathbf{r}_0,\omega)\cdot\mathbf{p}(\omega)\ . \tag{3.18}$$

Thus we have arrived at a transparent, physical interpretation of the Green's function: $\hat{\mathbf{n}}_1\cdot\overleftrightarrow{\mathbf{G}}(\mathbf{r},\mathbf{r}',\omega)\cdot\hat{\mathbf{n}}_2$ describes the electric field at $\mathbf{r}$ along the $\hat{\mathbf{n}}_1$ direction which is generated by a point dipole source located at $\mathbf{r}'$ whose dipole moment is oriented in the $\hat{\mathbf{n}}_2$ direction [238].

Clearly, the Green's function depends sensitively on the local electromagnetic environment and the corresponding boundary conditions. Throughout this thesis we will be studying the collective dynamics of dipoles which are embedded inside a cavity waveguide of width L. For simplicity, we assume that the cavity waveguide is formed by two perfect mirrors located at $z=\pm L/2$, where the electric field satisfies the boundary conditions

$$\hat{\mathbf{z}}\times\mathbf{E}(\mathbf{r},\omega)\Big|_{z=\pm\frac{L}{2}} = 0\,. \tag{3.19}$$

It will be convenient to decompose the Green's function into its longitudinal and transverse components

$$\overleftrightarrow{\mathbf{G}}(\mathbf{r},\mathbf{r}',\omega)=\overleftrightarrow{\mathbf{G}}_{\|}(\mathbf{r},\mathbf{r}')+\overleftrightarrow{\mathbf{G}}_{\perp}(\mathbf{r},\mathbf{r}',\omega)\,, \tag{3.20}$$

where the longitudinal Green's function describes the longitudinal electric field via the integral relation

$$\mathbf{E}_{\|}(\mathbf{r},\omega)=-\frac{1}{\mathrm{i}\epsilon_0\omega\mathcal{V}}\iiint\limits_V \mathrm{d}^3\mathbf{r}'\,\overleftrightarrow{\mathbf{G}}_{\|}(\mathbf{r},\mathbf{r}')\cdot\mathbf{J}(\mathbf{r}',\omega)\,, \tag{3.21}$$

and the transverse Green's function describes the transverse electric field via the integral relation

$$\mathbf{E}_{\perp}(\mathbf{r},\omega)=-\frac{1}{\mathrm{i}\epsilon_0\omega\mathcal{V}}\iiint\limits_V \mathrm{d}^3\mathbf{r}'\,\overleftrightarrow{\mathbf{G}}_{\perp}(\mathbf{r},\mathbf{r}',\omega)\cdot\mathbf{J}(\mathbf{r}',\omega)\,. \tag{3.22}$$

For the special case of a point dipole source located at $\mathbf{r}_0$, equation (3.21) and equation (3.22) simplify to

$$\mathbf{E}_{\|}(\mathbf{r},\omega)=\frac{1}{\epsilon_0\mathcal{V}}\overleftrightarrow{\mathbf{G}}_{\|}(\mathbf{r},\mathbf{r}_0)\cdot\mathbf{p}(\omega)\,,\qquad \mathbf{E}_{\perp}(\mathbf{r},\omega)=\frac{1}{\epsilon_0\mathcal{V}}\overleftrightarrow{\mathbf{G}}_{\perp}(\mathbf{r},\mathbf{r}_0,\omega)\cdot\mathbf{p}(\omega)\,. \tag{3.23}$$

In the next sections we will derive the longitudinal and transverse components of the cavity Green's function via the scalar and vector potential, respectively.

3.3.1 Eigenfunction expansion of the longitudinal Green's function

We will begin by deriving the longitudinal component of the cavity Green's function using the scalar potential which, in the Coulomb gauge, satisfies Poisson's equation

$$\nabla^2\phi(\mathbf{r},\omega)=-\frac{1}{\epsilon_0}\rho(\mathbf{r},\omega)\,,\qquad \phi(\mathbf{r},\omega)\Big|_{z=\pm\frac{L}{2}}=0\,, \tag{3.24}$$

and is subject to homogeneous Dirichlet boundary conditions on the cavity walls. To solve equation (3.24) we can introduce the scalar Green's function $G_\phi(\mathbf{r},\mathbf{r}')$ which satisfies Poisson's equation with a Dirac delta function source

$$\nabla^2 G_\phi(\mathbf{r},\mathbf{r}')=-\delta(\mathbf{r}-\mathbf{r}')\,,\qquad G_\phi(\mathbf{r},\mathbf{r}')\Big|_{z=\pm\frac{L}{2}}=0\,, \tag{3.25}$$

and is subject to the same boundary conditions as the scalar potential. Using the scalar Green's function we can calculate the scalar potential generated by an arbitrary charge distribution via the following integral relation

$$\phi(\mathbf{r},\omega) = \frac{1}{\epsilon_0}\iiint\limits_V \mathrm{d}^3\mathbf{r}'\, G_\phi(\mathbf{r},\mathbf{r}')\rho(\mathbf{r}',\omega)\,. \tag{3.26}$$

If we substitute equation (3.14) into equation (3.26) and integrate by parts, then we can use equation (3.10) to write the longitudinal electric field as in equation (3.21) where the longitudinal Green's function is given by

$$\overset{\leftrightarrow}{\mathbf{G}}_{\|}(\mathbf{r},\mathbf{r}') = -\mathcal{V}\boldsymbol{\nabla}\boldsymbol{\nabla}' G_\phi(\mathbf{r},\mathbf{r}')\,. \tag{3.27}$$

Here the gradient operator $\boldsymbol{\nabla}'$ operates on the source coordinates $\mathbf{r}'$, and $\boldsymbol{\nabla}\boldsymbol{\nabla}'$ is the dyadic product of the operators which explicitly reads

$$\boldsymbol{\nabla}\boldsymbol{\nabla}' = \begin{bmatrix} \frac{\partial}{\partial x}\frac{\partial}{\partial x'} & \frac{\partial}{\partial x}\frac{\partial}{\partial y'} & \frac{\partial}{\partial x}\frac{\partial}{\partial z'} \\ \frac{\partial}{\partial y}\frac{\partial}{\partial x'} & \frac{\partial}{\partial y}\frac{\partial}{\partial y'} & \frac{\partial}{\partial y}\frac{\partial}{\partial z'} \\ \frac{\partial}{\partial z}\frac{\partial}{\partial x'} & \frac{\partial}{\partial z}\frac{\partial}{\partial y'} & \frac{\partial}{\partial z}\frac{\partial}{\partial z'} \end{bmatrix}\,. \tag{3.28}$$

Our task is then to find the scalar Green's function for the cavity waveguide which we will do using the eigenfunction expansion technique that is outlined in many textbooks [239, 240]. First, we introduce the scalar functions $f_\kappa(\mathbf{r})$ which satisfy the scalar Helmholtz equation

$$(\nabla^2 + \kappa^2) f_\kappa(\mathbf{r}) = 0\,, \qquad f_\kappa(\mathbf{r})\Big|_{z=\pm\frac{L}{2}} = 0\,, \tag{3.29}$$

and are subject to the same boundary conditions as the scalar Green's function. Using the separation of variables method one finds

$$f_\kappa(\mathbf{r}) = \sin(k_m \tilde{z})\mathrm{e}^{\mathrm{i}\mathbf{k}\cdot\boldsymbol{\rho}}\,, \tag{3.30}$$

with $\kappa^2 = k^2 + k_m^2$. Here $k_m = m\pi/L$ is quantized due to the boundary conditions where $m \in \mathbb{N}$ is a positive integer, and $\mathbf{k} = [\,k_x\,,\,k_y\,]$ is the in-plane wavevector where k_x and k_y takes continuous values due to the translational invariance in the xy-plane. Note, in equation (3.30) the subscript κ should be understood as labelling distinct combinations of the parameters $\{\mathbf{k}, k_m\}$. Note, we have also decomposed the position vector as $\mathbf{r} = \boldsymbol{\rho} + z\hat{\mathbf{z}}$ where

$\boldsymbol{\rho} = [\,x\,,\,y\,]$ is the in-plane position vector, and we have introduced the shifted coordinate $\tilde{z} = z + L/2$ for convenience.

Since the Laplacian is a Hermitian operator, the eigenfunctions in equation (3.30) form a complete orthogonal basis for a general scalar field that is subject to the same boundary conditions. The orthogonality and normalization condition reads

$$\iint\limits_{-\infty}^{\infty} \mathrm{d}^2\boldsymbol{\rho} \int\limits_{-L/2}^{L/2} \mathrm{d}z\, f_\kappa(\mathbf{r}) f^*_{\kappa'}(\mathbf{r}) = (2\pi)^2 \frac{L}{2} \delta(\mathbf{k}-\mathbf{k}')\delta_{mm'}\,, \tag{3.31}$$

where $\delta_{mm'}$ is the Kronecker delta function. Moreover, we can expand the Dirac delta function as

$$\delta(\mathbf{r}-\mathbf{r}') = \frac{2}{L}\sum_{m=1}^{\infty} \sin(k_m\tilde{z})\sin(k_m\tilde{z}') \iint\limits_{-\infty}^{\infty} \frac{\mathrm{d}^2\mathbf{k}}{(2\pi)^2} \mathrm{e}^{\mathrm{i}\mathbf{k}\cdot(\boldsymbol{\rho}-\boldsymbol{\rho}')}\,, \tag{3.32}$$

which is the so-called completeness or closure relation. In order to find an expression for the scalar Green's function we can expand it in terms of the eigenfunctions

$$G_\phi(\mathbf{r},\mathbf{r}') = \frac{2}{L}\sum_{m=1}^{\infty} \sin(k_m\tilde{z})\sin(k_m\tilde{z}') \iint\limits_{-\infty}^{\infty} \frac{\mathrm{d}^2\mathbf{k}}{(2\pi)^2} a_\kappa \mathrm{e}^{\mathrm{i}\mathbf{k}\cdot(\boldsymbol{\rho}-\boldsymbol{\rho}')}\,, \tag{3.33}$$

where the unknown coefficients a_κ can be found by substituting equation (3.32) and equation (3.33) into equation (3.25), which yields

$$a_\kappa = \frac{1}{k^2 + k_m^2}\,. \tag{3.34}$$

Therefore, the eigenfunction expansion of the scalar Green's function reads

$$G_\phi(\mathbf{r},\mathbf{r}') = \frac{2}{L}\sum_{m=1}^{\infty} \sin(k_m\tilde{z})\sin(k_m\tilde{z}') \iint\limits_{-\infty}^{\infty} \frac{\mathrm{d}^2\mathbf{k}}{(2\pi)^2} \frac{\mathrm{e}^{\mathrm{i}\mathbf{k}\cdot(\boldsymbol{\rho}-\boldsymbol{\rho}')}}{k^2 + k_m^2}\,. \tag{3.35}$$

The final task is to evaluate the integral in equation (3.35) in order to obtain a closed form expression for each term in the sum. To achieve this, we convert the integral over $\mathbf{k}$ into polar coordinates and choose $\boldsymbol{\rho} - \boldsymbol{\rho}'$ to be aligned parallel with the $\phi_{\mathbf{k}} = 0$ axis

$$G_\phi(\mathbf{r}, \mathbf{r}') = \frac{2}{L} \sum_{m=1}^{\infty} \sin(k_m \tilde{z}) \sin(k_m \tilde{z}') \int_0^{\infty} \frac{\mathrm{d}k}{2\pi} k \int_0^{2\pi} \frac{\mathrm{d}\phi_{\mathbf{k}}}{2\pi} \frac{\mathrm{e}^{\mathrm{i}k\cos\phi_{\mathbf{k}}|\boldsymbol{\rho}-\boldsymbol{\rho}'|}}{k^2 + k_m^2} \,. \tag{3.36}$$

We can then decompose the plane waves into Bessel functions of the first kind J_n using the Jacobi-Anger identity

$$\mathrm{e}^{\mathrm{i}k\cos\phi_{\mathbf{k}}|\boldsymbol{\rho}-\boldsymbol{\rho}'|} = \sum_{n=-\infty}^{\infty} \mathrm{i}^n J_n(k|\boldsymbol{\rho} - \boldsymbol{\rho}'|) \mathrm{e}^{\mathrm{i}n\phi_{\mathbf{k}}} \,, \tag{3.37}$$

and after performing the integration over the angular variable we obtain

$$G_\phi(\mathbf{r}, \mathbf{r}') = \frac{2}{L} \sum_{m=1}^{\infty} \sin(k_m \tilde{z}) \sin(k_m \tilde{z}') \int_0^{\infty} \frac{\mathrm{d}k}{2\pi} \frac{k J_0(k|\boldsymbol{\rho} - \boldsymbol{\rho}'|)}{k^2 + k_m^2} \,, \tag{3.38}$$

since only the $n = 0$ term survives.

To calculate the integral in equation (3.38), we can consider the following auxiliary complex integral

$$I = \oint_{\mathit{\Gamma}} \frac{\mathrm{d}k}{2\pi} \frac{k H_0^{(1)}(k|\boldsymbol{\rho} - \boldsymbol{\rho}'|)}{k^2 + k_m^2} \,, \tag{3.39}$$

where $H_0^{(1)}$ is the Hankel function of first kind and zeroth order. Here, $\mathit{\Gamma}$ is the (infinite) semi-circle contour in the upper-half complex plane which is indented at the origin to avoid the logarithmic singularity. Using the residue theorem one can evaluate equation (3.39) by simply calculating the residue of the pole located along the positive imaginary axis at $k = \mathrm{i}k_m$. This gives

$$I = \frac{1}{\pi} K(k_m |\boldsymbol{\rho} - \boldsymbol{\rho}'|) \,, \tag{3.40}$$

where we have used the relation $H_0^{(1)}(\mathrm{i}x) = -\mathrm{i}(2/\pi) K_0(x)$ with K_0 being the modified Bessel function of first kind and zeroth order [241].

Furthermore, since the asymptotic behaviour of the Hankel function is [241]

$$H_0^{(1)}(z) \sim \sqrt{\frac{2}{\pi z}} \mathrm{e}^{\mathrm{i}(z - \pi/4)} \,, \qquad -\pi < \arg(z) \leq 2\pi \,, \tag{3.41}$$

the outer semi-circle contribution vanishes by Jordan's lemma, and the small semi-circle contour used to avoid the logarithmic singularity also vanishes. Therefore, we can use the following analytic continuation property [241]

$$H_0^{(1)}(\mathrm{e}^{\mathrm{i}\pi}z) = -H_0^{(2)}(z)\,, \tag{3.42}$$

where $H_0^{(2)}$ is the Hankel function of second kind and zeroth order, and the following relation

$$J_0(x) = \frac{1}{2}\left[H_0^{(1)}(x) + H_0^{(2)}(x)\right]\,, \tag{3.43}$$

to show that equation (3.38) is equal to

$$G_\phi(\mathbf{r},\mathbf{r}') = \frac{1}{\pi L}\sum_{m=1}^{\infty}\sin(k_m\tilde{z})\sin(k_m\tilde{z}')K_0\left(k_m|\boldsymbol{\rho}-\boldsymbol{\rho}'|\right)\,. \tag{3.44}$$

Finally, from equation (3.27) we obtain the following representation of the longitudinal Green's function

$$\overleftrightarrow{\mathbf{G}}_{\parallel}(\mathbf{r},\mathbf{r}') = -\frac{\mathcal{V}}{\pi L}\sum_{m=1}^{\infty}\boldsymbol{\nabla}\boldsymbol{\nabla}'\sin(k_m\tilde{z})\sin(k_m\tilde{z}')K_0\left(k_m|\boldsymbol{\rho}-\boldsymbol{\rho}'|\right)\,, \tag{3.45}$$

which describes the longitudinal electric field generated by a point dipole source inside a cavity waveguide.

3.3.2 Eigenfunction expansion of the transverse Green's function

To derive the transverse component of the cavity Green's function we will use the vector potential which, in the Coulomb gauge, satisfies the inhomogeneous vector Helmholtz equation

$$(\nabla^2 + k_\omega^2)\mathbf{A}(\mathbf{r},\omega) = -\mu_0\mathbf{J}_\perp(\mathbf{r},\omega)\,, \qquad \hat{\mathbf{z}}\times\mathbf{A}(\mathbf{r},\omega)\Big|_{z=\pm\frac{L}{2}} = 0\,, \tag{3.46}$$

and is subject to homogeneous Dirichlet boundary conditions on the cavity walls. To solve equation (3.46), we introduce the vector potential Green's function $\overleftrightarrow{\mathbf{G}}_A(\mathbf{r},\mathbf{r}',\omega)$ which is the solution to the inhomogeneous Helmholtz equation

$$(\nabla^2 + k_\omega^2)\overleftrightarrow{\mathbf{G}}_A(\mathbf{r},\mathbf{r}',\omega) = -\overleftrightarrow{\boldsymbol{\delta}}_\perp(\mathbf{r}-\mathbf{r}')\,, \qquad \hat{\mathbf{z}}\times\overleftrightarrow{\mathbf{G}}_A(\mathbf{r},\mathbf{r}',\omega)\Big|_{z=\pm\frac{L}{2}} = 0\,, \tag{3.47}$$

and is subject to the same boundary conditions as the vector potential. Because the vector potential is transverse, the source on the right hand side of equation (3.47) is the transverse delta function dyadic which has the following property

$$\mathbf{E}_\perp(\mathbf{r},\omega) = \iiint \mathrm{d}^3\mathbf{r}'\, \overset{\leftrightarrow}{\boldsymbol{\delta}}_\perp(\mathbf{r}-\mathbf{r}') \cdot \mathbf{E}(\mathbf{r}',\omega)\ , \tag{3.48}$$

where only the transverse component of the field survives the integration [242]. Using the Green's function we can calculate the vector potential generated by an arbitrary current source via the following integral relation

$$\mathbf{A}(\mathbf{r},\omega) = \mu_0 \iiint\limits_V \mathrm{d}^3\mathbf{r}'\, \overset{\leftrightarrow}{\mathbf{G}}_A(\mathbf{r},\mathbf{r}',\omega) \cdot \mathbf{J}(\mathbf{r}',\omega)\ . \tag{3.49}$$

From equation (3.11) we can see that the transverse electric field can be written as equation (3.22) where the transverse Green's function is given by

$$\overset{\leftrightarrow}{\mathbf{G}}_\perp(\mathbf{r},\mathbf{r}',\omega) = \mathcal{V}k_\omega^2 \overset{\leftrightarrow}{\mathbf{G}}_A(\mathbf{r},\mathbf{r}',\omega)\,. \tag{3.50}$$

To find the eigenfunction expansion of the vector potential Green's function we introduce two sets of vector eigenfunctions, $\boldsymbol{\mathcal{E}}_\kappa^{\mathrm{TE}}(\mathbf{r})$ and $\boldsymbol{\mathcal{E}}_\kappa^{\mathrm{TM}}(\mathbf{r})$, which are transverse solutions to the vector Helmholtz equation

$$(\boldsymbol{\nabla}\times\boldsymbol{\nabla}\times-\kappa^2)\begin{cases}\boldsymbol{\mathcal{E}}_\kappa^{\mathrm{TE}}(\mathbf{r})\\ \boldsymbol{\mathcal{E}}_\kappa^{\mathrm{TM}}(\mathbf{r})\end{cases} = 0\,, \qquad \hat{\mathbf{z}}\times\begin{cases}\boldsymbol{\mathcal{E}}_\kappa^{\mathrm{TE}}(\mathbf{r})\\ \boldsymbol{\mathcal{E}}_\kappa^{\mathrm{TM}}(\mathbf{r})\end{cases}\Bigg|_{z=\pm\frac{L}{2}} = 0\,, \tag{3.51}$$

and are subject to the same boundary conditions as the Green's function. Note, we use the superscript labels TE and TM due to the nature of these eigenfunctions, which will turn out to be the usual transverse electric (TE) and transverse magnetic (TM) modes of a cavity waveguide. We can write these vector eigenfunctions in a manifestly transverse form

$$\boldsymbol{\mathcal{E}}_\kappa^{\mathrm{TE}}(\mathbf{r}) = \boldsymbol{\nabla}\times\left[f_\kappa^{\mathrm{TE}}(\mathbf{r})\hat{\mathbf{z}}\right]\,, \qquad \boldsymbol{\mathcal{E}}_\kappa^{\mathrm{TM}}(\mathbf{r}) = \frac{1}{\kappa}\boldsymbol{\nabla}\times\boldsymbol{\nabla}\times\left[f_\kappa^{\mathrm{TM}}(\mathbf{r})\hat{\mathbf{z}}\right]\,, \tag{3.52}$$

where f_κ^{TE} and f_κ^{TM} are the scalar generator functions that satisfy a simpler scalar Helmholtz equation

$$(\nabla^2+\kappa^2)\begin{cases}f_\kappa^{\mathrm{TE}}(\mathbf{r})\\ f_\kappa^{\mathrm{TM}}(\mathbf{r})\end{cases} = 0\,, \qquad \begin{matrix}f_\kappa^{\mathrm{TE}}(\mathbf{r})\\ \frac{\partial}{\partial z}f_\kappa^{\mathrm{TM}}(\mathbf{r})\end{matrix}\Bigg|_{z=\pm\frac{L}{2}} = 0\,. \tag{3.53}$$

Note, in order for the vector eigenfunctions to satisfy the correct boundary conditions, the scalar generator functions must satisfy different boundary conditions; $f_\kappa^{\mathrm{TE}}(\mathbf{r})$ and $f_\kappa^{\mathrm{TM}}(\mathbf{r})$

satisfy homogeneous Dirichlet and Neumann boundary conditions, respectively. After using the separation of variables method and imposing the boundary conditions one obtains the following scalar generating functions

$$f_\kappa^{\mathrm{TE}}(\mathbf{r}) = \sin(k_m\tilde{z})\mathrm{e}^{\mathrm{i}\mathbf{k}\cdot\boldsymbol{\rho}}\,, \qquad f_\kappa^{\mathrm{TM}}(\mathbf{r}) = \cos(k_m\tilde{z})\mathrm{e}^{\mathrm{i}\mathbf{k}\cdot\boldsymbol{\rho}}\,, \tag{3.54}$$

where the parameters are the same as in equation (3.30). However, we must include $m = 0$ for the TM eigenfunction as it corresponds to the fundamental transverse electromagnetic (TEM) mode of the cavity waveguide.

If we substitute equation (3.54) into equation (3.52) then we find the following explicit expressions for the transverse vector eigenfunctions (after multiplying by a constant)

$$\boldsymbol{\mathcal{E}}_\kappa^{\mathrm{TE}}(\mathbf{r}) = \mathrm{e}^{\mathrm{i}\mathbf{k}\cdot\boldsymbol{\rho}}\begin{bmatrix} k_y\sin(k_m\tilde{z}) \\ -k_x\sin(k_m\tilde{z}) \\ 0 \end{bmatrix}\,, \quad \boldsymbol{\mathcal{E}}_\kappa^{\mathrm{TM}}(\mathbf{r}) = \frac{1}{\kappa}\mathrm{e}^{\mathrm{i}\mathbf{k}\cdot\boldsymbol{\rho}}\begin{bmatrix} k_xk_m\sin(k_m\tilde{z}) \\ k_yk_m\sin(k_m\tilde{z}) \\ \mathrm{i}k^2\cos(k_m\tilde{z}) \end{bmatrix}\,, \tag{3.55}$$

whose TE and TM nature is now evident. The TE and TM eigenfunctions are manifestly orthogonal to one another

$$\iint\limits_{-\infty}^{\infty}\mathrm{d}^2\boldsymbol{\rho}\int\limits_{-L/2}^{L/2}\mathrm{d}z\,\boldsymbol{\mathcal{E}}_\kappa^{\mathrm{TE}}(\mathbf{r})\cdot\boldsymbol{\mathcal{E}}_{\kappa'}^{\mathrm{TM}*}(\mathbf{r}) = 0\,, \tag{3.56}$$

since $\boldsymbol{\mathcal{E}}_\kappa^{\mathrm{TE}}(\mathbf{r})\cdot\boldsymbol{\mathcal{E}}_{\kappa'}^{\mathrm{TM}*}(\mathbf{r}) = 0$. Moreover, the TE eigenfunctions satisfy the orthogonality relations

$$\iint\limits_{-\infty}^{\infty}\mathrm{d}^2\boldsymbol{\rho}\int\limits_{-L/2}^{L/2}\mathrm{d}z\,\boldsymbol{\mathcal{E}}_\kappa^{\mathrm{TE}}(\mathbf{r})\cdot\boldsymbol{\mathcal{E}}_{\kappa'}^{\mathrm{TE}*}(\mathbf{r}) = (2\pi)^2\frac{L}{2}k^2\delta(\mathbf{k}-\mathbf{k}')\delta_{mm'}\,, \tag{3.57}$$

while the TM eigenfunctions satisfy the orthogonality relations

$$\iint\limits_{-\infty}^{\infty}\mathrm{d}^2\boldsymbol{\rho}\int\limits_{-L/2}^{L/2}\mathrm{d}z\,\boldsymbol{\mathcal{E}}_\kappa^{\mathrm{TM}}(\mathbf{r})\cdot\boldsymbol{\mathcal{E}}_{\kappa'}^{\mathrm{TM}*}(\mathbf{r}) = (2\pi)^2\frac{L}{N_m}k^2\delta(\mathbf{k}-\mathbf{k}')\delta_{mm'}\,, \tag{3.58}$$

where $N_m = 2 - \delta_{m0}$. These eigenfunctions form a complete orthogonal basis for transverse vector fields that are subject to the same boundary conditions, which allows us to expand the transverse delta function as

$$\overset{\leftrightarrow}{\boldsymbol{\delta}}_{\perp}(\mathbf{r}-\mathbf{r}') = \sum_{m=0}^{\infty} \frac{N_m}{L} \iint\limits_{-\infty}^{\infty} \frac{\mathrm{d}^2\mathbf{k}}{(2\pi)^2} \left[\frac{1}{k^2} \boldsymbol{\mathcal{E}}_{\kappa}^{\mathrm{TE}}(\mathbf{r}) \boldsymbol{\mathcal{E}}_{\kappa}^{\mathrm{TE}*}(\mathbf{r}') + \frac{1}{k^2} \boldsymbol{\mathcal{E}}_{\kappa}^{\mathrm{TM}}(\mathbf{r}) \boldsymbol{\mathcal{E}}_{\kappa}^{\mathrm{TM}*}(\mathbf{r}') \right], \tag{3.59}$$

which is the corresponding completeness relation. In equation (3.59), the dyad formed by the TE vector eigenfunctions reads

$$\boldsymbol{\mathcal{E}}_{\kappa}^{\mathrm{TE}}(\mathbf{r}) \boldsymbol{\mathcal{E}}_{\kappa}^{\mathrm{TE}*}(\mathbf{r}') = \mathrm{e}^{\mathrm{i}\mathbf{k}\cdot(\boldsymbol{\rho}-\boldsymbol{\rho}')} \begin{bmatrix} k_y^2 SS' & -k_x k_y SS' & 0 \\ -k_x k_y SS' & k_x^2 SS' & 0 \\ 0 & 0 & 0 \end{bmatrix}, \tag{3.60}$$

while the dyad formed by the TM vector eigenfunctions is given by

$$\boldsymbol{\mathcal{E}}_{\kappa}^{\mathrm{TM}}(\mathbf{r}) \boldsymbol{\mathcal{E}}_{\kappa}^{\mathrm{TM}*}(\mathbf{r}') = \frac{1}{\kappa^2} \mathrm{e}^{\mathrm{i}\mathbf{k}\cdot(\boldsymbol{\rho}-\boldsymbol{\rho}')} \begin{bmatrix} k_x^2 k_m^2 SS' & k_x k_y k_m^2 SS' & -\mathrm{i}k_x k_m k^2 C'S \\ k_x k_y k_m^2 SS' & k_y^2 k_m^2 SS' & -\mathrm{i}k_y k_m k^2 C'S \\ \mathrm{i}k_x k_m k^2 CS' & \mathrm{i}k_y k_m k^2 CS' & k^4 CC' \end{bmatrix}. \tag{3.61}$$

For brevity we have introduced the shorthand notation $C = \cos(k_m \tilde{z})$, $S = \sin(k_m \tilde{z})$, $C' = \cos(k_m \tilde{z}')$, and $S' = \sin(k_m \tilde{z}')$.

Similarly, we can expand the vector potential Green's function in terms of the transverse eigenfunctions

$$\overset{\leftrightarrow}{\mathbf{G}}_A(\mathbf{r},\mathbf{r}',\omega) = \sum_{m=0}^{\infty} \frac{N_m}{L} \iint\limits_{-\infty}^{\infty} \frac{\mathrm{d}^2\mathbf{k}}{(2\pi)^2} \left[\frac{a_{\kappa}^{\mathrm{TE}}}{k^2} \boldsymbol{\mathcal{E}}_{\kappa}^{\mathrm{TE}}(\mathbf{r}) \boldsymbol{\mathcal{E}}_{\kappa}^{\mathrm{TE}*}(\mathbf{r}') + \frac{a_{\kappa}^{\mathrm{TM}}}{k^2} \boldsymbol{\mathcal{E}}_{\kappa}^{\mathrm{TM}}(\mathbf{r}) \boldsymbol{\mathcal{E}}_{\kappa}^{\mathrm{TM}*}(\mathbf{r}') \right], \tag{3.62}$$

where the unknown coefficients $a_{\kappa}^{\mathrm{TE/TM}}$ can be found by substituting equation (3.62) and equation (3.59) into equation (3.47), which yields

$$a_{\kappa}^{\mathrm{TE}} = a_{\kappa}^{\mathrm{TM}} = \frac{1}{\kappa^2 - k_{\omega}^2}. \tag{3.63}$$

Therefore, the eigenfunction expansion of the vector potential Green's function reads

$$\overset{\leftrightarrow}{\mathbf{G}}_A(\mathbf{r},\mathbf{r}',\omega) = \sum_{m=0}^{\infty} \frac{N_m}{L} \iint\limits_{-\infty}^{\infty} \frac{\mathrm{d}^2\mathbf{k}}{(2\pi)^2} \left[\frac{\boldsymbol{\mathcal{E}}_{\kappa}^{\mathrm{TE}}(\mathbf{r}) \boldsymbol{\mathcal{E}}_{\kappa}^{\mathrm{TE}*}(\mathbf{r}')}{k^2(\kappa^2 - k_{\omega}^2)} + \frac{\boldsymbol{\mathcal{E}}_{\kappa}^{\mathrm{TM}}(\mathbf{r}) \boldsymbol{\mathcal{E}}_{\kappa}^{\mathrm{TM}*}(\mathbf{r}')}{k^2(\kappa^2 - k_{\omega}^2)} \right], \tag{3.64}$$

which will be useful when we discuss periodic arrays of dipoles in the following sections.

Our final task is to evaluate the integrals in equation (3.64) to have a closed form expression for each term in the sum. If we combine the dyadics in equation (3.60) and equation (3.61) then we can re-express equation (3.64) as

$$\overleftrightarrow{\mathbf{G}}_A(\mathbf{r},\mathbf{r}',\omega) = \sum_{m=0}^{\infty} \frac{N_m}{L} \iint\limits_{-\infty}^{\infty} \frac{\mathrm{d}^2\mathbf{k}}{(2\pi)^2} \left(\overleftrightarrow{\mathbf{I}} + \frac{1}{\kappa^2}\boldsymbol{\nabla}\boldsymbol{\nabla}\right) \frac{\mathrm{e}^{\mathrm{i}\mathbf{k}\cdot(\boldsymbol{\rho}-\boldsymbol{\rho}')}}{\kappa^2 - k_\omega^2} \overleftrightarrow{\mathbf{C}}_m(z,z')\,, \tag{3.65}$$

where $\overleftrightarrow{\mathbf{I}}$ is the unit dyadic and we have introduced the diagonal dyadic

$$\overleftrightarrow{\mathbf{C}}_m(z,z') = \begin{bmatrix} SS' & 0 & 0 \\ 0 & SS' & 0 \\ 0 & 0 & CC' \end{bmatrix}. \tag{3.66}$$

It is convenient to split the Green's function into two parts

$$\overleftrightarrow{\mathbf{G}}_A(\mathbf{r},\mathbf{r}',\omega) = \overleftrightarrow{\mathbf{G}}_A^{(1)}(\mathbf{r},\mathbf{r}',\omega) + \overleftrightarrow{\mathbf{G}}_A^{(2)}(\mathbf{r},\mathbf{r}',\omega)\,, \tag{3.67}$$

where the first part reads

$$\overleftrightarrow{\mathbf{G}}_A^{(1)}(\mathbf{r},\mathbf{r}',\omega) = \sum_{m=0}^{\infty} \frac{N_m}{L} \left(\overleftrightarrow{\mathbf{I}} + \frac{1}{k_\omega^2}\boldsymbol{\nabla}\boldsymbol{\nabla}\right) \iint\limits_{-\infty}^{\infty} \frac{\mathrm{d}^2\mathbf{k}}{(2\pi)^2} \frac{\mathrm{e}^{\mathrm{i}\mathbf{k}\cdot(\boldsymbol{\rho}-\boldsymbol{\rho}')}}{k^2 + k_m^2 - k_\omega^2 - \mathrm{i}0^+} \overleftrightarrow{\mathbf{C}}_m(z,z')\,. \tag{3.68}$$

Here we have included an infinitesimal imaginary component in the denominator of the integrand in order to shift the pole off the real axis when $k_m < k_\omega$ – this prescription ensures that we have outward propagating waves from the source. We can perform this integral using the same method that we outlined in section 3.3.1, from which we obtain

$$\overleftrightarrow{\mathbf{G}}_A^{(1)}(\mathbf{r},\mathbf{r}',\omega) = \mathrm{i} \sum_{m=0}^{\infty} \frac{N_m}{4L} \left(\overleftrightarrow{\mathbf{I}} + \frac{1}{k_\omega^2}\boldsymbol{\nabla}\boldsymbol{\nabla}\right) H_0^{(1)}\left(\sqrt{k_\omega^2 - k_m^2}\,|\boldsymbol{\rho}-\boldsymbol{\rho}'|\right) \overleftrightarrow{\mathbf{C}}_m(z,z')\,. \tag{3.69}$$

The second part in equation (3.67) reads

$$\overleftrightarrow{\mathbf{G}}_A^{(2)}(\mathbf{r},\mathbf{r}',\omega) = -\frac{1}{k_\omega^2} \sum_{m=0}^{\infty} \frac{N_m}{L} \boldsymbol{\nabla}\boldsymbol{\nabla} \iint\limits_{-\infty}^{\infty} \frac{\mathrm{d}^2\mathbf{k}}{(2\pi)^2} \frac{\mathrm{e}^{\mathrm{i}\mathbf{k}\cdot(\boldsymbol{\rho}-\boldsymbol{\rho}')}}{k^2 + k_m^2} \overleftrightarrow{\mathbf{C}}_m(z,z')\,, \tag{3.70}$$

and after performing the integral using the method outlined in section 3.3.1 we obtain

$$\overleftrightarrow{\mathbf{G}}^{(2)}_{A}(\mathbf{r},\mathbf{r}',\omega) = -\frac{1}{k_\omega^2}\sum_{m=0}^{\infty}\frac{N_m}{\pi L}\boldsymbol{\nabla}\boldsymbol{\nabla}\, K_0(k_m|\boldsymbol{\rho}-\boldsymbol{\rho}'|)\overleftrightarrow{\mathbf{C}}_m(z,z')\,. \tag{3.71}$$

Finally, combining equation (3.69) and equation (3.71) and using equation (3.50) we obtain the transverse Green's function

$$\begin{aligned}\overleftrightarrow{\mathbf{G}}_{\perp}(\mathbf{r},\mathbf{r}',\omega) = \mathrm{i}\frac{\mathcal{V}}{4L}\sum_{m=0}^{\infty}N_m\left(k_\omega^2\overleftrightarrow{\mathbf{I}}+\boldsymbol{\nabla}\boldsymbol{\nabla}\right)H_0^{(1)}\left(\sqrt{k_\omega^2-k_m^2}\,|\boldsymbol{\rho}-\boldsymbol{\rho}'|\right)\overleftrightarrow{\mathbf{C}}_m(z,z')\\ -\frac{\mathcal{V}}{\pi L}\sum_{m=0}^{\infty}\boldsymbol{\nabla}\boldsymbol{\nabla}K_0\left(k_m|\boldsymbol{\rho}-\boldsymbol{\rho}'|\right)\overleftrightarrow{\mathbf{C}}_m(z,z')\,,\end{aligned} \tag{3.72}$$

which describes the transverse electric field generated by a point dipole source inside a cavity waveguide.

3.3.3 Total Green's function

The total Green's function for the cavity waveguide is equal to the sum of the longitudinal and transverse components given by equation (3.45) and equation (3.72), respectively. Moreover, it is simple to show that

$$\sum_{m=0}^{\infty}\boldsymbol{\nabla}\boldsymbol{\nabla}K_0\left(k_m|\boldsymbol{\rho}-\boldsymbol{\rho}'|\right)\overleftrightarrow{\mathbf{C}}_m(z,z') = -\sum_{m=1}^{\infty}\boldsymbol{\nabla}\boldsymbol{\nabla}'\sin(k_m\tilde{z})\sin(k_m\tilde{z}')K_0\left(k_m|\boldsymbol{\rho}-\boldsymbol{\rho}'|\right)\,, \tag{3.73}$$

since the $m = 0$ term vanishes and we can remove the need for $\overleftrightarrow{\mathbf{C}}_m(z,z')$ by switching one of the gradient operators to operate on the source coordinates rather than the field coordinates. Therefore, the instantaneous contribution from the longitudinal Green's function is completely cancelled by the non-retarded contribution in the transverse Green's function. This leads to a fully retarded and causal Green's function for the cavity waveguide which reads

$$\overleftrightarrow{\mathbf{G}}(\mathbf{r},\mathbf{r}',\omega) = \mathrm{i}\frac{\mathcal{V}}{4L}\sum_{m=0}^{\infty}N_m\left(k_\omega^2\overleftrightarrow{\mathbf{I}}+\boldsymbol{\nabla}\boldsymbol{\nabla}\right)H_0^{(1)}\left(\sqrt{k_\omega^2-k_m^2}\,|\boldsymbol{\rho}-\boldsymbol{\rho}'|\right)\overleftrightarrow{\mathbf{C}}_m(z,z')\,. \tag{3.74}$$

3.3.4 Image expansion of the Green's function

The representation of the cavity Green's function in equation (3.74) converges very slowly near the source when $|\boldsymbol{\rho}-\boldsymbol{\rho}'| \ll L$. Moreover, it does not permit an easy decomposition into the primary field emitted by a dipole and the secondary field scattered from the boundary,

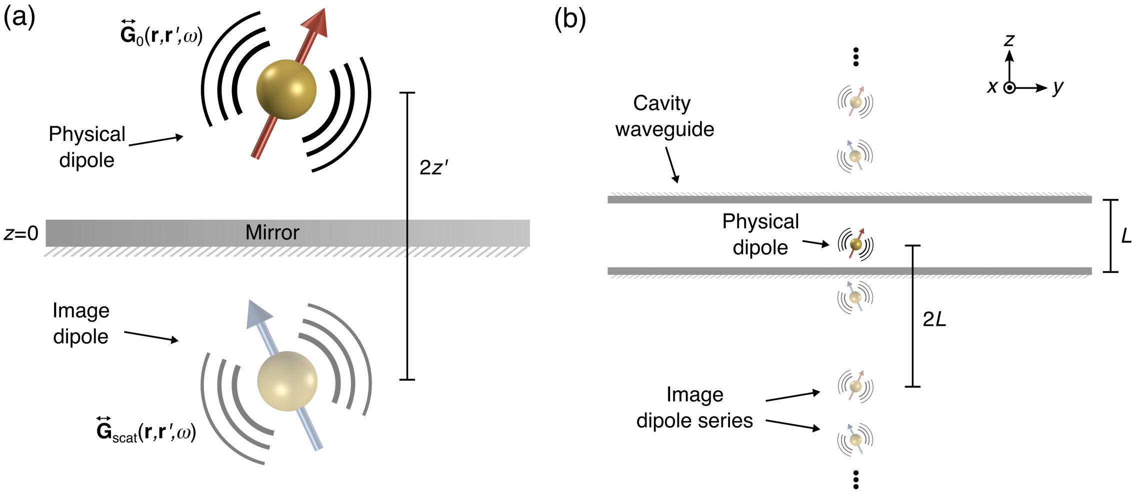

Figure 3.1 | Method of images. (a) To calculate the field generated by a point dipole source (red) located at a position z' above a perfect mirror at $z = 0$, one can effectively replace the mirror with an image dipole (blue) located outside the region of interest at position $-z'$. Note, the orientation of the image dipole is inverted in the xy-plane to ensure that the correct boundary conditions are satisfied. (b) To calculate the field generated by a point dipole source located inside a cavity waveguide of width L, one can effectively replace the two mirrors at $z = \pm L/2$ with two infinite series of image dipoles located outside the cavity at positions $\mathbf{r}' - \mathbf{R}_l$ (red) and $\mathbf{r}' + (L - 2z')\hat{\mathbf{z}} - \mathbf{R}_l$ (blue), where $\mathbf{R}_l = 2lL\hat{\mathbf{z}}$ and l is an integer. Therefore, both sets of image dipoles have a period of $2L$, and their different orientations are related by inversion in the xy-plane.

which will be important when we discuss how the cavity modifies the polarizability of the dipoles. Therefore, in this section we will derive an alternative representation of the cavity Green's function via the image expansion method [239].

Let us first consider the simpler case of a single perfect mirror placed at $z = 0$, where a dipole is located above the mirror at $\mathbf{r}' = \boldsymbol{\rho}' + z'\hat{\mathbf{z}}$ as schematically depicted in figure 3.1(a). We can decompose the Green's function as

$$\overleftrightarrow{\mathbf{G}}(\mathbf{r},\mathbf{r}',\omega) = \overleftrightarrow{\mathbf{G}}_0(\mathbf{r},\mathbf{r}',\omega) + \overleftrightarrow{\mathbf{G}}_{\text{scat}}(\mathbf{r},\mathbf{r}',\omega)\,, \tag{3.75}$$

where the primary field is described by the free space Green's function which has the familiar closed form representation [238]

$$\overleftrightarrow{\mathbf{G}}_0(\mathbf{r},\mathbf{r}',\omega) = \mathcal{V}\left(k_\omega^2\overleftrightarrow{\mathbf{I}} + \boldsymbol{\nabla}\boldsymbol{\nabla}\right)\frac{e^{ik_\omega|\mathbf{r}-\mathbf{r}'|}}{4\pi|\mathbf{r}-\mathbf{r}'|}\,, \tag{3.76}$$

and $\overleftrightarrow{\mathbf{G}}_{\text{scat}}(\mathbf{r},\mathbf{r}',\omega)$ describes the secondary field that is scattered from the boundary. Using the method of images [239], the boundary can be effectively replaced by an image dipole located outside the region of interest at position $\mathbf{r}' - 2z'\hat{\mathbf{z}}$ as depicted in figure 3.1(a). The

Green's function can then be written as the superposition of the two fields generated by the physical dipole and the image dipole which reads

$$\overleftrightarrow{\mathbf{G}}(\mathbf{r},\mathbf{r}',\omega) = \overleftrightarrow{\mathbf{G}}_0(\mathbf{r},\mathbf{r}',\omega) + \overleftrightarrow{\mathbf{G}}_0(\mathbf{r},\mathbf{r}'-2z'\hat{\mathbf{z}},\omega)\cdot\overleftrightarrow{\mathbf{I}}_{xy}\,. \tag{3.77}$$

In equation (3.77) we have introduced the dyadic

$$\overleftrightarrow{\mathbf{I}}_{xy} = \begin{bmatrix} -1 & 0 & 0 \\ 0 & -1 & 0 \\ 0 & 0 & 1 \end{bmatrix}, \tag{3.78}$$

which is crucial to ensure the following boundary conditions are satisfied

$$\hat{\mathbf{z}}\times\overleftrightarrow{\mathbf{G}}(\mathbf{r},\mathbf{r}',\omega)\Big|_{z=0} = 0\,. \tag{3.79}$$

This requirement means that the orientation of the image dipole is related to the physical dipole by inversion in the xy-plane as shown in figure 3.1(a).

Now let us consider the cavity waveguide which is formed by two perfect mirrors placed at $z=\pm L/2$ as schematically depicted in figure 3.1(b). To obtain $\overleftrightarrow{\mathbf{G}}_{\text{scat}}(\mathbf{r},\mathbf{r}',\omega)$, we can use the method of images in a stepwise fashion by disregarding each mirror in turn [239]. This procedure results in two infinite series of image dipoles located outside the cavity at positions $\mathbf{r}'-\mathbf{R}_l$ and $\mathbf{r}'+(L-2z')\hat{\mathbf{z}}-\mathbf{R}_l$, as shown in figure 3.1(b), where $\mathbf{R}_l = 2lL\hat{\mathbf{z}}$ and $l\in\mathbb{Z}$ is an integer. Importantly, in order to satisfy the boundary conditions

$$\hat{\mathbf{z}}\times\overleftrightarrow{\mathbf{G}}(\mathbf{r},\mathbf{r}',\omega)\Big|_{z=\pm L/2} = 0\,, \tag{3.80}$$

the orientation of the two sets of image dipoles are related by inversion in the xy-plane. Therefore, the image expansion of the cavity Green's function reads

$$\overleftrightarrow{\mathbf{G}}(\mathbf{r},\mathbf{r}',\omega) = \overleftrightarrow{\mathbf{G}}_{1\mathrm{D}}(\mathbf{r},\mathbf{r}',\omega) + \overleftrightarrow{\mathbf{G}}_{1\mathrm{D}}(\mathbf{r},\mathbf{r}'+(L-2z')\hat{\mathbf{z}},\omega)\cdot\overleftrightarrow{\mathbf{I}}_{xy}\,, \tag{3.81}$$

where $\overleftrightarrow{\mathbf{G}}_{1\mathrm{D}}(\mathbf{r},\mathbf{r}',\omega)$ is the Green's function for a 1D array of in-phase dipoles with a period of $2L$, which is given by

$$\overleftrightarrow{\mathbf{G}}_{1\mathrm{D}}(\mathbf{r},\mathbf{r}',\omega) = \frac{\mathcal{V}}{4\pi}\sum_{l=-\infty}^{\infty}\left(k_\omega^2\overleftrightarrow{\mathbf{I}} + \boldsymbol{\nabla}\boldsymbol{\nabla}\right)\frac{\mathrm{e}^{\mathrm{i}k_\omega|\mathbf{r}-\mathbf{r}'+\mathbf{R}_l|}}{|\mathbf{r}-\mathbf{r}'+\mathbf{R}_l|}\,. \tag{3.82}$$

In appendix B.1 we show that this image expansion representation of the cavity Green's function is equivalent to the representation in equation (3.74) which was derived using the eigenfunction expansion method.

3.4 Metasurfaces embedded inside a cavity waveguide

Throughout this thesis we will be exploring interesting phenomena that emerge in metasurfaces composed of 2D subwavelength arrays of dipoles. While metamaterials have traditionally been described by integrating out the matter degrees of freedom and encoding their response in terms of a homogenized effective permittivity and permeability, here we take a different approach. Instead, we choose to integrate out the photonic degrees of freedom and encode their response in terms of the cavity Green's function that we derived in the previous sections. In what follows we will develop a self-consistent coupled-dipole theory that describes the collective dynamics of the dipoles inside a cavity waveguide. For the sake of concreteness, we will present this theory using the simplest possible metasurface – a square Bravais lattice of dipoles.

3.4.1 Minimal model of a square metasurface

In figure 3.2(a) we schematically depict a square metasurface embedded inside a cavity waveguide. The metasurface is composed of a square Bravais lattice of dipoles located at periodic positions given by the set of lattice vectors $\mathbf{R} = l_1\mathbf{a}_1 + l_2\mathbf{a}_2$, where $l_1, l_2 \in \mathbb{Z}$ are integers, and

$$\mathbf{a}_1 = a\Big[1\,,\,0\Big]\,, \quad \mathbf{a}_2 = a\Big[0\,,\,1\Big]\,, \tag{3.83}$$

are the primitive lattice vectors. Each unit cell contains a single dipole as shown in figure 3.2(b). The corresponding reciprocal lattice vectors are $\mathbf{g} = n_1\mathbf{b}_1 + n_2\mathbf{b}_2$, where $n_1, n_2 \in \mathbb{Z}$ are integers, and

$$\mathbf{b}_1 = \frac{\pi}{a}\Big[1\,,\,0\Big]\,, \quad \mathbf{b}_2 = \frac{\pi}{a}\Big[0\,,\,1\Big]\,, \tag{3.84}$$

are the primitive reciprocal lattice vectors that define the Brillouin zone shown in figure 3.2(c). Furthermore, we assume a subwavelength nearest-neighbour separation $a \ll \lambda_0$, where λ_0 is the free space resonant wavelength of the dipoles. This ensures that the collective dynamics of the interacting dipoles result in subradiant polaritons that are evanescently bound to the

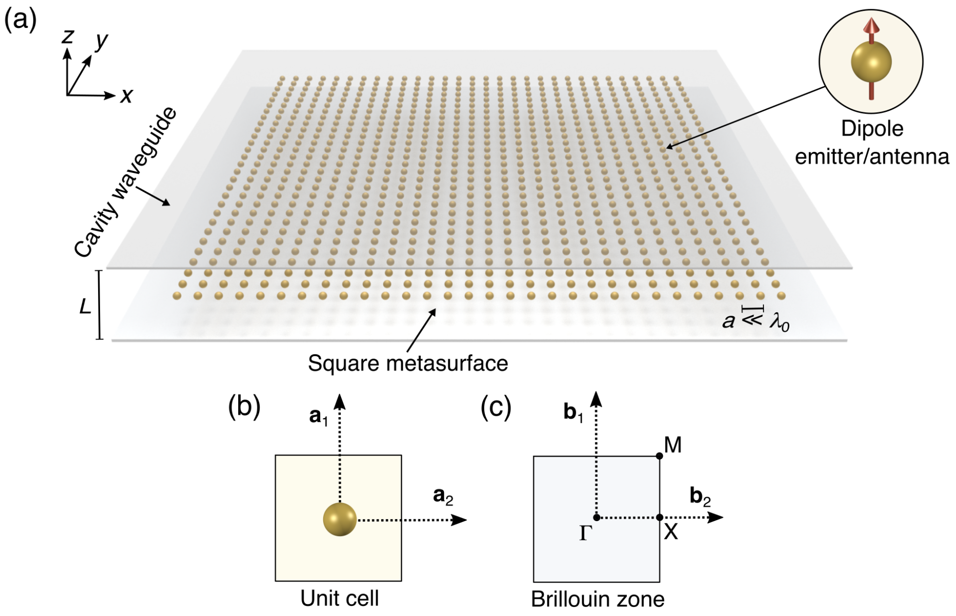

Figure 3.2 | Square metasurface inside a cavity waveguide. (a) Schematic of a simple metasurface composed of a square Bravais lattice of dipole emitters/antennas with subwavelength nearest-neighbour separation $a \ll \lambda_0$. The induced dipole moments are assumed to point in the z-direction (see inset). Furthermore, the square metasurface is embedded inside a cavity waveguide of width L, where the cavity walls are assumed to be perfect mirrors. (b) Corresponding unit cell which contains a single dipole, and $\mathbf{a}_1$ and $\mathbf{a}_2$ are the primitive lattice vectors. (c) Corresponding first Brillouin zone where the high-symmetry points are labeled, and $\mathbf{b}_1$ and $\mathbf{b}_2$ are the primitive reciprocal lattice vectors.

lattice. Finally, we embed the metasurface at the centre of a cavity waveguide of width L, where the cavity walls are assumed to be perfect mirrors.

Furthermore, throughout this thesis we restrict our attention to transverse polariton excitations. Consequently, we assume that each dipole is characterized by an anisotropic free space polarizability tensor $\overset{\leftrightarrow}{\boldsymbol{\alpha}}_0(\omega) = \alpha_0(\omega)\hat{\mathbf{z}}\hat{\mathbf{z}}$ such that the induced dipole moment $\mathbf{p}_{\mathbf{R}}(\omega)$ on the emitter located at $\mathbf{R}$ is oriented in the z-direction

$$\mathbf{p}_{\mathbf{R}}(\omega) = \epsilon_0 \mathcal{V} \overset{\leftrightarrow}{\boldsymbol{\alpha}}_0(\omega) \cdot \mathbf{E}_0(\mathbf{R}, \omega) = \epsilon_0 \mathcal{V} \alpha_0(\omega) E_0(\mathbf{R}, \omega) \hat{\mathbf{z}} \,, \tag{3.85}$$

where $E_0(\mathbf{r}, \omega)$ is the z-component of the external field $\mathbf{E}_0(\mathbf{r}, \omega)$. Note, in what follows we set the characteristic volume to be related to the nearest-neighbour separation distance $\mathcal{V} = 4\pi a^3$. Furthermore, we assume a generic free space polarizability of the form

$$\alpha_0(\omega) = \left[\alpha_{\mathrm{B}}^{-1}(\omega) - \Sigma_0(\omega)\right]^{-1} \,, \tag{3.86}$$

where the bare polarizability reads

$$\alpha_{\mathrm{B}}(\omega) = \frac{2\omega_0\mu}{\omega_0^2 - \omega^2 - \mathrm{i}\omega\gamma_{\mathrm{nr}}} . \tag{3.87}$$

Here, ω_0 is the free space resonant frequency of the dipole, μ characterizes the strength of the polarizability, and γ_{nr} is a phenomenological damping constant that accounts for any non-radiative losses in the emitter. Moreover, in equation (3.86) the free space polarizability correction accounts for the interaction with its own scattered field and reads

$$\varSigma_0(\omega) = \mathrm{i}\,\mathrm{Im}[G_0(\mathbf{R},\mathbf{R},\omega)] = \mathrm{i}\frac{\mathcal{V}k_\omega^3}{6\pi} , \tag{3.88}$$

where $G_0(\mathbf{r},\mathbf{r}',\omega) = \hat{\mathbf{z}}\cdot\overset{\leftrightarrow}{\mathbf{G}}_0(\mathbf{r},\mathbf{r}',\omega)\cdot\hat{\mathbf{z}}$ represents the zz-component of the free space dyadic Green's function.

Equation (3.88) is the usual radiation reaction term that accounts for radiative losses in free space [243]. Note, we neglect the divergent real part of the Green's function and assume any corrections to the resonant frequency in free space (such as the free space Lamb shift) are already encoded into the definition of ω_0. Furthermore, we have kept the model general since the polarizability could apply to both classical antennas and quantum emitters in their linear regime.

3.4.2 Renormalized polarizability inside the cavity waveguide

It is well known that the radiative properties of an emitter/antenna depend sensitively on the local electromagnetic environment which can produce modifications to both the resonant frequency and radiative losses. We have seen in equation (3.75) that the cavity Green's function can be decomposed into the primary field and the secondary field that is scattered by the cavity. Since we have already included the back action of the primary scattered field in the definition of the free space polarizability, we can write the induced dipole moment inside the cavity as

$$\mathbf{p}_{\mathbf{R}}(\omega) = \epsilon_0\mathcal{V}\overset{\leftrightarrow}{\boldsymbol{\alpha}}_0(\omega)\cdot\left[\mathbf{E}_0(\mathbf{R},\omega) + \mathbf{E}_{\mathrm{self}}(\mathbf{R},\omega)\right] . \tag{3.89}$$

This shows that the dipole is driven by the external field and its own self-generated field that is scattered back by the cavity

$$\mathbf{E}_{\mathrm{self}}(\mathbf{R},\omega) = \frac{1}{\epsilon_0\mathcal{V}}\overset{\leftrightarrow}{\mathbf{G}}_{\mathrm{scat}}(\mathbf{R},\mathbf{R},\omega)\cdot\mathbf{p}_{\mathbf{R}}(\omega) . \tag{3.90}$$

We can express the induced dipole moment in terms of only the external driving field

$$\mathbf{p}_{\mathbf{R}}(\omega) = \epsilon_0 \mathcal{V} \overset{\leftrightarrow}{\boldsymbol{\alpha}}(\omega) \cdot \mathbf{E}_0(\mathbf{R}, \omega) \tag{3.91}$$

if we introduce a renormalized polarizability $\overset{\leftrightarrow}{\boldsymbol{\alpha}}(\omega) = \alpha(\omega)\hat{\mathbf{z}}\hat{\mathbf{z}}$, where

$$\alpha(\omega) = \left[\alpha_{\mathrm{B}}^{-1}(\omega) - \Sigma(\omega)\right]^{-1} . \tag{3.92}$$

Here the polarizability correction that encodes the renormalization due to the back action of its own scattered field inside the cavity reads

$$\Sigma(\omega) = \mathrm{i}\,\mathrm{Im}[G_0(\mathbf{R}, \mathbf{R}, \omega)] + G_{\mathrm{scat}}(\mathbf{R}, \mathbf{R}, \omega)\,, \tag{3.93}$$

where $G_{\mathrm{scat}}(\mathbf{r}, \mathbf{r}', \omega) = \hat{\mathbf{z}} \cdot \overset{\leftrightarrow}{\mathbf{G}}_{\mathrm{scat}}(\mathbf{r}, \mathbf{r}', \omega) \cdot \hat{\mathbf{z}}$ is the zz-component of the dyadic. The secondary field can be found by simply subtracting the free space Green's function from the image expansion of the cavity Green's function which yields

$$G_{\mathrm{scat}}(\mathbf{R}, \mathbf{R}, \omega) = 2\sum_{l=1}^{\infty} G_0(\mathbf{R}, \mathbf{R} + lL\hat{\mathbf{z}}, \omega) = \frac{\mathcal{V}}{\pi L^3} \sum_{l=1}^{\infty} \frac{\mathrm{e}^{\mathrm{i}k_\omega lL}}{l^3}(1 - \mathrm{i}k_\omega lL)\,. \tag{3.94}$$

Putting these results together we obtain the explicit expression

$$\Sigma(\omega) = \mathrm{i}\frac{\mathcal{V}k_\omega^3}{6\pi} + \frac{\mathcal{V}}{\pi L^3}\left[\mathrm{Li}_3\left(\mathrm{e}^{\mathrm{i}k_\omega L}\right) - \mathrm{i}k_\omega L\,\mathrm{Li}_2\left(\mathrm{e}^{\mathrm{i}k_\omega L}\right)\right] , \tag{3.95}$$

where $\mathrm{Li}_n(z) = \sum_{l=1}^{\infty} z^l/l^n$ is the polylogarithm of order n.

In figure 3.3 we plot the spectral function $\mathrm{Im}[\alpha(\omega)]$ of an individual dipole for different cavity widths. Since the polarizability correction is a slowly-varying function of frequency on the scale of the peak width, the spectral function lineshapes are Lorentzian to a very good approximation. Therefore, the renormalized polarizability can be well approximated as

$$\alpha(\omega) \approx \frac{2\omega_0\mu}{\omega_{\mathrm{cav}}^2 - \omega^2 - \mathrm{i}\omega\gamma} , \tag{3.96}$$

which describes a resonant dipole emitter/antenna with a renormalized resonant frequency ω_{cav} and a renormalized damping constant $\gamma = \gamma_{\mathrm{nr}} + \gamma_{\mathrm{rad}}$, where γ_{rad} describes the radiative losses. The renormalized resonant frequency can be found by numerically solving

$$\omega^2 - \omega_0^2 - 2\omega_0\mu\,\mathrm{Re}[\Sigma(\omega)] = 0\,, \tag{3.97}$$

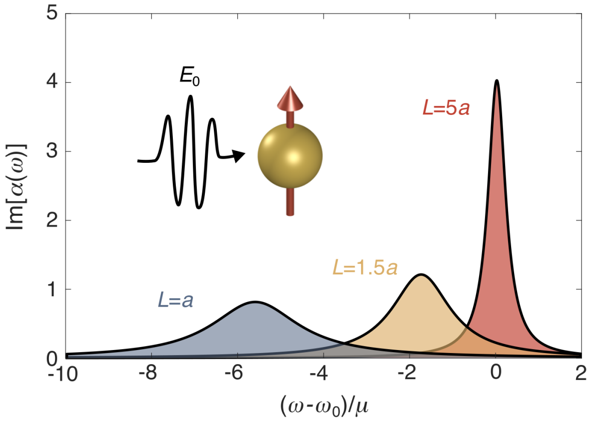

Figure 3.3 | Renormalized polarizability inside a cavity waveguide. Spectral function of an individual resonant dipole inside a cavity waveguide of width $L = 5a$ (red), $L = 1.5a$ (orange), and $L = a$ (blue). Note, to highlight the effect of radiative losses we have set the non-radiative losses to zero ($\gamma_{\text{nr}} = 0$) so that the width of the resonant peaks is solely due to radiative broadening. Results obtained with $\lambda_0 = 10a$ and $\mu = 0.001\omega_0$.

where the real part of the scattered Green's function gives rise to a cavity-induced Lamb shift. The radiative losses can then by approximated as

$$\gamma_{\text{rad}} = \frac{2\omega_0\mu}{\omega_{\text{cav}}} \operatorname{Im} \Sigma(\omega_{\text{cav}}) \,, \tag{3.98}$$

which is determined by the imaginary part of the scattered Green's function.

For cavity widths $L < \lambda_0$, we can observe from figure 3.3 that the resonant frequency decreases as the cavity width is reduced; this is predominantly due to the strong Coulomb interactions with its image dipoles. Furthermore, the radiative losses increase as the cavity width is reduced resulting in the resonant peaks becoming broader; this is primarily due to the reducing mode volume of the TEM eigenmodes which increases the projected local density of states.

3.4.3 Coupled-dipole equations inside a cavity waveguide

To characterize the collective dynamics of the dipoles within the metasurface, we note that the induced dipole located at $\mathbf{R}$ is not only driven by the external field but also by the field that is scattered by all the other dipoles in the metasurface located at $\mathbf{R}' \neq \mathbf{R}$. Therefore we can write the induced dipole moment as

$$\mathbf{p}_{\mathbf{R}}(\omega) = \epsilon_0 \mathcal{V} \overset{\leftrightarrow}{\boldsymbol{\alpha}}(\omega) \cdot \left[\mathbf{E}_0(\mathbf{R},\omega) + \mathbf{E}_{\text{scat}}(\mathbf{R},\omega)\right] , \tag{3.99}$$

where the scattered field can be expressed in terms of the cavity Green's function as

$$\mathbf{E}_{\text{scat}}(\mathbf{R},\omega) = \frac{1}{\epsilon_0 \mathcal{V}} \sum_{\mathbf{R}'\neq\mathbf{R}} \overset{\leftrightarrow}{\mathbf{G}}(\mathbf{R},\mathbf{R}',\omega)\cdot \mathbf{p}_{\mathbf{R}'}(\omega)\,. \tag{3.100}$$

If we insert equation (3.100) into equation (3.99) we obtain a set of self-consistent coupled-dipole equations

$$\frac{1}{\alpha(\omega)} p_{\mathbf{R}}(\omega) = \epsilon_0 \mathcal{V} E_0(\mathbf{R},\omega) + \sum_{\mathbf{R}'\neq\mathbf{R}} G(\mathbf{R}-\mathbf{R}',\omega) p_{\mathbf{R}'}(\omega)\,, \tag{3.101}$$

where $G(\boldsymbol{\rho}-\boldsymbol{\rho}',\omega) = \hat{\mathbf{z}}\cdot\overset{\leftrightarrow}{\mathbf{G}}(\boldsymbol{\rho},\boldsymbol{\rho}',\omega)\cdot\hat{\mathbf{z}}$ is the zz-component of the cavity Green's function where both the source and field are evaluated at the centre of the cavity ($z = z' = 0$).

From equation (3.74) we can extract the explicit expression for the zz-component which reads

$$G(\boldsymbol{\rho}-\boldsymbol{\rho}',\omega) = \mathrm{i}\frac{\mathcal{V}}{4L}\sum_{m=0}^{\infty} N_m \left(k_\omega^2 - q_m^2\right) H_0^{(1)}\left(\sqrt{k_\omega^2 - q_m^2}\,|\boldsymbol{\rho}-\boldsymbol{\rho}'|\right)\,. \tag{3.102}$$

Here we have introduced the quantized wavevector $q_m = k_{2m} = 2m\pi/L$ since the terms with odd values of m vanish at the centre of the cavity waveguide where the dipoles are located. For reference later, we can also extract the zz-component of the longitudinal Green's function in equation (3.45) which reads

$$G_{\parallel}(\boldsymbol{\rho}-\boldsymbol{\rho}') = -\frac{\mathcal{V}}{\pi L}\sum_{m=1}^{\infty} q_m^2 K_0\left(q_m|\boldsymbol{\rho}-\boldsymbol{\rho}'|\right)\,. \tag{3.103}$$

Furthermore, the zz-component of the transverse Green's function can be extracted from equation (3.72) and reads

$$\begin{aligned} G_{\perp}(\boldsymbol{\rho}-\boldsymbol{\rho}',\omega) =& \mathrm{i}\frac{\mathcal{V}}{4L}\sum_{m=0}^{\infty} N_m \left(k_\omega^2 - q_m^2\right) H_0^{(1)}\left(\sqrt{k_\omega^2 - q_m^2}\,|\boldsymbol{\rho}-\boldsymbol{\rho}'|\right) \\ &+\frac{\mathcal{V}}{\pi L}\sum_{m=1}^{\infty} q_m^2 K_0\left(q_m|\boldsymbol{\rho}-\boldsymbol{\rho}'|\right)\,. \end{aligned} \tag{3.104}$$

However, it will prove useful to have the eigenfunction expansion of the zz-component which can be obtained from equation (3.50) and equation (3.64) and reads

$$G_{\perp}(\boldsymbol{\rho}-\boldsymbol{\rho}',\omega) = \frac{\mathcal{V}}{L}\sum_{m=0}^{\infty} N_m \iint_{-\infty}^{\infty} \frac{\mathrm{d}^2\mathbf{k}}{(2\pi)^2}\frac{k_\omega^2 k^2}{(k^2+q_m^2)(k^2+q_m^2-k_\omega^2)} \mathrm{e}^{\mathrm{i}\mathbf{k}\cdot(\boldsymbol{\rho}-\boldsymbol{\rho}')}\,. \tag{3.105}$$

It is evident that the dipoles can only couple to the TM cavity modes since the TE cavity modes have no field component in the z-direction. Furthermore, only the even TM modes contribute since the odd TM modes have nodes at the centre of the cavity waveguide.

3.4.4 Coulomb vs photon-mediated interactions

Before we analyze the coupled-dipole equations for the square metasurface, it is useful to explore how the nature of the interactions between the dipoles evolve as one modifies the cavity width. The decomposition of the Green's function into its longitudinal and transverse components allows us to treat the static and dynamic aspects of the system separately. The longitudinal Green's function describes the instantaneous Coulomb field generated by a dipole, and therefore encodes the quasistatic Coulomb interactions between the dipoles in the metasurface. Moreover, the transverse Green's function describes the retarded interactions between the dipoles that are mediated by the transverse cavity photons. Throughout this thesis we will restrict our attention to the regime of cavity widths $L < \lambda_0$, where the cavity begins to significantly alter the nature of the interactions between neighbouring dipoles.

In free space, the Coulomb interactions are short-range and decay like $1/|\boldsymbol{\rho} - \boldsymbol{\rho}'|^3$. However, inside the cavity waveguide we can observe from equation (3.103) that the Coulomb interactions decay as

$$G_{\parallel}(\boldsymbol{\rho} - \boldsymbol{\rho}') \sim \frac{\mathrm{e}^{-2\pi|\boldsymbol{\rho}-\boldsymbol{\rho}'|/L}}{L^3\sqrt{|\boldsymbol{\rho} - \boldsymbol{\rho}'|}}\,, \tag{3.106}$$

which decrease more rapidly with the separation distance as shown in figure 3.4(a). As the cavity width is reduced the Coulomb interactions become suppressed due to the screening effect of the cavity waveguide.

In free space, the photon-mediated interactions are long-range and decay like $1/|\boldsymbol{\rho} - \boldsymbol{\rho}'|$. For the regime of cavity widths $L < \lambda_0$, only the fundamental TEM mode contributes to the long-range interactions because the quantized cavity modes that can couple to the dipoles are off-resonant. Consequently, the photon-mediated interactions inside the cavity waveguide decay as

$$G_{\perp}(\boldsymbol{\rho} - \boldsymbol{\rho}', \omega_0) \sim \frac{\mathrm{e}^{\mathrm{i}2\pi|\boldsymbol{\rho}-\boldsymbol{\rho}'|/\lambda_0}}{L\sqrt{|\boldsymbol{\rho} - \boldsymbol{\rho}'|}}\,, \tag{3.107}$$

where the real part describes coherent interactions whose strength oscillates with the separation distance as shown in figure 3.4(b). Furthermore, in stark contrast to the Coulomb interactions, the strength of the photon-mediated interactions increases as the cavity width

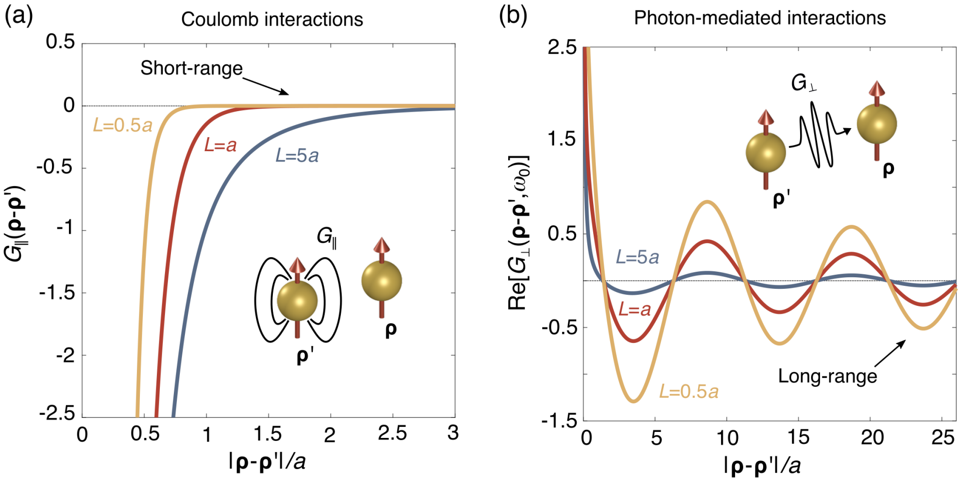

Figure 3.4 | Coulomb vs photon-mediated interactions inside a cavity waveguide. (a) Longitudinal Green's function for cavity widths of $L = 5a$ (blue line), $L = a$ (red line) and $L = 0.5a$ (orange line). This shows that the Coulomb interactions are short-range and are suppressed as the cavity width is reduced – this is due to the screening effect of the cavity waveguide. (b) Real part of the transverse Green's function for cavity widths of $L = 5a$ (blue line), $L = a$ (red line) and $L = 0.5a$ (orange line). This shows that the coherent photon-mediated interactions are long-range and oscillate with separation distance, and thus the metasurface is not amenable to a simple tight-binding description. In contrast to the Coulomb interactions, the strength of the photon-mediated interactions increase as the cavity width is reduced – this is because the light-matter interaction strength increases as the mode volume is decreased. Therefore, by varying the cavity width one can modify the strength and nature of the dipole-dipole interactions. Results obtained with $\lambda_0 = 10a$.

is reduced. This is because the TEM mode has no cut-off frequency, and the mode volume decreases with the cavity width which increases the light-matter interaction strength.

This non-trivial, long-range nature of the dipole-dipole interactions means that the metasurface cannot be described by a simple tight-binding model. In fact, we must include all the photon-mediated interactions between all pairs of dipoles to accurately describe the emergent physics. Furthermore, the ability to tune the nature of the dipole-dipole interactions by varying the cavity width lies at the heart of many of the interesting phenomena that we will present in the subsequent chapters.

3.4.5 Coupled-dipole equations in momentum space

In the absence of an external driving field the coupled-dipole equations read

$$\frac{1}{\alpha(\omega)}p_{\mathbf{R}}(\omega) = \sum_{\mathbf{R}'\neq\mathbf{R}} G(\mathbf{R}-\mathbf{R}',\omega)p_{\mathbf{R}'}(\omega)\,. \tag{3.108}$$

To find the dispersion of the cavity polaritons we can exploit the discrete translational symmetry of the metasurface by introducing the Fourier transform of the dipole moments

$$\widetilde{p}(\mathbf{q},\omega) = \frac{\sqrt{\mathcal{A}}}{2\pi}\sum_{\mathbf{R}} p_{\mathbf{R}}(\omega)\mathrm{e}^{-\mathrm{i}\mathbf{q}\cdot\mathbf{R}}\,, \tag{3.109}$$

where $\mathbf{q} = [\,q_x\,,\,q_y\,]$ is the Bloch wavevector that is restricted to the first Brillouin zone shown in figure 3.2(c), and $\mathcal{A} = a^2$ is the area of the unit cell shown in figure 3.2(b). Using the Fourier variables in equation (3.109), we can diagonalize the coupled-dipole equations in momentum space

$$\frac{1}{\alpha(\omega)}\widetilde{p}(\mathbf{q},\omega) = \left[\sum_{\mathbf{R}\neq 0} G_{\|}(\mathbf{R})\mathrm{e}^{-\mathrm{i}\mathbf{q}\cdot\mathbf{R}} + \sum_{\mathbf{R}\neq 0} G_{\perp}(\mathbf{R})\mathrm{e}^{-\mathrm{i}\mathbf{q}\cdot\mathbf{R}}\right]\widetilde{p}(\mathbf{q},\omega)\,. \tag{3.110}$$

Since the Coulomb interactions are short-range the first lattice sum converges rapidly. In stark contrast, the photon-mediated interactions are long-range and therefore we must accelerate the computation of the second sum. We can achieve this using the Poisson summation technique, where one transforms the real space lattice sum into a rapidly converging sum over reciprocal lattice vectors.

To facilitate this transformation, we add and subtract the self-interaction term $G_{\perp}(0,\omega)$ so that the second sum can be written as a sum over all lattice vectors including $\mathbf{R} = 0$. Note that the imaginary part of this self-interaction term cancels the imaginary part of the inverse polarizability since $\mathrm{Im}[G(0,\omega)] = \mathrm{Im}[G_{\perp}(0,\omega)]$. Therefore we can introduce a modified polarizability

$$\breve{\alpha}(\omega) = \left\{\alpha_{\mathrm{B}}^{-1}(\omega) - \mathrm{Re}[\Sigma(\omega)]\right\}^{-1}\,, \tag{3.111}$$

and write equation (3.110) as

$$\frac{1}{\breve{\alpha}(\omega)}\widetilde{p}(\mathbf{q},\omega) = \left[\mathcal{D}_{\|}(\mathbf{q}) + \mathcal{D}_{\perp}(\mathbf{q},\omega)\right]\widetilde{p}(\mathbf{q},\omega)\,. \tag{3.112}$$

Here, $\mathcal{D}_{\|}(\mathbf{q})$ is the longitudinal dynamical matrix that encodes the frequency shifts induced by the Coulomb interactions and reads

$$\mathcal{D}_{\|}(\mathbf{q}) = \sum_{\mathbf{R}\neq 0} G_{\|}(\mathbf{R})\mathrm{e}^{-\mathrm{i}\mathbf{q}\cdot\mathbf{R}}\,. \tag{3.113}$$

Furthermore, $\mathcal{D}_\perp(\mathbf{q},\omega)$ is the transverse dynamical matrix that encodes the frequency shifts due to the photon-mediated interactions and reads

$$\mathcal{D}_\perp(\mathbf{q},\omega) = \sum_{\mathbf{R}} G_\perp(\mathbf{R},\omega)\mathrm{e}^{-\mathrm{i}\mathbf{q}\cdot\mathbf{R}} - \mathrm{Re}[G_\perp(0,\omega)]\,. \tag{3.114}$$

We are now in a position to accelerate the lattice sum in equation (3.114). We can use the eigenfunction expansion of the transverse Green's function in equation (3.105) to express the lattice sum as

$$\sum_{\mathbf{R}} G_\perp(\mathbf{R},\omega)\mathrm{e}^{-\mathrm{i}\mathbf{q}\cdot\mathbf{R}} = \frac{\mathcal{V}}{L}\sum_{\mathbf{R}}\sum_{m=0}^{\infty} N_m \iint\limits_{-\infty}^{\infty} \frac{\mathrm{d}^2\mathbf{k}}{(2\pi)^2}\frac{k_\omega^2 k^2}{(k^2+q_m^2)(k^2+q_m^2-k_\omega^2)}\mathrm{e}^{\mathrm{i}(\mathbf{k}-\mathbf{q})\cdot\mathbf{R}}\,. \tag{3.115}$$

Finally, we can invoke the 2D version of Poisson's summation identity

$$\sum_{\mathbf{R}} \mathrm{e}^{\mathrm{i}(\mathbf{k}-\mathbf{q})\cdot\mathbf{R}} = \frac{(2\pi)^2}{\mathcal{A}}\sum_{\mathbf{g}}\delta(\mathbf{k}-\mathbf{q}+\mathbf{g})\,, \tag{3.116}$$

to transform equation (3.115) into

$$\mathcal{D}_\perp(\mathbf{q},\omega) = \sum_{m=0}^{\infty}\sum_{\mathbf{g}} \frac{\xi_m^2\omega^2\omega_{\mathbf{q}-\mathbf{g},0}^2}{\omega_{\mathbf{q}-\mathbf{g},m}^2(\omega_{\mathbf{q}-\mathbf{g},m}^2-\omega^2)} - \mathrm{Re}[G_\perp(0,\omega)]\,. \tag{3.117}$$

This transformation permits a simple reinterpretation of the light-matter interactions which is more in line with Hopfield's original treatment of polaritons [244]. Hopfield used a minimal-coupling Hamiltonian formalism to describe exciton-polaritons that arise from the strong-coupling between a single exciton band of a 3D crystal and free space photons [244]. From equation (3.117) we can see that the transverse dynamical matrix describes the frequency shifts that result from the hybridization between the quasistatic dipolar excitations with Bloch wavevector $\mathbf{q}$ and the cavity photons with dispersion

$$\omega_{\mathbf{q}-\mathbf{g},m} = c\sqrt{|\mathbf{q}-\mathbf{g}|^2+q_m^2}\,, \tag{3.118}$$

where the strength of the light-matter coupling is parameterized by

$$\xi_m = \sqrt{\frac{N_m\mathcal{V}}{\mathcal{A}L}}\,. \tag{3.119}$$

Since the metasurface only has discrete translational symmetry in the xy-plane, the interactions between the photons and the dipolar excitations only conserve the in-plane momentum modulo a reciprocal lattice vector. Furthermore, due to the broken translational invariance in the z-direction, the out-of-plane wavevector is not conserved. In the absence of a cavity waveguide, this would give rise to two distinct types of polaritons; evanescently bound polaritons which exist outside the light-cone and are decoupled from the free space photons, and also radiative polaritons which exist inside the light-cone and can decay into free space photons. However, the cavity waveguide breaks the continuum of photons into a discrete set with quantized wavevectors in the z-direction and, as a result, there is no density of final states that the dipolar excitations can decay into. Furthermore, we assume that the metasurface is infinite and therefore the dipolar excitations cannot radiate from the edge of the lattice. Consequently, both the longitudinal and transverse dynamical matrices will be Hermitian throughout this thesis.

3.4.6 Regularization of the divergent terms

Before we analyze the polariton spectrum, we need to address an issue in the transverse dynamical matrix. While equation (3.117) is well defined and finite, the two terms separately diverge rendering it impossible to evaluate. A method to deal with similar divergence issues has been proposed for 3D [245] and 2D [219] lattices in free space, which involves regularizing the large momentum behaviour of the free space Green's function. Therefore, in this section we introduce a similar regularization procedure for the cavity waveguide.

To this end, we introduce a regularized transverse Green's function which reads

$$\check{G}_\perp(\boldsymbol{\rho} - \boldsymbol{\rho}', \omega) = \frac{\mathcal{V}}{L} \sum_{m=0}^{\infty} N_m \iint\limits_{-\infty}^{\infty} \frac{\mathrm{d}^2\mathbf{k}}{(2\pi)^2} \frac{k_\omega^2 k^2 \mathrm{e}^{-\eta^2(k^2+q_m^2)}}{(k^2 + q_m^2)(k^2 + q_m^2 - k_\omega^2 - \mathrm{i}0^+)} \mathrm{e}^{\mathrm{i}\mathbf{k}\cdot(\boldsymbol{\rho}-\boldsymbol{\rho}')} \,, \tag{3.120}$$

where we have included a Gaussian cut-off for large wavevectors. Note that we only introduce this regularization procedure to be able to numerically calculate the transverse dynamical matrix elements, not to study finite-size effects of the emitters/antennas. Therefore, we choose the cut-off parameter to be $\eta \ll a$ such that it has a negligible effect on the interactions between dipoles. However, the Gaussian cut-off effectively smears out the divergent part of the transverse Green's function over a small volume, rendering it finite and well defined at the source location. To evaluate equation (3.117) we only need the real part of the regularized transverse Green's function at the source location which we will write as

$$\mathrm{Re}[\check{G}_\perp(0, \omega)] = \sum_{m=0}^{\infty} \mathcal{G}_m(\omega) \,, \tag{3.121}$$

where each term in the sum reads

$$\mathcal{G}_m(\omega) = \mathrm{Re}\left[\frac{N_m\mathcal{V}}{L}\iint\limits_{-\infty}^{\infty}\frac{\mathrm{d}^2\mathbf{k}}{(2\pi)^2}\frac{k_\omega^2 k^2 \mathrm{e}^{-\eta^2(k^2+q_m^2)}}{(k^2+q_m^2)(k^2+q_m^2-k_\omega^2-\mathrm{i}0^+)}\right]. \tag{3.122}$$

To evaluate the integral in equation (3.122), we will split it into two parts as $\mathcal{G}_m(\omega) = \mathcal{G}_m^{(1)}(\omega) + \mathcal{G}_m^{(2)}(\omega)$. The first part reads

$$\mathcal{G}_m^{(1)}(\omega) = -\frac{N_m\mathcal{V}}{2\pi L}\int\limits_0^{\infty}\mathrm{d}k\,\frac{k^3}{k^2+q_m^2}\mathrm{e}^{-\eta^2(k^2+q_m^2)}\,, \tag{3.123}$$

where we have used polar coordinates and performed the trivial angular integral. If we make the substitution $s = \eta^2(k^2+q_m^2)$ then equation (3.123) transforms into

$$\mathcal{G}_m^{(1)}(\omega) = -\frac{N_m\mathcal{V}}{4\pi L}\int\limits_{\eta^2 q_m^2}^{\infty}\mathrm{d}s\left(\frac{1}{\eta^2}-\frac{q_m^2}{s}\right)\mathrm{e}^{-s}\,. \tag{3.124}$$

After performing the integral of the first term we obtain

$$\mathcal{G}_m^{(1)}(\omega) = -\frac{N_m\mathcal{V}}{4\pi L}\left[\frac{1}{\eta^2}\mathrm{e}^{-\eta^2 q_m^2} + q_m^2\,\mathrm{Ei}(-\eta^2 q_m^2)\right], \tag{3.125}$$

where we have introduced the exponential integral which is defined as

$$\mathrm{Ei}(x) = -P.V.\int\limits_{-x}^{\infty}\mathrm{d}s\,\frac{\mathrm{e}^{-s}}{s}\,, \tag{3.126}$$

where $P.V.$ denotes the principal value. The second part of equation (3.122) reads

$$\mathcal{G}_m^{(2)}(\omega) = \frac{N_m\mathcal{V}}{2\pi L}P.V.\int\limits_0^{\infty}\mathrm{d}k\,\frac{k^3}{k^2+q_m^2-k_\omega^2}\mathrm{e}^{-\eta^2(k^2+q_m^2)}\,, \tag{3.127}$$

where we have performed the trivial angular integral and used the Sokhotski-Plemelj formula

$$\frac{1}{x-\mathrm{i}0^+} = P.V.\left(\frac{1}{x}\right) + \mathrm{i}\pi\delta(x)\,. \tag{3.128}$$

As before, we can make a substitution $s = \eta^2(k^2+q_m^2-k_\omega^2)$ which transforms equation (3.127) into

$$\mathcal{G}_m^{(2)}(\omega) = \frac{N_m \mathcal{V}}{4\pi L} \mathrm{e}^{-\eta^2 k_\omega^2} P.V. \int\limits_{-\eta^2(k_\omega^2-q_m^2)}^{\infty} \mathrm{d}s \left(\frac{1}{\eta^2} - \frac{q_m^2 - k_\omega^2}{s} \right) \mathrm{e}^{-s} , \tag{3.129}$$

and after performing the resulting integral we obtain

$$\mathcal{G}_m^{(2)}(\omega) = \frac{N_m \mathcal{V}}{4\pi L} \left[\frac{1}{\eta^2} \mathrm{e}^{-\eta^2 q_m^2} + (q_m^2 - k_\omega^2)\, \mathrm{Ei}\left(\eta^2 (k_\omega^2 - q_m^2) \right) \right] . \tag{3.130}$$

Putting together equation (3.125) and equation (3.130) yields

$$\mathcal{G}_m(\omega) = \frac{N_m \mathcal{V}}{4\pi L} \left[(q_m^2 - k_\omega^2) \mathrm{e}^{-\eta^2 k_\omega^2}\, \mathrm{Ei}\left(\eta^2 (k_\omega^2 - q_m^2) \right) - q_m^2\, \mathrm{Ei}(-\eta^2 q_m^2) \right] . \tag{3.131}$$

Finally, we can now use equation (3.120) and equation (3.131) to obtain the regularized version of the transverse dynamical matrix

$$\mathcal{D}_\perp(\mathbf{q},\omega) = \sum_{m=0}^{\infty} \sum_{\mathbf{g}} \left[\frac{\xi_m^2 \omega^2 \omega_{\mathbf{q}-\mathbf{g},0}^2 \mathrm{e}^{-\eta^2(|\mathbf{q}-\mathbf{g}|^2 + q_m^2)}}{\omega_{\mathbf{q}-\mathbf{g},m}^2 (\omega_{\mathbf{q}-\mathbf{g},m}^2 - \omega^2)} - \mathcal{G}_m(\omega) \right] , \tag{3.132}$$

which converges to an η-independent value as $\eta \to 0$.

3.4.7 Single mode and pole approximations

For the regime of cavity widths $L < \lambda_0$ we can make a single mode approximation where, for the interactions between the dipoles, we retain only the contribution from the fundamental TEM mode. The corresponding single mode Green's function in closed form reads

$$G_\perp^{\mathrm{TEM}}(\boldsymbol{\rho} - \boldsymbol{\rho}', \omega) = \mathrm{i} \frac{\mathcal{V} k_\omega^2}{4L} H_0^{(1)} \left(k_\omega |\boldsymbol{\rho} - \boldsymbol{\rho}'| \right) , \tag{3.133}$$

which is equal to the $m = 0$ term of equation (3.104). Therefore the transverse dynamical matrix in equation (3.132) simplifies to

$$\mathcal{D}_\perp(\mathbf{q},\omega) = \sum_{\mathbf{g}} \left\{ \frac{\xi^2 \omega^2 \mathrm{e}^{-\eta^2 |\mathbf{q}-\mathbf{g}|^2}}{\omega_{\mathbf{q}-\mathbf{g}}^2 - \omega^2} - \mathrm{Re}[\check{G}_\perp^{\mathrm{TEM}}(0,\omega)] \right\} , \tag{3.134}$$

where $\xi = \sqrt{\mathcal{V}/\mathcal{A}L}$ and

$$\mathrm{Re}[\check{G}_{\perp}^{\mathrm{TEM}}(0,\omega)] = -\frac{\mathcal{V}k_{\omega}^{2}}{4\pi L}\mathrm{e}^{-\eta^{2}k_{\omega}^{2}}\,\mathrm{Ei}(\eta^{2}k_{\omega}^{2})\,, \tag{3.135}$$

which is the $m = 0$ term of equation (3.131).

Furthermore, a significant penalty that we pay for integrating out the photonic degrees of freedom is that the corresponding eigenvalue equation becomes non-linear. This is evident from equation (3.112) where both the transverse dynamical matrix and polarizability correction depend on the frequency, which ultimately stems from the fact that the Green's function is frequency-dependent. Therefore, to obtain the dispersion of the cavity polaritons one must numerically solve the following characteristic equation

$$\omega^{2} - \omega_{0}^{2} + 2\mu\omega_{0}\,\mathrm{Re}[\Sigma(\omega)] + 2\mu\omega_{0}\mathcal{D}_{\parallel}(\mathbf{q}) + 2\mu\omega_{0}\mathcal{D}_{\perp}(\mathbf{q},\omega) = 0\,, \tag{3.136}$$

where we have neglected non-radiative losses for simplicity. This is not ideal as it makes it difficult to extract analytical insight from the coupled-dipole equations.

As we will be focused on the dynamics of the dipoles within the vicinity of their resonant frequency, we can make a pole approximation by evaluating the polarizability correction and transverse dynamical matrix at the renormalized cavity frequency. This approximation introduces divergences whenever the photon frequency is equal to the cavity resonant frequency due to the poles in equation (3.132). However, it is a very good approximation away from the light-line, especially near the edge of the Brillouin zone which is where our attention will be focused. By applying this pole approximation we can linearize the eigenvalue problem in equation (3.112) and the corresponding polariton dispersion is explicitly given by

$$\omega = \sqrt{\omega_{\mathrm{cav}}^{2} - 2\mu\omega_{0}\mathcal{D}_{\parallel}(\mathbf{q}) - 2\mu\omega_{0}\mathcal{D}_{\perp}(\mathbf{q},\omega_{\mathrm{cav}})}\,. \tag{3.137}$$

3.4.8 Polariton dispersion for a square metasurface

Before we study the full polariton dispersion, let us first artificially switch off the light-matter interactions and consider the quasistatic dispersion

$$\omega = \sqrt{\omega_{\mathrm{cav}}^{2} - 2\mu\omega_{0}\mathcal{D}_{\parallel}(\mathbf{q})}\,, \tag{3.138}$$

where we include only the short-range Coulomb interactions between the dipoles. In figure 3.5(a) we plot the quasistatic dispersion (solid black line) for a large cavity width, and we

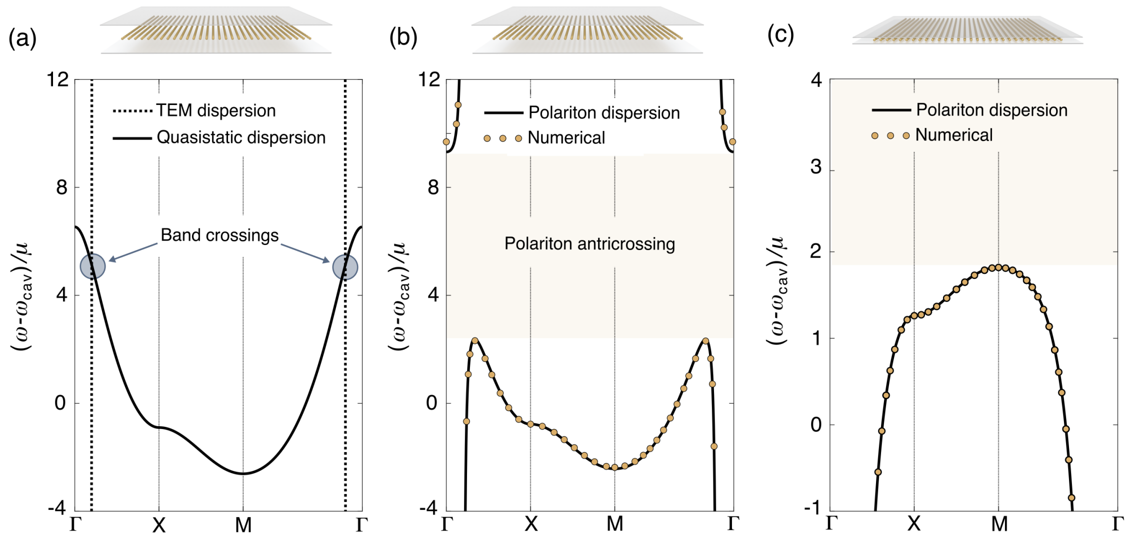

Figure 3.5 | Polariton dispersion for a square metasurface. (a) Quasistatic dispersion (solid black line) for the square metasurface with a large cavity width ($L = 5a$), where we have included only the short-range Coulomb interactions. We also plot the linear dispersion of the TEM cavity mode (dashed black line). Since the light-matter interaction is switched off, there are inevitable band crossings between the photonic modes and the quasistatic modes. (b) Polariton dispersion for the same metasurface and cavity width, where we have included the long-range photon-mediated interactions. The light-matter interaction results in a polaritonic anticrossing, but the spectrum near the Brillouin zone edge is very similar to the quasistatic case. (c) Polariton dispersion for the same metasurface with a small cavity width ($L = 0.5a$), which is qualitatively different to the quasistatic case. In panels (b) and (c) we also plot the numerical solutions to the full non-linear coupled-dipole equations (orange circles) which shows a very good agreement with the approximate dispersions, thus verifying the validity of the single mode and pole approximations. Results obtained with $\lambda_0 = 10a$ and $\mu = 0.001\omega_0$.

also plot the linear dispersion of the TEM cavity mode (dotted black line). Since the interaction is artificially switched off, there are inevitable band crossings between the photonic modes and the quasistatic modes.

In figure 3.5(b) we plot the polariton dispersion (solid black line) given by equation (3.137) which includes the long-range interactions mediated by the cavity photons. When the light-matter interaction is switched on we observe that the band crossings are avoided, resulting in a polaritonic band gap which is a characteristic feature of polaritonic systems [244]. Moreover, near the edge of the Brillouin zone the Coulomb interactions dominate the physics of the polaritons due to the subwavelength spacing of the metasurface – one can observe that the polariton dispersion is very similar to the quasistatic case. In figure 3.5(c) we plot the polariton dispersion for a small cavity width. Since the light-matter interactions are much stronger for smaller cavity widths and the Coulomb interactions are suppressed, the photon-mediated interactions dominate the physics of the polaritons, even near the corners of the Brillouin zone. In fact, the polariton dispersion is qualitatively different to the quasistatic case; for example, the effective mass of the polaritons at the M point has changed sign.

Finally, to verify the validity of the single mode and pole approximations that we outlined in section 3.4.6, in figure 3.5(b) and figure 3.5(c) we also plot the numerical solutions to the full non-linear coupled-dipole equations (orange circles) where we include all the cavity modes and retain the frequency dependence in the Green's function. We observe a very good agreement with the approximate polariton dispersion, thus verifying the validity of the approximations for the regime of parameters that we are interested in.

3.5 Conclusion

In this chapter we have developed a self-consistent coupled-dipole theory using a Green's function formalism, which can describe the collective dynamics of dipoles embedded inside a cavity waveguide. In particular, we have derived the longitudinal and transverse components of the cavity Green's function which describe the Coulomb interactions and photon-mediated interactions, respectively. Focusing on transverse excitations, we have shown how this theory can be used to derive the dispersion of the cavity polaritons supported by a simple square metasurface. Importantly, we have highlighted that for large cavity widths the physics near the Brillouin zone edge is dominated by the short-range Coulomb interactions, while the long-range photon-mediated interactions dominate for small cavity widths. In the following chapters, we will use this coupled-dipole theory to explore a range of interesting phenomena that can emerge in non-trivial metasurfaces.

4

Manipulating type-I and type-II Dirac polaritons in honeycomb metasurfaces

GRAPHENE physics has been emulated in a myriad of artificial systems by simulating a tight-binding model on a honeycomb lattice. Within this paradigm it is notoriously difficult to manipulate the fundamental properties of the corresponding Dirac quasiparticles as they are primarily determined by the nearest-neighbour hopping parameter. In this chapter, we study the Dirac polaritons that emerge in honeycomb metasurfaces composed of subwavelength arrays of dipole emitters/antennas, thereby going beyond the paradigm of tight-binding physics. Crucially, due to the hybrid light-matter nature of the Dirac polaritons, their properties depend qualitatively on the local electromagnetic environment which mediates the dipole-dipole interactions. Despite the superficial similarity with graphene, the metasurface exhibits both deterministic type-I Dirac points and accidental type-II Dirac points, where the latter emerge from a non-trivial winding in the light-matter interaction. By enclosing the metasurface inside a cavity waveguide, one can induce the multi-merging of the type-I and type-II Dirac points and the subsequent annihilation of the type-II Dirac points by varying only the cavity width. Consequently, we unveil a morphing between a linear and a quadratic spectrum accompanied by a change in the topological winding number, and also a cavity-induced inversion of chirality. This unique scenario has no analog in real or artificial graphene systems and could open opportunities to explore novel Dirac-related physics in a variety of experimental platforms.

This chapter presents original research that was published as follows:

Mann, C.-R., Sturges, T. J., Weick, G., Barnes, W. L. & Mariani, E. Manipulating type-I and type-II Dirac polaritons in cavity-embedded honeycomb metasurfaces. *Nature Communications* **9,** 2194 (2018).

4.1 Introduction

Graphene is a peculiar material whose low-energy quasiparticles are effectively described by a massless Dirac Hamiltonian, rather than the more conventional massive Schrödinger Hamiltonian [7]. This remarkable feature stems from the emergence of linearly dispersing energy bands that coalesce at the Dirac points, which exhibit a vortex structure in momentum space. Consequently, the massless Dirac quasiparticles are endowed with a chirality which leads to a wealth of extraordinary phenomena including Klein tunnelling [18, 120, 123–125] and an unconventional quantum Hall effect [143, 144, 149–151]. Shortly after the successful isolation of graphene [10], it became widely appreciated that the emergent Dirac physics was inextricably linked to the symmetry of the honeycomb lattice, and was not restricted to the specific physics of graphene. This realization sparked an extensive quest to engineer deterministic Dirac points in a myriad of artificial hexagonal lattices in entirely distinct physical platforms [44–60]. Within the realm of photonics, the most fruitful artificial graphene systems include honeycomb lattices of evanescently coupled waveguides [60, 66, 68, 184], microwave resonators [58, 65, 70], and semiconductor micropillars [59, 67, 69, 179], which have enabled one to simulate tight-binding physics in regimes that are difficult, if not impossible to reach in graphene itself.

Unfortunately, it is notoriously difficult to manipulate the fundamental properties of the massless Dirac fermions in graphene; the only parameter entering the effective Dirac Hamiltonian is the Dirac velocity which is primarily determined by the nearest-neighbour hopping parameter. Consequently, the enticing concept of strain-engineering has attracted considerable interest as a mechanism to modify graphene's band structure [62, 156]. However, the Dirac points are characterized by a topological winding number which renders them remarkably stable against lattice perturbations that preserve $\mathcal{T}$ and $\mathcal{I}$ symmetry [21]. Applying strain generates anisotropic hopping parameters which decouples the Dirac points from the high symmetry points, and the Dirac cones become tilted with an anisotropic Dirac velocity due to the broken $\mathcal{C}_3$ symmetry. When the lattice anisotropy exceeds a critical value, a phase transition from a gapless semi-metal to a gapped insulator occurs via the merging and annihilation of the Dirac points with opposite topological winding numbers [61–64]. While this tantalizing transition has remained elusive in graphene due to the large strains required [62], it has been successfully observed in photonic graphene systems where one has meticulous control over the lattice parameters [65–67].

This raises an interesting question: is it possible to manipulate the fundamental properties of the Dirac quasiparticles while preserving the underlying symmetries? While the symmetries constrain the form of the effective Hamiltonian, the Hamiltonian parameters depend on the details of the system and modifying them can have dramatic consequences. For example, one can switch the chirality of the massless Dirac quasiparticles by changing the sign of the Dirac velocity; however, this is impossible to achieve in graphene or its photonic analogs as it requires one to switch the sign of the nearest-neighbour hopping parameter.

Here we unveil a new mechanism to generate and manipulate different types of Dirac points in a honeycomb metasurface composed of a subwavelength array of interacting dipole emitters/antennas. Despite its superficial similarity with graphene and its photonic analogs, the metasurface simultaneously exhibits two distinct species of massless Dirac polaritons: type-I and type-II. The latter, more exotic class have no analog in high-energy physics because they strongly violate Lorentz-invariance, and they have attracted growing interest since the recent discovery of type-II Dirac/Weyl semimetals [246–250]. They are classified according to the topology of the isofrequency contours and are thus related via a Lifshitz transition. While the type-I Dirac points exhibit closed, circular isofrequency contours and are the conventional ones that emerge in graphene, the type-II Dirac points exhibit critically tilted Dirac cones with open, hyperbolic isofrequency contours. Previous work has shown that type-II Dirac points can be engineered in highly anisotropic 2D photonic lattices [251, 252]. In stark contrast, here the type-II Dirac points in the polariton spectrum emerge from a non-trivial winding in the light-matter interaction. Furthermore, while the type-I Dirac points are deterministic and protected by the symmetries of the metasurface, the type-II Dirac points are accidental band degeneracies and their existence depends critically on the nature of the dipole-dipole interactions.

Consequently, by embedding the metasurface inside a cavity waveguide and varying only the cavity width, we show that one can manipulate the location of the type-II Dirac points within the Brillouin zone. This leads to qualitatively different polariton phases, despite the preserved lattice symmetries. Specifically, at a critical cavity width, we unveil a multi-merging of the type-I and type-II Dirac points as the Dirac velocity vanishes which results in a hybrid Dirac point. This gives rise to massive chiral polaritons that are characterized by a quadratic dispersion and a topological winding number of ± 2. Beyond this critical width, we observe the merging and subsequent annihilation of the type-II Dirac points; a transition that leaves only the type-I Dirac points remaining in the polariton spectrum. Finally, for small cavity widths where the Coulomb interactions are suppressed and the photon-mediated interactions are dominant, we recover the linear spectrum near the type-I Dirac points but the Dirac velocity switches sign. Consequently, the massless Dirac polaritons re-emerge but with a cavity-induced inversion of chirality.

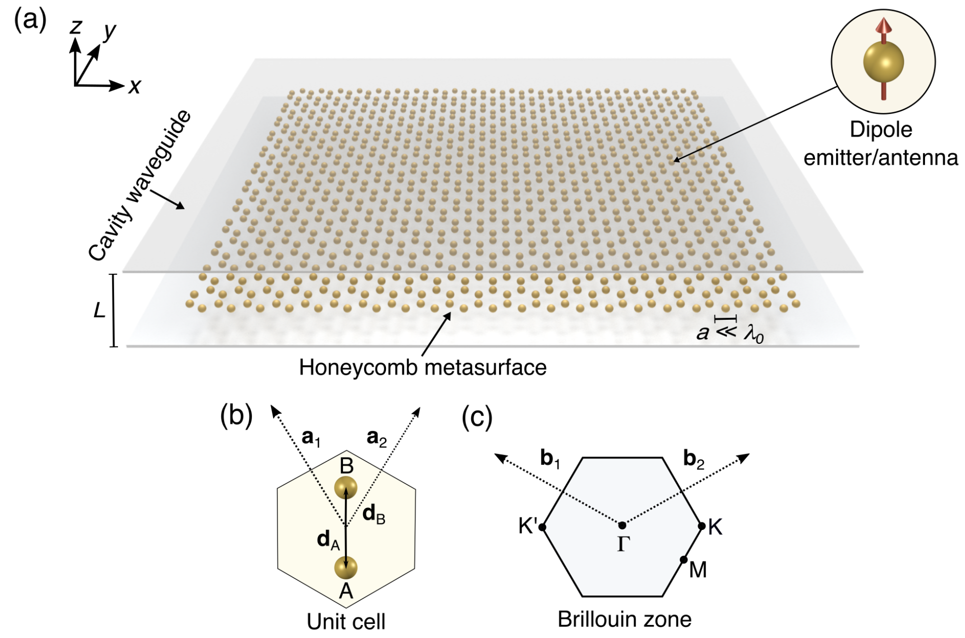

Figure 4.1 | Honeycomb metasurface inside a cavity waveguide. (a) Schematic of a honeycomb metasurface composed of an array of dipole emitters/antennas with subwavelength nearest-neighbour separation $a \ll \lambda_0$. The induced dipole moments are assumed to point in the z-direction (see inset). Furthermore, the honeycomb metasurface is embedded inside a cavity waveguide of width L, where the cavity walls are assumed to be perfect mirrors. (b) Corresponding unit cell that contains two dipoles with basis vectors $\mathbf{d}_\mathrm{A}$ and $\mathbf{d}_\mathrm{B}$, which gives rise to the A and B hexagonal sublattices, respectively. The primitive lattice vectors are $\mathbf{a}_1$ and $\mathbf{a}_2$. (c) Corresponding first Brillouin zone where the high-symmetry points are labeled, and $\mathbf{b}_1$ and $\mathbf{b}_2$ are the primitive reciprocal lattice vectors.

4.2 Honeycomb metasurface

A schematic of a honeycomb metasurface embedded inside a cavity waveguide is depicted in figure 4.1(a). We consider an elementary metasurface that is composed of an array of dipole emitters/antennas which we describe using the same minimal model that we presented in section 3.4. Specifically, we describe the dipoles with a bare polarizability of the form

$$\alpha_\mathrm{B}(\omega) = \frac{2\omega_0\mu}{\omega_0^2 - \omega^2 - \mathrm{i}\omega\gamma_\mathrm{nr}}\,, \tag{4.1}$$

where the corresponding induced dipole moments are assumed to point in the z-direction (see inset). For simplicity, we will neglect non-radiative losses throughout this chapter ($\gamma_\mathrm{nr} = 0$). The dipoles are located at periodic positions $\mathbf{R}_\mathrm{A} = \mathbf{R} + \mathbf{d}_\mathrm{A}$ and $\mathbf{R}_\mathrm{B} = \mathbf{R} + \mathbf{d}_\mathrm{B}$, which form the A and B inequivalent hexagonal sublattices, respectively. Here, the basis vectors

$$\mathbf{d}_\mathrm{A} = \frac{a}{2}\Big[0\,,\,-1\Big]\,, \quad \mathbf{d}_\mathrm{B} = \frac{a}{2}\Big[0\,,\,1\Big]\,, \tag{4.2}$$

locate the positions of the dipoles within a unit cell as depicted in figure 4.1(b). Furthermore, $\mathbf{R} = l_1\mathbf{a}_1 + l_2\mathbf{a}_2$ represents the set of lattice translation vectors, where $l_1, l_2 \in \mathbb{Z}$ are integers, and

$$\mathbf{a}_1 = \frac{\sqrt{3}a}{2}\Big[-1\,,\,\sqrt{3}\Big]\,, \quad \mathbf{a}_2 = \frac{\sqrt{3}a}{2}\Big[1\,,\,\sqrt{3}\Big]\,, \tag{4.3}$$

are the primitive lattice vectors. The corresponding set of reciprocal lattice vectors are $\mathbf{g} = n_1\mathbf{b}_1 + n_2\mathbf{b}_2$, where $n_1, n_2 \in \mathbb{Z}$ are integers, and

$$\mathbf{b}_1 = \frac{2\pi}{3a}\Big[-\sqrt{3}\,,\,1\Big]\,, \quad \mathbf{b}_2 = \frac{2\pi}{3a}\Big[\sqrt{3}\,,\,1\Big]\,, \tag{4.4}$$

are the primitive reciprocal lattice vectors that define the Brillouin zone which is shown in figure 4.1(c). Moreover, we consider the nearest-neighbour separation distance to be subwavelength $a \ll \lambda_0$, so that the polaritons near the K/K' points are subradiant and evanescently bound to the lattice. Finally, we embed the metasurface at the centre of a cavity waveguide of width L, where the cavity walls are assumed to be perfect mirrors.

4.2.1 Coupled-dipole equations

The collective dynamics of the dipoles within the honeycomb metasurface are governed by a set of self-consistent coupled-dipole equations, where the induced dipole moment $p_{\mathbf{R}_\mathrm{A}}(\omega)$ located at $\mathbf{R}_\mathrm{A}$ on the A sublattice is given by

$$\frac{1}{\alpha(\omega)}p_{\mathbf{R}_\mathrm{A}}(\omega) = \sum_{\mathbf{R}'_\mathrm{A}\neq\mathbf{R}_\mathrm{A}} G(\mathbf{R}_\mathrm{A} - \mathbf{R}'_\mathrm{A}, \omega)p_{\mathbf{R}'_\mathrm{A}}(\omega) + \sum_{\mathbf{R}_\mathrm{B}} G(\mathbf{R}_\mathrm{A} - \mathbf{R}_\mathrm{B}, \omega)p_{\mathbf{R}_\mathrm{B}}(\omega)\,, \tag{4.5}$$

and the induced dipole moment $p_{\mathbf{R}_\mathrm{B}}(\omega)$ located at $\mathbf{R}_\mathrm{B}$ on the B sublattice is given by

$$\frac{1}{\alpha(\omega)}p_{\mathbf{R}_\mathrm{B}}(\omega) = \sum_{\mathbf{R}'_\mathrm{B}\neq\mathbf{R}_\mathrm{B}} G(\mathbf{R}_\mathrm{B} - \mathbf{R}'_\mathrm{B}, \omega)p_{\mathbf{R}'_\mathrm{B}}(\omega) + \sum_{\mathbf{R}_\mathrm{A}} G(\mathbf{R}_\mathrm{B} - \mathbf{R}_\mathrm{A}, \omega)p_{\mathbf{R}_\mathrm{A}}(\omega)\,. \tag{4.6}$$

Here, $\alpha(\omega) = [\alpha_\mathrm{B}^{-1}(\omega) - \Sigma(\omega)]^{-1}$ is the renormalized polarizability that was derived in section 3.4.2, where the polarizability correction inside the cavity waveguide reads

$$\Sigma(\omega) = \mathrm{i}\frac{\mathcal{V}k_\omega^3}{6\pi} + \frac{\mathcal{V}}{\pi L^3}\Big[\mathrm{Li}_3\left(\mathrm{e}^{\mathrm{i}k_\omega L}\right) - \mathrm{i}k_\omega L\,\mathrm{Li}_2\left(\mathrm{e}^{\mathrm{i}k_\omega L}\right)\Big]\,. \tag{4.7}$$

Moreover, $G(\boldsymbol{\rho} - \boldsymbol{\rho}', \omega)$ is the zz-component of the cavity Green's function that was derived in section 3.3 and reads

$$G(\boldsymbol{\rho} - \boldsymbol{\rho}', \omega) = \mathrm{i}\frac{\mathcal{V}}{4L}\sum_{m=0}^{\infty} N_m \left(k_\omega^2 - q_m^2\right) H_0^{(1)}\left(\sqrt{k_\omega^2 - q_m^2}\,|\boldsymbol{\rho} - \boldsymbol{\rho}'|\right) . \tag{4.8}$$

Therefore, the first sums in equation (4.5) and equation (4.6) describe intrasublattice interactions between dipoles that reside on the same sublattice, while the second sums describe intersublattice interactions between dipoles that reside on opposite sublattices.

4.3 Quasistatic approximation

To unravel the intricate physics arising from the complex nature of the dipole-dipole interactions, we will explore the physics of the honeycomb metasurface in a step-wise manner. Given the subwavelength spacing between the dipoles, it is natural to assume that the short-range Coulomb interactions dominate the physics away from the light-line for relatively large cavity widths – indeed, this was the case for the square metasurface in section 3.4. Therefore, we will begin our analysis within the quasistatic approximation where we neglect the long-range photon-mediated interactions and consider only the short-range Coulomb interactions between the dipoles.

4.3.1 Short-range Coulomb interactions

The Coulomb interactions are encoded in the longitudinal component of the cavity Green's function that was derived in section 3.3 and reads

$$G_{\|}(\boldsymbol{\rho} - \boldsymbol{\rho}') = -\frac{\mathcal{V}}{\pi L}\sum_{m=1}^{\infty} q_m^2 K_0\left(q_m|\boldsymbol{\rho} - \boldsymbol{\rho}'|\right) . \tag{4.9}$$

To study the collective dipolar excitations we introduce the Fourier transform of the dipole moments on the two sublattices

$$\tilde{p}_{\mathrm{A}}(\mathbf{q}, \omega) = \frac{\sqrt{\mathcal{A}}}{2\pi}\sum_{\mathbf{R}_{\mathrm{A}}} p_{\mathbf{R}_{\mathrm{A}}}(\omega)\mathrm{e}^{-\mathrm{i}\mathbf{q}\cdot\mathbf{R}_{\mathrm{A}}} , \quad \tilde{p}_{\mathrm{B}}(\mathbf{q}, \omega) = \frac{\sqrt{\mathcal{A}}}{2\pi}\sum_{\mathbf{R}_{\mathrm{B}}} p_{\mathbf{R}_{\mathrm{B}}}(\omega)\mathrm{e}^{-\mathrm{i}\mathbf{q}\cdot\mathbf{R}_{\mathrm{B}}} , \tag{4.10}$$

where $\mathbf{q} = [\, q_x \, , \, q_y \,]$ is the Bloch wavevector that is restricted to the first Brillouin zone shown in figure 4.1(c), and $\mathcal{A} = 3\sqrt{3}a^2/2$ is the area of the unit cell shown in figure 4.1(b). Using the Fourier variables in equation (4.10) we can block diagonalize the coupled-dipole equations and recast them into simple 2 × 2 matrix eigenvalue equations

$$\frac{1}{\breve{\alpha}(\omega)}\left|\psi(\mathbf{q})\right\rangle = \mathcal{D}_{\|}(\mathbf{q})\left|\psi(\mathbf{q})\right\rangle\,, \tag{4.11}$$

where $\breve{\alpha}^{-1}(\omega) = \alpha_{\mathrm{B}}^{-1}(\omega) - \mathrm{Re}[\Sigma(\omega)]$ and $|\psi(\mathbf{q})\rangle$ represents the vector of Fourier variables

$$|\psi(\mathbf{q})\rangle = \begin{bmatrix} \widetilde{p}_{\mathrm{A}}(\mathbf{q}) \\ \widetilde{p}_{\mathrm{B}}(\mathbf{q}) \end{bmatrix}. \tag{4.12}$$

Also in equation (4.11), $\mathcal{D}_{\|}(\mathbf{q})$ is the longitudinal dynamical matrix that encodes the frequency shifts due to the Coulomb interactions and reads

$$\mathcal{D}_{\|}(\mathbf{q}) = \begin{bmatrix} \mathcal{D}_{\|}^{\mathrm{AA}}(\mathbf{q}) & \mathcal{D}_{\|}^{\mathrm{AB}}(\mathbf{q}) \\ \mathcal{D}_{\|}^{\mathrm{AB}*}(\mathbf{q}) & \mathcal{D}_{\|}^{\mathrm{BB}}(\mathbf{q}) \end{bmatrix}. \tag{4.13}$$

The intrasublattice matrix elements read

$$\mathcal{D}_{\|}^{\mathrm{AA/BB}}(\mathbf{q}) = \sum_{\mathbf{R}\neq 0} G_{\|}(\mathbf{R})\mathrm{e}^{-\mathrm{i}\mathbf{q}\cdot\mathbf{R}}\,, \tag{4.14}$$

while the intersublattice matrix elements are given by

$$\mathcal{D}_{\|}^{\mathrm{AB}}(\mathbf{q}) = \sum_{\mathbf{R}} G_{\|}(\mathbf{R}-\mathbf{d})\mathrm{e}^{-\mathrm{i}\mathbf{q}\cdot(\mathbf{R}-\mathbf{d})}\,, \tag{4.15}$$

where we have introduced the vector $\mathbf{d} = \mathbf{d}_{\mathrm{B}} - \mathbf{d}_{\mathrm{A}}$ which connects the two sublattices within the unit cell.

4.3.2 Emergence of type-I deterministic Dirac points

For simplicity, we evaluate the polarizability correction at the cavity resonant frequency, which we have shown is a very good approximation in section 3.4.2. Then, by solving the characteristic equation associated with equation (4.11) , one finds the following quasistatic dispersion for the dipolar excitations on the honeycomb metasurface

$$\omega_{\lambda}^{\|}(\mathbf{q}) = \sqrt{\omega_{\mathrm{cav}}^{2} - 2\omega_{0}\mu\mathcal{D}_{\|}^{\mathrm{AA}}(\mathbf{q}) + 2\omega_{0}\mu\lambda|\mathcal{D}_{\|}^{\mathrm{AB}}(\mathbf{q})|}\,, \tag{4.16}$$

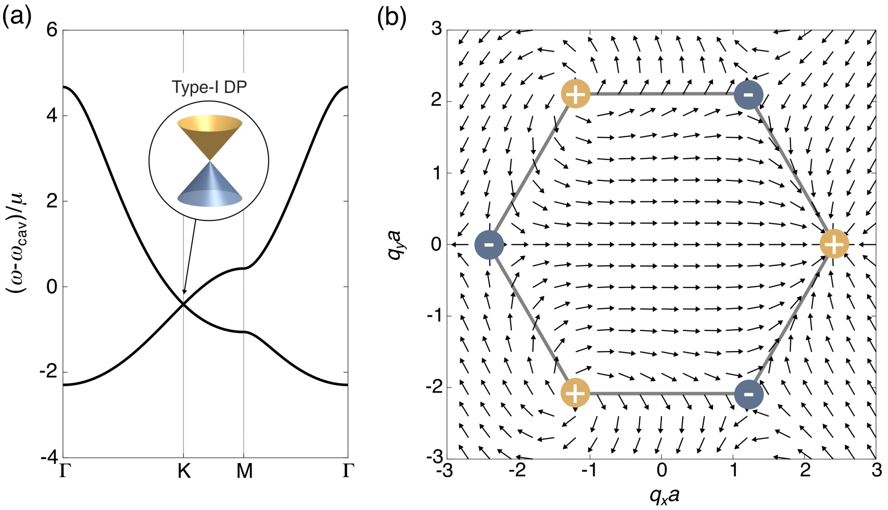

Figure 4.2 | Quasistatic dispersion and pseudo-spin field. (a) Quasistatic dispersion for the honeycomb metasurface with a large cavity width ($L = 5a$), where we include only the short-range Coulomb interactions. The spectrum exhibits deterministic Dirac points at the high-symmetry K/K′ points – these belong to the type-I class that are characterized by massless Dirac cones with circular isofrequency contours (see inset). (b) Corresponding pseudo-spin field for the upper band. The Dirac points correspond to vortices (yellow and blue circle) which we label according to their topological winding numbers. Results obtained with $\lambda_0 = 10a$ and $\mu = 0.001\omega_0$.

where $\lambda = \pm$ labels the upper ($\lambda = +$) and lower ($\lambda = -$) bands. In analogy with graphene, the corresponding spinor eigenstates

$$|\psi_\lambda^{\parallel}(\mathbf{q})\rangle = \frac{1}{\sqrt{2}}\begin{bmatrix} 1 \\ \lambda \mathrm{e}^{\mathrm{i}\varphi_{\parallel}(\mathbf{q})} \end{bmatrix} \tag{4.17}$$

encode a pseudo-spin degree of freedom, where the two components describe how the amplitude and phase of the dipolar excitation is distributed on the A and B sublattices. We can therefore represent the spinor eigenstates by a pseudo-spin vector on the Bloch sphere

$$\mathbf{S}_\lambda^{\parallel}(\mathbf{q}) = \langle\psi_\lambda^{\parallel}(\mathbf{q})|\,\boldsymbol{\sigma}\,|\psi_\lambda^{\parallel}(\mathbf{q})\rangle = \lambda\Big[\cos\varphi_{\parallel}(\mathbf{q})\,,\,\sin\varphi_{\parallel}(\mathbf{q})\,,\,0\Big]\,, \tag{4.18}$$

where the azimuthal angle is given by

$$\varphi_{\parallel}(\mathbf{q}) = \arg\Big[-\mathcal{D}_{\parallel}^{\mathrm{AB}*}(\mathbf{q})\Big]\,. \tag{4.19}$$

Note, because the honeycomb metasurface exhibits $\mathcal{T}$ and $\mathcal{I}$ symmetry, no σ_z term appears in the dynamical matrix and therefore the pseudo-spin vector is pinned to the equatorial plane of the Bloch sphere.

In figure 4.2(a) we plot the quasistatic dispersion for a large cavity width where the coupling between neighbouring dipoles is dominated by the Coulomb interactions. Furthermore, in figure 4.2(b) we show the corresponding pseudo-spin field for the upper quasistatic band. One observes that the quasistatic dispersion is very reminiscent of the electronic band structure of graphene. In particular, the spectrum exhibits Dirac points at the high-symmetry K/K' points located at $\tau\mathbf{K} = \tau[\,4\pi/3\sqrt{3}a\,,0\,]$, where $\tau = \pm$ is the valley index, and these coincide with vortices in the pseudo-spin field. Moreover, the Dirac points evidently belong to the type-I class where the massless Dirac cone is characterized by closed, circular isofrequency contours. This correspondence between graphene and the metasurface is not particularly surprising since they share the same honeycomb lattice structure and the Coulomb interactions are short-range, decreasing rapidly with the separation distance.

We can explicitly show that the $\mathcal{C}_3$ symmetry of the honeycomb metasurface enforces the intersublattice matrix elements to vanish at the K/K' points which read

$$\mathcal{D}_{\parallel}^{\mathrm{AB}}(\tau\mathbf{K}) = \sum_{\mathbf{R}} G_{\parallel}(\mathbf{R}-\mathbf{d})\mathrm{e}^{-\mathrm{i}\tau\mathbf{K}\cdot(\mathbf{R}-\mathbf{d})}\,. \tag{4.20}$$

According to equation (4.9) the interactions between the dipoles depend only on the separation distance $G_{\parallel}(\boldsymbol{\rho}-\boldsymbol{\rho}') = G_{\parallel}(|\boldsymbol{\rho}-\boldsymbol{\rho}'|)$, so we can facilitate the evaluation of equation (4.20) by summing the phase contributions from equidistant dipoles. For a given lattice vector in the sum, we can use the $\mathcal{C}_3$ symmetry of the honeycomb lattice to find three separation vectors that have equal magnitudes. This allows us to rewrite equation (4.20) as

$$\mathcal{D}_{\parallel}^{\mathrm{AB}}(\tau\mathbf{K}) = \frac{1}{3}\sum_{\mathbf{R}} G_{\parallel}(\mathbf{R}-\mathbf{d})\sum_{j=0}^{2}\mathrm{e}^{-\mathrm{i}\tau\mathbf{K}\cdot\mathcal{R}(j2\pi/3)\cdot(\mathbf{R}-\mathbf{d})}\,, \tag{4.21}$$

where we have introduced the 2D rotation matrix

$$\mathcal{R}(\theta) = \begin{bmatrix} \cos(\theta) & -\sin(\theta) \\ \sin(\theta) & \cos(\theta) \end{bmatrix}, \tag{4.22}$$

and we have included the factor of $1/3$ to avoid over counting. Finally, after a few manipulations, it is simple to show that the sum of the phase contributions vanishes identically

$$\sum_{j=0}^{2}\mathrm{e}^{-\mathrm{i}\tau\mathbf{K}\cdot\mathcal{R}(j2\pi/3)\cdot(\mathbf{R}-\mathbf{d})} = \mathrm{e}^{\mathrm{i}\tau\mathbf{K}\cdot\mathbf{d}}\mathrm{e}^{-\mathrm{i}\tau\frac{2\pi}{3}(l_2-l_1)}\left(1+\mathrm{e}^{\mathrm{i}\tau\frac{2\pi}{3}}+\mathrm{e}^{-\mathrm{i}\tau\frac{2\pi}{3}}\right) = 0\,. \tag{4.23}$$

Since this is true for all lattice vectors in the sum, the intersublattice matrix elements must vanish identically at the K/K' points.

It is important to emphasize that in the preceding analysis we did not use the precise form of the Coulomb interactions. In fact, the arguments that we presented are insensitive to the exact nature of the dipole-dipole interactions; the only strict requirement is that the interactions exhibit $\mathcal{C}_3$ symmetry. This is why these Dirac points are described as deterministic – their existence does not depend on the details of the system parameters because they are enforced by the symmetry.

4.4 Tunable Dirac polaritons

Within the quasistatic approximation there is essentially a one-to-one correspondence between the honeycomb metasurface and graphene – this has been pointed out in previous work which studied the quasistatic plasmons supported by a honeycomb lattice of metallic nanoparticles in free space [51]. However, the natural question is: does the quasistatic approximation capture all the interesting physics? Naively, one may be tempted to assume that nothing peculiar could emerge from the long-range photon-mediated interactions, especially for large cavity widths where they are relatively weak. Contrary to these expectations, in this section we reveal that the quasistatic approximation completely misses important physics; in fact, the hybridization with the cavity photons qualitatively alters the geometrical and topological properties of the polaritons.

4.4.1 Long-range photon-mediated interactions

The interaction between the dipoles and the cavity photons results in long-range dipole-dipole interactions that are described by the transverse component of the cavity Green's function which is given by $G_\perp(\boldsymbol{\rho}-\boldsymbol{\rho}',\omega) = G(\boldsymbol{\rho}-\boldsymbol{\rho}',\omega) - G_\parallel(\boldsymbol{\rho}-\boldsymbol{\rho}')$. However, since we are interested in the regime of cavity widths $L < \lambda_0$, we retain only the contribution from the TEM cavity mode. The corresponding single mode Green's function was derived in section 3.3 and reads

$$G_\perp^{\mathrm{TEM}}(\boldsymbol{\rho}-\boldsymbol{\rho}',\omega) = \mathrm{i}\frac{\mathcal{V}k_\omega^2}{4L} H_0^{(1)}\left(k_\omega|\boldsymbol{\rho}-\boldsymbol{\rho}'|\right) . \tag{4.24}$$

If we include the photon-mediated interactions then the matrix eigenvalue equation becomes

$$\frac{1}{\breve{\alpha}(\omega)} |\psi(\mathbf{q})\rangle = \left[\mathcal{D}_\parallel(\mathbf{q}) + \mathcal{D}_\perp(\mathbf{q},\omega)\right] |\psi(\mathbf{q})\rangle , \tag{4.25}$$

where $\mathcal{D}_\perp(\mathbf{q},\omega)$ is the transverse dynamical matrix that encodes the frequency shifts due to the photon-mediated interactions and reads

$$\mathcal{D}_\perp(\mathbf{q},\omega) = \begin{bmatrix} \mathcal{D}_\perp^{\mathrm{AA}}(\mathbf{q},\omega) & \mathcal{D}_\perp^{\mathrm{AB}}(\mathbf{q},\omega) \\ \mathcal{D}_\perp^{\mathrm{AB}*}(\mathbf{q},\omega) & \mathcal{D}_\perp^{\mathrm{BB}}(\mathbf{q},\omega) \end{bmatrix} . \tag{4.26}$$

The intrasublattice matrix elements read

$$\mathcal{D}_\perp^{\mathrm{AA/BB}}(\mathbf{q},\omega) = \sum_{\mathbf{g}} \frac{\omega^2\xi^2}{\omega_{\mathbf{q}-\mathbf{g}}^2 - \omega^2} - \mathrm{Re}[G_\perp^{\mathrm{TEM}}(0,\omega)] \, , \tag{4.27}$$

where we have used the Poisson summation technique outlined in section 3.4.5 due to the long-range nature of the photon-mediated interactions. Furthermore, the intersublattice matrix elements are given by

$$\mathcal{D}_\perp^{\mathrm{AB}}(\mathbf{q},\omega) = \sum_{\mathbf{g}} \frac{\omega^2\xi^2\phi_{\mathbf{g}}}{\omega_{\mathbf{q}-\mathbf{g}}^2 - \omega^2} \, , \tag{4.28}$$

where $\xi = \sqrt{\mathcal{V}/\mathcal{A}L}$ parameterizes the strength of the light-matter interaction with the TEM mode. Note that the non-trivial phase factors

$$\phi_{\mathbf{g}} = \mathrm{e}^{\mathrm{i}\mathbf{g}\cdot\mathbf{d}} \tag{4.29}$$

arise due to the non-Bravais nature of the honeycomb lattice and they must be retained as they are critical for maintaining the correct symmetry.

Before we analyze the polariton dispersion, it is worthwhile addressing an important point. It is common in the polariton literature, including Hopfield's original work [244], to retain only the near-resonant photons ($\mathrm{g} = 0$) and neglect the Umklapp processes ($\mathrm{g} \neq 0$) since the frequency of these photons are typically much larger than the dipole resonant frequency ($\omega_{\mathbf{q}-\mathbf{g}} \gg \omega_0$) in subwavelength lattices. However, this is only strictly valid away from the Brillouin zone edge. To be more explicit, at the K point there are three degenerate photonic modes with the same frequency as the first photon band $\omega_{\mathbf{K}}$, which therefore couple to the quasistatic excitations with equal strength. Since we are particularly interested in the physics near the edge of the Brillouin zone, it is not acceptable to neglect these Umklapp processes since it would destroy the $\mathcal{C}_3$ symmetry that protects the deterministic Dirac points. For large cavity widths (and in free space), one may not notice this symmetry-breaking effect because even the lowest photon branches are far off-resonance ($\omega_{\mathbf{K}} \gg \omega_0$) with the dipoles, and therefore the denominators in equation (4.28) and equation (4.27) are large. Consequently,

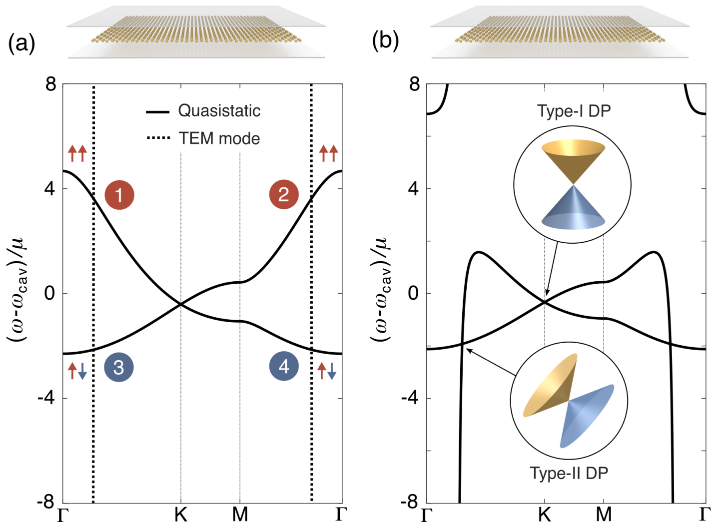

Figure 4.3 | Emergence of type-II accidental Dirac points. (a) Quasistatic dispersion (solid black line) for the honeycomb metasurface with a large cavity width ($L = 5a$) and the linear dispersion of the TEM cavity mode (dashed black line). We label the band crossings along the high-symmetry lines 1-4. (b) Polariton dispersion for the same metasurface and cavity width where we include the long-range photon-mediated interactions. Switching on the light-matter interaction results in a large anticrossing with the upper quasistatic band because they correspond to bright, symmetric dipole configurations (↑↑). In contrast, we observe a very small anticrossing with the lower quasistatic band along the $\Gamma \rightarrow \mathrm{M}$ directions because they correspond to dark, antisymmetric dipole configurations (↑↓). Due to a non-trivial winding in the light–matter coupling parameter (see figure 4.4), the light-matter interaction vanishes identically along the $\Gamma \rightarrow \mathrm{K}(\mathrm{K}')$ directions. This generates six accidental Dirac points in the Brillouin zone which belong to the type-II class that are characterized by critically tilted Dirac cones (see inset). Results obtained with $\lambda_0 = 10a$ and $\mu = 0.001\omega_0$.

the hybridization with the photons only slightly perturbs the quasistatic bands near the edge of the Brillouin zone. However, the symmetry breaking becomes increasingly apparent as one reduces the cavity width, because the light-matter coupling strength increases rapidly and eventually the photon-mediated interactions dominate over the Coulomb interactions.

4.4.2 Emergence of type-II accidental Dirac points

In figure 4.3(a) we show the linear dispersion of the TEM mode along with the quasistatic dispersion for a large cavity width. When the light-matter interaction is artificially switched off there are inevitable band crossings which we label $1-4$ along the high-symmetry lines. Given the elementary nature of the individual dipoles, one could easily be lured into thinking that these band crossings will be avoided when the light-matter interaction is switched on; after all, this is a characteristic feature of polaritonic systems and is precisely what we observed for the square metasurface in figure 3.5(b). However, the story is not so simple for the honeycomb metasurface.

To obtain the polariton dispersion, we first linearize the eigenvalue problem in equation (4.25) by evaluating the polarizability correction and transverse dynamical matrix at the cavity resonant frequency as discussed in section 3.4. Then, by solving the associated characteristic equation we obtain the following polariton dispersion

$$\omega_\lambda(\mathbf{q}) = \sqrt{\omega_{\mathrm{cav}}^2 - 2\omega_0\mu\left[\mathcal{D}_\parallel^{\mathrm{AA}}(\mathbf{q}) + \mathcal{D}_\perp^{\mathrm{AA}}(\mathbf{q},\omega_{\mathrm{cav}})\right] + 2\omega_0\mu\lambda\left|\mathcal{D}_\parallel^{\mathrm{AB}}(\mathbf{q}) + \mathcal{D}_\perp^{\mathrm{AB}}(\mathbf{q},\omega_{\mathrm{cav}})\right|}\,. \tag{4.30}$$

Note, one must use the regularization procedure outlined in section 3.4 in order to numerically evaluate the polariton dispersion. The corresponding polariton spinor eigenstates read

$$|\psi_\lambda(\mathbf{q})\rangle = \frac{1}{\sqrt{2}}\begin{bmatrix} 1 \\ \lambda \mathrm{e}^{\mathrm{i}\varphi(\mathbf{q})} \end{bmatrix}, \tag{4.31}$$

which can be represented by a pseudo-spin vector on the Bloch sphere

$$\mathbf{S}_\lambda(\mathbf{q}) = \langle\psi_\lambda(\mathbf{q})|\,\boldsymbol{\sigma}\,|\psi_\lambda(\mathbf{q})\rangle = \lambda\,[\,\cos\varphi(\mathbf{q})\,,\,\sin\varphi(\mathbf{q})\,,\,0\,]\,, \tag{4.32}$$

where the azimuthal angle is given by

$$\varphi(\mathbf{q}) = \arg\left[-\mathcal{D}_\parallel^{\mathrm{AB}*}(\mathbf{q}) - \mathcal{D}_\perp^{\mathrm{AB}*}(\mathbf{q},\omega_{\mathrm{cav}})\right]. \tag{4.33}$$

In figure 4.3(b) we show the polariton dispersion for the same large cavity width. Interestingly, despite the light-matter interaction being switched on, not all of the band crossings are avoided. To further elucidate this non-trivial nature of the honeycomb metasurface, it is convenient to re-express the transverse dynamical matrix in the basis of the quasistatic eigenstates given by equation (4.17). The corresponding intraband matrix elements read

$$\mathcal{D}_\perp^{\lambda\lambda}(\mathbf{q},\omega) = \langle\psi_\lambda^\parallel(\mathbf{q})|\,\mathcal{D}_\perp(\mathbf{q},\omega)\,|\psi_\lambda^\parallel(\mathbf{q})\rangle = \sum_{\mathbf{g}}\frac{\omega^2|\Lambda_{\lambda\mathbf{g}}(\mathbf{q})|^2}{\omega_{\mathbf{q}-\mathbf{g}}^2-\omega^2} - \mathrm{Re}[G_\perp^{\mathrm{TEM}}(0,\omega)]\,, \tag{4.34}$$

while the interband matrix elements are given by

$$\mathcal{D}_\perp^{\lambda\lambda'}(\mathbf{q},\omega) = \langle\psi_\lambda^\parallel(\mathbf{q})|\,\mathcal{D}_\perp(\mathbf{q},\omega)\,|\psi_{\lambda'}^\parallel(\mathbf{q})\rangle = \sum_{\mathbf{g}}\frac{\omega^2\Lambda_{\lambda\mathbf{g}}^*(\mathbf{q})\Lambda_{\lambda'\mathbf{g}}(\mathbf{q})}{\omega_{\mathbf{q}-\mathbf{g}}^2-\omega^2}\,. \tag{4.35}$$

This transformation unveils a non-trivial winding in the new light-matter coupling parameter

$$\Lambda_{\lambda\mathbf{g}}(\mathbf{q}) = \frac{\xi}{\sqrt{2}}\left[1 + \lambda\mathrm{e}^{\mathrm{i}\varphi_\parallel(\mathbf{q})}\phi_{\mathbf{g}}\right], \tag{4.36}$$

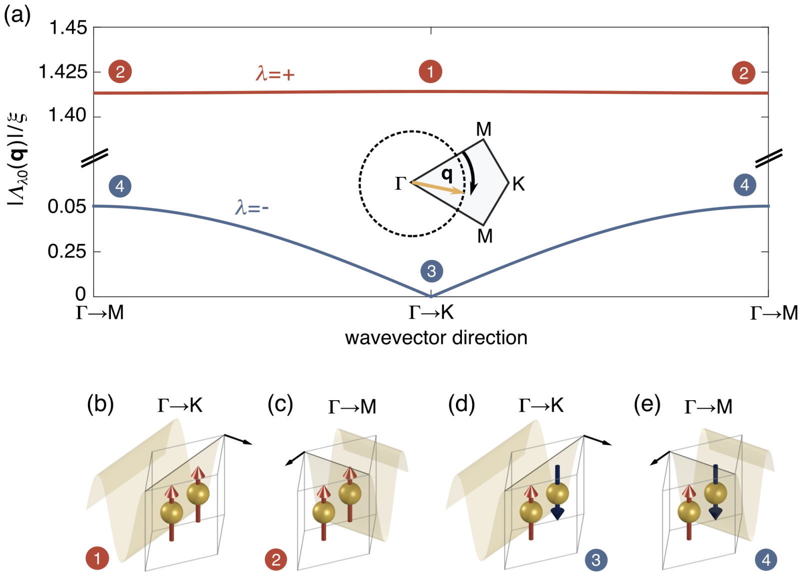

Figure 4.4 | Non-trivial winding in the light-matter interaction. (a) Evolution of the light–matter coupling strength with the upper (red line) and lower (blue line) quasistatic bands as the wavevector direction is swept across the Brillouin zone. (b)–(e) Schematics of the bright (↑↑) and dark (↑↓) dipole configurations interacting with a photonic mode that is indicated by the field profile. Panels (b) and (d) correspond to crossings 1 and 3 along the $\Gamma \to \mathrm{K}$ direction in figure 4.3, respectively, while (c) and (e) correspond to crossings 2 and 4 along the $\Gamma \to \mathrm{M}$ direction, respectively. The light–matter interaction strength for the lower quasistatic band varies significantly and vanishes along the $\Gamma \to \mathrm{K}(\mathrm{K}')$ directions due to the complete destructive interference between the two sublattices. Results obtained with $\lambda_0 = 10a$, $\mu = 0.001\omega_0$ and $|\mathbf{q}| = \mathbf{K}/2$.

which characterizes the strength of the coupling between the TEM photons and the quasistatic dipolar excitations.

In figure 4.4(a) we show how the magnitude of the transformed coupling parameter varies as a function of the wavevector direction for the first photon band ($\mathrm{g} = 0$). For the upper quasistatic band (red line), the magnitude of the coupling parameter is very large and does not vary significantly as the wavevector direction is swept across the Brillouin zone. Intuitively, we can understand this because the quasistatic eigenstates in the upper band correspond to predominantly in-phase dipole configurations (↑↑) as schematically depicted in figures 4.4(b)-(c). These are optically bright configurations which couple strongly to the photons, resulting in a large anticrossing along the $\Gamma - \mathrm{K}(\mathrm{K}')$ and $\Gamma - \mathrm{M}$ lines as observed in figure 4.3(b).

In stark contrast, for the lower quasistatic band (blue line) the transformed coupling parameter is very small and varies significantly as the wavevector direction is swept across the Brillouin zone. This is because the quasistatic eigenstates in the lower band correspond to predominantly out-of-phase dipole configurations (↑↓) as schematically depicted in figures 4.4(d)-(e), which are optically dark and couple weakly to the photons. Consequently, this results in a small anticrossing for a general wavevector direction which is maximum along the $\Gamma - \mathrm{M}$ lines. Note that this anticrossing cannot be easily observed in figure 4.3(b) for the chosen parameters, but it does exist.

Crucially, however, the light-matter interaction for the lower quasistatic band completely vanishes along the $\Gamma - \mathrm{K}(\mathrm{K}')$ lines, due to the complete destructive interference between the out-of-phase sublattices. As a result, along the $\Gamma - \mathrm{K}(\mathrm{K}')$ lines the band crossings are not avoided, leading to six additional Dirac points emerging in the polariton spectrum within the first Brillouin zone. Moreover, one can infer from figure 4.3(b) that these Dirac points belong to the exotic type-II class with a critically tilted Dirac cone that is characterized by open, hyperbolic isofrequency contours – we will see this more explicitly in section 4.5.2.

4.4.3 Evolution of the polariton dispersion

It is important to draw a clear distinction between the two dinstinct species of Dirac points that have emerged in the polariton spectrum. On the one hand, we have the type-I Dirac points which are deterministic since they are enforced by the symmetry of the lattice and their existence is independent of the nature of the dipole-dipole interactions. As a result, the type-I Dirac points will remain pinned at the K/K' points as we vary the cavity width. On the other hand, we have the type-II Dirac points which are accidental since their existence is not guaranteed by the lattice symmetry. The question that naturally arises is: how stable are these type-II Dirac points as we modify the nature of the dipole-dipole interactions via the cavity width?

In figures 4.5(a)-(c) we show the evolution of the polariton dispersion as the cavity width is decreased, while in figures 4.6(a)-(d) we schematically depict the corresponding trajectories of the type-I and type-II Dirac points through the Brillouin zone. For large cavity widths ($L \gg L_v$) where the Coulomb interactions are dominant, the polariton spectrum simultaneously exhibits both type-I and type-II Dirac points which are both characterized by a linear dispersion as shown in figure 4.5(a). As the cavity width is progressively decreased, the type-II Dirac points migrate along the $\Gamma \to \mathrm{K}(\mathrm{K}')$ lines towards the type-I Dirac points as depicted by the red arrows in figure 4.6(a). At a critical cavity width ($L = L_v$), the type-II Dirac points merge together with the type-I Dirac points at the K/K' points as depicted in figure 4.6(b); this merging transition forms a hybrid Dirac point that is characterized by a quadratic dispersion as shown in figure 4.5(b). Just beyond this critical cavity width ($L < L_v$), the type-II Dirac points re-emerge and migrate along the $\mathrm{K}(\mathrm{K}') \to \mathrm{M}$ lines as depicted by the red arrows in figure 4.6(c). This migration continues until they merge

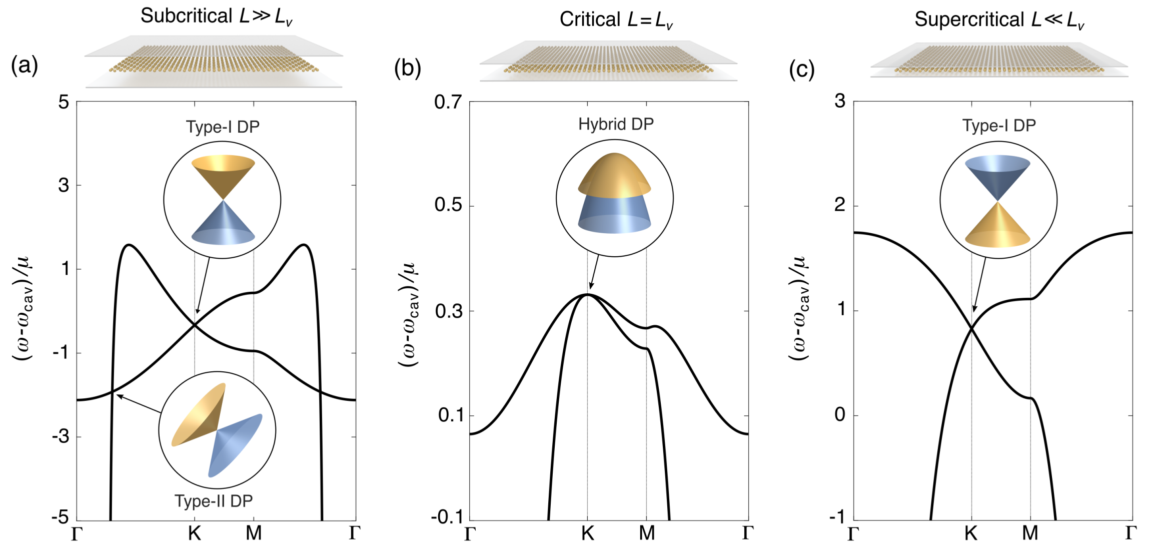

Figure 4.5 | Evolution of the polariton dispersion. (a) Polariton dispersion for the honeycomb metasurface with a subcritical cavity width ($L \gg L_v$), which simultaneously exhibits both type-I and type-II Dirac points that are both characterized by a linear Dirac cone spectrum (see insets). (b) Polariton dispersion for the same metasurface but with the critical cavity width ($L = L_v$), which exhibits hybrid Dirac points that are characterized by a quadratic dispersion (see inset). (c) Polariton dispersion for the same metasurface but with a supercritical cavity width ($L \ll L_v$). Here the type-II Dirac points have vanished from the spectrum leaving only the type-I Dirac points which are characterized by a linear Dirac cone spectrum (see inset). Modifying the cavity width thus gives rise to qualitatively distinct polariton phases. Results obtained with $\lambda_0 = 10a$ and $\mu = 0.001\omega_0$. For panels (a), (b) and (c) we use cavity widths given by $a/L = 0.2$, $a/L = 0.864262$ and $a/L = 2$, respectively.

together and annihilate each other at the M points. For small cavity widths ($L \ll L_v$) where the photon-mediated interactions are dominant, only the type-I Dirac points remain in the polariton spectrum as depicted in figure 4.6(d) which are characterized by a linear dispersion as shown in figure 4.5(c).

4.5 Effective polariton Hamiltonian

To gain some analytical insight into these qualitatively distinct polariton phases, in this section we derive a minimal effective Hamiltonian that describes the polaritons near the K/K' points. In what follows we focus on the K point since the equivalent physics near the K' point can be deduced from $\mathcal{T}$ symmetry.

In order to capture the essential physics for all cavity widths, it is evident from figure 4.5(b) that we must include terms up to quadratic order in $\mathbf{k} = \mathbf{q} - \mathbf{K}$. The intrasublattice matrix

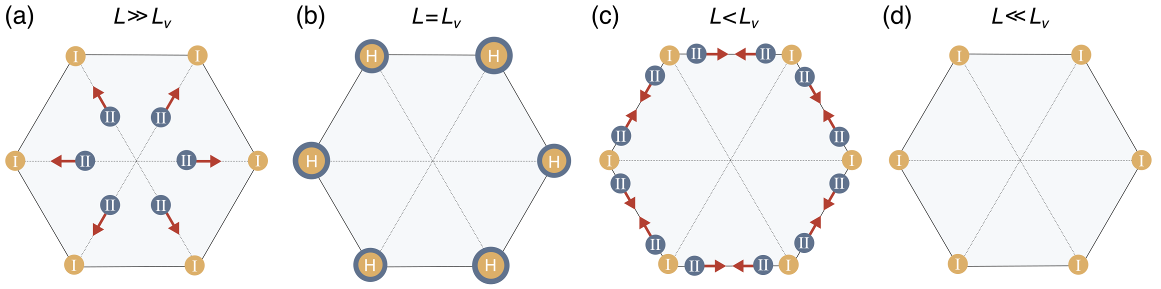

Figure 4.6 | Trajectories of the type-I and type-II Dirac points. (a)-(d) Schematic depiction of how the location of the type-I (yellow circles) and type-II (blue circles) Dirac points evolve throughout the Brillouin zone as the cavity width is reduced. (a) For subcritical cavity widths ($L \gg L_v$), the type-II Dirac points migrate along the $\Gamma \to \mathrm{K}(\mathrm{K}')$ lines as depicted by the red arrows, while the type-I Dirac points remain pinned at the high-symmetry K/K' points. (b) At the critical cavity width ($L = L_v$), the type-II Dirac points merge together with the type-I Dirac points at the K/K' points forming hybrid Dirac points. (c) Just beyond the critical width ($L < L_v$), the type-II Dirac points re-emerge and migrate along the $\mathrm{K}(\mathrm{K}') \to \mathrm{M}$ lines as depicted by the red arrows. This migration continues until they eventually merge together and annihilate one another at the M points. (d) For supercritical cavity widths ($L \ll L_v$), only the type-I Dirac points remain in the polariton spectrum.

elements of the full dynamical matrix expand as (see appendix C.1 for details)

$$\mathcal{D}_{+}^{\mathrm{AA}}(\mathbf{k}) \simeq \sum_{\mathbf{R}\neq 0} G_{\parallel}(\mathbf{R})\mathrm{e}^{-\mathrm{i}\mathbf{K}\cdot\mathbf{R}} + \sum_{\mathbf{g}} \frac{\omega^2\xi^2}{\omega_{\mathbf{K}-\mathbf{g}}^2 - \omega^2} - \mathrm{Re}[G_{\perp}^{\mathrm{TEM}}(0,\omega)]$$
$$-\frac{1}{2}\left\{\sum_{\mathbf{R}\neq 0} G_{\parallel}(\mathbf{R})\mathrm{e}^{-\mathrm{i}\mathbf{K}\cdot\mathbf{R}}(\mathbf{R})_x^2 + \sum_{\mathbf{g}}\left[\frac{2c^2\omega^2\xi^2}{(\omega_{\mathbf{K}-\mathbf{g}}^2 - \omega^2)^2} - \frac{8\omega^2\xi^2c^4(\mathbf{K}-\mathbf{g})_x^2}{(\omega_{\mathbf{K}-\mathbf{g}}^2 - \omega^2)^3}\right]\right\}(k_x^2 + k_y^2)\,, \tag{4.37}$$

while the intersublattice matrix elements expand as (see appendix C.1 for details)

$$\mathcal{D}_{+}^{\mathrm{AB}}(\mathbf{k}) \simeq -\left\{\mathrm{i}\sum_{\mathbf{R}} G_{\parallel}(\mathbf{R}-\mathbf{d})\mathrm{e}^{-\mathrm{i}\mathbf{K}\cdot(\mathbf{R}-\mathbf{d})}(\mathbf{R}-\mathbf{d})_x + \sum_{\mathbf{g}} \frac{2\omega^2\xi^2c^2(\mathbf{K}-\mathbf{g})_x\phi_{\mathbf{g}}}{(\omega_{\mathbf{K}-\mathbf{g}}^2 - \omega^2)^2}\right\}(k_x - \mathrm{i}k_y)$$
$$-\frac{1}{2}\left\{\sum_{\mathbf{R}\neq 0} G_{\parallel}(\mathbf{R}-\mathbf{d})\mathrm{e}^{-\mathrm{i}\mathbf{K}\cdot\mathbf{R}}(\mathbf{R}-\mathbf{d})_x^2 - \sum_{\mathbf{g}} \frac{8\omega^2\xi^2c^4(\mathbf{K}-\mathbf{g})_x^2\phi_{\mathbf{g}}}{(\omega_{\mathbf{K}-\mathbf{g}}^2 - \omega^2)^3}\right\}(k_x^2 - k_y^2 + 2\mathrm{i}k_xk_y)\,. \tag{4.38}$$

Next we evaluate the polarizability correction and the transverse dynamical matrix at the cavity resonant frequency and we approximate $\omega_{\mathrm{cav}}^2 - \omega^2 \simeq 2\omega_{\mathrm{cav}}(\omega_{\mathrm{cav}} - \omega)$. This allows us to write a simplified eigenvalue equation near the K/K' points ($\hbar = 1$)

$$\omega\,|\psi_\tau(\mathbf{k})\rangle = \mathcal{H}_\tau(\mathbf{k})\,|\psi_\tau(\mathbf{k})\rangle\ , \tag{4.39}$$

where the effective Hamiltonian near the K point is given by

$$\mathcal{H}_{+}(\mathbf{k}) = \omega_{\mathrm{D}}(L)\mathbb{1}_2 - v_{\mathrm{D}}(L)\boldsymbol{\sigma}\cdot\mathbf{k} + t(L)(\boldsymbol{\sigma}^{*}\cdot\mathbf{k})^{\circ 2} + D(L)|\mathbf{k}|^2\mathbb{1}_2\,, \tag{4.40}$$

and the corresponding Hamiltonian near the K' point is related via $\mathcal{T}$ symmetry $\mathcal{H}_{-}(\mathbf{k}) = \mathcal{H}_{+}^{*}(-\mathbf{k})$. Note, in equation (4.40) the symbol $^{\circ 2}$ represents the Hadamard (element-wise) square of the matrix.

As expected from the symmetry analysis in section 2.2.6, the form of the effective Hamiltonian in equation (4.40) coincides precisely with the general Hamiltonian in equation (2.74). However, the Hamiltonian parameters depend sensitively on the nature of the dipole-dipole interactions. Specifically, the Dirac frequency in equation (4.40) reads

$$\begin{aligned}\omega_{\mathrm{D}}(L) = \omega_{\mathrm{cav}} - \mu\frac{\omega_0}{\omega_{\mathrm{cav}}}\sum_{\mathbf{R}\neq 0} G_{\parallel}(\mathbf{R})\mathrm{e}^{-\mathrm{i}\mathbf{K}\cdot\mathbf{R}} + \mu\frac{\omega_0}{\omega_{\mathrm{cav}}}\,\mathrm{Re}[\check{G}_{\perp}^{\mathrm{TEM}}(0,\omega_{\mathrm{cav}})] \\ -\mu\frac{\omega_0}{\omega_{\mathrm{cav}}}\sum_{\mathbf{g}}\frac{\omega_{\mathrm{cav}}^2\xi^2\mathrm{e}^{-\eta^2|\mathbf{K}-\mathbf{g}|^2}}{\omega_{\mathbf{K}-\mathbf{g}}^2-\omega_{\mathrm{cav}}^2}\,,\end{aligned} \tag{4.41}$$

and the Dirac velocity is given by

$$v_{\mathrm{D}}(L) = -\mathrm{i}\mu\frac{\omega_0}{\omega_{\mathrm{cav}}}\sum_{\mathbf{R}} G_{\parallel}(\mathbf{R}-\mathbf{d})\mathrm{e}^{-\mathrm{i}\mathbf{K}\cdot(\mathbf{R}-\mathbf{d})}(\mathbf{R}-\mathbf{d})_x - \mu\frac{\omega_0}{\omega_{\mathrm{cav}}}\sum_{\mathbf{g}}\frac{2\omega_{\mathrm{cav}}^2\xi^2c^2(\mathbf{K}-\mathbf{g})_x\phi_{\mathbf{g}}}{(\omega_{\mathbf{K}-\mathbf{g}}^2-\omega_{\mathrm{cav}}^2)^2}\,. \tag{4.42}$$

Note, we have used the regularization procedure outlined in section 3.4.6 in order to evaluate the difference between the last two divergent terms in equation (4.41). Furthermore, the trigonal warping parameter in equation (4.40) reads

$$t(L) = \frac{\mu}{2}\frac{\omega_0}{\omega_{\mathrm{cav}}}\sum_{\mathbf{R}} G_{\parallel}(\mathbf{R}-\mathbf{d})\mathrm{e}^{-\mathrm{i}\mathbf{K}\cdot(\mathbf{R}-\mathbf{d})}(\mathbf{R}-\mathbf{d})_x^2 - \mu\frac{\omega_0}{\omega_{\mathrm{cav}}}\sum_{\mathbf{g}}\frac{4\omega_{\mathrm{cav}}^2\xi^2c^4(\mathbf{K}-\mathbf{g})_x^2\phi_{\mathbf{g}}}{(\omega_{\mathbf{K}-\mathbf{g}}^2-\omega_{\mathrm{cav}}^2)^3}\,, \tag{4.43}$$

and the band asymmetry parameter is given by

$$\begin{aligned}D(L) = \frac{\mu}{2}\frac{\omega_0}{\omega_{\mathrm{cav}}}\sum_{\mathbf{R}\neq 0} G_{\parallel}(\mathbf{R})\mathrm{e}^{-\mathrm{i}\mathbf{K}\cdot\mathbf{R}}(\mathbf{R})_x^2 \\ +\mu\frac{\omega_0}{\omega_{\mathrm{cav}}}\sum_{\mathbf{g}}\left[\frac{\omega_{\mathrm{cav}}^2\xi^2}{(\omega_{\mathbf{K}-\mathbf{g}}^2-\omega_{\mathrm{cav}}^2)^2} - \frac{4\omega_{\mathrm{cav}}^2\xi^2c^4(\mathbf{K}-\mathbf{g})_x^2}{(\omega_{\mathbf{K}-\mathbf{g}}^2-\omega_{\mathrm{cav}}^2)^3}\right].\end{aligned} \tag{4.44}$$

In figures 4.7(a)-(d) we show how these effective Hamiltonian parameters evolve as the cavity width is reduced (solid black lines), and we also show the separate contributions from the Coulomb interactions (blue dotted lines) and the photon-mediated interactions (orange

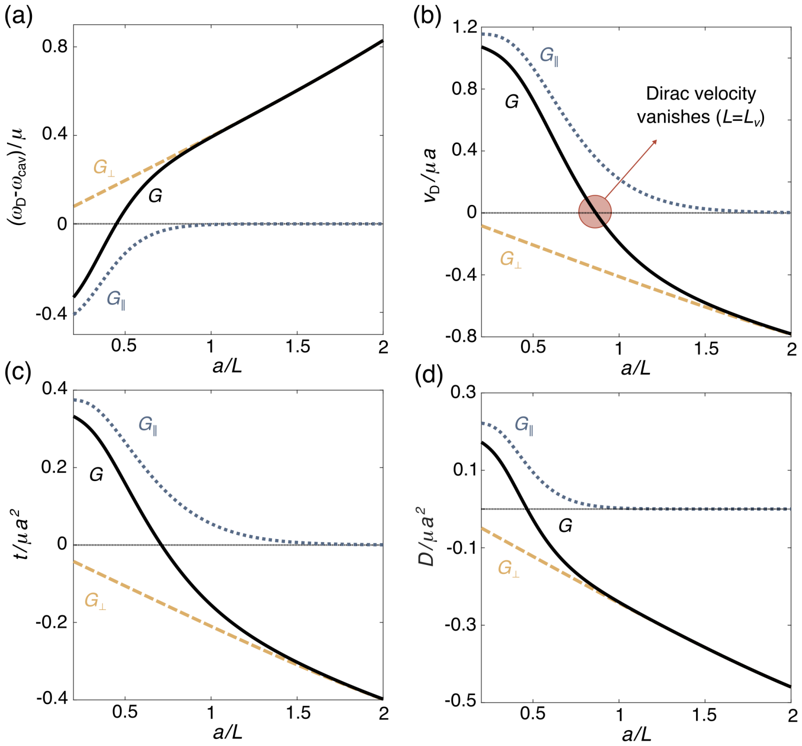

Figure 4.7 | Effective Hamiltonian parameters at the K/K′ points. (a)-(d) Evolution of the effective Hamiltonian parameters at the K/K′ points as the cavity width is reduced (solid black lines). We also show the separate contributions from the Coulomb interactions (blue dotted lines) and the photon-mediated interactions (orange dashed lines). Crucially, there exists a critical cavity width L_v where the Dirac velocity vanishes $v_\mathrm{D}(L_v) = 0$, as highlighted in panel (b), which coincides with the multi-merging of the type-I and type-II Dirac points. Furthermore, the Dirac velocity changes sign through this transition which inverts the chirality of the massless Dirac polaritons. Results obtained with $\lambda_0 = 10a$ and $\mu = 0.001\omega_0$.

dashed lines). Of particular importance is the Dirac velocity that is shown in figure 4.7(b). Crucially, one observes that the two distinct interactions contribute with opposite signs and thus tend to compensate each other. Moreover, for large cavity widths the contribution from the Coulomb interactions is dominant, while for small cavity widths the contribution from the photon-mediated interactions is dominant. Consequently, there exists a critical crossover regime where these contributions perfectly cancel, making the Dirac velocity vanish identically at the critical cavity width $v_\mathrm{D}(L_v) = 0$.

4.5.1 Type-I massless Dirac polaritons

Let us first focus on the regime of subcritical cavity widths ($L \gg L_v$) where the Coulomb interactions are dominant. One can see from figures 4.7(b)-(d) that $|v_\mathrm{D}| > |t|/a$ and $|v_\mathrm{D}| > |D|/a$ for this regime. Consequently, one can safely neglect the quadratic terms in equation (4.40) and the effective Hamiltonian reads

$$\mathcal{H}_+(\mathbf{k}) = \omega_\mathrm{D}(L)\mathbb{1}_2 - v_\mathrm{D}(L)\boldsymbol{\sigma}\cdot\mathbf{k}\,, \tag{4.45}$$

which is equivalent to a 2D massless Dirac Hamiltonian. The corresponding spectrum of the polaritons is an isotropic linear Dirac cone dispersion

$$\omega_\lambda(\mathbf{k}) = \omega_\mathrm{D} + \lambda|v_\mathrm{D}||\mathbf{k}|\,, \tag{4.46}$$

which is characterized by closed, circular isofrequency contours. Therefore, the deterministic Dirac points remain in the type-I class when the light-matter interaction is switched on; this is not surprising given the constraints imposed by the symmetries.

Since $v_\mathrm{D} > 0$ in the subcritical regime, the spinor eigenstates read

$$|\psi_{+\lambda}(\mathbf{k})\rangle = \frac{1}{\sqrt{2}}\begin{bmatrix} 1 \\ -\lambda e^{i\phi_\mathbf{k}} \end{bmatrix}\,, \tag{4.47}$$

where $\phi_\mathbf{k} = \arctan(k_y/k_x)$, and the corresponding pseudo-spin vector is

$$\mathbf{S}_{+\lambda}(\mathbf{k}) = \langle\psi_{+\lambda}(\mathbf{k})|\,\boldsymbol{\sigma}\,|\psi_{+\lambda}(\mathbf{k})\rangle = -\lambda\,[\cos\phi_\mathbf{k}\,,\,\sin\phi_\mathbf{k}\,,\,0]\;. \tag{4.48}$$

These represent type-I massless Dirac polaritons which are simultaneous eigenstates of the chirality operator

$$\boldsymbol{\sigma}\cdot\hat{\mathbf{k}}\,|\psi_{+\lambda}(\mathbf{k})\rangle = -\lambda\,|\psi_{+\lambda}(\mathbf{k})\rangle\;. \tag{4.49}$$

This shows that the pseudo-spin is locked antiparallel/parallel to the momentum in the upper/lower bands, respectively, giving rise to a topological winding number of $+1$. Therefore, within this subcritical regime of cavity widths, the photon-mediated interactions do not qualitatively affect the nature of the type-I massless Dirac polaritons at the K/K' points, they simply renormalize the Dirac frequency and Dirac velocity.

4.5.2 Type-II massless Dirac Polaritons

In stark contrast, the type-II Dirac points only exist due to the hybridization with the cavity photons. Unfortunately, since these accidental Dirac points emerge at an arbitrary point along the $\Gamma \to \mathrm{K}(\mathrm{K}')$ lines in the Brillouin zone, it is impossible to gain analytical insight by directly expanding the dynamical matrix. However, we can gain some qualitative insight by using the effective Hamiltonian in equation (4.40) which also captures the accidental Dirac points when $t < 0$, and it becomes increasingly accurate within the vicinity of the critical cavity width.

The band degeneracies in the effective polariton dispersion near the K point occur when the intersublattice matrix elements in equation (4.40) vanish

$$-v_{\mathrm{D}}(k_x + \mathrm{i}k_y) + t(k_x - \mathrm{i}k_y)^2 = 0\,. \tag{4.50}$$

Apart from the trivial solution that corresponds to the deterministic type-I Dirac point ($\mathbf{k} = 0$), equation (4.50) also has three non-trivial solutions that are given by

$$\mathbf{k}_{\mathrm{II}}^{n} = -\operatorname{sgn}(v_{\mathrm{D}}) \left|\frac{v_{\mathrm{D}}}{t}\right| \left[\cos\left(\frac{2\pi n}{3}\right), \sin\left(\frac{2\pi n}{3}\right)\right], \qquad n = 0, 1, 2\ . \tag{4.51}$$

These are located along the $\Gamma \to \mathrm{K}(\mathrm{K}')$ lines in the subcritical regime since $v_{\mathrm{D}} > 0$, and they are distributed in such a way that is consistent with the $\mathcal{C}_3$ symmetry. If we focus on the accidental Dirac point corresponding to $n = 0$, we can expand the effective Hamiltonian in equation (4.40) to leading order in $\mathbf{k}' = \mathbf{k} - \mathbf{k}_{\mathrm{II}}^{0}$. The resulting effective Hamiltonian reads

$$\mathcal{H}_{\mathbf{k}_{\mathrm{II}}}(\mathbf{k}') = \left(\omega_{\mathrm{D}} + \frac{Dv_{\mathrm{D}}^2}{t^2} + \frac{2Dv_{\mathrm{D}}}{t}k_x'\right)\mathbb{1}_2 + \boldsymbol{\sigma}^* \cdot \boldsymbol{v} \cdot \mathbf{k}', \quad \boldsymbol{v} = \begin{bmatrix} v_{\mathrm{D}} & 0 \\ 0 & 3v_{\mathrm{D}} \end{bmatrix}, \tag{4.52}$$

which takes the form of a generalized 2D massless Dirac Hamiltonian with an anisotropic Dirac cone dispersion

$$\omega_{\lambda}(\mathbf{k}') = \omega_{\mathrm{D}} + \frac{Dv_{\mathrm{D}}^2}{t^2} + \frac{2Dv_{\mathrm{D}}}{t}k_x' + \lambda\sqrt{v_{\mathrm{D}}^2 k_x^2 + 9v_{\mathrm{D}}^2 k_y^2}\,, \tag{4.53}$$

whose axis is tilted towards the Γ point. More specifically, since the condition $2|D|/|t| > 1$ is satisfied for the regime of cavity widths that we are interested in, the corresponding Dirac cone is critically tilted such that the isofrequency contours are hyperbolic and not circular; this confirms that the accidental Dirac points do indeed belong to the type-II class, as we inferred directly from the polariton dispersion in figure 4.5(a). Furthermore, since the type-II Dirac Hamiltonian in equation (4.52) is expressed in terms of $\boldsymbol{\sigma}^*$, as opposed to $\boldsymbol{\sigma}$, the corresponding vortex in pseudo-spin field must carry a topological charge of -1, which is opposite to the type-I Dirac point.

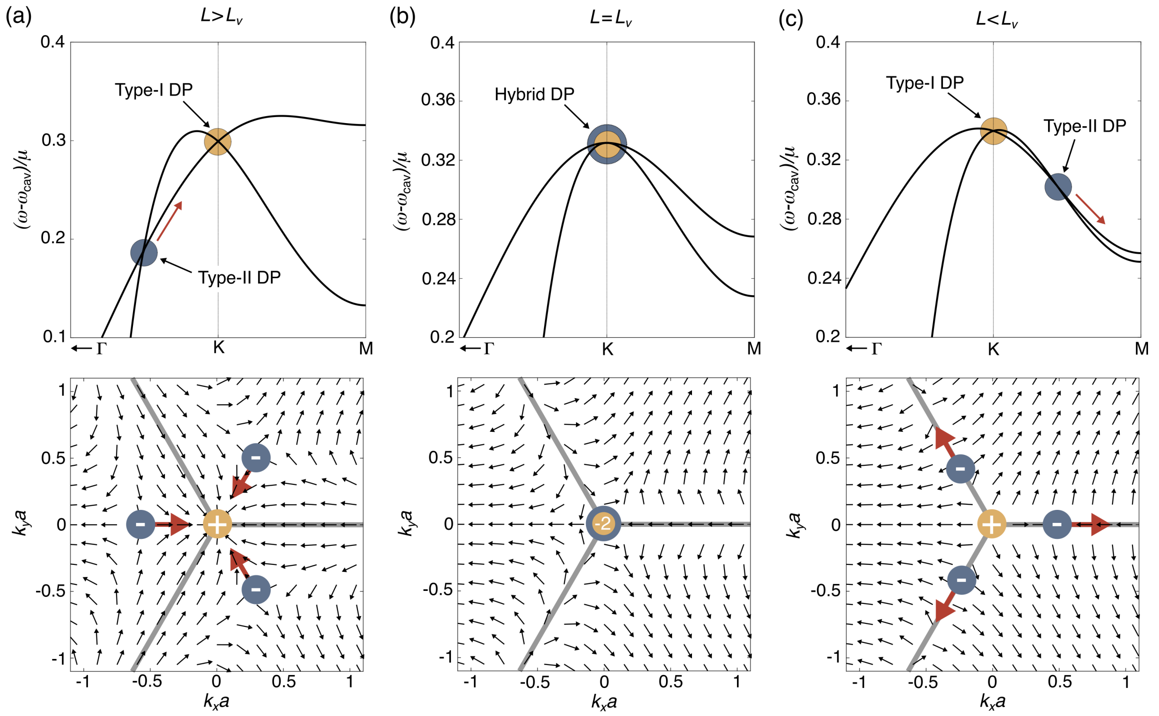

Figure 4.8 | Cavity-induced multi-merging of the type-I and type-II Dirac points. (a)-(c) Evolution of the polariton dispersion (top panels) and pseudo-spin field for the upper band (bottom panels) near the K point within the vicinity of the critical cavity width L_v. (a) For subcritical widths ($L > L_v$), three satellite vortices with a topological charge of -1 can be observed along the $\Gamma \to \mathrm{K}$ lines, which correspond to the accidental type-II Dirac points (blue circles). These surround a central vortex at the K point with a topological charge of +1, which corresponds to the deterministic type-I Dirac point (yellow circle). (b) At the critical cavity width ($L = L_v$), the three type-II Dirac points merge with the type-I Dirac point at the K point, which forms a hybrid Dirac point with a topological charge of -2. (c) As the cavity width is decreased further ($L < L_v$), the three type-II Dirac points re-emerge and migrate along the $\mathrm{K} \to \mathrm{M}$ lines, while the type-I Dirac point remains pinned at the K point. Results obtained with $\lambda_0 = 10a$ and $\mu = 0.001\omega_0$. For panels (a), (b) and (c) we use cavity widths given by $a/L = 0.8$, $a/L = 0.864262$ and $a/L = 0.881$, respectively.

4.5.3 Multi-merging of the type-I and type-II Dirac points

We will now proceed to analyze the first interesting transition that occurs in the polariton spectrum as the cavity width is reduced: the multi-merging of the type-I and type-II Dirac points. The essential physics related to this transition is captured by the effective Hamiltonian in equation (4.40). In figure 4.8(a) we plot the full polariton dispersion near the K point given by equation (4.30) for a cavity width just larger than the critical width ($L > L_v$), and we also show the corresponding pseudo-spin field for the upper band using equation (4.32). In this regime of cavity widths, one observes three vortices in the pseudo-spin field located along the $\Gamma \to \mathrm{K}$ lines with a topological charge of -1, and these directly correspond to the accidental type-II Dirac points. These satellite vortices surround a central vortex located at the K point which has a topological charge of $+1$, and this corresponds to the deterministic type-I Dirac point.

As the cavity width is reduced, the three type-II Dirac points migrate along the $\Gamma \to \mathrm{K}$ lines as depicted by the red arrows in figure 4.8(a), until the critical width ($L = L_v$) where they merge together with the central type-I Dirac point. Since the topological charge must be conserved through the transition, this multi-merging results in a hybrid Dirac point that is characterized by a higher order topological charge of -2 as observed in figure 4.8(b).

We note that this merging coincides with the vanishing of the Dirac velocity as highlighted in figure 4.7(b). Therefore, the effective Hamiltonian describing the polaritons at this critical width reads

$$\mathcal{H}_+(\mathbf{k}) = \omega_\mathrm{D}(L_v)\mathbb{1}_2 + t(L_v)(\boldsymbol{\sigma}^* \cdot \mathbf{k})^{\circ 2} + D(L_v)|\mathbf{k}|^2\mathbb{1}_2 \,, \tag{4.54}$$

which is a generalized chiral Hamiltonian that has several qualitatively different properties to the massless Dirac Hamiltonian in equation (4.45). First, we note that the chiral polaritons are no longer massless since the dispersion is purely quadratic at the critical cavity width

$$\omega_\lambda(\mathbf{k}) = \omega_\mathrm{D} + (D + \lambda|t|)|\mathbf{k}|^2 \,, \tag{4.55}$$

as observed in figure 4.8(b). Moreover, the upper/lower band symmetry about the Dirac frequency is strongly broken ($|D| > |t|$) such that both of the bands have a negative effective mass. Furthermore, the corresponding eigenstates of equation (4.54) read

$$|\psi_{+\lambda}(\mathbf{k})\rangle = \frac{1}{\sqrt{2}} \begin{bmatrix} 1 \\ -\lambda \mathrm{e}^{-\mathrm{i}2\phi_\mathbf{k}} \end{bmatrix} , \tag{4.56}$$

which are simultaneous eigenstates of a more generalized chirality operator

$$(\boldsymbol{\sigma}^* \cdot \hat{\mathbf{k}})^{\circ 2} \, |\psi_{+\lambda}(\mathbf{k})\rangle = -\lambda \, |\psi_{+\lambda}(\mathbf{k})\rangle \ . \tag{4.57}$$

Consequently, the pseudo-spin vector

$$\mathbf{S}_{+\lambda}(\mathbf{k}) = -\lambda \, [\, \cos(-2\phi_\mathbf{k}) \, , \, \sin(-2\phi_\mathbf{k}) \, , \, 0 \,] \ , \tag{4.58}$$

winds twice in the anticlockwise direction as one traverses a clockwise loop around the hybrid Dirac point as can be seen in figure 4.8(b).

This scenario bears some resemblance with bilayer graphene whose low-energy quasiparticles also exhibit a predominantly quadratic spectrum and a topological winding number of ± 2. This doubling of the winding number in bilayer graphene results in markedly different properties compared to graphene as we discussed in section 2.2.6. Therefore, one would expect the polaritons in this critical regime to exhibit qualitatively different properties compared to the subcritical regime.

However, this hybrid Dirac point in the polariton spectrum is not stable as it is not protected by any symmetry; it has emerged from the perfect cancellation of the Coulomb and photon-mediated contributions to the Dirac velocity. Therefore, it is interesting to explore what happens when we reduce the cavity width further. Since the topological charge must be preserved through the transition, there are several theoretical possibilities. For example, in principle the hybrid Dirac point could split into two Dirac points each with a topological charge of -1, although such a scenario would clearly require one to break the $\mathcal{C}_3$ symmetry of the lattice. Since modifying the cavity width preserves the $\mathcal{C}_3$ symmetry, the hybrid Dirac point splits into four Dirac points; the type-I Dirac point remains pinned at the K point with a topological charge of $+1$, while the three type-II Dirac points re-emerge with a topological charge of -1 and migrate along the $\mathrm{K} \to \mathrm{M}$ lines as depicted by the red arrows in figure 4.8(c).

4.5.4 Annihilation of the type-II accidental Dirac points

Next we explore another peculiar, but entirely distinct transition that occurs in the polariton spectrum as the cavity width is reduced further: the merging and subsequent annihilation of the type-II Dirac points. Unfortunately, the effective Hamiltonian near the K point given by equation (4.40) cannot capture this transition as it also involves the type-II Dirac points that emerge from the K' point. Therefore, to gain some analytical insight, we must derive an effective Hamiltonian near one of the M points which we choose to be located at $\mathbf{M} = [\,2\pi/\sqrt{3}\,,\,0\,]$ for convenience.

Following the same expansion method that we outlined in section 4.5 we obtain the following effective Hamiltonian near the M point (see appendix C.2 for details)

$$\mathcal{H}_{\mathrm{M}}(\mathbf{k}) = \omega_{\mathrm{M}}(L)\mathbb{1}_2 + [t_{\mathrm{M}}(L)k_x^2 - \varDelta_{\mathrm{M}}(L)]\sigma_x - v_{\mathrm{M}}(L)k_y\sigma_y - D_{\mathrm{M}}(L)k_x^2\mathbb{1}_2\,, \tag{4.59}$$

where we have retained only the leading order terms in $\mathbf{k} = \mathbf{q} - \mathbf{M}$, and the corresponding polariton spectrum reads

$$\omega_\lambda(\mathbf{k}) = \omega_{\mathrm{M}}(L) - D_{\mathrm{M}}(L)k_x^2 + \lambda\sqrt{[t_{\mathrm{M}}(L)k_x^2 - \varDelta_{\mathrm{M}}(L)]^2 + v_{\mathrm{M}}^2(L)k_y^2}\,. \tag{4.60}$$

Note that equation (4.59) is consistent with the general form of the Hamiltonian that we derived through symmetry analysis in appendix A.2.

In equation (4.59), the zeroth order diagonal term reads

$$\begin{aligned}\omega_{\mathrm{M}}(L) = \omega_{\mathrm{cav}} - \mu\frac{\omega_0}{\omega_{\mathrm{cav}}}\sum_{\mathbf{R}\neq 0} G_{\parallel}(\mathbf{R})\mathrm{e}^{-\mathrm{i}\mathbf{M}\cdot\mathbf{R}} + \mu\frac{\omega_0}{\omega_{\mathrm{cav}}}\,\mathrm{Re}[\check{G}_{\perp}^{\mathrm{TEM}}(0,\omega_{\mathrm{cav}})] \\ - \mu\frac{\omega_0}{\omega_{\mathrm{cav}}}\sum_{\mathbf{g}}\frac{\omega_{\mathrm{cav}}^2\xi^2\mathrm{e}^{-\eta^2|\mathbf{M}-\mathbf{g}|^2}}{\omega_{\mathbf{M}-\mathbf{g}}^2-\omega_{\mathrm{cav}}^2}\,,\end{aligned} \tag{4.61}$$

and the zeroth order σ_x term is given by

$$\mathit{\Delta}_{\mathrm{M}}(L) = \mu\frac{\omega_0}{\omega_{\mathrm{cav}}}\sum_{\mathbf{R}\neq 0} G_{\parallel}(\mathbf{R}-\mathbf{d})\mathrm{e}^{-\mathrm{i}\mathbf{M}\cdot(\mathbf{R}-\mathbf{d})} + \mu\frac{\omega_0}{\omega_{\mathrm{cav}}}\sum_{\mathbf{g}}\frac{\omega_{\mathrm{cav}}^2\xi^2\phi_{\mathbf{g}}}{\omega_{\mathbf{M}-\mathbf{g}}^2-\omega_{\mathrm{cav}}^2}\,. \tag{4.62}$$

As before, we have used the regularization procedure outlined in section 3.4.6 in order to evaluate the difference between the last two divergent terms in equation (4.61). Moreover, the coefficient of the linear σ_y term reads

$$v_{\mathrm{M}}(L) = \mu\frac{\omega_0}{\omega_{\mathrm{cav}}}\sum_{\mathbf{R}} G_{\parallel}(\mathbf{R}-\mathbf{d})\mathrm{e}^{-\mathrm{i}\mathbf{M}\cdot(\mathbf{R}-\mathbf{d})}(\mathbf{R}-\mathbf{d})_y - \mathrm{i}\mu\frac{\omega_0}{\omega_{\mathrm{cav}}}\sum_{\mathbf{g}}\frac{2\omega_{\mathrm{cav}}^2\xi^2c^2(\mathbf{M}-\mathbf{g})_y\phi_{\mathbf{g}}}{(\omega_{\mathbf{M}-\mathbf{g}}^2-\omega_{\mathrm{cav}}^2)^2}\,, \tag{4.63}$$

the coefficient of the quadratic diagonal term is given by

$$\begin{aligned}D_{\mathrm{M}}(L) = {} & -\frac{\mu}{2}\frac{\omega_0}{\omega_{\mathrm{cav}}}\sum_{\mathbf{R}\neq 0} G_{\parallel}(\mathbf{R})\mathrm{e}^{-\mathrm{i}\mathbf{M}\cdot\mathbf{R}}(\mathbf{R})_x^2 \\ & -\mu\frac{\omega_0}{\omega_{\mathrm{cav}}}\sum_{\mathbf{g}}\left[\frac{\omega_{\mathrm{cav}}^2\xi^2}{(\omega_{\mathbf{M}-\mathbf{g}}^2-\omega_{\mathrm{cav}}^2)^2} - \frac{4\omega_{\mathrm{cav}}^2\xi^2c^4(\mathbf{M}-\mathbf{g})_x^2}{(\omega_{\mathbf{M}-\mathbf{g}}^2-\omega_{\mathrm{cav}}^2)^3}\right],\end{aligned} \tag{4.64}$$

and the coefficient of the quadratic σ_x term reads

$$\begin{aligned}t_{\mathrm{M}}(L) = {} & \frac{\mu}{2}\frac{\omega_0}{\omega_{\mathrm{cav}}}\sum_{\mathbf{R}\neq 0} G_{\parallel}(\mathbf{R}-\mathbf{d})\mathrm{e}^{-\mathrm{i}\mathbf{M}\cdot(\mathbf{R}-\mathbf{d})}(\mathbf{R}-\mathbf{d})_x^2 \\ & +\mu\frac{\omega_0}{\omega_{\mathrm{cav}}}\sum_{\mathbf{g}}\left[\frac{\omega_{\mathrm{cav}}^2\xi^2\phi_{\mathbf{g}}}{(\omega_{\mathbf{M}-\mathbf{g}}^2-\omega_{\mathrm{cav}}^2)^2} - \frac{4\omega_{\mathrm{cav}}^2\xi^2c^4(\mathbf{M}-\mathbf{g})_x^2\phi_{\mathbf{g}}}{(\omega_{\mathbf{M}-\mathbf{g}}^2-\omega_{\mathrm{cav}}^2)^3}\right].\end{aligned} \tag{4.65}$$

In figures 4.9(a)-(d) we show the evolution of these effective Hamiltonian parameters as the cavity width is reduced (black solid lines), and we also show the separate contributions from the Coulomb interactions (blue dotted lines) and the photon-mediated interactions (orange dashed lines). Of particular importance is the parameter $\mathit{\Delta}_{\mathrm{M}}$ shown in figure 4.9(a),

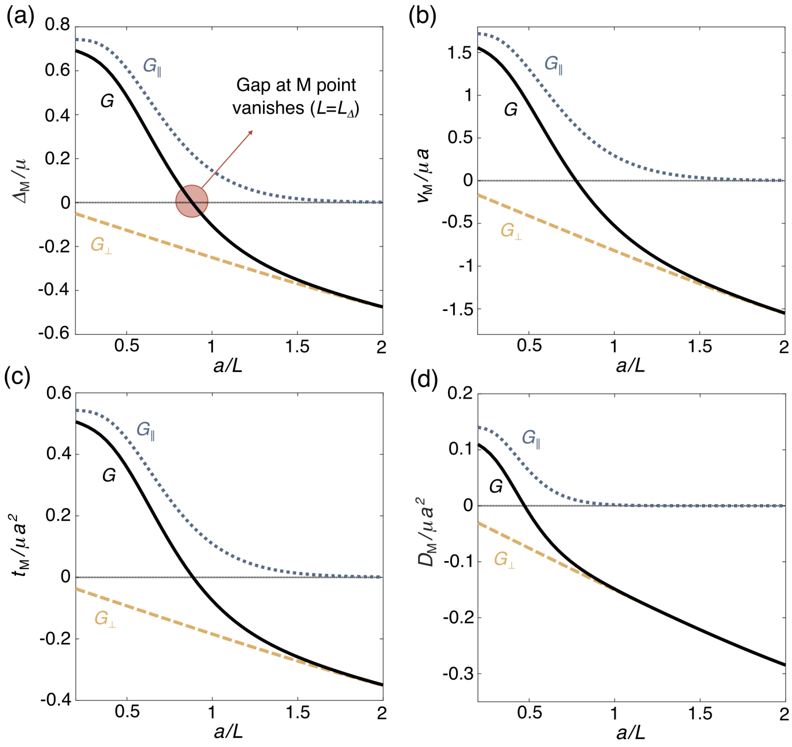

Figure 4.9 | Effective Hamiltonian parameters at the M point. (a)-(d) Evolution of the effective Hamiltonian parameters at the M point as the cavity width is reduced (solid black lines). We also show the separate contributions from the Coulomb interactions (blue dotted lines) and the photon-mediated interactions (orange dashed lines). Crucially, there exists a critical cavity width L_Δ where the gap parameter vanishes $\Delta_\mathrm{M}(L_\Delta) = 0$, as highlighted in panel (a), which coincides with the merging of the type-II Dirac points at the M point. Results obtained with $\lambda_0 = 10a$ and $\mu = 0.001\omega_0$.

since it dictates the size of the gap between the polariton bands at the M point. We observe that the Coulomb and photon-mediated interactions contribute to the gap parameter with opposite signs and thus tend to compensate each other. Therefore, there exists a critical cavity width L_Δ where these contributions perfectly cancel and the gap at the M point vanishes $\Delta_\mathrm{M}(L_\Delta) = 0$ as highlighted in figure 4.9(a).

For cavity widths just beyond the critical width where the multi-merging transition occurs ($L_\Delta < L < L_v$), both of the parameters in the σ_x term are positive $t_\mathrm{M}, \Delta_\mathrm{M} > 0$. Therefore, one can conclude from equation (4.60) that there exists two band degeneracies located at positions $\mathbf{k}_\pm = \pm[\sqrt{\Delta_\mathrm{M}/t_\mathrm{M}}, 0]$ along the $\mathrm{K}(\mathrm{K}') \to \mathrm{M}$ lines. To see this explicitly, in figure 4.10(a) we plot the full polariton dispersion given by equation (4.30) for a cavity width in this regime, and we also show the corresponding pseudo-spin field for the upper band using equation (4.32). One can observe that these band degeneracies directly correspond to the type-II Dirac points that emerge from the K/K' points after the multi-merging transition. Furthermore, one can also observe from the vortices in the pseudo-spin field, that the type-II

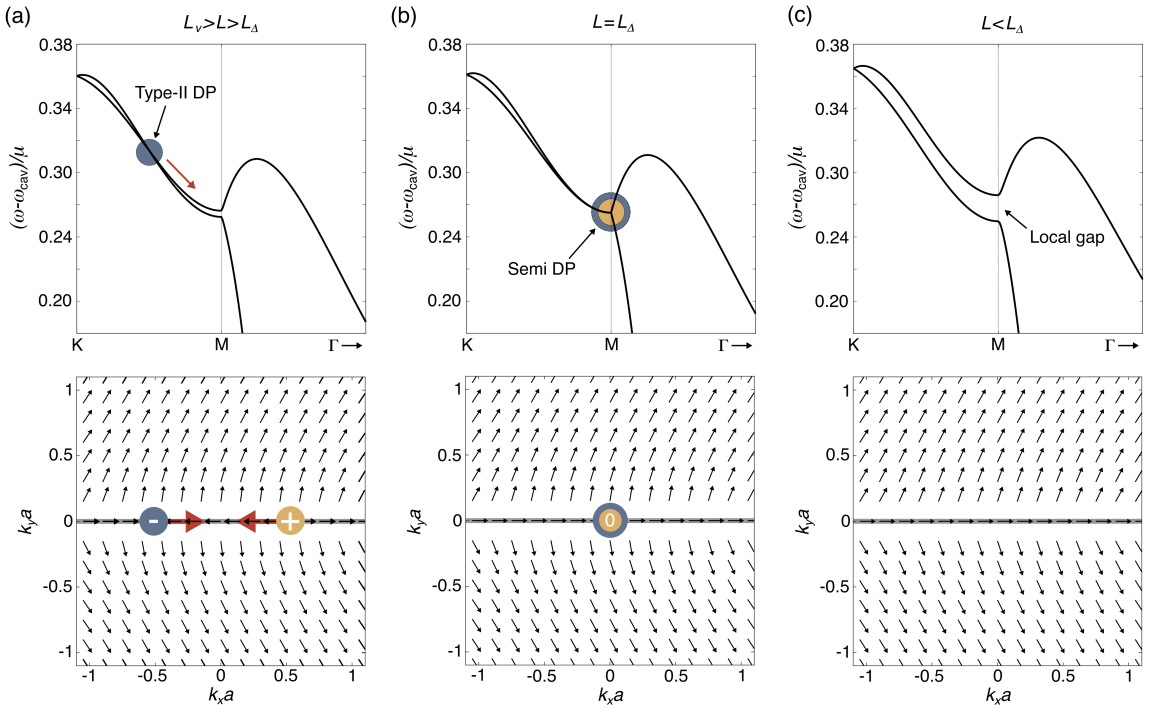

Figure 4.10 | Cavity-induced merging and annihilation of the type-II Dirac points. (a)-(c) Evolution of the polariton dispersion (top panels) and pseudo-spin field for the upper band (bottom panels) near the M point within the vicinity of the critical cavity width L_Δ. (a) Just after the multi-merging transition ($L_v > L > L_\Delta$), a pair of vortices emerge along the $\mathrm{K}(\mathrm{K}') \to \mathrm{M}$ lines with opposite topological charges of -1 (blue circle) and +1 (yellow circle), which correspond to the type-II Dirac points that emerge from the K and K' points, respectively. (b) At the critical cavity width ($L = L_\Delta$), the type-II Dirac points merge together at the M point to form a semi-Dirac point with a trivial topological charge of 0, which is characterized by a linear dispersion along the k_y direction and a quadratic dispersion along the k_x direction. (c) Beyond this critical cavity width ($L < L_\Delta$), the type-II Dirac points annihilate one another giving rise to a local gap at the M point, and the vorticity in the pseudo-spin field vanishes. Results obtained with $\lambda_0 = 10a$ and $\mu = 0.001\omega_0$. For panels (a), (b) and (c) we use cavity widths given by $a/L = 0.882$, $a/L = 0.8839$ and $a/L = 0.892$, respectively.

Dirac points emerging from opposite valleys have opposite topological charges of ± 1, as required by $\mathcal{T}$ symmetry.

As the cavity width is reduced further, the type-II Dirac points migrate along the $\mathrm{K}(\mathrm{K}') \to \mathrm{M}$ lines towards each other as indicated by the red arrows in figure 4.10(a). This migration continues until the critical cavity width ($L = L_\Delta$) where they merge together and the gap at the M point vanishes as shown in figure 4.10(b). In stark contrast to the previous multi-merging transition, the merging of the type-II Dirac points results in a highly anisotropic semi-Dirac point, which is characterized by a linear dispersion along the k_y direction and a quadratic dispersion along the k_x direction. Crucially, the semi-Dirac point has a trivial topological charge of 0; this renders the semi-Dirac point susceptible to a gap-opening perturbation which is exactly what we observe in figure 4.10(c) when we reduce the cavity width further ($L < L_{\Delta}$). The gap parameter changes sign through this transition and therefore the type-II Dirac points annihilate one another which opens a local gap near the M point, and the corresponding vortices in the pseudo-spin field disappear.

This transition is reminiscent of the strain-induced merging and annihilation of the Dirac points that we discussed in section 2.3.2, which has been studied extensively within real and artificial graphene systems [57, 61–67]. However, that merging transition is of a very different nature; it requires one to strongly break the $\mathcal{C}_3$ symmetry to decouple the deterministic Dirac points from the high-symmetry points and induce the merging transition. In stark contrast, here the merging and annihilation of the accidental Dirac points can occur while preserving the lattice symmetry, and it does not result in a global gap since the deterministic type-I Dirac points always remain pinned at the K/K' points.

As a brief remark, we note that the generation and manipulation of accidental type-I Dirac points has been demonstrated within honeycomb tight-binding models [253]; however, this toy model involves the artificial tuning of third-nearest-neighbour hopping amplitudes which, to the author's knowledge, has no physical realization thus far. Moreover, a similar evolution of accidental type-I Dirac points has been predicted within a honeycomb spring-mass model by modifying the tension in the springs via an isotropic stretch of the lattice [52]. In stark contrast, here the generation and manipulation of the accidental type-II Dirac points requires no changes to the lattice structure – it is induced by modifying only the surrounding electromagnetic environment via the cavity width.

4.5.5 Inversion of chirality

In this final section we will explore another interesting phenomenon that occurs as one reduces the cavity width further: a cavity-induced inversion of chirality. For supercritical cavity widths ($L \ll L_v$) where the photon-mediated interactions become dominant, we can observe from figures 4.7(b)-(d) that $|v_{\mathrm{D}}| > |t|/a$ and $|v_{\mathrm{D}}| > |D|/a$. Consequently, one can safely neglect the quadratic terms in equation (4.40) and the effective Hamiltonian near the K point once again is given by

$$\mathcal{H}_{+}(\mathbf{k}) = \omega_{\mathrm{D}}(L)\mathbb{1}_2 - v_{\mathrm{D}}(L)\boldsymbol{\sigma} \cdot \mathbf{k}\,, \tag{4.66}$$

which is equivalent to a 2D massless Dirac Hamiltonian. Therefore, the corresponding spinor eigenstates

$$|\psi_{+\lambda}(\mathbf{k})\rangle = \frac{1}{\sqrt{2}} \begin{bmatrix} 1 \\ \lambda e^{i\phi_{\mathbf{k}}} \end{bmatrix}, \tag{4.67}$$

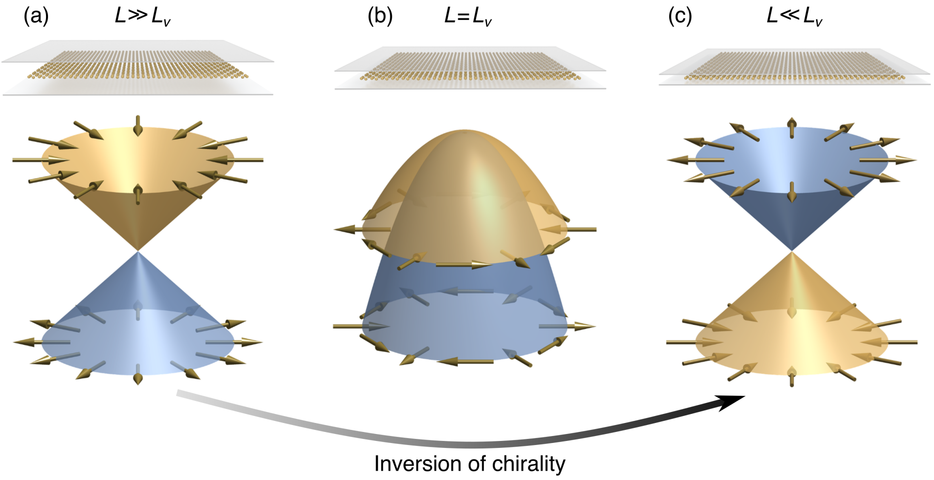

Figure 4.11 | Cavity-induced inversion of chirality. (a)-(c) Evolution of the polariton spectrum near the K point to leading order in $\mathbf{k}$ as the cavity width is decreased. The pseudo-spin is depicted by gold arrows, and the band colour corresponds to the chirality of the polaritons as defined in the main text, where the orange and blue bands indicate a chirality of $+1$ and -1, respectively. (a) For subcritical cavity widths ($L \gg L_v$), the metasurface exhibits massless Dirac polaritons characterized by a linear dispersion and a topological winding number of $+1$. (b) At the critical cavity width ($L = L_v$), the metasurface exhibits massive chiral polaritons characterized by a quadratic dispersion and a topological winding number of -2. (c) For supercritical cavity widths ($L \ll L_v$), the massless Dirac polaritons re-emerge but with a cavity-induced inversion of chirality where the orientation of the pseudo-spin is flipped.

represent type-I massless Dirac polaritons that exhibit an isotropic linear Dirac cone spectrum

$$\omega_\lambda(\mathbf{k}) = \omega_\mathrm{D} + \lambda|v_\mathrm{D}||\mathbf{k}| \tag{4.68}$$

and are characterized by a topological winding number of $+1$.

While this is very similar to the subcritical regime, there is one significant difference. Crucially, the Dirac velocity changes sign at the critical cavity width L_v as shown in figure 4.7(b), and this flips the orientation of the pseudo-spin. Therefore, in the supercritical regime the massless Dirac polaritons re-emerge but with an inverted chirality with respect to the subcritical regime

$$\boldsymbol{\sigma} \cdot \hat{\mathbf{k}} \,|\psi_{+\lambda}(\mathbf{k})\rangle = \lambda \,|\psi_{+\lambda}(\mathbf{k})\rangle \ . \tag{4.69}$$

In other words, the pseudo-spin vector

$$\mathbf{S}_{+\lambda}(\mathbf{k}) = \lambda \left[\, \cos\phi_\mathbf{k} \,,\, \sin\phi_\mathbf{k} \,,\, 0 \,\right] \tag{4.70}$$

is now locked parallel/antiparallel to the momentum in the upper/lower bands, respectively. Consequently, if one was to excite the eigenstate $|\psi_{+\lambda}(\mathbf{k})\rangle = [\,1\,,\,1\,]^\mathrm{T}/\sqrt{2}$ – which corresponds to a pseudo-spin pointing to the right – then this polariton would propagate to the left in the subcritical regime, while in the supercritical regime it would propagate to the right. To summarize, in figures 4.11(a)-(c) we schematically depict how the nature of the polaritons near the K point evolves as the cavity width is reduced.

4.6 Conclusion

In this chapter we have shown that rich Dirac physics emerges in a simple honeycomb metasurface which is not amenable to a simple tight-binding model. In particular, we have unveiled a mechanism that enables one to tune the fundamental properties of the Dirac polaritons without modifying the underlying lattice symmetries. Ultimately, this unique tunability stems from the hybrid light-matter nature of the polaritons, whose properties are intimately connected to the local electromagnetic environment that mediates the dipole-dipole interactions. Exploiting this, we have demonstrated that one can induce exotic merging transitions of the Dirac points, and also manipulate the winding number and chirality of the Dirac polaritons by varying a single external parameter: the cavity width. This rich scenario stands in sharp contrast to graphene and its photonic analogs where the properties are usually fixed by the lattice structure since there is little room to modify the nature of the coupling between lattice sites.

5

Tunable pseudo-magnetic fields for polaritons in strained metasurfaces

Artificial magnetic fields are revolutionizing our ability to manipulate neutral particles by enabling the emulation of exotic phenomena once thought to be exclusive to charged particles. Inspired by graphene physics, pseudo-magnetic fields generated by inhomogeneous strain have attracted considerable interest because of their simple geometrical origin. However, to date, these strain-induced pseudo-magnetic fields have failed to emulate the tunability of real magnetic fields because they are dictated solely by the engineered strain configuration, rendering them fixed by design. In this chapter, we demonstrate that one can generate a pseudo-magnetic field for polaritons by straining a honeycomb metasurface composed of a subwavelength array of dipole emitters/antennas. Without altering the strain configuration, we unveil how one can tune the pseudo-magnetic field strength by modifying the photonic environment via an enclosing cavity waveguide. In fact, we show that one can even switch off the pseudo-magnetic field entirely at a critical cavity width, without removing the strain – a counter-intuitive result that is impossible to achieve with photonic systems that emulate the tight-binding physics of graphene. Exploiting this, we demonstrate that one can induce a collapse and revival of the polariton Landau levels by varying only the cavity width. Unlocking this tunable pseudo-magnetism poses new intriguing questions beyond the paradigm of conventional tight-binding physics.

This chapter presents original research that was published as follows:

Mann, C.-R., Horsley, S. A. R. & Mariani, E. Tunable pseudo-magnetic fields for polaritons in strained metasurfaces. *Nature Photonics* **14**, 669-674 (2020).

5.1 Introduction

Unfortunately, the fundamental laws of physics dictate that neutral particles do not directly couple to the electromagnetic gauge potentials. Therefore, exotic phenomena exhibited by charged particles in magnetic fields, such as the Lorentz force, Aharonov-Bohm effect, and Landau quantization, remain elusive for neutral particles. This fundamental limitation has inspired various methods of engineering artificial magnetic fields which are revolutionizing our ability to manipulate neutral particles in ways that were once thought to be exclusive to charged particles [68, 77, 78, 165–169, 254–263]. Within this paradigm, one tantalizingly straightforward approach has emerged from the concept of strain-engineering in graphene physics. In particular, as a remarkable consequence of the Dirac-like nature of the charge carriers, it has been shown that smooth deformations of the graphene membrane translate into synthetic gauge fields in the effective Dirac Hamiltonian [19–21].

This beautiful result stems from the topological stability of the Dirac points, where smooth lattice distortions that break the $\mathcal{C}_3$ symmetry but locally preserve the $\mathcal{I}$ symmetry can only shift the Dirac cone in momentum space, thereby mimicking the effect of a gauge field. As a result, inhomogeneous strain configurations can give rise to pseudo-magnetic fields [22–24] which have been shown to reconstruct the electronic spectrum into quantized Landau levels despite the absence of a real magnetic field [27]. The true power of this approach lies in its purely geometric origin which can be emulated in any hexagonal lattice that exhibits deterministic Dirac points, even within entirely different physical systems [68, 165–171]. In the realm of photonics, these pseudo-magnetic fields have been realized for photons by judiciously engineering aperiodicity in honeycomb lattices of evanescently coupled waveguides which mimic the tight-binding physics of graphene [68].

However, these emergent pseudo-magnetic fields in photonic graphene lattices have so far failed to emulate one key property of real magnetic fields: *tunability*. While real magnetic fields that are applied across samples in the lab can be tuned by varying external parameters (e.g., the current through a solenoid), these pseudo-magnetic fields are usually determined solely by the strain configuration, rendering them fixed by design. Consequently, if one wants to modify the pseudo-magnetic field then one has to fabricate a new structure with a different strain pattern [68]. While, in principle, one could envisage fabricating a photonic lattice on a flexible substrate, it would remain extremely challenging to precisely engineer the strain patterns that are required to generate a uniform pseudo-magnetic field over a large area by applying external forces [22]. Therefore, an interesting question arises: is it possible to tune the strain-induced pseudo-magnetic fields without modifying the strain? Moreover, is it possible to switch off the pseudo-magnetic field without removing the strain? Based on the naive intuition that is built from the simple tight-binding physics of graphene, the latter seems impossible since any anisotropy in the hopping parameters will inevitably shift the Dirac cone. However, while breaking the $\mathcal{C}_3$ symmetry permits a gauge field-like term to appear in the effective Hamiltonian, it does not guarantee it. In principle, it can be tuned to zero – but how?

In this chapter we will show that one can generate a pseudo-magnetic field for polaritons by straining a honeycomb metasurface composed of a subwavelength array of interacting dipole emitters/antennas. The dipoles hybridize with the surrounding photons which can mediate long-range dipole–dipole interactions. Therefore, previous results derived from simple tight-binding models do not trivially extend to lattices of interacting dipoles; a priori, it is not obvious that anisotropy in the dipole-dipole interactions will generate a significant pseudo-vector potential. Crucially, the nature of the dipole–dipole interactions depends qualitatively on the surrounding electromagnetic environment in which the dipoles are embedded. By exploiting this feature of emitters we show that, without altering the strain configuration, one can tune the artificial magnetic field by modifying the real electromagnetic environment.

To illustrate this, we embed the strained metasurface inside a cavity waveguide and unveil that the strength of the pseudo-magnetic field can be tuned by varying a single external parameter: the cavity width. Remarkably, there exists a critical cavity width where the pseudo-magnetic field generated by the Coulomb interactions is completely cancelled by the long-range photon-mediated interactions, resulting in the pseudo-magnetic field being switched off for any strain configuration – this striking result is impossible to achieve with photonic systems that emulate the tight-binding physics of graphene [58–60]. Consequently, for small strains we demonstrate a Lorentz-like force that can be switched on/off, deflecting polariton wavepackets into effective cyclotron orbits whose radius can be controlled via the cavity width. For large strains, we also demonstrate Landau quantization of the polariton cyclotron orbits, where decreasing the cavity width can induce a collapse and revival of the polariton Landau levels.

5.2 Strained honeycomb metasurface

A schematic of a strained honeycomb metasurface embedded inside a cavity waveguide is depicted in figure 5.1. We describe the metasurface using the same minimal model that we presented in section 4.2 for the unstrained case, which we will repeat here for convenience.

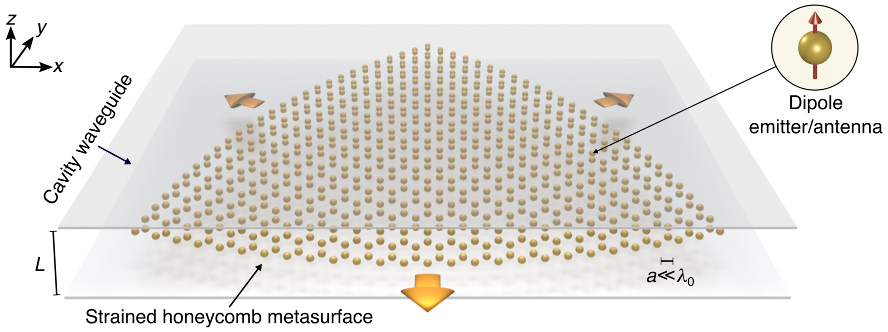

Figure 5.1 | Strained honeycomb metasurface inside a cavity waveguide. Schematic of a strained honeycomb metasurface composed of an array of dipole emitters/antennas with subwavelength nearest-neighbour separation. The induced dipole moments are assumed to point in the z-direction (see inset). Furthermore, the strained metasurface is embedded inside a cavity waveguide of width L, where the cavity walls are assumed to be perfect mirrors.

In particular, we describe the dipoles with a bare polarizability of the form

$$\alpha_{\mathrm{B}}(\omega) = \frac{2\omega_0\mu}{\omega_0^2 - \omega^2 - \mathrm{i}\omega\gamma_{\mathrm{nr}}}\,, \tag{5.1}$$

where the corresponding induced dipole moments are assumed to point in the z-direction (see inset). For the unstrained honeycomb metasurface, the dipoles are located at periodic positions $\mathbf{R}_{\mathrm{A}} = \mathbf{R} + \mathbf{d}_{\mathrm{A}}$ and $\mathbf{R}_{\mathrm{B}} = \mathbf{R} + \mathbf{d}_{\mathrm{B}}$, which form the A and B inequivalent hexagonal sublattices, respectively. Here, the basis vectors

$$\mathbf{d}_{\mathrm{A}} = \frac{a}{2}\big[\,0\,,\,-1\,\big]\,, \quad \mathbf{d}_{\mathrm{B}} = \frac{a}{2}\big[\,0\,,\,1\,\big]\,, \tag{5.2}$$

locate the positions of the dipoles within a unit cell and $\mathbf{d} = \mathbf{d}_{\mathrm{B}} - \mathbf{d}_{\mathrm{A}}$ is the vector that connects the sublattices. Furthermore, $\mathbf{R} = l_1\mathbf{a}_1 + l_2\mathbf{a}_2$ represents the set of lattice translation vectors, where $l_1, l_2 \in \mathbb{Z}$ are integers, and

$$\mathbf{a}_1 = \frac{\sqrt{3}a}{2}\big[\,-1\,,\,\sqrt{3}\,\big]\,, \quad \mathbf{a}_2 = \frac{\sqrt{3}a}{2}\big[\,1\,,\,\sqrt{3}\,\big]\,, \tag{5.3}$$

are the primitive lattice vectors. The corresponding set of reciprocal lattice vectors are $\mathbf{g} = n_1\mathbf{b}_1 + n_2\mathbf{b}_2$, where $n_1, n_2 \in \mathbb{Z}$ are integers, and

$$\mathbf{b}_1 = \frac{2\pi}{3a}\big[\,-\sqrt{3}\,,\,1\,\big]\,, \quad \mathbf{b}_2 = \frac{2\pi}{3a}\big[\,\sqrt{3}\,,\,1\,\big]\,, \tag{5.4}$$

are the primitive reciprocal lattice vectors that define the Brillouin zone of the unstrained lattice. Next we assume that the metasurface has been engineered with a fixed strain pattern, where the dipoles are displaced to new, aperiodic positions given by

$$\bar{\mathbf{R}}_{\mathrm{A}} = \mathbf{R}_{\mathrm{A}} + \mathbf{u}(\mathbf{R}_{\mathrm{A}})\,, \quad \bar{\mathbf{R}}_{\mathrm{B}} = \mathbf{R}_{\mathrm{B}} + \mathbf{u}(\mathbf{R}_{\mathrm{B}})\,. \tag{5.5}$$

Here we have introduced the in-plane displacement field

$$\mathbf{u}(\boldsymbol{\rho}) = [u_x(\boldsymbol{\rho})\,,\, u_y(\boldsymbol{\rho})]\ , \tag{5.6}$$

which characterizes the strain configuration. We will assume that the displacement field varies slowly on the scale of the lattice constant so that the corresponding strain tensor

$$\varepsilon_{\nu\nu'}(\boldsymbol{\rho}) = \frac{1}{2}\left(\frac{\partial u_\nu}{\partial \rho_{\nu'}} + \frac{\partial u_{\nu'}}{\partial \rho_\nu}\right)\,, \qquad \nu, \nu' = x, y \tag{5.7}$$

remains small across the metasurface. Finally, we embed the strained metasurface at the centre of a cavity waveguide of width L, where the cavity walls are assumed to be perfect mirrors.

5.2.1 Coupled-dipole equations

In the absence of a driving field, the collective dynamics of the dipoles within the strained metasurface is described by a system of coupled-dipole equations that read

$$\frac{1}{\alpha(\omega)} p_{\mathbf{R}_{\mathrm{A}}}(\omega) = \sum_{\mathbf{R}'_{\mathrm{A}} \neq \mathbf{R}_{\mathrm{A}}} G(\bar{\mathbf{R}}_{\mathrm{A}} - \bar{\mathbf{R}}'_{\mathrm{A}}, \omega) p_{\mathbf{R}'_{\mathrm{A}}}(\omega) + \sum_{\mathbf{R}_{\mathrm{B}}} G(\bar{\mathbf{R}}_{\mathrm{A}} - \bar{\mathbf{R}}_{\mathrm{B}}, \omega) p_{\mathbf{R}_{\mathrm{B}}}(\omega) \tag{5.8}$$

and

$$\frac{1}{\alpha(\omega)} p_{\mathbf{R}_{\mathrm{B}}}(\omega) = \sum_{\mathbf{R}'_{\mathrm{B}} \neq \mathbf{R}_{\mathrm{B}}} G(\bar{\mathbf{R}}_{\mathrm{B}} - \bar{\mathbf{R}}'_{\mathrm{B}}, \omega) p_{\mathbf{R}'_{\mathrm{B}}}(\omega) + \sum_{\mathbf{R}_{\mathrm{A}}} G(\bar{\mathbf{R}}_{\mathrm{B}} - \bar{\mathbf{R}}_{\mathrm{A}}, \omega) p_{\mathbf{R}_{\mathrm{A}}}(\omega)\,. \tag{5.9}$$

Here $p_{\mathbf{R}_{\mathrm{A}}}(\omega)$ and $p_{\mathbf{R}_{\mathrm{B}}}(\omega)$ now represent the dipole moments at positions $\bar{\mathbf{R}}_{\mathrm{A}}$ and $\bar{\mathbf{R}}_{\mathrm{B}}$, respectively. As before, $\alpha(\omega) = [\alpha_{\mathrm{B}}^{-1}(\omega) - \varSigma(\omega)]^{-1}$ is the renormalized polarizability that was derived in section 3.4.2, where the polarizability correction inside the cavity waveguide reads

$$\varSigma(\omega) = \mathrm{i}\frac{\mathcal{V} k_\omega^3}{6\pi} + \frac{\mathcal{V}}{\pi L^3}\left[\mathrm{Li}_3\left(\mathrm{e}^{\mathrm{i}k_\omega L}\right) - \mathrm{i}k_\omega L\,\mathrm{Li}_2\left(\mathrm{e}^{\mathrm{i}k_\omega L}\right)\right]\,. \tag{5.10}$$

Furthermore, $G(\boldsymbol{\rho}-\boldsymbol{\rho}',\omega)$ is the zz-component of the cavity Green's function that was derived in section 3.3 and reads

$$G(\boldsymbol{\rho}-\boldsymbol{\rho}',\omega)=\mathrm{i}\frac{\mathcal{V}}{4L}\sum_{m=0}^{\infty}N_m\left(k_\omega^2-q_m^2\right)H_0^{(1)}\left(\sqrt{k_\omega^2-q_m^2}|\boldsymbol{\rho}-\boldsymbol{\rho}'|\right). \tag{5.11}$$

Note, the interactions between every pair of dipoles has been modified as a result of the strain-induced shift of the dipole locations.

5.3 Effective polariton Hamiltonian

Since the discrete translational symmetry of the honeycomb metasurface is broken by the lattice distortion, one cannot exploit Bloch's theorem to block diagonalize the coupled-dipole equations in momentum space, as we did for the unstrained honeycomb metasurface in section 4.3.1. Instead, we seek to derive an effective Hamiltonian for the polaritons near the K/K' points which we assume are decoupled. Therefore, we write the dipole moments as

$$p_{\mathbf{R}_\mathrm{A}}(\omega)=\mathrm{e}^{\mathrm{i}\tau\mathbf{K}\cdot\mathbf{R}_\mathrm{A}}\psi_\mathrm{A}^\tau(\mathbf{R}_\mathrm{A},\omega)\,,\quad p_{\mathbf{R}_\mathrm{B}}(\omega)=\mathrm{e}^{\mathrm{i}\tau\mathbf{K}\cdot\mathbf{R}_\mathrm{B}}\psi_\mathrm{B}^\tau(\mathbf{R}_\mathrm{B},\omega)\,, \tag{5.12}$$

where we have introduced envelope fields $\psi_\mathrm{A}^\tau(\boldsymbol{\rho},\omega)$ and $\psi_\mathrm{B}^\tau(\boldsymbol{\rho},\omega)$ that describe the slow variation of the dipole moments on the A and B sublattices, respectively, where $\tau=\pm$ is the valley index. Note, here we have used the crystal reference frame which captures the effects of the modified dipole interactions but not the geometric effects associated with the lattice distortion – it has been shown that the latter does not contribute to the emergent pseudo-magnetic field as its contribution can be removed by a gauge transformation [157]. Furthermore, in what follows we will focus on the K valley since the equivalent physics near the K' valley is related via $\mathcal{T}$ symmetry, and therefore we will temporarily suppress the valley index to ease notation.

To proceed we introduce the Fourier transform of the envelope fields

$$\widetilde{\psi}_\mathrm{A}(\mathbf{k},\omega)=\iint\frac{\mathrm{d}^2\boldsymbol{\rho}}{2\pi}\psi_\mathrm{A}(\boldsymbol{\rho},\omega)\mathrm{e}^{-\mathrm{i}\mathbf{k}\cdot\boldsymbol{\rho}}\,,\quad \widetilde{\psi}_\mathrm{B}(\mathbf{k},\omega)=\iint\frac{\mathrm{d}^2\boldsymbol{\rho}}{2\pi}\psi_\mathrm{B}(\boldsymbol{\rho},\omega)\mathrm{e}^{-\mathrm{i}\mathbf{k}\cdot\boldsymbol{\rho}}\,, \tag{5.13}$$

which enables us to transform the coupled-dipole equations into matrix form as

$$\frac{1}{\breve{\alpha}(\omega)}\widetilde{\psi}(\mathbf{k},\omega)=\iint\mathrm{d}^2\mathbf{k}'\left[\mathcal{D}_\parallel(\mathbf{k},\mathbf{k}')+\mathcal{D}_\perp(\mathbf{k},\mathbf{k}',\omega)\right]\widetilde{\psi}(\mathbf{k}',\omega)\,, \tag{5.14}$$

where $\breve{\alpha}^{-1}(\omega) = \alpha_{\mathrm{B}}^{-1}(\omega) - \mathrm{Re}[\Sigma(\omega)]$. In equation (5.14), the Fourier transform of the spinor envelope field reads

$$\tilde{\psi}(\mathbf{k},\omega) = \begin{bmatrix} \tilde{\psi}_{\mathrm{A}}(\mathbf{k},\omega) \\ \tilde{\psi}_{\mathrm{B}}(\mathbf{k},\omega) \end{bmatrix} , \tag{5.15}$$

the longitudinal dynamical matrix encoding the Coulomb interactions is given by

$$\mathcal{D}_{\parallel}(\mathbf{k},\mathbf{k}') = \begin{bmatrix} \mathcal{D}_{\parallel}^{\mathrm{AA}}(\mathbf{k},\mathbf{k}') & \mathcal{D}_{\parallel}^{\mathrm{AB}}(\mathbf{k},\mathbf{k}') \\ \mathcal{D}_{\parallel}^{\mathrm{AB}*}(\mathbf{k}',\mathbf{k}) & \mathcal{D}_{\parallel}^{\mathrm{BB}}(\mathbf{k},\mathbf{k}') \end{bmatrix} , \tag{5.16}$$

and the transverse dynamical matrix encoding the photon-mediated interactions reads

$$\mathcal{D}_{\perp}(\mathbf{k},\mathbf{k}',\omega) = \begin{bmatrix} \mathcal{D}_{\perp}^{\mathrm{AA}}(\mathbf{k},\mathbf{k}',\omega) & \mathcal{D}_{\perp}^{\mathrm{AB}}(\mathbf{k},\mathbf{k}',\omega) \\ \mathcal{D}_{\perp}^{\mathrm{AB}*}(\mathbf{k}',\mathbf{k},\omega) & \mathcal{D}_{\perp}^{\mathrm{BB}}(\mathbf{k},\mathbf{k}',\omega) \end{bmatrix} . \tag{5.17}$$

Note, as we eluded to earlier, the coupled-dipole equations are not block diagonal in momentum space since the polaritons with wavevector $\mathbf{k}$ and $\mathbf{k}'$ are coupled due to the lattice distortion. For an arbitrary displacement field, it is difficult to extract any general physics from the coupled-dipole equations. Therefore, we will restrict our analysis to displacement fields that vary slowly on the scale of the lattice constant, and seek an effective Hamiltonian to leading order in the strain tensor by expanding the dynamical matrix to leading order in the displacement field and wavevector.

5.3.1 Expansion of the longitudinal dynamical matrix

We will first analyze the longitudinal dynamical matrix elements in equation (5.16). The intersublattice matrix elements are given by

$$\mathcal{D}_{\parallel}^{\mathrm{AB}}(\mathbf{k},\mathbf{k}') = \iint \frac{\mathrm{d}^2\boldsymbol{\rho}}{(2\pi)^2} \sum_{\mathbf{R}} G_{\parallel}(\mathbf{R}-\mathbf{d}+\mathbf{u}(\boldsymbol{\rho})-\mathbf{u}(\boldsymbol{\rho}-\mathbf{R}+\mathbf{d}))\mathrm{e}^{-\mathrm{i}(\mathbf{K}+\mathbf{k}')\cdot(\mathbf{R}-\mathbf{d})}\mathrm{e}^{\mathrm{i}(\mathbf{k}'-\mathbf{k})\cdot\boldsymbol{\rho}} , \tag{5.18}$$

where $G_{\parallel}(\boldsymbol{\rho}-\boldsymbol{\rho}')$ is the longitudinal component of the cavity Green's function that was derived in section 3.3 and reads

$$G_{\parallel}(\boldsymbol{\rho}-\boldsymbol{\rho}') = -\frac{\mathcal{V}}{\pi L}\sum_{m=1}^{\infty} q_m^2 K_0\left(q_m|\boldsymbol{\rho}-\boldsymbol{\rho}'|\right) . \tag{5.19}$$

Since the Coulomb interactions are short-range the lattice sums converge rapidly in real space.

After expanding equation (5.18) to leading order in the displacement field we obtain

$$\begin{aligned}\mathcal{D}_{\parallel}^{\mathrm{AB}}(\mathbf{k},\mathbf{k}') = &\iint \frac{\mathrm{d}^2\boldsymbol{\rho}}{(2\pi)^2} \sum_{\mathbf{R}} G_{\parallel}(\mathbf{R}-\mathbf{d})\mathrm{e}^{-\mathrm{i}(\mathbf{K}+\mathbf{k}')\cdot(\mathbf{R}-\mathbf{d})}\mathrm{e}^{\mathrm{i}(\mathbf{k}'-\mathbf{k})\cdot\boldsymbol{\rho}} \\ &\times \left[1 - \frac{\beta(\mathbf{R}-\mathbf{d})}{2\pi}\frac{(\mathbf{R}-\mathbf{d})_\nu}{|\mathbf{R}-\mathbf{d}|^2} \iint \mathrm{d}^2\mathbf{q}\,\tilde{u}_\nu(\mathbf{q})\Big[1-\mathrm{e}^{-\mathrm{i}\mathbf{q}\cdot(\mathbf{R}-\mathbf{d})}\Big]\mathrm{e}^{\mathrm{i}\mathbf{q}\cdot\boldsymbol{\rho}}\right],\end{aligned} \tag{5.20}$$

where

$$\tilde{\mathbf{u}}(\mathbf{q}) = \iint \frac{\mathrm{d}^2\boldsymbol{\rho}}{2\pi}\,\mathbf{u}(\boldsymbol{\rho})\mathrm{e}^{-\mathrm{i}\mathbf{q}\cdot\boldsymbol{\rho}} \tag{5.21}$$

is the Fourier transform of the displacement field and we assume Einstein's summation convention. Furthermore, the parameter

$$\beta(\boldsymbol{\rho}) = \left|\frac{\partial\log[G_{\parallel}(\boldsymbol{\rho})]}{\partial\log(\rho)}\right| = \left|\frac{\rho\sum_{m=1}^{\infty} q_m^3 K_1(q_m\rho)}{\sum_{m=1}^{\infty} q_m^2 K_0(q_m\rho)}\right| \tag{5.22}$$

encodes how the Coulomb interaction strength changes with respect to small changes in the separation distance, where K_1 is the modified Bessel function of first order and second kind. Next, we can perform the spatial integral in equation (5.20) which yields

$$\begin{aligned}\mathcal{D}_{\parallel}^{\mathrm{AB}}(\mathbf{k},\mathbf{k}') = \sum_{\mathbf{R}} G_{\parallel}(\mathbf{R}-\mathbf{d})\mathrm{e}^{-\mathrm{i}(\mathbf{K}+\mathbf{k}')\cdot(\mathbf{R}-\mathbf{d})}\Bigg\{&\delta(\mathbf{k}'-\mathbf{k}) \\ - \frac{\beta(\mathbf{R}-\mathbf{d})}{2\pi}\frac{(\mathbf{R}-\mathbf{d})_\nu}{|\mathbf{R}-\mathbf{d}|^2}\tilde{u}_\nu(\mathbf{k}-\mathbf{k}')&\left[1-\mathrm{e}^{-\mathrm{i}(\mathbf{k}-\mathbf{k}')\cdot(\mathbf{R}-\mathbf{d})}\right]\Bigg\},\end{aligned} \tag{5.23}$$

and after expanding equation (5.23) to leading order in $\mathbf{k}$ and $\mathbf{k}'$ we obtain

$$\begin{aligned}\mathcal{D}_{\parallel}^{\mathrm{AB}}(\mathbf{k},\mathbf{k}') = \sum_{\mathbf{R}} G_{\parallel}(\mathbf{R}-\mathbf{d})\mathrm{e}^{-\mathrm{i}\mathbf{K}\cdot(\mathbf{R}-\mathbf{d})}\Bigg\{&[1-\mathrm{i}(\mathbf{R}-\mathbf{d})_\nu k'_\nu]\delta(\mathbf{k}'-\mathbf{k}) \\ - \frac{\beta(\mathbf{R}-\mathbf{d})}{2\pi}\frac{(\mathbf{R}-\mathbf{d})_\nu(\mathbf{R}-\mathbf{d})_{\nu'}}{|\mathbf{R}-\mathbf{d}|^2}&\widetilde{\boldsymbol{\nabla} u}_{\nu\nu'}(\mathbf{k}-\mathbf{k}')\Bigg\}.\end{aligned} \tag{5.24}$$

Here we have identified $\mathrm{i}k_\nu\tilde{u}_{\nu'}(\mathbf{k}) = \widetilde{\boldsymbol{\nabla} u}_{\nu\nu'}(\mathbf{k})$, which is the Fourier transform of the displacement gradient tensor $\boldsymbol{\nabla} u_{\nu\nu'} = \partial u_{\nu'}/\partial\rho_\nu$. Performing similar analysis for the intrasublattice matrix elements in equation (5.16) yields

$$\mathcal{D}_{\parallel}^{\text{AA/BB}}(\mathbf{k},\mathbf{k}') = \sum_{\mathbf{R}\neq 0} G_{\parallel}(\mathbf{R})\mathrm{e}^{-\mathrm{i}\mathbf{K}\cdot\mathbf{R}}\left\{[1-\mathrm{i}(\mathbf{R})_{\nu}k'_{\nu}]\delta(\mathbf{k}'-\mathbf{k}) - \frac{\beta(\mathbf{R})}{2\pi}\frac{(\mathbf{R})_{\nu}(\mathbf{R})_{\nu'}}{|\mathbf{R}|^2}\widetilde{\boldsymbol{\nabla} u}_{\nu\nu'}(\mathbf{k}-\mathbf{k}')\right\}. \tag{5.25}$$

Finally, after exploiting the symmetry of the unstrained lattice (see appendix C.1 for details) one can simplify equation (5.24) to obtain

$$\begin{aligned}\mathcal{D}_{\parallel}^{\text{AB}}(\mathbf{k},\mathbf{k}') = \sum_{\mathbf{R}} G_{\parallel}(\mathbf{R}-\mathbf{d})\mathrm{e}^{-\mathrm{i}\mathbf{K}\cdot(\mathbf{R}-\mathbf{d})}\bigg\{ & -\mathrm{i}(\mathbf{R}-\mathbf{d})_x(k'_x-\mathrm{i}k'_y)\delta(\mathbf{k}'-\mathbf{k}) \\ & -\frac{\beta(\mathbf{R}-\mathbf{d})}{2\pi}\frac{(\mathbf{R}-\mathbf{d})_x^2}{|\mathbf{R}-\mathbf{d}|^2}[\widetilde{\varepsilon}_{xx}(\mathbf{k}-\mathbf{k}')-\widetilde{\varepsilon}_{yy}(\mathbf{k}-\mathbf{k}')+2\mathrm{i}\widetilde{\varepsilon}_{xy}(\mathbf{k}-\mathbf{k}')]\bigg\},\end{aligned} \tag{5.26}$$

and one can simplify equation (5.25) to obtain

$$\mathcal{D}_{\parallel}^{\text{AA/BB}}(\mathbf{k},\mathbf{k}') = \sum_{\mathbf{R}\neq 0} G_{\parallel}(\mathbf{R})\mathrm{e}^{-\mathrm{i}\mathbf{K}\cdot\mathbf{R}}\left\{\delta(\mathbf{k}'-\mathbf{k}) - \frac{\beta(\mathbf{R})}{2\pi}\frac{(\mathbf{R})_x^2}{|\mathbf{R}|^2}[\widetilde{\varepsilon}_{xx}(\mathbf{k}-\mathbf{k}')+\widetilde{\varepsilon}_{yy}(\mathbf{k}-\mathbf{k}')]\right\}, \tag{5.27}$$

where $\widetilde{\varepsilon}_{\nu\nu'}(\mathbf{k})$ is the Fourier transform of the strain tensor.

5.3.2 Expansion of the transverse dynamical matrix

We will now analyze the transverse dynamical matrix elements in equation (5.17). Since we are interested in the regime of cavity widths $L < \lambda_0$, we will only consider the TEM cavity mode as we did for the unstrained honeycomb metasurface in chapter 4. The corresponding single mode Green's function was derived in section 3.3 and reads

$$G_{\perp}^{\text{TEM}}(\boldsymbol{\rho}-\boldsymbol{\rho}',\omega) = \mathrm{i}\frac{\mathcal{V}k_{\omega}^2}{4L}H_0^{(1)}\left(k_{\omega}|\boldsymbol{\rho}-\boldsymbol{\rho}'|\right). \tag{5.28}$$

Within this single mode approximation the intersublattice matrix elements read

$$\begin{aligned}\mathcal{D}_{\perp}^{\text{AB}}(\mathbf{k},\mathbf{k}',\omega) = \iint\frac{\mathrm{d}^2\boldsymbol{\rho}}{(2\pi)^2}\sum_{\mathbf{R}} & G_{\perp}^{\text{TEM}}(\mathbf{R}-\mathbf{d}+\mathbf{u}(\boldsymbol{\rho})-\mathbf{u}(\boldsymbol{\rho}-\mathbf{R}+\mathbf{d}),\omega) \\ & \times\mathrm{e}^{-\mathrm{i}(\mathbf{K}+\mathbf{k}')\cdot(\mathbf{R}-\mathbf{d})}\mathrm{e}^{\mathrm{i}(\mathbf{k}'-\mathbf{k})\cdot\boldsymbol{\rho}}.\end{aligned} \tag{5.29}$$

Since the photon-mediated interactions are long-range we need to accelerate the computation of the lattice sums by performing them in reciprocal space.

To do this, we first insert the eigenfunction expansion of the TEM Green's function into equation (5.29) which gives

$$\begin{aligned}\mathcal{D}_{\perp}^{\mathrm{AB}}(\mathbf{k},\mathbf{k}',\omega) = \iint \frac{\mathrm{d}^2\boldsymbol{\rho}}{(2\pi)^2} \iint \frac{\mathrm{d}^2\mathbf{k}''}{2\pi} \sum_{\mathbf{R}} \widetilde{G}_{\perp}^{\mathrm{TEM}}(\mathbf{k}'',\omega) \mathrm{e}^{\mathrm{i}(\mathbf{k}'-\mathbf{k})\cdot\boldsymbol{\rho}} \\ \times\, \mathrm{e}^{\mathrm{i}(\mathbf{k}''-\mathbf{k}'-\mathbf{K})\cdot(\mathbf{R}-\mathbf{d})} \mathrm{e}^{\mathrm{i}\mathbf{k}''\cdot[\mathbf{u}(\boldsymbol{\rho})-\mathbf{u}(\boldsymbol{\rho}-\mathbf{R}+\mathbf{d})]}\,,\end{aligned} \tag{5.30}$$

where we have defined

$$\widetilde{G}_{\perp}^{\mathrm{TEM}}(\mathbf{k},\omega) = \frac{\mathcal{V}k_{\omega}^2}{2\pi L}\frac{1}{k^2-k_{\omega}^2}\,, \tag{5.31}$$

which is essentially the 2D Fourier transform of the TEM Green's function. Expanding equation (5.30) to leading order in the displacement field yields

$$\begin{aligned}\mathcal{D}_{\perp}^{\mathrm{AB}}(\mathbf{k},\mathbf{k}',\omega) = \iint \frac{\mathrm{d}^2\boldsymbol{\rho}}{(2\pi)^2} \iint \frac{\mathrm{d}^2\mathbf{k}''}{2\pi} \sum_{\mathbf{R}} \widetilde{G}_{\perp}^{\mathrm{TEM}}(\mathbf{k}'',\omega) \mathrm{e}^{\mathrm{i}(\mathbf{k}'-\mathbf{k})\cdot\boldsymbol{\rho}} \\ \times \mathrm{e}^{\mathrm{i}(\mathbf{k}''-\mathbf{k}'-\mathbf{K})\cdot(\mathbf{R}-\mathbf{d})}\left\{1+\frac{\mathrm{i}}{2\pi}k_{\nu}''\iint \mathrm{d}^2\mathbf{q}\,\widetilde{u}_{\nu}(\mathbf{q})\left[1-\mathrm{e}^{-\mathrm{i}\mathbf{q}\cdot(\mathbf{R}-\mathbf{d})}\right]\mathrm{e}^{\mathrm{i}\mathbf{q}\cdot\boldsymbol{\rho}}\right\},\end{aligned} \tag{5.32}$$

and after performing the spatial integral in equation (5.32) we obtain

$$\begin{aligned}\mathcal{D}_{\perp}^{\mathrm{AB}}(\mathbf{k},\mathbf{k}',\omega) = \iint \frac{\mathrm{d}^2\mathbf{k}''}{2\pi} \sum_{\mathbf{R}} \widetilde{G}_{\perp}^{\mathrm{TEM}}(\mathbf{k}'',\omega) \mathrm{e}^{\mathrm{i}(\mathbf{k}''-\mathbf{k}'-\mathbf{K})\cdot(\mathbf{R}-\mathbf{d})} \\ \times\left\{\delta(\mathbf{k}'-\mathbf{k})+\frac{\mathrm{i}}{2\pi}k_{\nu}''\,\widetilde{u}_{\nu}(\mathbf{k}-\mathbf{k}')\left[1-\mathrm{e}^{-\mathrm{i}(\mathbf{k}-\mathbf{k}')\cdot(\mathbf{R}-\mathbf{d})}\right]\right\}.\end{aligned} \tag{5.33}$$

We can now invoke Poisson's summation identity

$$\sum_{\mathbf{R}} \mathrm{e}^{\mathrm{i}(\mathbf{k}'-\mathbf{k})\cdot\mathbf{R}} = \frac{(2\pi)^2}{\mathcal{A}}\sum_{\mathbf{g}}\delta(\mathbf{k}'-\mathbf{k}+\mathbf{g})\,, \tag{5.34}$$

where $\mathcal{A}=3\sqrt{3}a^2/2$ is the area of the unit cell in the unstrained lattice, to convert the sum over lattice vectors to a sum over reciprocal lattice vectors which reads

$$\begin{aligned}\mathcal{D}_{\perp}^{\mathrm{AB}}(\mathbf{k},\mathbf{k}',\omega) = \frac{2\pi}{\mathcal{A}}\sum_{\mathbf{g}}\phi_{\mathbf{g}}\left\{\widetilde{G}_{\perp}^{\mathrm{TEM}}(\mathbf{k}'+\mathbf{K}-\mathbf{g},\omega)\delta(\mathbf{k}'-\mathbf{k})\right. \\ \left.+\frac{\mathrm{i}}{2\pi}\left[\widetilde{G}_{\perp}^{\mathrm{TEM}}(\mathbf{k}'+\mathbf{K}-\mathbf{g},\omega)(\mathbf{k}'+\mathbf{K}-\mathbf{g})_{\nu}-(\mathbf{k}'\leftrightarrow\mathbf{k})\right]\widetilde{u}_{\nu}(\mathbf{k}-\mathbf{k}')\right\}.\end{aligned} \tag{5.35}$$

The phase factors $\phi_{\mathbf{g}} = \mathrm{e}^{\mathrm{i}\mathbf{g}\cdot\mathbf{d}}$ are the same as those that emerged for the unstrained honeycomb metasurface and must be retained as they are crucial for maintaining the correct symmetry. Next, we expand equation (5.35) to leading order in $\mathbf{k}$ and $\mathbf{k}'$ which gives

$$\begin{aligned}\mathcal{D}_{\perp}^{\mathrm{AB}}(\mathbf{k},\mathbf{k}',\omega) = \sum_{\mathbf{g}} \frac{\omega^2\xi^2\phi_{\mathbf{g}}}{\omega_{\mathbf{K}-\mathbf{g}}^2-\omega^2} \Bigg\{ &\delta(\mathbf{k}'-\mathbf{k}) - \frac{1}{2\pi}\widetilde{\boldsymbol{\nabla} u}_{\nu\nu}(\mathbf{k}'-\mathbf{k}) \\ - \frac{2c^2(\mathbf{K}-\mathbf{g})_\nu}{\omega_{\mathbf{K}-\mathbf{g}}^2-\omega^2}&\left[k'_\nu\delta(\mathbf{k}'-\mathbf{k}) - \frac{1}{2\pi}(\mathbf{K}-\mathbf{g})_{\nu'}\widetilde{\boldsymbol{\nabla} u}_{\nu\nu'}(\mathbf{k}-\mathbf{k}')\right]\Bigg\}, \end{aligned} \tag{5.36}$$

where $\xi = \sqrt{\mathcal{V}/\mathcal{A}L}$ parameterizes the strength of the light-matter interaction. Performing similar analysis for the intrasublattice matrix elements in equation (5.17) yields

$$\begin{aligned}\mathcal{D}_{\perp}^{\mathrm{AA/BB}}(\mathbf{k},\mathbf{k}',\omega) =&\sum_{\mathbf{g}} \frac{\omega^2\xi^2}{\omega_{\mathbf{K}-\mathbf{g}}^2-\omega^2} \Bigg\{ \delta(\mathbf{k}'-\mathbf{k}) - \frac{1}{2\pi}\widetilde{\boldsymbol{\nabla} u}_{\nu\nu}(\mathbf{k}'-\mathbf{k}) \\ &- \frac{2c^2(\mathbf{K}-\mathbf{g})_\nu}{\omega_{\mathbf{K}-\mathbf{g}}^2-\omega^2}\left[k'_\nu\delta(\mathbf{k}'-\mathbf{k}) - \frac{1}{2\pi}(\mathbf{K}-\mathbf{g})_{\nu'}\widetilde{\boldsymbol{\nabla} u}_{\nu\nu'}(\mathbf{k}-\mathbf{k}')\right]\Bigg\} \\ &- \mathrm{Re}[G_{\perp}^{\mathrm{TEM}}(0,\omega)]\delta(\mathbf{k}'-\mathbf{k})\,. \end{aligned} \tag{5.37}$$

Finally, after exploiting the symmetry of the unstrained lattice (see appendix C.1 for details) one can simplify equation (5.36) to obtain

$$\begin{aligned}\mathcal{D}_{\perp}^{\mathrm{AB}}(\mathbf{k},\mathbf{k}',\omega) = -\sum_{\mathbf{g}} \frac{2c^2\omega^2\xi^2\phi_{\mathbf{g}}(\mathbf{K}-\mathbf{g})_x}{(\omega_{\mathbf{K}-\mathbf{g}}^2-\omega^2)^2} \Bigg\{ &(k'_x - \mathrm{i}k'_y)\delta(\mathbf{k}'-\mathbf{k}) \\ -\frac{1}{2\pi}(\mathbf{K}-\mathbf{g})_x\left[\tilde{\varepsilon}_{xx}(\mathbf{k}-\mathbf{k}') - \tilde{\varepsilon}_{yy}(\mathbf{k}-\mathbf{k}') + 2\mathrm{i}\tilde{\varepsilon}_{xy}(\mathbf{k}-\mathbf{k}')\right]&\Bigg\}, \end{aligned} \tag{5.38}$$

and one can simplify equation (5.37) to obtain

$$\begin{aligned}\mathcal{D}_{\perp}^{\mathrm{AA/BB}}(\mathbf{k},\mathbf{k}',\omega) = -\mathrm{Re}[G_{\perp}^{\mathrm{TEM}}(0,\omega)]\delta(\mathbf{k}'-\mathbf{k}) + \sum_{\mathbf{g}} \frac{\omega^2\xi^2}{\omega_{\mathbf{K}-\mathbf{g}}^2-\omega^2} \Bigg\{ &\delta(\mathbf{k}'-\mathbf{k}) \\ -\frac{1}{2\pi}\left[\tilde{\varepsilon}_{xx}(\mathbf{k}'-\mathbf{k}) + \tilde{\varepsilon}_{yy}(\mathbf{k}'-\mathbf{k})\right]\left[1 - \frac{2c^2(\mathbf{K}-\mathbf{g})_x^2}{\omega_{\mathbf{K}-\mathbf{g}}^2-\omega^2}\right]&\Bigg\}. \end{aligned} \tag{5.39}$$

5.3.3 Effective Hamiltonian with strain-induced pseudo-gauge fields

To obtain an effective Hamiltonian for the polariton envelope fields, we first linearize the coupled-dipole equations by evaluating the polarizability correction and the transverse dynamical matrix at the cavity resonant frequency. Next, we neglect non-radiative losses for simplicity and approximate $\omega_{\mathrm{cav}}^2 - \omega^2 \simeq 2\omega_{\mathrm{cav}}(\omega_{\mathrm{cav}} - \omega)$. Finally, after Fourier transforming equation (5.14) to the real-space and time domains, we obtain an effective equation of motion which reads ($\hbar = 1$)

$$\mathrm{i}\frac{\partial}{\partial t}\psi_\tau(\boldsymbol{\rho}, t) = \mathcal{H}_\tau \psi_\tau(\boldsymbol{\rho}, t)\,, \tag{5.40}$$

where the spinor envelope field in the K/K' valley is given by

$$\psi_\tau(\boldsymbol{\rho}, t) = \begin{bmatrix} \psi_{\mathrm{A}}^\tau(\boldsymbol{\rho}, t) \\ \psi_{\mathrm{B}}^\tau(\boldsymbol{\rho}, t) \end{bmatrix}. \tag{5.41}$$

The effective Hamiltonian governing the evolution of the spinor envelope field in the K valley reads

$$\mathcal{H}_+ = \omega_{\mathrm{D}}(L)\mathbb{1}_2 + \mathrm{i}v_{\mathrm{D}}(L)\boldsymbol{\sigma}\cdot\boldsymbol{\nabla} + \mathit{\Phi}(\boldsymbol{\rho}, L)\mathbb{1}_2 + \boldsymbol{\sigma}\cdot\mathbf{A}(\boldsymbol{\rho}, L)\,, \tag{5.42}$$

while the effective Hamiltonian for the K' valley is related via $\mathcal{T}$ symmetry $\mathcal{H}_- = \mathcal{H}_+^*$.

Therefore, in the absence of strain, the polaritons are effectively described by a 2D massless Dirac Hamiltonian with a linear Dirac cone dispersion, where the Dirac frequency and Dirac velocity were derived in chapter 4 and are given by equation (4.41) and equation (4.42), respectively. As schematically shown in figure 5.2, the applied strain can shift the Dirac cone in frequency which is effectively described by a pseudo-scalar potential that reads

$$\mathit{\Phi}(\boldsymbol{\rho}, L) = \mathit{\Phi}_0(L)[\varepsilon_{xx}(\boldsymbol{\rho}) + \varepsilon_{yy}(\boldsymbol{\rho})]\,. \tag{5.43}$$

Furthermore, since the strain breaks the $\mathcal{C}_3$ symmetry, it can also shift the Dirac cone in momentum space which is effectively described by a pseudo-vector potential that reads

$$\mathbf{A}(\boldsymbol{\rho}, L) = A_0(L)\left[\,\varepsilon_{xx}(\boldsymbol{\rho}) - \varepsilon_{yy}(\boldsymbol{\rho})\,,\, -2\varepsilon_{xy}(\boldsymbol{\rho})\,\right]. \tag{5.44}$$

Consequently, if the strain pattern varies with position then the pseudo-scalar potential can give rise to an effective pseudo-electric field

$$\mathbf{E}(\boldsymbol{\rho}, L) = \boldsymbol{\nabla}\mathit{\Phi}(\boldsymbol{\rho}, L)\,, \tag{5.45}$$

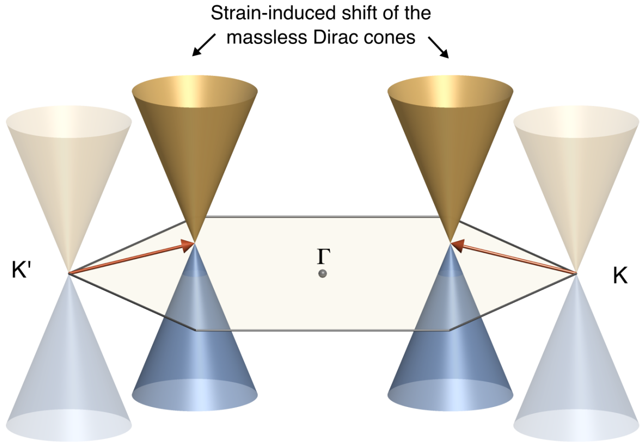

Figure 5.2 | Strain-induced shift of the massless Dirac cones. The unstrained honeycomb metasurface supports massless Dirac polaritons which are characterized by massless Dirac cones near the high-symmetry K/K′ points. Applying a strain pattern renders the dipole-dipole interactions anisotropic which breaks $\mathcal{C}_3$ symmetry but preserves $\mathcal{T}$ and $\mathcal{I}$ symmetry. This leads to a shift of the massless Dirac cones in frequency and momentum space which is effectively described by a pseudo-scalar and pseudo-vector potential, respectively. Therefore, by judiciously engineering an inhomogeneous strain pattern one can generate a pseudo-electric and pseudo-magnetic field for the polaritons, where the latter has opposite signs for the two valleys by virtue of $\mathcal{T}$ symmetry.

while the pseudo-vector potential can give rise to an effective pseudo-magnetic field

$$\mathbf{B}_\tau(\boldsymbol{\rho}, L) = \tau \boldsymbol{\nabla} \times \mathbf{A}(\boldsymbol{\rho}, L) \tag{5.46}$$

which, by virtue of $\mathcal{T}$ symmetry, has opposite signs for the K/K' valleys.

It is important to stress that the symmetry of the honeycomb metasurface dictates how the pseudo-gauge potentials depend on the strain tensor [21]; in fact, the general form of the pseudo-gauge potentials in equation (5.43) and equation (5.44) is precisely what is found for graphene and artificial graphene systems. However, the symmetry tells us nothing about the magnitude of the pseudo-gauge potentials for a given strain configuration because this depends on the specific details of the system. For the honeycomb metasurface, the strain-independent parameter in the pseudo-scalar potential reads

$$\begin{aligned}\Phi_0(L) = {} & \mu\frac{\omega_0}{\omega_\mathrm{cav}}\sum_{\mathbf{R}\neq 0} G_\parallel(\mathbf{R})\mathrm{e}^{-\mathrm{i}\mathbf{K}\cdot\mathbf{R}}\frac{(\mathbf{R})_x^2}{|\mathbf{R}|^2}\beta(\mathbf{R}) \\ & +\mu\frac{\omega_0}{\omega_\mathrm{cav}}\sum_{\mathbf{g}}\left[\frac{\omega_\mathrm{cav}^2\xi^2}{\omega_{\mathbf{K}-\mathbf{g}}^2-\omega_\mathrm{cav}^2} - \frac{2\omega_\mathrm{cav}^2\xi^2c^2(\mathbf{K}-\mathbf{g})_x^2}{(\omega_{\mathbf{K}-\mathbf{g}}^2-\omega_\mathrm{cav}^2)^2}\right],\end{aligned} \tag{5.47}$$

and the strain-independent parameter in the pseudo-vector potential is given by

$$\begin{aligned} A_0(L) = &\mu\frac{\omega_0}{\omega_{\text{cav}}}\sum_{\mathbf{R}} G_{\parallel}(\mathbf{R}-\mathbf{d})\mathrm{e}^{-\mathrm{i}\mathbf{K}\cdot(\mathbf{R}-\mathbf{d})}\frac{(\mathbf{R}-\mathbf{d})_x^2}{|\mathbf{R}-\mathbf{d}|^2}\beta(\mathbf{R}-\mathbf{d}) \\ &-\mu\frac{\omega_0}{\omega_{\text{cav}}}\sum_{\mathbf{g}}\frac{2\omega_{\text{cav}}^2\xi^2c^2(\mathbf{K}-\mathbf{g})_x^2\phi_{\mathbf{g}}}{(\omega_{\mathbf{K}-\mathbf{g}}^2-\omega_{\text{cav}}^2)^2}\,. \end{aligned} \tag{5.48}$$

It is clear from equation (5.47) and equation (5.48) that the magnitude of the pseudo-gauge potentials in the strained metasurface, and therefore the corresponding pseudo-electromagnetic fields, depend critically on the nature of the dipole-dipole interactions.

5.3.4 Cavity-tunable pseudo-gauge potentials

In figures 5.3(a)-(b) we show how the strain-independent parameters in the pseudo-gauge potentials can be tuned by varying only the cavity width (solid black lines). We also show the separate contributions from the Coulomb interactions (dotted blue lines) and the photon-mediated interactions (dashed orange lines). Remarkably, there exists critical cavity widths (L_Φ and L_A) where these parameters vanish identically, thereby switching off the pseudo-gauge potentials entirely.

We stress that this is a highly non-trivial result. It says that, at the critical cavity width L_A, you can perturb the lattice with any strain pattern that you choose and no pseudo-vector potential will be generated, despite the anisotropy in the dipole-dipole interactions. Physically, this means that the strain-induced change in the dipole locations within the metasurface does not change the interaction energy between the sublattices. Within a nearest-neighbour tight-binding model this would require one to engineer a hopping parameter that does not vary with distance; this is obviously impossible to achieve with photonic analogs of graphene where the strength of the evanescent coupling strictly decreases with the separation distance [58–60].

In general, the strain does change the interaction energy between any pair of dipoles in the metasurface; however, the sum of all these changes can be made to vanish. Crucially, while the contributions from the short-range Coulomb interactions and long-range photon-mediated interactions are always finite and never vanish individually, they have opposite signs and thus tend to compensate each other in the pseudo-gauge potentials. At the critical cavity widths, these contributions perfectly cancel making the pseudo-gauge potentials vanish. This ability to switch off and tune the pseudo-gauge potentials without modifying the strain opens up new perspectives beyond previously studied tight-binding models.

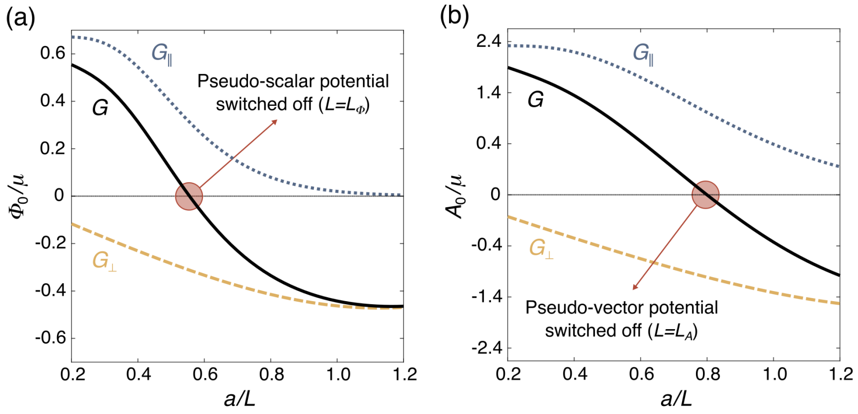

Figure 5.3 | Cavity-tunable pseudo-gauge potentials. (a)-(b) Evolution of the strain-independent parameters in the pseudo-scalar potential (Φ_0) and pseudo-vector potential (A_0) as the cavity width is reduced (black solid lines). We also show the separate contributions emerging from the Coulomb interactions (blue dotted lines) and the photon-mediated interactions (orange dashed lines) which have opposite signs. At critical cavity widths (L_Φ and L_A) these contributions perfectly cancel resulting in the pseudo-gauge potentials being switched off for any strain configuration. Results obtained with $\lambda_0 = 6.5a$ and $\mu = 0.01\omega_0$.

5.4 Tunable Lorentz-like force for polaritons

Throughout the rest of this chapter, we will focus on some of the implications of the tunable pseudo-vector potential and the corresponding pseudo-magnetic field. Specifically, we consider a strain configuration described by the displacement field [22]

$$\mathbf{u}(\boldsymbol{\rho}) = \frac{\Delta}{a}\Big[\, 2xy\,,\, x^2 - y^2 \,\Big]\,, \tag{5.49}$$

where Δ is a measure of the strain magnitude. This trigonal strain configuration gives rise to a vanishing pseudo-scalar potential (because the trace of the strain tensor is zero) and a pseudo-vector potential that reads

$$\mathbf{A}(\boldsymbol{\rho}, L) = \frac{4\Delta A_0}{a}\Big[\, y\,,\, -x \,\Big]\,. \tag{5.50}$$

This is analogous to the symmetric gauge in electrodynamics and leads to a uniform pseudo-magnetic field

$$\mathbf{B}_\tau(L) = -\tau\frac{8\Delta A_0}{a}\hat{\mathbf{z}} \tag{5.51}$$

which points normal to the plane of the metasurface.

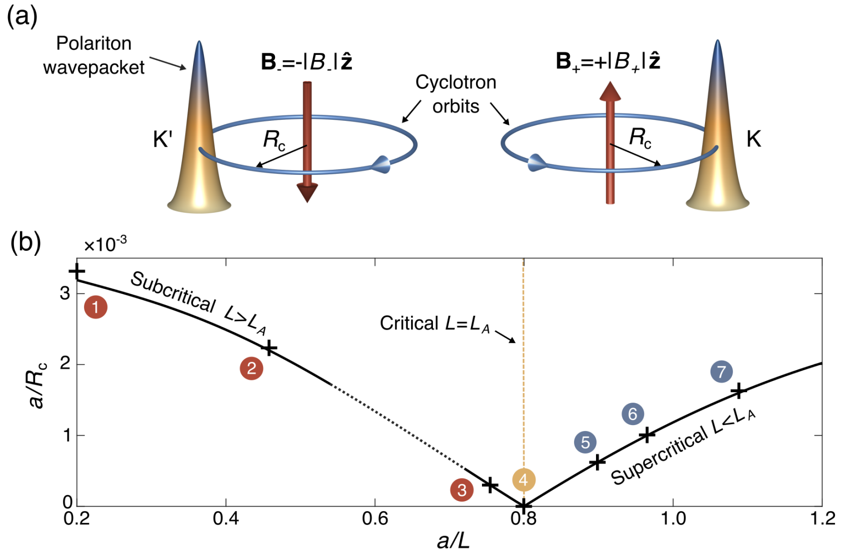

Figure 5.4 | Cavity-tunable cyclotron orbits. (a) Schematic of the cyclotron motion exhibited by polariton wavepackets due to a Lorentz-like force generated by a pseudo-magnetic field which has opposite signs in the K/K′ valleys. (b) Predicted evolution of the cyclotron orbit radius as the cavity width is reduced for a fixed strain configuration at a fixed frequency relative to the Dirac point. The crosses correspond to the calculated radii of the simulated trajectories in figure 5.5, which show very good agreement with the analytical predictions. Results obtained with $\lambda_0 = 6.5a$, $\mu = 0.01\omega_0$, $\delta\omega = -0.1\mu$ and $\varDelta = 2 \times 10^{-5}$.

Therefore, in the ‘semiclassical’ limit [264], polariton wavepackets propagating through the strained metasurface behave as if they were subjected to a Lorentz-like force

$$\mathbf{F}_\tau(L) = \operatorname{sgn}(v_\mathrm{D})\hat{\mathbf{v}} \times \mathbf{B}_\tau \tag{5.52}$$

which acts perpendicular to the group velocity direction $\hat{\mathbf{v}}$. Consequently, the polaritons will exhibit cyclotron motion, as schematically depicted in figure 5.4(a), in direct analogy with charged particles in real magnetic fields. Crucially, by modifying the cavity width one can tune the magnitude of the Lorentz-like force and the effective cyclotron mass of the Dirac polaritons which is given by

$$m_c(L) = \frac{\delta\omega}{v_\mathrm{D}^2}\,, \tag{5.53}$$

where $\delta\omega = \omega - \omega_\mathrm{D}$ is the frequency relative to the Dirac point.

The corresponding radius of the cyclotron orbit reads

$$R_\mathrm{c}(L) = \frac{|m_c| v_\mathrm{D}^2}{|\mathbf{F}_\tau|}\,, \tag{5.54}$$

and in figure 5.4(b) we show how this can be tuned by varying only the cavity width at a fixed frequency relative to the Dirac point. Note, the dotted line indicates the region of cavity widths for which the linear Dirac cone approximation breaks down due to the vanishing Dirac velocity (see appendix D.1 for details). One observes that the cyclotron orbit radius increases as the cavity width is reduced, until the critical width where the pseudo-magnetic field is switched off and the polaritons no longer exhibit cyclotron motion. Beyond this critical width, the polariton cyclotron radius decreases as the cavity width is reduced further.

5.4.1 Split-operator method for simulating polariton wavepackets

To verify these analytical predictions, we can simulate the evolution of polariton wavepackets in the strained metasurface using the effective Hamiltonian given by equation (5.42). To do this, we use the second-order split-operator method [25] to approximate the time evolution of the polariton envelope fields. After a small time δt has elapsed the polariton envelope field in the K valley is given by

$$\psi_+(\boldsymbol{\rho}, t+\delta t) = \mathrm{e}^{-\mathrm{i}\mathcal{H}_+\delta t}\psi_+(\boldsymbol{\rho}, t)\,. \tag{5.55}$$

In the second-order split operator method, the evolution operator in equation (5.55) is approximated as

$$\mathrm{e}^{-\mathrm{i}\mathcal{H}_+\delta t} = \mathrm{e}^{-\frac{\mathrm{i}}{2}\mathcal{H}^{\varepsilon}_+\delta t}\mathrm{e}^{-\mathrm{i}\mathcal{H}^{0}_+\delta t}\mathrm{e}^{-\frac{\mathrm{i}}{2}\mathcal{H}^{\varepsilon}_+\delta t} + \mathcal{O}(\delta t^3)\,, \tag{5.56}$$

where $\mathcal{H}^0_+ = \omega_\mathrm{D}\mathbb{1}_2 + \mathrm{i}v_\mathrm{D}\boldsymbol{\sigma}\cdot\boldsymbol{\nabla}$ and $\mathcal{H}^\varepsilon_+ = \varPhi(\boldsymbol{\rho})\mathbb{1}_2 + \boldsymbol{\sigma}\cdot\mathbf{A}(\boldsymbol{\rho})$. Note, the cubic error in δt is due to the noncommutativity of the position and gradient operators.

To calculate the field after time $N_t\delta t$ has elapsed we have to apply the operation in equation (5.56) iteratively

$$\psi_+(\boldsymbol{\rho}, t+N_t\delta t) \approx \prod_{i=1}^{N_t}\left(\mathcal{M}^+_{\boldsymbol{\rho}}\mathscr{F}^{-1}\mathcal{M}^+_{\mathbf{k}}\mathscr{F}\mathcal{M}^+_{\boldsymbol{\rho}}\right)\psi_+(\boldsymbol{\rho}, t)\,, \tag{5.57}$$

where $\mathscr{F}$ and $\mathscr{F}^{-1}$ represent the direct and inverse Fourier transform operations, respectively. Using the standard identity for the exponential of Pauli matrices, we can write the position-dependent operator in equation (5.57) as

$$\mathcal{M}^+_{\boldsymbol{\rho}} = \mathrm{e}^{-\mathrm{i}\delta t\varPhi/2}\left[\cos\left(\delta t A/2\right)\mathbb{1}_2 - \mathrm{i}\frac{\sin\left(\delta t A/2\right)}{A}\boldsymbol{\sigma}\cdot\mathbf{A}\right]\,, \tag{5.58}$$

and the momentum-dependent operator as

$$\mathcal{M}_{\mathbf{k}}^{+} = \mathrm{e}^{-\mathrm{i}\omega_{\mathrm{D}}\delta t} \left[\cos\left(v_{\mathrm{D}} k \delta t\right) \mathbb{1}_2 + \mathrm{i} \frac{\sin\left(v_{\mathrm{D}} k \delta t\right)}{k} \boldsymbol{\sigma} \cdot \mathbf{k} \right] . \tag{5.59}$$

Similarly, the evolution of the polariton envelope field in the K' valley can be approximated as

$$\psi_{-}(\boldsymbol{\rho}, t + N_t \delta t) \approx \prod_{i=1}^{N_t} \left(\mathcal{M}_{\boldsymbol{\rho}}^{-} \mathscr{F}^{-1} \mathcal{M}_{\mathbf{k}}^{-} \mathscr{F} \mathcal{M}_{\boldsymbol{\rho}}^{-} \right) \psi_{-}(\boldsymbol{\rho}, t) \,, \tag{5.60}$$

where the operators $\mathcal{M}_{\boldsymbol{\rho}}^{-}$ and $\mathcal{M}_{\mathbf{k}}^{-}$ are related to equations (5.58) and (5.59) by the replacement $\boldsymbol{\sigma} \leftrightarrow \boldsymbol{\sigma}^*$ and $\mathbf{k} \leftrightarrow -\mathbf{k}$.

For the simulations we initialize the following Gaussian wavepackets

$$\psi_{+}(\boldsymbol{\rho}, t = 0) = \frac{1}{2w\sqrt{2\pi}} \mathrm{e}^{-\frac{\rho^2}{2w^2}} \begin{bmatrix} 1 \\ -\operatorname{sgn}(v_{\mathrm{D}}) \end{bmatrix} \mathrm{e}^{\mathrm{i}\mathbf{k}_0 \cdot \boldsymbol{\rho}} \,, \tag{5.61}$$

and

$$\psi_{-}(\boldsymbol{\rho}, t = 0) = \frac{1}{2w\sqrt{2\pi}} \mathrm{e}^{-\frac{\rho^2}{2w^2}} \begin{bmatrix} 1 \\ \operatorname{sgn}(v_{\mathrm{D}}) \end{bmatrix} \mathrm{e}^{\mathrm{i}\mathbf{k}_0 \cdot \boldsymbol{\rho}} \,, \tag{5.62}$$

in the K and K' valleys, respectively. We consider wavepackets that are located in the lower polariton band with a fixed central frequency of $\delta\omega = -0.1\mu$ relative to the Dirac point, and an initial central wavevector $\mathbf{k}_0 = \left[-\left|\delta\omega / v_{\mathrm{D}}\right| , 0 \right]$. Furthermore, the wavepackets are initially centred at the origin with a width of $w = 100a$. We then track the centre-of-mass trajectory of the wavepackets for the two valleys which is given by

$$\langle \boldsymbol{\rho} \rangle_{\tau} = \frac{\iint \mathrm{d}^2\boldsymbol{\rho} \, |\psi_{\tau}|^2 \boldsymbol{\rho}}{\iint \mathrm{d}^2\boldsymbol{\rho} \, |\psi_{\tau}|^2} \,. \tag{5.63}$$

5.4.2 Tunable cyclotron orbits

In figure 5.5 we plot the trajectories of the wavepackets through a metasurface with a fixed strain configuration but different cavity widths. As expected, the polariton wavepackets in the K/K' valleys undergo cyclotron motion in opposite directions due to $\mathcal{T}$ symmetry (for example, see the snapshots along trajectory 6). Furthermore, the calculated orbit radii for trajectories 1-7 are given by the crosses in figure 5.4(b) and they agree very well with the

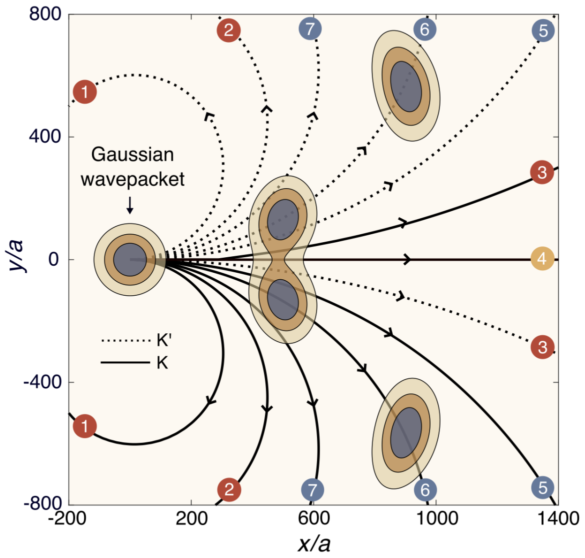

Figure 5.5 | Simulated cyclotron motion of polariton wavepackets. Simulated trajectories of Gaussian wavepackets propagating through a strained metasurface with different cavity widths. The calculated radii for trajectories 1-7 are given by the crosses in figure 5.4(b). The snapshots along trajectory 6 show that the wavepackets in the K/K' valleys exhibit cyclotron motion in opposite directions by virtue of $\mathcal{T}$ symmetry. For subcritical cavity widths ($L > L_A$), the cyclotron radius expands as the cavity width is reduced (trajectories 1-3), until the critical width ($L = L_A$) where the wavepackets feel no Lorentz-like force (trajectory 4). For supercritical cavity widths ($L < L_A$), the cyclotron orbits re-emerge and the orbit radius shrinks as the cavity width is reduced further (trajectories 5-7). Results obtained with $\lambda_0 = 6.5a$, $\mu = 0.01\omega_0$, $\delta\omega = -0.1\mu$ and $\Delta = 2 \times 10^{-5}$.

analytical predictions. Note that the direction of the orbit depends on the signs of the Dirac velocity, cyclotron mass and pseudo-magnetic field.

For subcritical cavity widths $L > L_A$, the cyclotron radius expands as the cavity width is reduced (see trajectories 1–3). At the critical cavity width $L = L_A$, the pseudo-magnetic field is switched off and the polariton wavepackets feel no Lorentz-like force; they propagate through the strained metasurface as if there was no strain present at all (see trajectory 4). For supercritical cavity widths $L < L_A$, the cyclotron orbits re-emerge and the cyclotron radius now shrinks as the cavity width is reduced further (see trajectories 5–7).

5.5 Collapse and revival of the polariton Landau levels

As the magnitude of the strain is increased, the pseudo-magnetic field can reach large enough values such that one enters the ‘quantum’ regime, where the polariton cyclotron orbits undergo Landau quantization in direct analogy with charged particles in real magnetic fields [133]. Therefore, as schematically depicted in figure 5.6(a), the massless Dirac cone collapses

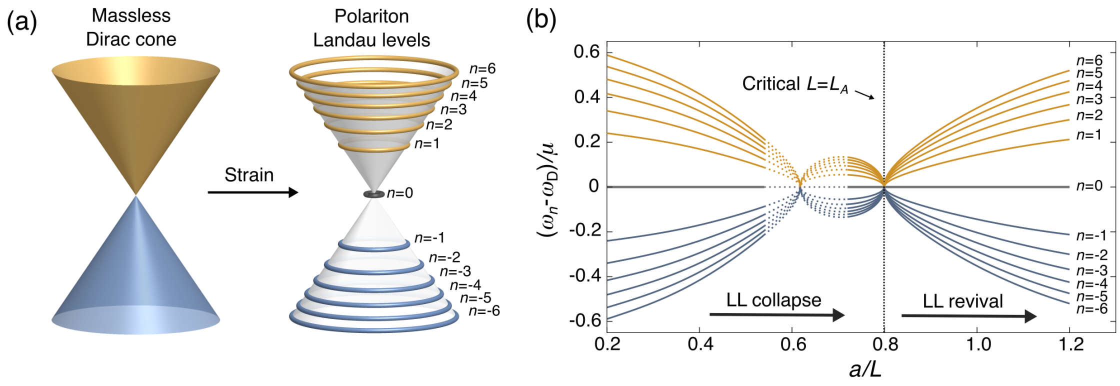

Figure 5.6 | Cavity-induced collapse and revival of the polariton Landau levels. (a) Schematic of the massless Dirac cone splitting into quantized polariton Landau levels due to a strain-induced pseudo-magnetic field. (b) Predicted evolution of the polariton Landau levels as the cavity width is reduced for a fixed strain configuration, where the dotted lines indicate the region of cavity widths where the linear Dirac cone approximation breaks down. The transition of the dominant dipolar coupling from Coulomb to photon-mediated interactions is accompanied by a collapse and revival of the polariton Landau levels. Results obtained with $\lambda_0 = 6.5a$, $\mu = 0.01\omega_0$ and $\mathit{\Delta} = 0.002$.

into a quantized Landau level spectrum

$$\omega_n(\mathit{\Delta}, L) = \omega_{\mathrm{D}}(L) + \mathrm{sgn}(n)\omega_{\mathrm{c}}(\mathit{\Delta}, L)\sqrt{|n|}\,, \tag{5.64}$$

where $n = 0, \pm1, \pm2\ldots$ is the Landau level index and $\omega_{\mathrm{c}}(\mathit{\Delta}, L) = \sqrt{2|v_{\mathrm{D}}||\mathbf{B}_\tau|}$. In analogy with graphene, the polariton Landau levels exhibit a square-root dependence on the Landau level index and the pseudo-magnetic field strength, and there also exists a $n = 0$ Landau level that is independent of the pseudo-magnetic field strength – this is a direct manifestation of the pseudo-relativistic nature of the massless Dirac polaritons (see appendix D.2 for more details).

In the previously realized photonic analog of graphene, the Landau level spectrum was fixed by the engineered strain configuration – to modify the pseudo-magnetic field they had to fabricate an entirely new structure with a different strain pattern [68]. In stark contrast, here the polariton Landau level spectrum depends qualitatively on the surrounding electromagnetic environment which mediates the dipole-dipole interactions. In fact, as shown in figure 5.6(b), one can drastically reconfigure the polariton Landau level spectrum by varying only the cavity width. As before, the dotted line indicates the region of cavity widths where the linear Dirac cone approximation breaks down (see appendix D.3 for more details). Remarkably, the transition of the dominant dipolar coupling from Coulomb to photon-mediated interactions as the cavity width is reduced results in a collapse and revival of the polariton Landau levels, despite the strain configuration being fixed.

5.5.1 Multiple scattering theory inside the cavity waveguide

It is important to stress that these analytical predictions are only valid within the approximations of the effective Hamiltonian. Therefore, a priori, it is not obvious that the predicted collapse and revival of the polariton Landau levels will be observable in a real finite system. For example, do higher order effects of the strain become more important when the interactions are long-range? To verify the analytical predictions, we go beyond the approximations of the effective Hamiltonian and develop a full multiple scattering theory.

The polarizability of a dipole emitter is altered by the electromagnetic environment in which it is embedded – for example, we have already seen that the presence of the cavity waveguide leads to a renormalized polarizability. Similarly, the presence of other dipoles within close proximity can dramatically modify their properties due to collective interactions. To describe how a dipole located at $\mathbf{R}_0$ responds to a local driving field we can introduce an effective polarizability

$$\alpha_{\text{eff}}(\omega) = \Big[\alpha^{-1}(\omega) - S(\mathbf{R}_0, \mathbf{R}_0, \omega)\Big]^{-1} . \tag{5.65}$$

Here, the scattered Green's function $S(\mathbf{R}_0, \mathbf{R}_0, \omega)$ describes the field at $\mathbf{R}_0$ that has been scattered back by all the other dipoles within the metasurface. From the effective polarizability we can define the local spectral function $\mathrm{Im}[\alpha_{\text{eff}}(\omega)]$ which is related to the local density of states and characterizes the full spectral response of the metasurface.

Let us first consider a simple case where there are only two additional dipoles located at $\mathbf{R}_1$ and $\mathbf{R}_2$. The scattered Green's function can be written as an infinite series of terms

$$\begin{aligned} S(\mathbf{R}_0, \mathbf{R}_0, \omega) &= G(\mathbf{R}_0 - \mathbf{R}_1, \omega)\alpha(\omega)G(\mathbf{R}_1 - \mathbf{R}_0, \omega) \\ &+ G(\mathbf{R}_0 - \mathbf{R}_2, \omega)\alpha(\omega)G(\mathbf{R}_2 - \mathbf{R}_0, \omega) \\ &+ G(\mathbf{R}_0 - \mathbf{R}_1, \omega)\alpha(\omega)G(\mathbf{R}_1 - \mathbf{R}_2, \omega)\alpha(\omega)G(\mathbf{R}_2 - \mathbf{R}_0, \omega) \\ &+ G(\mathbf{R}_0 - \mathbf{R}_2, \omega)\alpha(\omega)G(\mathbf{R}_2 - \mathbf{R}_1, \omega)\alpha(\omega)G(\mathbf{R}_1 - \mathbf{R}_0, \omega) + \dots , \end{aligned} \tag{5.66}$$

where each term describes a unique scattering event. The infinite series in equation (5.66) can be formally summed as

$$S(\mathbf{R}_0, \mathbf{R}_0, \omega) = \sum_{v=1}^{2} \sum_{v'=1}^{2} G(\mathbf{R}_0 - \mathbf{R}_v, \omega)[T^{(2)}(\omega)]_{vv'} G(\mathbf{R}_{v'} - \mathbf{R}_0, \omega) , \tag{5.67}$$

where the two-dipole T-matrix reads

$$T^{(2)}(\omega) = \frac{\alpha(\omega)}{1 - G(\mathbf{R}_1 - \mathbf{R}_2, \omega)\alpha(\omega)G(\mathbf{R}_2 - \mathbf{R}_1, \omega)\alpha(\omega)} \begin{bmatrix} 1 & G(\mathbf{R}_1 - \mathbf{R}_2, \omega)\alpha(\omega) \\ G(\mathbf{R}_2 - \mathbf{R}_1, \omega)\alpha(\omega) & 1 \end{bmatrix} . \tag{5.68}$$

We can now generalize this to include N addition dipoles where the scattered Green's function reads

$$S(\mathbf{R}_0, \mathbf{R}_0, \omega) = \sum_{v=1}^{N} \sum_{v'=1}^{N} G(\mathbf{R}_0 - \mathbf{R}_v, \omega)[T^{(N)}(\omega)]_{vv'} G(\mathbf{R}_{v'} - \mathbf{R}_0, \omega) , \tag{5.69}$$

which encodes all the multiple scattering events between the N additional dipoles. The N-dipole T-matrix is given by the inversion of a large $N \times N$ matrix $T^{(N)}(\omega) = [M^{(N)}(\omega)]^{-1}$ whose matrix elements are given by

$$[M(\omega)]_{vv'} = \alpha^{-1}(\omega)\delta_{vv'} - (1 - \delta_{vv'})G(\mathbf{R}_v - \mathbf{R}_{v'}, \omega) . \tag{5.70}$$

Note that this multiple scattering theory goes beyond the approximations of the effective Hamiltonian in several ways. Firstly, we use the full Green's function given by equation (6.8), and therefore it includes the effect of all cavity modes. Secondly, we keep the frequency dependence in the polarizability correction and the Green's function, thus going beyond the pole approximation that we made to linearize the coupled-dipole equations. Lastly, while the effective Hamiltonian is only strictly valid for small strains and for a small range of frequencies within the vicinity of the Dirac point, the multiple scattering theory determines the exact response for all frequencies and for any strain configuration.

5.5.2 Cavity-tunable polariton Landau levels

In the upper panel of figure 5.7(a), we show the local spectral function at the centre of the unstrained metasurface with a subcritical cavity width ($L \gg L_A$) where the Coulomb interactions are dominant. One observes that the strong multiple scattering within the metasurface drastically modifies the response of the dipole; we no longer have a single Lorentzian peak as shown in figure 3.3, but we have a continuum of polariton modes supported by the metasurface. In fact, the local spectral function is reminiscent of the electronic density of states in graphene [5]. We are particularly interested in the Dirac region which is highlighted in figure 5.7(a) – this region corresponds to the Dirac cone part of the polariton spectrum which is where our effective Hamiltonian is valid.

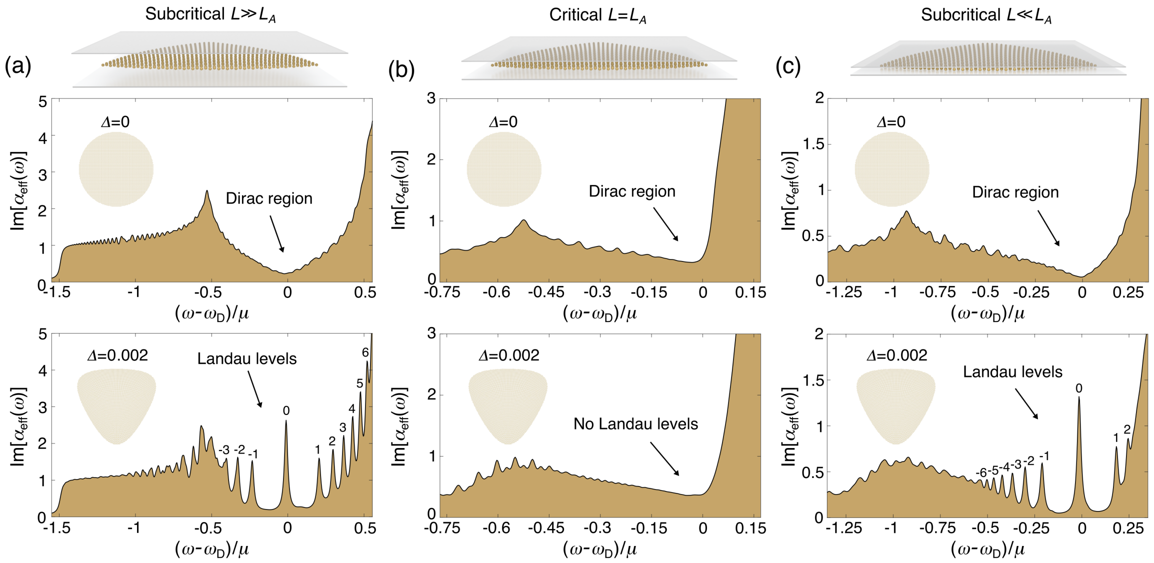

Figure 5.7 | Polariton Landau levels in the local spectral function. (a)-(c) Local spectral function at the centre of the metasurface on the B sublattice for varying cavity widths, where the upper panels correspond to the unstrained metasurface ($\varDelta = 0$) and the lower panels correspond to the strained metasurface ($\varDelta = 0.002$). (a) For subcritical cavity widths ($L \gg L_A$), we observe a series of sharp resonant peaks for the strained metasurface which are not present in the unstrained case – these directly correspond to the polariton Landau levels and they are labelled according to their Landau index. (b) At the critical cavity width ($L = L_A$), the pseudo-magnetic field is switched off and therefore no Landau level peaks are observed, despite the applied strain. (c) For supercritical cavity widths ($L \ll L_A$), we again observe Landau level peaks for the strained metasurface which are not present in the unstrained case, thus verifying the cavity-induced collapse and revival of the polariton Landau levels. Results obtained with parameters $\lambda_0 = 6.5a$, $\mu = 0.01\omega_0$ and $\gamma_{\mathrm{nr}} = 0.025\mu$, and the metasurfaces consist of approximately 14,000 dipoles (see insets). For panels (a), (b) and (c) we used cavity widths given by $a/L = 0.2$, $a/L = 0.83$ and $a/L = 1.2$, respectively.

In the lower panel of figure 5.7(a) we show the local spectral function for the strained metasurface with the same subcritical cavity width ($L \gg L_A$). One clearly observes a series of resonant peaks within the vicinity of the Dirac region which are not present in the unstrained case; these peaks directly correspond to the predicted polariton Landau levels and we label them according to their Landau index. Note that the spectral function has an asymmetry about the Dirac point due to the intrasublattice interactions which break the chiral symmetry. For example, more Landau levels can be observed above the Dirac point than below as the Dirac approximation holds for a wider frequency range. As the cavity width is reduced, the spacing between the Landau level peaks decreases in accordance with the analytical prediction (see appendix D.3 for more details).

In the upper panel of figure 5.7(b) we show the local spectral function for the unstrained metasurface at the critical cavity width ($L = L_A$). One observes that the spectrum is different compared to the subcritical regime – this is expected since the cavity modifies the polariton dispersion. In the lower panel of figure 5.7(b) we show the local spectral function for the strained metasurface with the same critical cavity width ($L = L_A$). Remarkably, despite the applied strain the Landau levels have completely vanished within the Dirac region; in fact, there is very little qualitative difference between the strained and unstrained cases. This is direct evidence that the pseudo-magnetic field is switched off at the critical cavity width. As the cavity width is reduced beyond this critical value, the Landau level peaks begin to re-emerge (see appendix D.3 for more details).

In the upper panel of figure 5.7(c) we show the local spectral function for the unstrained metasurface with a supercritical cavity width ($L \ll L_A$) where the photon-mediated interactions are dominant. One can see that the spectrum is qualitatively similar to critical cavity width case, albeit with a larger Dirac region. However, when strain is applied in the supercritical regime one observes a clear series of Landau level peaks as shown in the lower panel of figure 5.7(c), thus verifying the cavity-induced collapse and revival of the polariton Landau levels.

5.6 Conclusion

In this chapter we have shown that one can generate a pseudo-magnetic field for the polaritons by straining a honeycomb metasurface composed of a subwavelength array of dipole emitters/antennas. Crucially, in stark contrast to graphene, the emergent pseudo-magnetic field is not solely determined by the strain configuration, but it also depends sensitively on the surrounding electromagnetic environment which mediates the dipole-dipole interactions. Therefore, while the strain is required to create the pseudo-magnetic field, we have demonstrated that one can tune its strength by embedding the metasurface inside a cavity waveguide. Most interestingly, there exists a critical cavity width where the pseudo-magnetic is switched off entirely, despite the strain-induced anisotropy in the dipole-dipole interactions. This striking result challenges our naive intuition that has evolved from graphene and its artificial analogs, where anisotropic hopping parameters inevitably lead to a pseudo-vector potential. Consequently, we have shown that one can manipulate the cyclotron motion of polariton wavepackets and induce a collapse and revival of polariton Landau levels by varying a single external parameter: the cavity width. This is impossible to achieve with photonic systems that emulate the tight-binding physics of graphene where the pseudo-magnetic field is fixed by the engineered strain configuration.

6

Topological transitions for valley-Hall polaritons induced by cavity-mediated interactions

Topological valley-Hall edge states have been realized in a variety of photonic structures across the electromagnetic spectrum because they can be easily engineered by breaking certain lattice symmetries. However, the valley-Chern numbers that characterize the topological phase are usually fixed by design and therefore the valley-Hall edge states are forced to propagate in a fixed direction. In this chapter, we propose an alternative mechanism to induce topological transitions via accidental Dirac points in a kagome metasurface composed of dipole emitters/antennas. Crucially, the geometrical and topological properties of the polaritons are not solely determined by the symmetry-breaking perturbation, because they also depend qualitatively on the local electromagnetic environment which mediates the dipole-dipole interactions. To access different topological polariton phases, we embed the kagome metasurface inside a cavity waveguide which enables one to manipulate the Berry curvature within the Brillouin zone. Consequently, we demonstrate that one can invert the valley-Chern numbers and thus switch the chirality of the polariton valley-Hall edge states by modifying only the cavity width. This alternative approach to engineering topological transitions could have important implications for other topological phases such as photonic higher-order topological insulators.

This chapter presents original research that has been submitted for publication as follows:

Mann, C.-R. & Mariani, E. Topological transitions induced by cavity-mediated interactions in photonic metasurfaces. *arXiv:2010.01636* (2020).

6.1 Introduction

Topological phases of light exhibit unique properties beyond the realm of conventional photonics [73–75]. Within this paradigm, the valley-Hall topological insulator has attracted considerable interest because it does not require external magnetic fields or temporal modulation of the system parameters to break $\mathcal{T}$ symmetry; instead, the valley-Hall phase is easily induced by breaking certain lattice symmetries [82]. Due to this simple geometrical origin, valley-Hall topological insulators have been successfully realized in a variety of photonic structures at microwave [83–85], terahertz [86, 87] and optical [88–92] frequencies.

These works begin with hexagonal lattices that exhibit deterministic Dirac points at the K/K' points and then gap out the Dirac cones by breaking $\mathcal{I}$ symmetry (and/or $\mathcal{M}_y$ symmetry). These symmetry-breaking perturbations generate Berry curvature that is localized near the inequivalent valleys and the corresponding valley-Hall phase is characterized by non-trivial valley-Chern numbers. While these are not true topological invariants, there still exists a strong bulk-boundary correspondence for certain domain walls that separate regions with opposite valley-Chern numbers: the change in valley-Chern number across the interface predicts the number of valley-polarized chiral edge states that populate the interface. These can be exploited to transport light through certain disorder and sharp bends that do not mix the valleys – a tantalizing prospect that could have crucial implications for photonic devices such as topological waveguides [83–92], directional antennas [84], topological splitters [83], chiral quantum optical interfaces [91, 92] and topological lasers [86].

However, this simple geometrical origin of the valley-Hall phase comes at a price: the topological phase is usually dictated by the symmetry-breaking perturbation that is imprinted into the lattice design. To deterministically change the valley-Chern numbers one needs to invert the symmetry-breaking perturbation to induce a topological transition, passing through a critical point where the symmetry that gives rise to the deterministic Dirac points is restored. However, it is usually difficult, if not impossible to reconfigure every unit cell in the photonic lattice after it has been fabricated. Consequently, the valley-Chern numbers are generally fixed by design and therefore the topological edge states are forced to propagate in a fixed direction. This raises an intriguing question: is it possible to induce a topological transition without inverting the symmetry-breaking perturbation? While the symmetry-breaking perturbation generates a mass term in the Dirac Hamiltonian, the value of the mass depends on the details of the system and nothing in principle prevents us from tuning it to zero and switching its sign.

Here we propose a mechanism to induce topological transitions via accidental Dirac points in a kagome metasurface composed of a subwavelength array of dipole emitters/antennas. We break the $\mathcal{I}$ (and $\mathcal{M}_y$) symmetry by expanding/shrinking the distance between the dipoles within each unit cell. However, due to the hybrid light-matter nature of the polaritons, their geometric properties and the corresponding valley-Chern numbers are not fixed by this perturbation; they also depend qualitatively on the local electromagnetic environment which mediates the dipole-dipole interactions. Crucially, the short-range Coulomb interactions and long-range photon-mediated interactions generate a Dirac mass with opposite signs. This enables one to access different topological polariton phases by varying the nature of the dipole-dipole interactions via an enclosing cavity waveguide. At a critical cavity width the Dirac mass vanishes despite the broken symmetry; this results in accidental Dirac points emerging in the polariton spectrum which signifies a topological phase transition. Therefore, we demonstrate that one can invert the sign of the valley-Chern numbers and thus switch the propagation direction of the polariton valley-Hall edge states by modifying a single external parameter: the cavity width.

6.2 Symmetry-broken kagome metasurface

In figure 6.1(a) we schematically depict a kagome metasurface embedded inside a cavity waveguide. We model the dipoles with a bare polarizability of the form

$$\alpha_{\mathrm{B}}(\omega)=\frac{2\omega_0\mu}{\omega_0^2-\omega^2-\mathrm{i}\omega\gamma_{\mathrm{nr}}}\,, \tag{6.1}$$

where the corresponding induced dipole moments are assumed to point in the z-direction (see inset). In contrast to the honeycomb metasurface, the kagome metasurface has three inequivalent sublattices which are formed by placing dipoles at periodic positions $\mathbf{R}_i=\mathbf{R}+\mathbf{d}_i$ where $i=\mathrm{A},\mathrm{B},\mathrm{C}$ labels the three sublattices. Here, the basis vectors

$$\mathbf{d}_{\mathrm{A}}=\frac{a}{\sqrt{3}}\Big[0\,,\,1\Big]\,,\quad \mathbf{d}_{\mathrm{B}}=\frac{a}{2\sqrt{3}}\Big[\sqrt{3}\,,\,-1\Big]\,,\quad \mathbf{d}_{\mathrm{C}}=\frac{a}{2\sqrt{3}}\Big[-\sqrt{3}\,,\,-1\Big]\,, \tag{6.2}$$

locate the positions of the three dipoles within each unit cell as depicted in figure 6.1(b). Furthermore, $\mathbf{R}=l_1\mathbf{a}_1+l_2\mathbf{a}_2$ represents the set of lattice translation vectors, where $l_1,l_2\in\mathbb{Z}$ are integers, and

$$\mathbf{a}_1=a\Big[-1\,,\,\sqrt{3}\Big]\,,\quad \mathbf{a}_2=a\Big[1\,,\,\sqrt{3}\Big]\,, \tag{6.3}$$

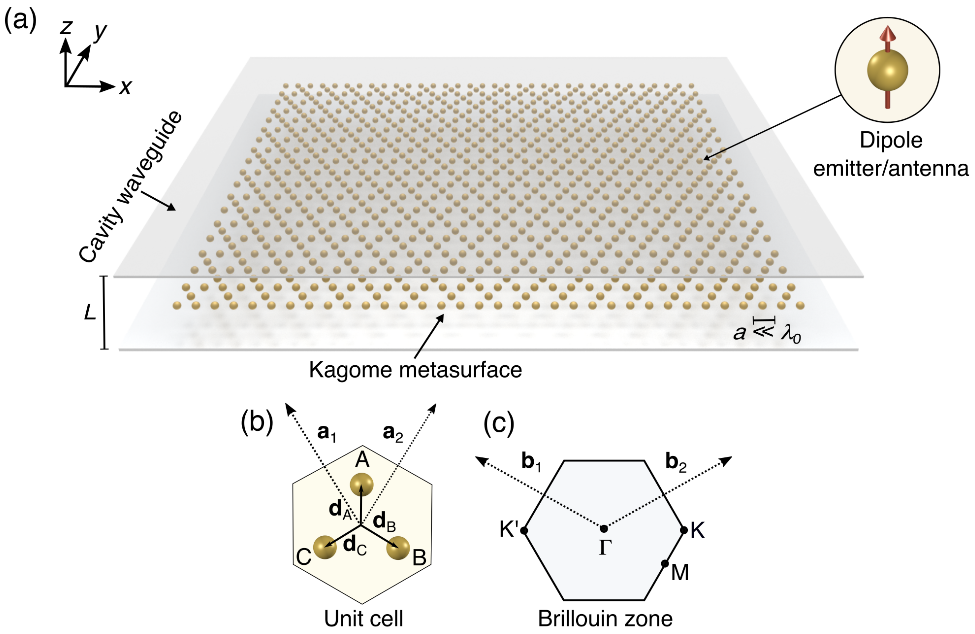

Figure 6.1 | Kagome metasurface inside a cavity waveguide. (a) Schematic of a kagome metasurface composed of an array of dipole emitters/antennas with subwavelength nearest-neighbour separation $a \ll \lambda_0$. The induced dipole moments are assumed to point in the z-direction (see inset). Furthermore, the kagome metasurface is embedded inside a cavity waveguide of width L, where the cavity walls are assumed to be perfect mirrors. (b) Corresponding unit cell that contains three dipoles with basis vectors $\mathbf{d}_\mathrm{A}$, $\mathbf{d}_\mathrm{B}$ and $\mathbf{d}_\mathrm{C}$, which gives rise to the A, B and C hexagonal sublattices, respectively. The primitive lattice vectors are $\mathbf{a}_1$ and $\mathbf{a}_2$. (c) Corresponding first Brillouin zone where the high-symmetry points are labeled, and $\mathbf{b}_1$ and $\mathbf{b}_2$ are the primitive reciprocal lattice vectors.

are the primitive lattice vectors. The corresponding set of reciprocal lattice vectors are $\mathbf{g} = n_1\mathbf{b}_1 + n_2\mathbf{b}_2$, where $n_1, n_2 \in \mathbb{Z}$ are integers, and

$$\mathbf{b}_1 = \frac{\pi}{\sqrt{3}a}\Big[-\sqrt{3}\,,\,1\Big], \quad \mathbf{b}_2 = \frac{\pi}{\sqrt{3}a}\Big[\sqrt{3}\,,\,1\Big], \tag{6.4}$$

are the primitive reciprocal lattice vectors that define the Brillouin zone shown in figure 6.1(c). Moreover, we consider the nearest-neighbour separation to be subwavelength $a \ll \lambda_0$, so that the polaritons near the K/K' points are subradiant and evanescently bound to the lattice. Finally, we embed the kagome metasurface at the centre of a cavity waveguide of width L, where the cavity walls are assumed to be perfect mirrors.

6.2.1 Symmetry-reducing perturbations

The point group symmetry of the unperturbed kagome metasurface is C_{6v}, while the little point group of the K/K' points is C_{3v}; consequently, the unperturbed kagome metasurface

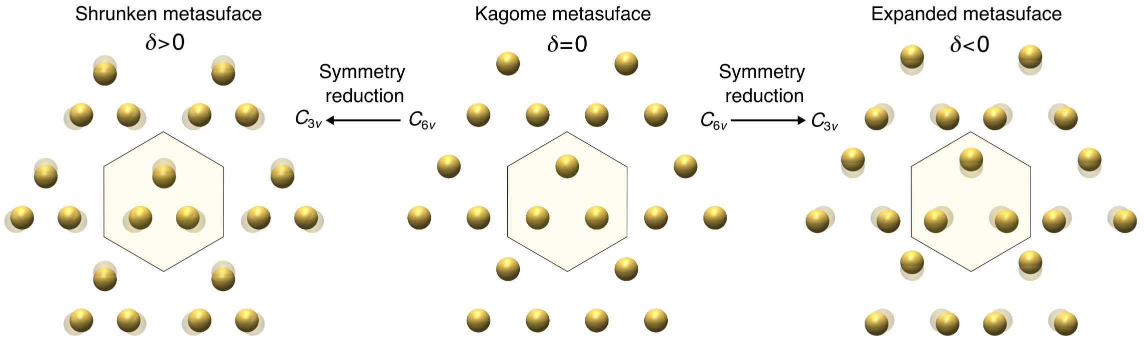

Figure 6.2 | Symmetry-reducing perturbations. The point group symmetry of the kagome metasurface is C_{6v} (centre panel), while the little point group of the K/K' points is C_{3v}. To break the $\mathcal{I}$ and $\mathcal{M}_y$ symmetries we shrink ($\delta > 0$) or expand ($\delta < 0$) the distances between the dipoles within the unit cell which forms the shrunken (left panel) and expanded (right panel) metasurfaces, respectively. This perturbation reduces the point group symmetry of the metasurface from C_{6v} to C_{3v}, and it reduces the little point group of the K/K' points from C_{3v} to C_3. The symmetry-breaking parameter δ encodes the fractional change in the nearest-neighbour separation distance.

can exhibit deterministic Dirac points at the K/K' points [265]. To gap out the Dirac points we introduce the following symmetry-reducing perturbation

$$\mathbf{d}_i \to (1-\delta)\mathbf{d}_i \,, \tag{6.5}$$

where the symmetry-breaking parameter δ describes the fractional change in the separation distance between the dipoles in the unit cell. Depending on the sign of δ, we have two distinct lattices which we call the shrunken metasurface ($\delta > 0$) and the expanded metasurface ($\delta < 0$) as schematically depicted in figure 6.2. We note that a similar strategy has been considered in other artificial kagome lattices [189, 266–271]. This perturbation breaks the $\mathcal{I}$ symmetry and the $\mathcal{M}_y$ symmetry, which reduces the point group symmetry of the metasurface to C_{3v} and the little point group of the K/K' valleys to C_3; consequently, the symmetry-broken kagome metasurface cannot exhibit deterministic Dirac points [265].

6.2.2 Coupled-dipole equations

In the absence of a driving field, the collective dynamics of the dipoles within the kagome metasurface is described by a set of coupled-dipole equations

$$\frac{1}{\alpha(\omega)} p_{\mathbf{R}_i}(\omega) = \sum_{\mathbf{R}_i' \neq \mathbf{R}_i} G(\mathbf{R}_i - \mathbf{R}_i', \omega) p_{\mathbf{R}_i'}(\omega) + \sum_{j\neq i} \sum_{\mathbf{R}_j'} G(\mathbf{R}_i - \mathbf{R}_j', \omega) p_{\mathbf{R}_j'}(\omega) \,, \tag{6.6}$$

where $p_{\mathbf{R}_i}$ is the induced dipole moment located at position $\mathbf{R} + \mathbf{d}_i$ on the i^{th} sublattice. As before, $\alpha(\omega) = [\alpha_{\text{B}}^{-1}(\omega) - \Sigma(\omega)]^{-1}$ is the renormalized polarizability that was derived in section 3.4.2, where the polarizability correction inside the cavity waveguide reads

$$\Sigma(\omega) = \mathrm{i}\frac{\mathcal{V}k_\omega^3}{6\pi} + \frac{\mathcal{V}}{\pi L^3}\left[\mathrm{Li}_3\left(\mathrm{e}^{\mathrm{i}k_\omega L}\right) - \mathrm{i}k_\omega L\,\mathrm{Li}_2\left(\mathrm{e}^{\mathrm{i}k_\omega L}\right)\right] . \tag{6.7}$$

Furthermore, $G(\boldsymbol{\rho} - \boldsymbol{\rho}', \omega)$ is the zz-component of the cavity Green's function that was derived in section 3.3 and reads

$$G(\boldsymbol{\rho} - \boldsymbol{\rho}', \omega) = \mathrm{i}\frac{\mathcal{V}}{4L}\sum_{m=0}^{\infty} N_m\left(k_\omega^2 - q_m^2\right) H_0^{(1)}\left(\sqrt{k_\omega^2 - q_m^2}|\boldsymbol{\rho} - \boldsymbol{\rho}'|\right) . \tag{6.8}$$

It is suggestive from equation (6.6) that the topological phase of the polaritons may not be solely dictated by the intrinsic properties of the dipoles and their geometrical arrangement; the topological phase could also depend on the nature of the dipole-dipole interactions which enters through the Green's function.

Following the approach in chapter 4 and chapter 5, we will decompose the cavity Green's function into its longitudinal and transverse components which were derived in section 3.3. The longitudinal component reads

$$G_\parallel(\boldsymbol{\rho} - \boldsymbol{\rho}') = -\frac{\mathcal{V}}{\pi L}\sum_{m=1}^{\infty} q_m^2 K_0\left(q_m|\boldsymbol{\rho} - \boldsymbol{\rho}'|\right) , \tag{6.9}$$

and describes the instantaneous Coulomb field generated by the dipoles. Since we are interested in the regime of cavity widths $L < \lambda_0$, we retain only the contribution from the TEM cavity mode for the transverse component, where the corresponding single mode Green's function reads

$$G_\perp^{\text{TEM}}(\boldsymbol{\rho} - \boldsymbol{\rho}', \omega) = \mathrm{i}\frac{\mathcal{V}k_\omega^2}{4L} H_0^{(1)}\left(k_\omega|\boldsymbol{\rho} - \boldsymbol{\rho}'|\right) . \tag{6.10}$$

In what follows we will see that the transition of the dominant dipolar coupling from Coulomb to photon-mediated interactions as the cavity width is reduced has dramatic consequences for the geometrical and topological properties of the polaritons.

6.2.3 Dynamical matrix

The symmetry-reducing perturbations preserve the discrete translational symmetry of the metasurface, and therefore we can block diagonalize the coupled-dipole equations in momentum space. To achieve this we follow the method presented in section 3.4. We exploit the periodicity of the metasurface by introducing the Fourier transform of the dipole moments

$$\widetilde{p}_i(\mathbf{q},\omega) = \frac{\sqrt{\mathcal{A}}}{2\pi} \sum_{\mathbf{R}} p_{\mathbf{R}_i}(\omega) \mathrm{e}^{-\mathrm{i}\mathbf{q}\cdot\mathbf{R}_i} , \tag{6.11}$$

where $\mathbf{q} = [\, q_x \, , \, q_y \,]$ is the Bloch wavevector that is restricted to the first Brillouin zone shown in figure 6.1(c), and $\mathcal{A} = 2\sqrt{3}a^2$ is the area of the unit cell shown in figure 6.1(b). Using the Fourier variables, we can recast the coupled-dipole equations into 3×3 matrix eigenvalue equations

$$\frac{1}{\breve{\alpha}(\omega)} \left|\varphi(\mathbf{q})\right\rangle = \left[\mathcal{D}_{\parallel}(\mathbf{q}) + \mathcal{D}_{\perp}(\mathbf{q},\omega)\right] \left|\varphi(\mathbf{q})\right\rangle , \tag{6.12}$$

where $\breve{\alpha}^{-1}(\omega) = \alpha_{\mathrm{B}}^{-1}(\omega) - \mathrm{Re}[\varSigma(\omega)]$ and $|\varphi(\mathbf{q})\rangle$ represents the vector of Fourier variables

$$\left|\varphi(\mathbf{q})\right\rangle = \begin{bmatrix} \widetilde{p}_{\mathrm{A}}(\mathbf{q}) \\ \widetilde{p}_{\mathrm{B}}(\mathbf{q}) \\ \widetilde{p}_{\mathrm{C}}(\mathbf{q}) \end{bmatrix} . \tag{6.13}$$

Furthermore, the longitudinal dynamical matrix which encodes the frequency shifts due to the Coulomb interactions is given by

$$\mathcal{D}_{\parallel}(\mathbf{q}) = \begin{bmatrix} \mathcal{D}_{\parallel}^{\mathrm{AA}}(\mathbf{q}) & \mathcal{D}_{\parallel}^{\mathrm{AB}}(\mathbf{q}) & \mathcal{D}_{\parallel}^{\mathrm{AC}}(\mathbf{q}) \\ \mathcal{D}_{\parallel}^{\mathrm{AB}*}(\mathbf{q}) & \mathcal{D}_{\parallel}^{\mathrm{BB}}(\mathbf{q}) & \mathcal{D}_{\parallel}^{\mathrm{BC}}(\mathbf{q}) \\ \mathcal{D}_{\parallel}^{\mathrm{AC}*}(\mathbf{q}) & \mathcal{D}_{\parallel}^{\mathrm{BC}*}(\mathbf{q}) & \mathcal{D}_{\parallel}^{\mathrm{CC}}(\mathbf{q}) \end{bmatrix} , \tag{6.14}$$

where the intrasublattice matrix elements read

$$\mathcal{D}_{\parallel}^{ii}(\mathbf{q}) = \sum_{\mathbf{R}\neq 0} G_{\parallel}(\mathbf{R}) \mathrm{e}^{-\mathrm{i}\mathbf{q}\cdot\mathbf{R}} , \tag{6.15}$$

and the intersublattice matrix elements are given by

$$\mathcal{D}_{\parallel}^{ij}(\mathbf{q}) = \sum_{\mathbf{R}} G_{\parallel}(\mathbf{R} + \mathbf{d}_i - \mathbf{d}_j) \mathrm{e}^{-\mathrm{i}\mathbf{q}\cdot(\mathbf{R}+\mathbf{d}_i-\mathbf{d}_j)} . \tag{6.16}$$

Since the Coulomb interactions are short-range these lattice sums converge rapidly in real space.

Furthermore, the transverse dynamical matrix which encodes the frequency shifts due to the photon-mediated interactions is given by

$$\mathcal{D}_\perp(\mathbf{q},\omega)=\begin{bmatrix}\mathcal{D}_\perp^{\mathrm{AA}}(\mathbf{q},\omega) & \mathcal{D}_\perp^{\mathrm{AB}}(\mathbf{q},\omega) & \mathcal{D}_\perp^{\mathrm{AC}}(\mathbf{q},\omega)\\ \mathcal{D}_\perp^{\mathrm{AB}*}(\mathbf{q},\omega) & \mathcal{D}_\perp^{\mathrm{BB}}(\mathbf{q},\omega) & \mathcal{D}_\perp^{\mathrm{BC}}(\mathbf{q},\omega)\\ \mathcal{D}_\perp^{\mathrm{AC}*}(\mathbf{q},\omega) & \mathcal{D}_\perp^{\mathrm{BC}*}(\mathbf{q},\omega) & \mathcal{D}_\perp^{\mathrm{CC}}(\mathbf{q},\omega)\end{bmatrix}, \tag{6.17}$$

where the intrasublattice matrix elements read

$$\mathcal{D}_\perp^{ii}(\mathbf{q},\omega)=\sum_{\mathbf{g}}\frac{\omega^2\xi^2}{\omega_{\mathbf{q}-\mathbf{g}}^2-\omega^2}-\mathrm{Re}[G_\perp^{\mathrm{TEM}}(0,\omega)]\,, \tag{6.18}$$

and the intersublattice matrix elements are given by

$$\mathcal{D}_\perp^{ij}(\mathbf{q},\omega)=\sum_{\mathbf{g}}\frac{\omega^2\xi^2\phi_{\mathbf{q}}^{ij}}{\omega_{\mathbf{q}-\mathbf{g}}^2-\omega^2}\,, \tag{6.19}$$

Here, $\xi=\sqrt{\mathcal{V}/\mathcal{A}L}$ parameterizes the strength of the light-matter coupling in the kagome metasurface and the phase factors are given by

$$\phi_{\mathbf{g}}^{ij}=\mathrm{e}^{\mathrm{i}\mathbf{g}\cdot(\mathbf{d}_j-\mathbf{d}_i)}\,. \tag{6.20}$$

Note, to derive equation (6.18) and equation (6.19) we have used the Poisson summation technique outlined in section 3.4.5 due to the long-range nature of the photon-mediated interactions.

6.2.4 Polariton dispersion

To obtain the polariton dispersion we first linearize the non-linear eigenvalue problem in equation (6.12) by evaluating the polarizability correction and the transverse dynamical matrix at the cavity resonant frequency. We can then obtain the polariton dispersion by solving the following characteristic equation

$$\det[(\omega^2-\omega_{\mathrm{cav}}^2)\mathbb{1}_3+2\omega_0\mu\mathcal{D}_\parallel(\mathbf{q})+2\omega_0\mu\mathcal{D}_\perp(\mathbf{q},\omega_{\mathrm{cav}})]=0\,, \tag{6.21}$$

where $\mathbb{1}_3$ is the 3×3 identity matrix and we have neglected non-radiative losses for simplicity. Note, one also needs to use the regularization procedure outlined in section 3.4.6 to numerically evaluate the dispersion.

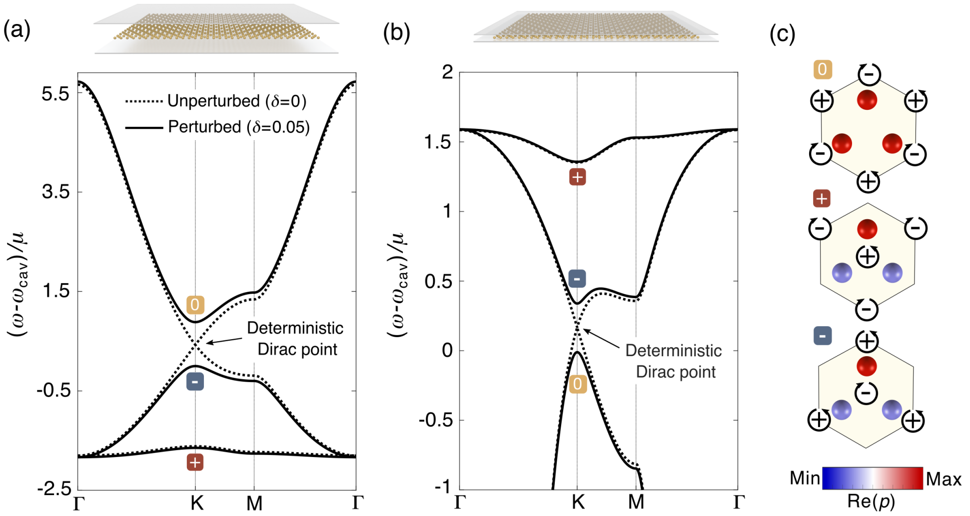

Figure 6.3 | Polariton dispersion for the kagome metasurface. (a) Dispersion for the unperturbed kagome metasurface $\delta = 0$ (dashed line) and the shrunken metasurface $\delta = 0.05$ (solid line) with a large cavity width ($L = 5a$). (b) Same as panel (a) but for a small cavity width ($L = 0.5a$). In both interaction regimes, the symmetry-reducing perturbation gaps out the deterministic Dirac points located at the high-symmetry K/K' points. The bands at the K point are labelled according to the pseudo-angular momentum number of the eigenstates. (c) Corresponding dipole distributions where $+/-$ correspond to anticlockwise/clockwise phase vortices. Results obtained with $\lambda_0 = 10a$ and $\mu = 0.001\omega_0$.

In figure 6.3(a) we show the polariton dispersion (solid line) for the shrunken kagome metasurface ($\delta = 0.05$) with a large cavity width where the Coulomb interactions are dominant. Note, for clarity we have neglected the weak photon-mediated interactions which have a negligible effect near the K/K' valleys (see appendix E.1 for more details). In figure 6.3(b) we show the polariton dispersion for the same metasurface but now with a small cavity width where the photon-mediated interactions are dominant. In both interaction regimes, the symmetry-reducing perturbation removes the deterministic Dirac points exhibited by the unperturbed metasurface (dashed lines), thereby opening a gap at the K/K' points. While they share this feature, the dispersion in the two regimes looks qualitatively different – for example, the (approximate) flat band is above/below the Dirac point for the small/large cavity width.

6.2.5 Eigenstates at the K/K′ points

To further elucidate the difference between the two interaction regimes we can study the eigenstates at the K ($\tau = +$) and K′ ($\tau = -$) points located at $\tau\mathbf{K} = \tau[\,2\pi/3a\,,\,0\,]$, where $\tau = \pm$ is the valley index. Since the symmetry-breaking perturbation preserves the $\mathcal{C}_3$ symmetry of the metasurface, the eigenstates at the K/K' points will be simultaneous eigenstates of the $\mathcal{C}_3$ operator

$$\mathcal{U}^{\tau}_{\mathcal{C}_3} \left|\varphi^{l}_{\tau}\right\rangle = \mathrm{e}^{\mathrm{i}\frac{2\pi}{3}l} \left|\varphi^{l}_{\tau}\right\rangle \, . \tag{6.22}$$

Here the unitary operator

$$\mathcal{U}^{\tau}_{\mathcal{C}_3} = \begin{bmatrix} 0 & 0 & \mathrm{e}^{-\mathrm{i}\frac{\pi}{3}(1-\delta)\tau} \\ \mathrm{e}^{-\mathrm{i}\frac{\pi}{3}(1-\delta)\tau} & 0 & 0 \\ 0 & \mathrm{e}^{\mathrm{i}\frac{2\pi}{3}(1-\delta)\tau} & 0 \end{bmatrix} \tag{6.23}$$

represents a rotation of $2\pi/3$ about the centre of the unit cell, $\left|\varphi^{l}_{\tau}\right\rangle$ are the corresponding eigenstates and $l = 0, \pm 1$ are the pseudo-angular momentum eigenvalues.

The eigenstates at the K point therefore read

$$\left|\varphi^{0}_{+}\right\rangle = \frac{1}{\sqrt{3}} \begin{bmatrix} 1 \\ \mathrm{e}^{-\mathrm{i}\frac{\pi}{3}(1-\delta)} \\ \mathrm{e}^{\mathrm{i}\frac{\pi}{3}(1-\delta)} \end{bmatrix} , \; \left|\varphi^{-}_{+}\right\rangle = \frac{1}{\sqrt{3}} \begin{bmatrix} 1 \\ \mathrm{e}^{\mathrm{i}\frac{\pi}{3}(1+\delta)} \\ \mathrm{e}^{-\mathrm{i}\frac{\pi}{3}(1+\delta)} \end{bmatrix} , \; \left|\varphi^{+}_{+}\right\rangle = \frac{1}{\sqrt{3}} \begin{bmatrix} -1 \\ \mathrm{e}^{\mathrm{i}\frac{\pi}{3}\delta} \\ \mathrm{e}^{-\mathrm{i}\frac{\pi}{3}\delta} \end{bmatrix} , \tag{6.24}$$

and in figure 6.3(c) we schematically depict the corresponding dipole distributions within a unit cell, where $-/+$ corresponds to a clockwise/anticlockwise phase vortex. Furthermore, the eigenvectors at the K' point are related by $\mathcal{T}$ symmetry and are given by $\left|\varphi^{0}_{-}\right\rangle = \left|\varphi^{0}_{+}\right\rangle^{*}$, $\left|\varphi^{-}_{-}\right\rangle = \left|\varphi^{+}_{+}\right\rangle^{*}$, and $\left|\varphi^{+}_{-}\right\rangle = \left|\varphi^{-}_{+}\right\rangle^{*}$.

6.2.6 Cavity-induced band inversions

In figures 6.3(a)-(b) we label the polariton bands at the K point according to the pseudo-angular momentum number of the eigenstates. Interestingly, for the same symmetry-breaking parameter ($\delta = 0.05$), the ordering of the eigenstates is entirely reversed for the two limiting interaction regimes. To elucidate this further, in figure 6.4(a) we show the frequency evolution of the eigenstates at the K point as the cavity width is reduced. Due to the competition between the Coulomb and photon-mediated interactions we observe three band inversions. The first two band inversions result in $l = +1$ eigenstate evolving from being the lowest in frequency to the highest. However, here we are particularly interested in the third band inversion. At this critical cavity width $L = L_m$, the degeneracy between the $l = 0$ and $l = -1$ eigenstates is restored, despite the broken lattice symmetry. Consequently, the polariton dispersion exhibits accidental Dirac points at this critical cavity width as shown in figure 6.4(b).

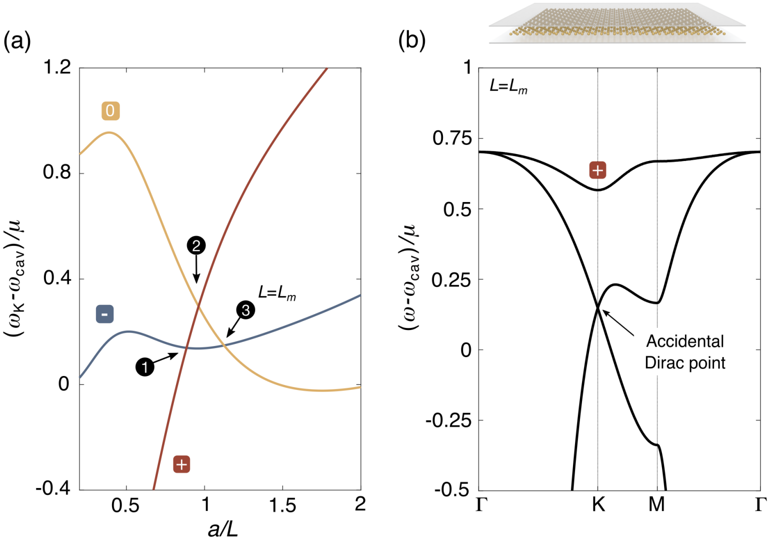

Figure 6.4 | Cavity-induced band inversions. (a) Frequency evolution of the eigenstates at the K point for the shrunken metasurface ($\delta = 0.05$) as the cavity width is reduced. One observes three band inversions (labelled 1-3), where the first two result in the $l = 1$ eigenstate evolving from being the lowest in frequency to the highest. The third band inversion occurs at a critical cavity width L_m, where the degeneracy between the $l = 0$ and $l = +1$ eigenstates is restored, despite the broken symmetry of the metasurface. (b) Shows the polariton dispersion at the critical width ($L = L_m$) which exhibits accidental Dirac points. Results obtained with $\lambda_0 = 10a$ and $\mu = 0.001\omega_0$.

6.3 Cavity-induced topological transition

To characterize the essential topology related to the third band inversion, we will derive an effective two-band Hamiltonian that describes the polaritons near the K/K' valleys within the subspace spanned by the degenerate eigenstates of the unperturbed lattice. In what follows we will focus on the K valley since the effective Hamiltonian for the K' valley is related via $\mathcal{T}$ symmetry.

6.3.1 Expansion of the dynamical matrix

We first expand the total dynamical matrix $\mathcal{D}(\mathbf{q}, \omega) = \mathcal{D}_{\|}(\mathbf{q}) + \mathcal{D}_{\perp}(\mathbf{q}, \omega)$ to leading order in $\mathbf{k} = \mathbf{q} - \mathbf{K}$, which represents the wavevector measured from the K point. The intrasublattice matrix elements expand as

$$\mathcal{D}_{+}^{ii}(\mathbf{k}, \omega) \simeq \sum_{\mathbf{R} \neq 0} G_{\|}(\mathbf{R}) \mathrm{e}^{-\mathrm{i}\mathbf{K}\cdot\mathbf{R}} + \sum_{\mathbf{g}} \frac{\omega^2 \xi^2}{\omega_{\mathbf{K}-\mathbf{g}}^2 - \omega^2} - \mathrm{Re}[G_{\perp}^{\mathrm{TEM}}(0, \omega)] \,, \tag{6.25}$$

while the intersublattice matrix elements expand as

$$\begin{aligned}\mathcal{D}_{+}^{ij}(\mathbf{k}) \simeq \sum_{\mathbf{R}} G_{\parallel}(\mathbf{R}+\mathbf{d}_i-\mathbf{d}_j)\mathrm{e}^{-\mathrm{i}\mathbf{K}\cdot(\mathbf{R}+\mathbf{d}_i-\mathbf{d}_j)} + \sum_{\mathbf{g}} \frac{\omega^2\xi^2\phi_{\mathbf{g}}^{ij}}{\omega_{\mathbf{K}-\mathbf{g}}^2-\omega^2} \\ -\left[\mathrm{i}\sum_{\mathbf{R}} G_{\parallel}(\mathbf{R}+\mathbf{d}_i-\mathbf{d}_j)\mathrm{e}^{-\mathrm{i}\mathbf{K}\cdot(\mathbf{R}+\mathbf{d}_i-\mathbf{d}_j)}(\mathbf{R}+\mathbf{d}_i-\mathbf{d}_j)_\nu + \sum_{\mathbf{g}} \frac{2c^2\omega^2\xi^2\phi_{\mathbf{g}}^{ij}}{(\omega_{\mathbf{K}-\mathbf{g}}^2-\omega^2)^2}(\mathbf{K}-\mathbf{g})_\nu\right] k_\nu\,.\end{aligned} \tag{6.26}$$

Next we reduce the full 3×3 matrix eigenvalue equation to an effective 2×2 matrix eigenvalue equation in the $\{\,|\varphi_{+}^{0}\rangle\ ,\ |\varphi_{+}^{-}\rangle\}$ subspace which is spanned by the degenerate eigenstates of the unperturbed lattice. The corresponding simplified eigenvalue equation for the K valley reads

$$\frac{1}{\breve{\alpha}(\omega)}\,|\psi_{+}(\mathbf{k})\rangle = \mathcal{D}_{+}^{\text{eff}}(\mathbf{k},\omega)\,|\psi_{+}(\mathbf{k})\rangle\ , \tag{6.27}$$

where the new basis is related to the sublattice basis via

$$|\psi_{+}(\mathbf{k})\rangle = \begin{bmatrix} \langle\varphi_{+}^{0}|\varphi(\mathbf{k})\rangle \\ \langle\varphi_{+}^{-}|\varphi(\mathbf{k})\rangle \end{bmatrix}\ , \tag{6.28}$$

and the effective dynamical matrix is given by

$$\mathcal{D}_{+}^{\text{eff}}(\mathbf{k},\omega) = \begin{bmatrix} \langle\varphi_{+}^{0}|\mathcal{D}_{+}|\varphi_{+}^{0}\rangle & \langle\varphi_{+}^{0}|\mathcal{D}_{+}|\varphi_{+}^{-}\rangle \\ \langle\varphi_{+}^{-}|\mathcal{D}_{+}|\varphi_{+}^{0}\rangle & \langle\varphi_{+}^{-}|\mathcal{D}_{+}|\varphi_{+}^{-}\rangle \end{bmatrix}\ . \tag{6.29}$$

Note, this effective dynamical matrix is only valid when the other band is well separated in frequency and thus does not accurately describe the polaritons during the first two band inversions shown in figure 6.4(a). Moreover, the effective interactions with the other band contribute to higher order corrections in $\mathbf{k}$ which are neglected here as we only wish to capture the essential physics.

6.3.2 Massive Dirac polariton Hamiltonian

Finally, to obtain an effective Hamiltonian we linearize the effective eigenvalue problem in equation (6.27) by evaluating the polarizability correction and effective dynamical matrix at the cavity resonant frequency, and we approximate $\omega_{\text{cav}}^2 - \omega^2 \simeq 2\omega_{\text{cav}}(\omega_{\text{cav}} - \omega)$. This allows us to write a simplified eigenvalue equation which reads ($\hbar = 1$)

$$\omega\,|\psi_{+}(\mathbf{k})\rangle = \mathcal{H}_{+}(\mathbf{k})\,|\psi_{+}(\mathbf{k})\rangle\ , \tag{6.30}$$

where the effective Hamiltonian is given by

$$\mathcal{H}_{+}(\mathbf{k}) = \omega_{\mathrm{cav}}\mathbb{1}_2 - \mu\frac{\omega_0}{\omega_{\mathrm{cav}}}\mathcal{D}^{\mathrm{eff}}_{+}(\mathbf{k},\omega_{\mathrm{cav}})\,. \tag{6.31}$$

After evaluating the matrix elements in equation (6.29), and performing similar analysis for the K' valley in the $\{\,|\varphi^0_-\rangle\;,\;|\varphi^+_-\rangle\}$ subspace, we obtain the following effective Hamiltonian

$$\mathcal{H}_{\tau}(\mathbf{k}) = \omega_{\mathrm{D}}(L)\mathbb{1}_2 + v_{\mathrm{D}}(L)(\tau\sigma_x k_x + \sigma_y k_y) + m(L)\sigma_z\,, \tag{6.32}$$

which is equivalent to a 2D massive Dirac Hamiltonian.

The Dirac frequency in equation (6.32) can be decomposed as $\omega_{\mathrm{D}} = \omega_{\mathrm{cav}} + \omega_{\parallel} + \omega_{\perp}$, where the contribution from the Coulomb interactions is

$$\begin{aligned}\omega_{\parallel} = &-\mu\frac{\omega_0}{\omega_{\mathrm{cav}}}\sum_{\mathbf{R}\neq 0} G_{\parallel}(\mathbf{R})\mathrm{e}^{-\mathrm{i}\mathbf{K}\cdot\mathbf{R}} - \frac{\mu}{3}\frac{\omega_0}{\omega_{\mathrm{cav}}}\sum_{\mathbf{R}}\mathrm{Re}\Big[G_{\parallel}(\mathbf{R}+\mathbf{d}_{\mathrm{A}}-\mathbf{d}_{\mathrm{B}})\mathrm{e}^{\mathrm{i}\frac{\pi}{3}\delta}\mathrm{e}^{-\mathrm{i}\mathbf{K}\cdot(\mathbf{R}+\mathbf{d}_{\mathrm{A}}-\mathbf{d}_{\mathrm{B}})}\\ &+G_{\parallel}(\mathbf{R}+\mathbf{d}_{\mathrm{A}}-\mathbf{d}_{\mathrm{C}})\mathrm{e}^{-\mathrm{i}\frac{\pi}{3}\delta}\mathrm{e}^{-\mathrm{i}\mathbf{K}\cdot(\mathbf{R}+\mathbf{d}_{\mathrm{A}}-\mathbf{d}_{\mathrm{C}})} - G_{\parallel}(\mathbf{R}+\mathbf{d}_{\mathrm{B}}-\mathbf{d}_{\mathrm{C}})\mathrm{e}^{-\mathrm{i}\frac{2\pi}{3}\delta}\mathrm{e}^{-\mathrm{i}\mathbf{K}\cdot(\mathbf{R}+\mathbf{d}_{\mathrm{B}}-\mathbf{d}_{\mathrm{C}})}\Big]\,,\end{aligned} \tag{6.33}$$

and the contribution from the photon-mediated interactions reads

$$\begin{aligned}\omega_{\perp} = &\,\mu\frac{\omega_0}{\omega_{\mathrm{cav}}}\mathrm{Re}[\check{G}^{\mathrm{TEM}}_{\perp}(0,\omega_{\mathrm{cav}})] - \mu\frac{\omega_0}{\omega_{\mathrm{cav}}}\sum_{\mathbf{g}}\frac{\omega_{\mathrm{cav}}^2\xi^2\mathrm{e}^{-\eta^2|\mathbf{K}-\mathbf{g}|^2}}{\omega^2_{\mathbf{K}-\mathbf{g}}-\omega^2_{\mathrm{cav}}}\\ &-\frac{\mu}{3}\frac{\omega_0}{\omega_{\mathrm{cav}}}\sum_{\mathbf{g}}\frac{\omega_{\mathrm{cav}}^2\xi^2}{\omega^2_{\mathbf{K}-\mathbf{g}}-\omega^2_{\mathrm{cav}}}\mathrm{Re}\Big[\mathrm{e}^{\mathrm{i}\frac{\pi}{3}\delta}\phi^{\mathrm{AB}}_{\mathbf{g}} + \mathrm{e}^{-\mathrm{i}\frac{\pi}{3}\delta}\phi^{\mathrm{AC}}_{\mathbf{g}} - \mathrm{e}^{-\mathrm{i}\frac{2\pi}{3}\delta}\phi^{\mathrm{BC}}_{\mathbf{g}}\Big]\,.\end{aligned} \tag{6.34}$$

Note we have used the regularization procedure outlined in section 3.4.6 to numerically evaluate the difference between the first two divergent terms in equation (6.34). Similarly, the Dirac velocity can be decomposed as $v_{\mathrm{D}} = v_{\parallel} + v_{\perp}$, where the contribution from the Coulomb interactions is

$$\begin{aligned}v_{\parallel} = &\,\frac{\mu}{\sqrt{3}}\frac{\omega_0}{\omega_{\mathrm{cav}}}\sum_{\mathbf{R}}\mathrm{Re}\Big[\mathrm{i}(\mathbf{R}+\mathbf{d}_{\mathrm{A}}-\mathbf{d}_{\mathrm{C}})_y G_{\parallel}(\mathbf{R}+\mathbf{d}_{\mathrm{A}}-\mathbf{d}_{\mathrm{C}})\mathrm{e}^{-\mathrm{i}\frac{\pi}{3}\delta}\mathrm{e}^{-\mathrm{i}\mathbf{K}\cdot(\mathbf{R}+\mathbf{d}_{\mathrm{A}}-\mathbf{d}_{\mathrm{C}})}\\ &-\mathrm{i}(\mathbf{R}+\mathbf{d}_{\mathrm{A}}-\mathbf{d}_{\mathrm{B}})_y G_{\parallel}(\mathbf{R}+\mathbf{d}_{\mathrm{A}}-\mathbf{d}_{\mathrm{B}})\mathrm{e}^{\mathrm{i}\frac{\pi}{3}\delta}\mathrm{e}^{-\mathrm{i}\mathbf{K}\cdot(\mathbf{R}+\mathbf{d}_{\mathrm{A}}-\mathbf{d}_{\mathrm{B}})}\Big]\,,\end{aligned} \tag{6.35}$$

and the contribution from the photon-mediated interactions reads

$$v_{\perp} = \frac{\mu}{\sqrt{3}}\frac{\omega_0}{\omega_{\mathrm{cav}}}\sum_{\mathbf{g}}\frac{2c^2\omega^2_{\mathrm{cav}}\xi^2}{(\omega^2_{\mathbf{K}-\mathbf{g}}-\omega^2_{\mathrm{cav}})^2}(\mathbf{K}-\mathbf{g})_y\,\mathrm{Re}\Big[\mathrm{e}^{-\mathrm{i}\frac{\pi}{3}\delta}\phi^{\mathrm{AC}}_{\mathbf{g}} - \mathrm{e}^{\mathrm{i}\frac{\pi}{3}\delta}\phi^{\mathrm{AB}}_{\mathbf{g}}\Big]\,. \tag{6.36}$$

Finally, the Dirac mass can be decomposed as $m = m_{\parallel} + m_{\perp}$, where the contribution from the Coulomb interactions is

$$
\begin{aligned}
m_{\parallel} = \frac{\mu}{\sqrt{3}} \frac{\omega_0}{\omega_{\text{cav}}} \sum_{\mathbf{R}} \operatorname{Re} \Big[& \mathrm{i} G_{\parallel}(\mathbf{R} + \mathbf{d}_{\mathrm{A}} - \mathbf{d}_{\mathrm{B}}) \mathrm{e}^{\mathrm{i}\frac{\pi}{3}\delta} \mathrm{e}^{-\mathrm{i}\mathbf{q}\cdot(\mathbf{R}+\mathbf{d}_{\mathrm{A}}-\mathbf{d}_{\mathrm{B}})} \\
& -\mathrm{i} G_{\parallel}(\mathbf{R}+\mathbf{d}_{\mathrm{A}} - \mathbf{d}_{\mathrm{C}}) \mathrm{e}^{-\mathrm{i}\frac{\pi}{3}\delta} \mathrm{e}^{-\mathrm{i}\mathbf{q}\cdot(\mathbf{R}+\mathbf{d}_{\mathrm{A}}-\mathbf{d}_{\mathrm{C}})} - \mathrm{i} G_{\parallel}(\mathbf{R} + \mathbf{d}_{\mathrm{B}} - \mathbf{d}_{\mathrm{C}}) \mathrm{e}^{-\mathrm{i}\frac{2\pi}{3}\delta} \mathrm{e}^{-\mathrm{i}\mathbf{q}\cdot(\mathbf{R}+\mathbf{d}_{\mathrm{B}}-\mathbf{d}_{\mathrm{C}})} \Big] ,
\end{aligned}
\tag{6.37}
$$

and the contribution from the photon-mediated interactions reads

$$
m_{\perp} = \frac{\mu}{\sqrt{3}} \frac{\omega_0}{\omega_{\text{cav}}} \sum_{\mathbf{g}} \frac{\omega_{\text{cav}}^2 \xi^2}{\omega_{\mathbf{K}-\mathbf{g}}^2 - \omega_{\text{cav}}^2} \operatorname{Re} \left[\mathrm{i}\mathrm{e}^{\mathrm{i}\frac{\pi}{3}\delta} \phi_{\mathbf{g}}^{\mathrm{AB}} - \mathrm{i}\mathrm{e}^{-\mathrm{i}\frac{\pi}{3}\delta} \phi_{\mathbf{g}}^{\mathrm{AC}} - \mathrm{i}\mathrm{e}^{-\mathrm{i}\frac{2\pi}{3}\delta} \phi_{\mathbf{g}}^{\mathrm{BC}} \right] . \tag{6.38}
$$

6.3.3 Switching the sign of the Dirac mass

For the unperturbed kagome metasurface ($\delta = 0$), the symmetry forces both the longitudinal and transverse mass to vanish separately $m_{\parallel} = m_{\perp} = 0$. This results in deterministic Dirac points for all cavity widths, which are characterized by a massless Dirac cone dispersion

$$
\omega_{\lambda}(\mathbf{k}) = \omega_{\mathrm{D}} + \lambda |v_{\mathrm{D}}| |\mathbf{k}| , \tag{6.39}
$$

where $\lambda = \pm$ is the band index. When the symmetry-reducing perturbation is applied, a finite mass term is produced in the effective Dirac Hamiltonian and the corresponding polariton spectrum is characterized by a massive Dirac cone

$$
\omega_{\lambda}(\mathbf{k}) = \omega_{\mathrm{D}} + \lambda \sqrt{v_{\mathrm{D}}^2 |\mathbf{k}|^2 + m^2} , \tag{6.40}
$$

as depicted in figure 6.5(a), where the size of the gap is equal to $2|m|$.

In figure 6.5(b) we show the evolution of the longitudinal (dotted orange line), transverse (dashed blue line), and total (solid black line) Dirac mass as the cavity width is reduced for the shrunken metasurface ($\delta = 0.05$). In stark contrast to the unperturbed kagome metasurface, here the longitudinal and transverse masses do not vanish for any cavity width due to the broken symmetry. However, they contribute with opposite signs and thus tend to compensate each other; the Coulomb interactions push the $l = 0$ eigenstate to higher frequencies, while the photon-mediated interactions push the $l = -1$ eigenstate to higher frequencies.

Moreover, for large cavity widths the gap induced by the perturbation is predominantly due to the change in near-field Coulomb interactions, while for small cavity widths it is

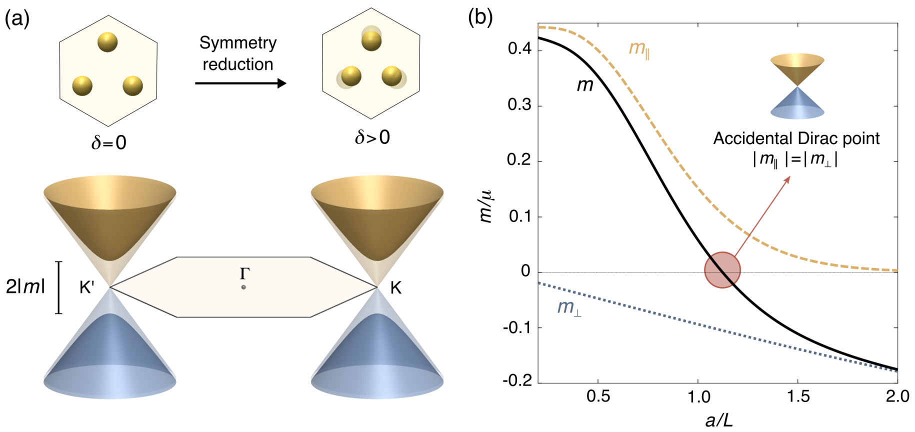

Figure 6.5 | Switching the sign of the Dirac mass. (a) The symmetry-reducing perturbation gaps out the deterministic Dirac points, where the size of the gap is determined by the Dirac mass. (b) Evolution of the longitudinal (dotted orange line), transverse (dashed blue line) and total (solid black line) Dirac mass as the cavity width is reduced for the shrunken metasurface ($\delta = 0.05$). The longitudinal and transverse masses have opposite signs and thus tend to compensate each other. At the critical cavity width ($L = L_m$), the longitudinal and transverse masses have equal magnitudes ($|m_\parallel| = |m_\perp|$) which leads to the vanishing of the total Dirac mass ($m = 0$), despite the broken symmetry of the metasurface. This results in a topological band inversion where the band gap closes and reopens, switching the sign of the Dirac mass. Results obtained with $\lambda_0 = 10a$ and $\mu = 0.001\omega_0$.

predominantly due to the change in long-range photon-mediated interactions. At the critical cavity width $L = L_m$, the photon-mediated interactions eliminate the gap induced by the Coulomb interactions ($|m_\parallel| = |m_\perp|$) and thus the Dirac mass vanishes ($m = 0$). As a result, the Dirac points are restored in the polariton spectrum; these are accidental since they are not enforced by the symmetry, but their existence depends critically on the nature of the dipole-dipole interactions. Therefore, by varying only the cavity width, one can switch the sign of the Dirac mass which has a dramatic effect on the geometrical and topological properties of the polaritons.

6.3.4 Cavity-induced inversion of the valley-Chern numbers

Using equation (2.117) we can obtain a simple analytical expression for the effective Berry curvature near the K/K' valleys which reads

$$\mathcal{F}_\lambda^\tau(\mathbf{k}) = -\tau\lambda \frac{m v_\mathrm{D}^2}{2(v_\mathrm{D}^2|\mathbf{k}|^2 + m^2)^{3/2}} \,. \tag{6.41}$$

In appendix E.2 we numerically calculate the exact Berry curvature from the dynamical matrix to verify that equation (6.41) captures the essential physics near the K/K' valleys for

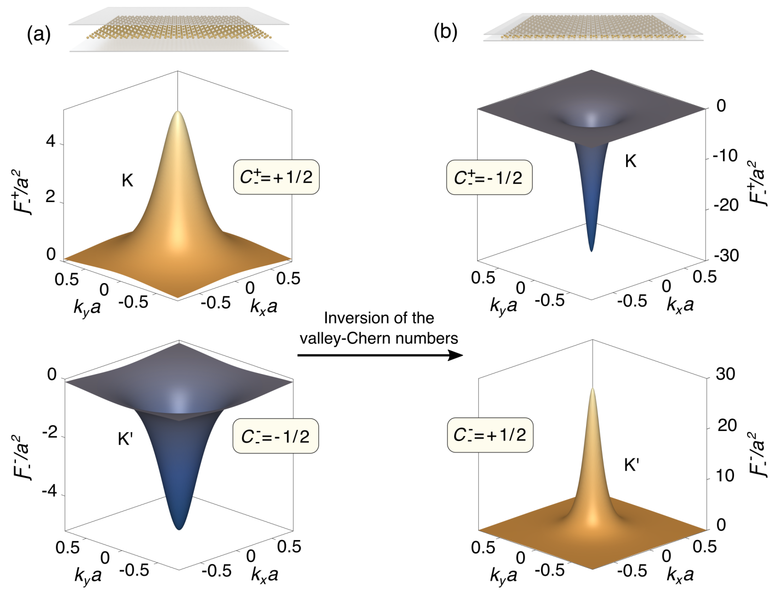

Figure 6.6 | Cavity-induced inversion of the valley-Chern numbers. (a) Localized Berry curvature corresponding to the lower effective polariton band near the K (top panel) and K' (bottom panel) points for the shrunken metasurface ($\delta = 0.05$) with a large cavity width ($L = 5a$). We also depict the corresponding valley-Chern numbers. (b) Same as panel (a) but for a small cavity width ($L = 0.5a$). The transition of the dominant dipolar coupling from Coulomb to photon-mediated interactions switches the sign of the Berry curvature within each valley and thus inverts the valley-Chern numbers. Results obtained with $\lambda_0 = 10a$ and $\mu = 0.001\omega_0$.

the two limiting interaction regimes. In figure 6.6(a) we plot the effective Berry curvature near the K/K' valleys for the shrunken metasurface ($\delta = 0.05$) with a large cavity width. We observe that the Berry curvature has opposite signs for the two valleys and therefore the Chern number vanishes as required by $\mathcal{T}$ symmetry.

However, provided that the perturbation is small enough, the Berry curvature is very localized around the K/K' points and therefore one can define valley-Chern numbers

$$C_\lambda^\tau = \frac{1}{2\pi} \iint\limits_{\mathbb{R}_2} \mathrm{d}^2\mathbf{k}\, \mathcal{F}_\lambda^\tau(\mathbf{k}) = -\tau\lambda\, \mathrm{sgn}(m)\frac{1}{2}. \tag{6.42}$$

For the large cavity width where the Coulomb interactions are dominant, the valley-Chern numbers for the lower band are $C_-^\tau = \tau/2$. In figure 6.6(b) we plot the Berry curvature for the same metasurface but now with a small cavity width where the photon-mediated interactions are dominant. Remarkably, the Berry curvature changes sign within each valley and, as a result, the valley-Chern numbers become inverted $C_-^\tau = -\tau/2$.

6.4 Switching the chirality of the valley-Hall edge states

Although the valley-Chern numbers are not topological invariants, there exists a bulk-boundary correspondence when one forms a domain wall between two regions with opposite valley-Chern numbers. Provided that the interface does not mix the two valleys and the Berry curvature remains very localized, then the change in valley-Chern number across the interface determines the number of valley-polarized chiral edge states.

6.4.1 Mass domain wall interface

To explore how the cavity-induced band inversion modifies the polariton valley-Hall edge states, we consider the domain wall shown in figure 6.7(a) where region A is a shrunken metasurface ($\delta_\mathrm{A} = 0.05$) and region B is an expanded metasurface ($\delta_\mathrm{B} = -0.05$), and we assume translational invariance along the x-direction. While the bulk polariton dispersion in the two regions are identical, the Dirac masses have opposite signs $m_\mathrm{B} = -m_\mathrm{A}$ and thus the interface separates regions with opposite valley-Chern numbers.

Before we numerically calculate the interface dispersion using the coupled-dipole equations, we can gain some analytical insight with the effective Dirac Hamiltonian

$$\mathcal{H}_\tau = \omega_\mathrm{D}\mathbb{1}_2 - \mathrm{i}v_\mathrm{D}(\tau\sigma_x\partial_x + \sigma_y\partial_y) + m(y)\sigma_z\,, \tag{6.43}$$

where the interface is modelled by a spatially-varying mass

$$m(y) = \begin{cases} +m_\mathrm{A}, & \text{for } y < 0 \\ -m_\mathrm{A}, & \text{for } y > 0 \end{cases} \tag{6.44}$$

Following the same analysis outlined in section 2.4.3 and section 2.4.5, we find that each valley exhibits one chiral (Jackiw-Rebbi-like) edge state

$$\psi_\tau(\boldsymbol{\rho}) \propto \begin{bmatrix} 1 \\ \operatorname{sgn}(v_\mathrm{D})\operatorname{sgn}(m_\mathrm{A}) \end{bmatrix} \mathrm{e}^{\mathrm{i}k_x x}\mathrm{e}^{-\frac{|m_\mathrm{A}|}{|v_\mathrm{D}|}|y|}\,, \tag{6.45}$$

which are exponentially localized at the interface – this is expected from the bulk-boundary correspondence since $|\Delta C_-^\tau| = 1$. These edge states exhibit a linear dispersion

$$\omega_\tau(k_x) = \omega_\mathrm{D} + \operatorname{sgn}(\Delta C_-^\tau)|v_\mathrm{D}|k_x\,, \tag{6.46}$$

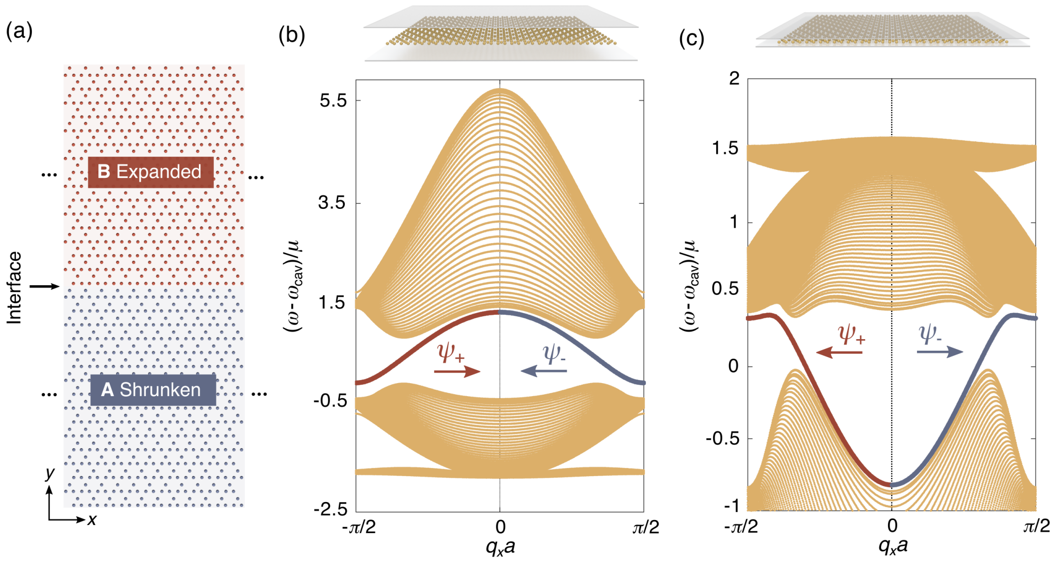

Figure 6.7 | Switching the chirality of the polariton valley-Hall edge states. (a) Schematic of a domain wall interface between two regions with opposite valley-Chern numbers, where region A is a shrunken metasurface ($\delta_\mathrm{A} = 0.05$) and region B is an expanded metasurface ($\delta_\mathrm{B} = -0.05$). (b) Interface dispersion for a large cavity width ($L = 5a$), where the orange bands represent the projected bulk bands that are identical in both regions. The red/blue bands represent the dispersion of the valley-Hall edge states ψ_+/ψ_- in the K/K' valleys which propagate in opposite directions by virtue of $\mathcal{T}$ symmetry. (c) Same as panel (a) but for a small cavity width ($L = 0.5a$). The propagation direction of the valley-Hall edge states has been reversed due to the cavity-induced inversion of the valley-Chern numbers which switches their chirality. Results obtained with $\lambda_0 = 10a$ and $\mu = 0.001\omega_0$.

where their group velocity is given by

$$v_\tau = \frac{\partial \omega_\tau}{\partial k_x} = \mathrm{sgn}(\Delta C_-^\tau)|v_\mathrm{D}|\,, \tag{6.47}$$

and therefore the sign of ΔC_-^τ determines the chirality of the valley-Hall edge states. For large cavity widths we have $\Delta C_-^\tau = \tau$, and therefore the K valley edge state (ψ_+) propagates to the right while the K' valley edge state (ψ_-) propagates to the left. However, for small cavity widths the valley-Chern numbers become inverted in both regions resulting in $\Delta C_-^\tau = -\tau$, and therefore the valley-Hall edge states should reverse their propagation direction.

6.4.2 Interface dispersion

To verify these analytical predictions we go beyond the approximations of the effective Dirac Hamiltonian and calculate the full dispersion for the interface. We consider a supercell which contains 40 unit cells in each region and apply periodic boundary conditions along the x-direction. To avoid edge states emerging in the spectrum that are associated with the boundary with free space we also apply periodic boundary conditions in the y-direction. To calculate the dispersion we use the same coupled-dipole model as outlined in the section 6.2.2 but generalized to the supercell. Since we focus on the A/B interface, for clarity we remove the edge states associated with the B/A interface which are formed due to the periodic boundary conditions in the y-direction.

In figure 6.7(b) we show the interface dispersion for a large cavity width, where we have neglected the weak photon-mediated interactions for clarity (see appendix E.1 for details). The orange bands correspond to the projected bulk states, while the red/blue bands correspond to the spectrum of the valley-Hall edge states near the K/K' valleys which traverse the bulk gap. In accordance with the analytical predictions, one observes that the K valley edge states (ψ_+) propagate to the right (red band) while the the K' valley edge states (ψ_-) propagate to the left (blue band). In figure 6.7(c) we show the dispersion for the same interface but now with a small cavity width. Remarkably, despite the interface geometry being fixed, we indeed observe that the propagation direction of the polariton valley-Hall edge states is reversed, thus verifying the cavity-induced inversion of the valley-Chern numbers.

6.4.3 Selective excitation of the valley-Hall edge states

In this final section we will show how one can selectively excite the valley-Hall edge states with a chiral source and route them around sharp corners. We consider an Ω-shaped interface between a shrunken and expanded metasurface which contains multiple sharp bends. Since there is no translational invariance, one has to numerically solve a system of N coupled-dipole equations

$$\frac{1}{\alpha(\omega)}p_i(\omega) = E_0(\boldsymbol{\rho}_i,\omega) + \sum_{j\neq i} G(\boldsymbol{\rho}_i - \boldsymbol{\rho}_j,\omega)p_j(\omega)\,, \tag{6.48}$$

where p_i represents the induced dipole moment of the $i = 1, 2, \dots, N$ dipole located at $\boldsymbol{\rho}_i$, and $E_0(\boldsymbol{\rho},\omega)$ is the external driving field. Note that we include non-radiative losses in the metasurface by setting $\gamma_{\mathrm{nr}} = 0.02\mu$.

Furthermore, we excite the metasurface with a left-handed chiral source which is comprised of six point sources with a fixed phase difference. The corresponding driving field reads

$$E_0(\boldsymbol{\rho}) \propto \sum_{\upsilon=1}^{6} \mathrm{e}^{-\mathrm{i}\frac{\upsilon\pi}{3}} G(\boldsymbol{\rho} - \boldsymbol{\rho}_0 - \mathbf{e}_\upsilon,\omega)\,, \tag{6.49}$$

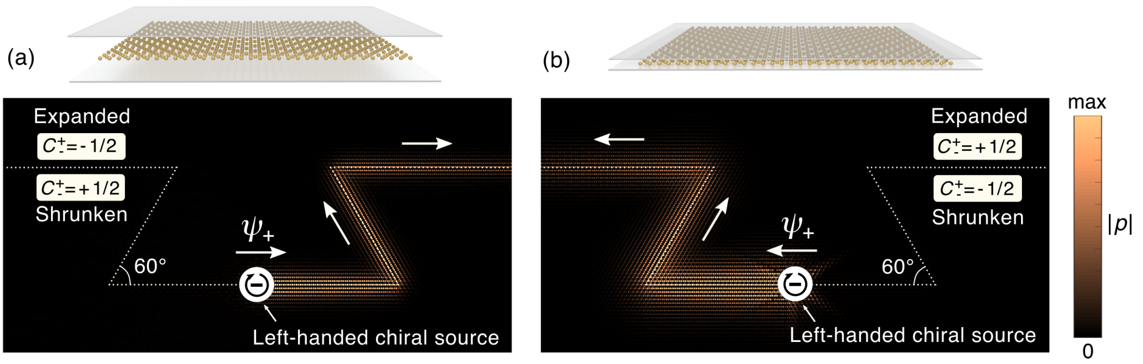

Figure 6.8 | Selective excitation of the polariton valley-Hall edge states. (a) Steady-state distribution of the dipole moments for an Ω-shaped interface (white dotted line) between an expanded (top) and shrunken (bottom) metasurface with a large cavity width ($L = 5a$). We excite the metasurface with a left-handed chiral source at a driving frequency that corresponds to the middle of the gap at the K/K' points. Furthermore, we position the source close to the interface such that it selectively couples only to the K valley edge state. One clearly observes the chiral nature of the valley-Hall edge state which only propagates to the right and is not backscattered by the sharp bends. (b) Same as panel (a) but for a small cavity width ($L = 0.5a$). The valley-Hall edge state in the K valley now propagates in the opposite direction due to the cavity-induced inversion of the valley-Chern numbers. Results obtained with $\lambda_0 = 10a$, $\mu = 0.001\omega_0$ and $\gamma_{\mathrm{nr}} = 0.02\mu$. For panels (a) and (b) we use driving frequencies given by $(\omega - \omega_{\mathrm{cav}}) = 0.471\mu$ and $(\omega - \omega_{\mathrm{cav}}) = 0.208\mu$, respectively.

where $\mathbf{e}_\upsilon = 0.01a[\cos(\upsilon\pi/3)\,,\,\sin(\upsilon\pi/3)\,]$ are the locations of the point sources with respect to the centre of the source located at $\boldsymbol{\rho}_0$. We chose the driving frequencies such that they correspond to the middle of the bulk gap at the K/K' points.

Moreover, we position the chiral source close to the interface so that it selectively excites only the topological edge state in the K valley. It is important to stress that the Dirac velocity also changes sign as the cavity width is reduced. Consequently, from equation (6.45) we can see that the spinor for each valley remains the same in the two limiting interaction regimes. Therefore, if we fix the position of the chiral source it will couple to the K valley edge state in both regimes.

In figure 6.8(a), we plot the steady-state amplitude of the dipole moments for a large cavity width where the Coulomb interactions are dominant. One clearly observes the chiral nature of the valley-Hall edge state which only propagates to the right and is not backscattered by the sharp bends in the interface. Figure 6.8(b) shows the simulation for the same interface but now with a small cavity width where the photon-mediated interactions are dominant. As predicted, the valley-Hall edge state now propagates in the opposite direction due to the cavity-induced inversion of the valley-Chern numbers, thus verifying the ability to switch the chirality of the valley-Hall edge states by varying only the cavity width.

6.5 Conclusion

In this chapter we have proposed an alternative method to engineer topological phase transitions in valley-Hall metasurfaces via accidental Dirac points. While the symmetry-breaking perturbation is required to induce the valley-Hall phase, one does not necessarily have to invert this symmetry-breaking perturbation in order to change the valley-Chern numbers. In particular, we have shown that the topological phase of the polaritons is not inherently fixed by the geometry of the metasurface, but it can depend sensitively on the local electromagnetic environment which mediates the dipole-dipole interactions. Consequently, we have shown that one can invert the valley-Chern numbers and thus switch the chirality of the polariton valley-Hall edge states by embedding the metasurface inside a cavity waveguide. This stands in contrast to previous studies where the valley-Chern numbers are usually fixed by design and the corresponding valley-Hall edge states are forced to propagate in a fixed direction. While this alternative approach is not entirely deterministic, it does not require one to reconfigure the lattice geometry and therefore it may provide an easier way of inducing topological transitions in a variety of metasurfaces.

7

Thesis conclusions and future perspectives

Graphene is a remarkable material where the low-energy electrons do not behave like the usual massive Schrödinger particles. Instead, the electrons hopping on the honeycomb lattice effectively lose their mass and are described by a more exotic massless Dirac Hamiltonian, which is responsible for most of graphene's remarkable electronic properties. The work presented in this thesis was motivated by a simple question: what happens if we replace every carbon atom with a dipole emitter or antenna? Do the polaritons supported by the metasurface inherit some of graphene's intriguing properties? It is evident that symmetries play an important role, endowing the polaritons with Dirac-like properties and constraining the form of the effective Hamiltonian. However, the metasurface hybridizes with the surrounding photons which can mediate long-range interactions between the dipoles, and thus the metasurface is not amenable to a simple tight-binding description.

Furthermore, the hybrid light-matter character of the polaritons affords a tunability that is impossible to achieve for the electrons in graphene, where the properties of the massless Dirac fermions are fixed by the rigid lattice structure. In particular, we have demonstrated that one can modify the nature of the dipole-dipole interactions by structuring the local photonic environment via a cavity waveguide. Exploiting this unique feature of the emitters/antennas, we have unveiled that one can tune the effective Hamiltonian parameters and thus dramatically alter the fundamental properties of the Dirac polaritons by varying the cavity width. This raises some interesting questions which can be explored both theoretically and experimentally in a variety of platforms across the electromagnetic spectrum.

In chapter 4 we demonstrated that a honeycomb metasurface can exhibit both type-I and type-II massless Dirac polaritons with distinct physical origins – in stark contrast to photonic analogs of graphene. Since the type-II Dirac points are accidental and not enforced by the symmetry, one can manipulate their location in the Brillouin zone to induce exotic merging transitions of the Dirac points by varying only the cavity width. Interestingly, one could exploit the tunability of the effective Hamiltonian parameters by engineering spatial variations in the cavity width to generate effective potential and velocity barriers for the Dirac polaritons. The former could give rise to Klein tunnelling and negative refraction which could be exploited for Veselago lensing of polaritons. Furthermore, while we have focused on the bulk properties, it would be interesting to explore how structuring the photonic environment modifies the edge states that usually connect the inequivalent Dirac points [272–276] – do novel edge states emerge from the presence of the accidental type-II Dirac points? In fact, the non-trivial winding in the light-matter interaction provides a relatively deterministic mechanism of generating accidental Dirac points, even in lattices that would not support deterministic Dirac points. Gapping out these accidental Dirac points could then give rise to valley-Hall edge states which could be created and annihilated by varying the cavity width. Finally, the cavity-induced inversion of chirality could have interesting consequences for the valley-Hall edge states that would emerge in a metasurface analog of the Semenoff insulator.

In chapter 5 we demonstrated that one can generate a pseudo-magnetic field for Dirac polaritons by straining the honeycomb metasurface. Interestingly, we have shown that one can tune the pseudo-magnetic field, and even switch it off entirely, by modifying the dipole-dipole interactions via the cavity width. It has been previously shown that there exist quantum-Hall-like edge states associated with the pseudo-magnetic Landau levels [171] – do they exist in the presence of long-range interactions? Can one controllably switch them on/off, or tune their properties, by structuring the photonic environment? Furthermore, one should also be able to observe Aharonov-Bohm-like interference effects [26] for the polaritons which could be tuned by varying the cavity width. Moreover, the polariton Landau levels provide a novel way of sculpting the local density of states which plays a crucial role in determining the radiative properties of emitters – this could be exploited for enhancing/suppressing light-matter interactions in subwavelength photonic structures. Finally, while we have focused on some of the implications of a tunable pseudo-magnetic field, it would be interesting to explore the implications of a tunable pseudo-electric field arising from the pseudo-scalar potential or a time-varying pseudo-vector potential.

In chapter 6 we showed that one can induce the valley-Hall phase for polaritons by perturbing a kagome metasurface. Without inverting the symmetry-breaking perturbation, we showed that one can invert the valley-Chern numbers and therefore switch the chirality of the valley-Hall edge states by varying the cavity width. While these topological transitions arise from the modified dipole-dipole interactions, there may be other environment-induced effects that one could utilize to induce topological transitions, such as the environment-induced Lamb shift. Furthermore, the underlying principle could also have implications for other topological phases that have attracted considerable attention in photonics. For example, perturbed kagome lattices have also been shown to exhibit a higher-order topological phase with topological corner states, where it is usually asserted that the shrunken/expanded lattice is the trivial/topological phase [271]. However, here we have shown the ability to induce multiple band inversions without ever modifying the lattice geometry of the metasurface; do these band inversions change the topological phase? If so, what is the fate of the topological corner states as the photonic environment is modified? Furthermore, perturbed honeycomb lattices have been shown to exhibit pseudo-spin polarized edge states [80] and topological corner states [277]. We suspect that our proposed mechanism could also induce topological band inversions for the metasurface analog of these systems.

The most promising platform for realizing the physics presented in this thesis would probably be a microwave metasurface as they are proving to be a versatile playground for exploring Dirac/topological physics. At these frequencies, metals behave approximately as perfect conductors and therefore losses are small, and cavity waveguides are commonly employed [76]. One particular advantage with microwave metamaterials is that there exists well-established experimental techniques for directly mapping the near-field and obtaining the dispersion of the modes. In particular, using a vector network analyzer, one can excite the metasurfaces using a near-field source antenna, and then the field can be measured using a second detecting antenna which can be scanned along the metasurface using an xyz-translation stage [83]. For the strained metasurface, one could map the entire Landau level spectrum in a single measurement by measuring the return loss of a near-field source antenna which can be related to the local density of states [58].

Furthermore, we note that the underlying principle presented in this thesis could be generalized to include metasurfaces composed of more complex antennas that exhibit large magnetic dipole and higher-order multipole moments. This could include resonant antennas such as split-ring resonators and dielectric Mie resonators which are commonly employed in metamaterial research and exhibit richer interactions. Moreover, our classical analysis is a valid description for a subwavelength array of quantum two-level emitters in the single-excitation subspace [233]. It would therefore be very interesting to explore these phenomena in the quantum regime, by considering subwavelength arrays of atomic (atom-like) quantum emitters, which have been attracting considerable theoretical interest in recent years [217–222] and have started to become an experimental reality [223–226]. Finally, while we have focused on the effect of a cavity waveguide, one could explore other ways of structuring the local photonic environment to modify the nature of the interactions between emitters/antennas – for example, one could consider interactions mediated by the surface plasmons in graphene [278] or the guided modes of photonic crystals [229–231] which may provide alternative mechanisms for tunability.

To conclude, while intense efforts are devoted to designing photonic systems that emulate tight-binding models, this work hints at a rich landscape of physics emerging from non-trivial long-range interactions which are prevalent in electromagnetic systems.

A

Supplementary information for chapter 2

A.1 Klein tunnelling at normal incidence

In this section we provide an alternative way to understand why massless Dirac fermions exhibit Klein tunnelling and thus cannot be localized with a simple potential barrier. At normal incidence the transverse wavevector is zero ($k_y = 0$) and therefore the wavefunction has no y-dependence $\psi(\mathbf{r}) = \psi(x)$. Consequently, the Hamiltonian reduces to an effective 1D massless Dirac Hamiltonian

$$\mathcal{H}_+ = -\mathrm{i}\hbar v_\mathrm{F}\sigma_x\partial_x + V(x)\mathbb{1}_2\,, \tag{A.1}$$

which, after performing a unitary transformation, decouples into two independent scalar Hamiltonians

$$\mathcal{H}_\mathrm{L} = \mathrm{i}\hbar v_\mathrm{F}\partial_x + V(x)\,, \quad \mathcal{H}_\mathrm{R} = -\mathrm{i}\hbar v_\mathrm{F}\partial_x + V(x)\,. \tag{A.2}$$

The first Hamiltonian acts on left-moving electrons described by a scalar wavefunction $\psi_\mathrm{L}(x)$ and free dispersion $E_\mathrm{L}(\mathbf{k}) = -\hbar v_\mathrm{F} k_x$, while the second Hamiltonian acts on right-moving electrons described by a scalar wavefunction $\psi_\mathrm{R}(x)$ and free dispersion $E_\mathrm{R}(\mathbf{k}) = \hbar v_\mathrm{F} k_x$. Since the right-movers and left-movers are completely decoupled the energy eigenstates are trivialy given by

$$\psi_\mathrm{L}(x) = \psi_\mathrm{L}(0)\mathrm{e}^{-\frac{\mathrm{i}}{\hbar v_\mathrm{F}}\int\limits_0^x [E_\mathrm{F}-V(x')]\mathrm{d}x'}\,, \quad \psi_\mathrm{R}(x) = \psi_\mathrm{R}(0)\mathrm{e}^{\frac{\mathrm{i}}{\hbar v_\mathrm{F}}\int\limits_0^x [E_\mathrm{F}-V(x')]\mathrm{d}x'}\,. \tag{A.3}$$

Therefore, there are no bound states and any potential barrier will appear transparent at normal incidence, irrespective of its shape and size.

A.2 Symmetry constraints on the effective Hamiltonian at the M point

In this section we analyze the constraints imposed on the form of the effective Hamiltonian near the M point by the corresponding C_{2v} little point group. Let us assume a general two-band Hamiltonian near the M point

$$\mathcal{H}_{\mathrm{M}}(\mathbf{k}) = \begin{bmatrix} d_0(\mathbf{k}) & d_x(\mathbf{k}) - \mathrm{i}d_y(\mathbf{k}) \\ d_x(\mathbf{k}) + \mathrm{i}d_y(\mathbf{k}) & d_0(\mathbf{k}) \end{bmatrix} = d_0(\mathbf{k})\mathbb{1}_2 + \boldsymbol{\sigma}\cdot\mathbf{d}(\mathbf{k})\,, \tag{A.4}$$

with

$$\mathbf{d}(\mathbf{k}) = [\, d_x(\mathbf{k})\,,\, d_y(\mathbf{k})\,]\,, \tag{A.5}$$

where $d_i(\mathbf{k}) \in \mathbb{R}$ are real functions ($i = 0, x, y$). Here we have already applied the constraint imposed by $\mathcal{IT}$ symmetry which enforces the σ_z term to vanish throughout the entire Brillouin zone.

The C_{2v} little point group is generated by $\{\,\mathcal{C}_2\,,\,\mathcal{M}_y\,\}$, where $\mathcal{C}_2$ represents a π rotation about the z-axis which is equivalent to $\mathcal{I}$ in two dimensions. Since $\mathcal{M}_y$ exchanges the two sublattices and sends $k_y \to -k_y$, it imposes the following constraint on the effective Hamiltonian

$$\mathcal{M}_y : \quad \sigma_x\mathcal{H}_{\mathrm{M}}(k_x\,,\,k_y)\sigma_x = \mathcal{H}_{\mathrm{M}}(k_x\,,\,-k_y)\,, \tag{A.6}$$

which is satisfied if

$$d_0(k_x\,,\,k_y) = d_0(k_x\,,\,-k_y)\,,\; d_x(k_x\,,\,k_y) = d_x(k_x\,,\,-k_y)\,,\; -d_y(k_x\,,\,k_y) = d_y(k_x\,,\,-k_y)\,. \tag{A.7}$$

Moreover, since $\mathcal{I}$ also exchanges the two sublattices and sends $\mathbf{k} \to -\mathbf{k}$, it imposes the following constraint on the effective Hamiltonian

$$\mathcal{I} : \quad \sigma_x\mathcal{H}_{\mathrm{M}}(k_x\,,\,k_y)\sigma_x = \mathcal{H}_{\mathrm{M}}(-k_x\,,\,-k_y)\,, \tag{A.8}$$

which is satisfied if

$$d_0(k_x\,,\,k_y) = d_0(-k_x\,,\,-k_y)\,,\; d_x(k_x\,,\,k_y) = d_x(-k_x\,,\,-k_y)\,,\; -d_y(k_x\,,\,k_y) = d_y(-k_x\,,\,-k_y)\,. \tag{A.9}$$

Furthermore, while the M point is also a $\mathcal{T}$ invariant point in the Brillouin zone, $\mathcal{T}$ symmetry alone does not impose any further constraints. Finally, putting all these constraints together, the most general form of the effective Hamiltonian near the M point up to quadratic order in $\mathbf{k}$ reads

$$\mathcal{H}_{\mathrm{M}}(\mathbf{k}) = (c_1 + c_2 k_x^2 + c_3 k_y^2)\mathbb{1}_2 + (c_4 + c_5 k_x^2 + c_6 k_y^2)\sigma_x + c_7 k_y \sigma_y \,, \tag{A.10}$$

where $c_i \in \mathbb{R}$ are real constants ($i = 1, 2, \ldots, 7$).

B

Supplementary information for chapter 3

B.1 Equivalence of the eigenfunction and image expansions

In this section we will show that the image expansion of the cavity Green's function is equivalent the eigenfunction expansion. For convenience, we reprint the image expansion given by equation (3.81) and equation (3.82) which read

$$\overleftrightarrow{\mathbf{G}}(\mathbf{r},\mathbf{r}',\omega) = \overleftrightarrow{\mathbf{G}}_{1\mathrm{D}}(\mathbf{r},\mathbf{r}',\omega) + \overleftrightarrow{\mathbf{G}}_{1\mathrm{D}}(\mathbf{r},\mathbf{r}'+(L-2z')\hat{\mathbf{z}},\omega)\cdot\overleftrightarrow{\mathbf{I}}_{xy}\,, \tag{B.1}$$

and

$$\overleftrightarrow{\mathbf{G}}_{1\mathrm{D}}(\mathbf{r},\mathbf{r}',\omega) = \frac{\mathcal{V}}{4\pi}\sum_{l=-\infty}^{\infty}\left(k_\omega^2\overleftrightarrow{\mathbf{I}} + \boldsymbol{\nabla}\boldsymbol{\nabla}\right)\frac{\mathrm{e}^{\mathrm{i}k_\omega|\mathbf{r}-\mathbf{r}'+\mathbf{R}_l|}}{|\mathbf{r}-\mathbf{r}'+\mathbf{R}_l|}\,, \tag{B.2}$$

respectively. To begin, we can use the following integral representation (see 6.677(8) in ref [279])

$$\frac{\mathrm{e}^{\mathrm{i}k_\omega|\mathbf{r}-\mathbf{r}'+\mathbf{R}_l|}}{|\mathbf{r}-\mathbf{r}'+\mathbf{R}_l|} = \frac{\mathrm{i}}{2}\int_{-\infty}^{\infty} H_0^{(1)}\left(|\boldsymbol{\rho}-\boldsymbol{\rho}'|\sqrt{k_\omega^2-q^2}\right)\mathrm{e}^{\mathrm{i}(z-z'+2lL)q}\mathrm{d}q \tag{B.3}$$

to transform equation (B.2) into

$$\overleftrightarrow{\mathbf{G}}_{1\mathrm{D}}(\mathbf{r},\mathbf{r}',\omega) = \mathrm{i}\frac{\mathcal{V}}{8\pi}\sum_{l=-\infty}^{\infty}\left(k_\omega^2\overleftrightarrow{\mathbf{I}} + \boldsymbol{\nabla}\boldsymbol{\nabla}\right)\int_{-\infty}^{\infty} H_0^{(1)}\left(|\boldsymbol{\rho}-\boldsymbol{\rho}'|\sqrt{k_\omega^2-q^2}\right)\mathrm{e}^{\mathrm{i}(z-z'+2lL)q}\mathrm{d}q\,. \tag{B.4}$$

Next, we can use the 1D form of Poisson's summation identity

$$\sum_{l=-\infty}^{\infty}\mathrm{e}^{\mathrm{i}2lLq} = \frac{\pi}{L}\sum_{m=-\infty}^{\infty}\delta\left(q-k_m\right)\,, \tag{B.5}$$

and after summing the positive and negative values of m we obtain

$$\overleftrightarrow{\mathbf{G}}_{\mathrm{1D}}(\mathbf{r},\mathbf{r}',\omega)=\mathrm{i}\frac{\mathcal{V}}{8}\sum_{m=0}^{\infty}\frac{N_m}{L}\left(k_\omega^2\overleftrightarrow{\mathbf{I}}+\nabla\nabla\right)\cos[(z-z')k_m]H_0^{(1)}\left(\sqrt{k_\omega^2-k_m^2}|\boldsymbol{\rho}-\boldsymbol{\rho}'|\right)\,. \tag{B.6}$$

By inserting equation (B.6) into equation (B.1) and using the following trigonometric identities

$$\begin{aligned}\cos[(z-z')k_m]+\cos[(z+z'+L)k_m]&=2\cos(k_m\tilde{z})\cos(k_m\tilde{z}')\\ \cos[(z-z')k_m]-\cos[(z+z'+L)k_m]&=2\sin(k_m\tilde{z})\sin(k_m\tilde{z}')\,,\end{aligned} \tag{B.7}$$

we can re-express equation (B.1) as

$$\overleftrightarrow{\mathbf{G}}(\mathbf{r},\mathbf{r}',\omega)=\mathrm{i}\frac{\mathcal{V}}{4}\sum_{m=0}^{\infty}\frac{N_m}{L}\left(k_\omega^2\overleftrightarrow{\mathbf{I}}+\nabla\nabla\right)H_0^{(1)}\left(\sqrt{k_\omega^2-k_m^2}|\boldsymbol{\rho}-\boldsymbol{\rho}'|\right)\overleftrightarrow{\mathbf{C}}_m(z,z')\,, \tag{B.8}$$

which is identical to equation (3.74) that we obtained via the eigenfunction expansion method.

C

Supplementary information for chapter 4

C.1 Expansion of the dynamical matrix near the K point

In this section we provide additional details for the expansion of the dynamical matrix near the K point which yielded equation (4.37) and equation (4.38). We will begin by expanding the intrasublattice elements of the longitudinal dynamical matrix in equation (4.14) which, to quadratic order in $\mathbf{k} = \mathbf{q} - \mathbf{K}$, read

$$\mathcal{D}_{\parallel +}^{\mathrm{AA/BB}}(\mathbf{k}) \simeq \sum_{\mathbf{R}\neq 0} \left[G_{\parallel}(\mathbf{R})\mathrm{e}^{-\mathrm{i}\mathbf{K}\cdot\mathbf{R}} - \mathrm{i}G_{\parallel}(\mathbf{R})\mathrm{e}^{-\mathrm{i}\mathbf{K}\cdot\mathbf{R}}(\mathbf{R})_{\nu}k_{\nu} - \frac{1}{2}G_{\parallel}(\mathbf{R})\mathrm{e}^{-\mathrm{i}\mathbf{K}\cdot\mathbf{R}}(\mathbf{R})_{\nu}(\mathbf{R})_{\nu'}k_{\nu}k_{\nu'} \right] . \tag{C.1}$$

From the symmetry analysis that we performed in section 2.2.6 we know that some of the terms in the expansion should vanish identically. We can see this explicitly within the coupled-dipole equations by exploiting the symmetry of the honeycomb lattice and summing the contributions from dipoles residing at the same separation distance. For a given lattice vector in the sum we can find six vectors that have the same magnitude

$$\mathbf{R}_{ij} = (\mathcal{M}_x)^i \mathcal{R}(j2\pi/3) \cdot \mathbf{R} , \quad i = 0, 1 , \ j = 0, 1, 2 , \tag{C.2}$$

where $\mathcal{M}_x : [\, x \, , y \,] \to [\, -x \, , \, y \,]$ represents a mirror reflection in the yz-plane and $\mathcal{R}(\theta)$ is the rotation matrix defined in equation (4.22). Note, these vectors are not necessarily all different but this over counting does not matter for the following symmetry analysis. One can show that the coefficients of the k_x, k_y and $k_x k_y$ terms vanish since

$$\sum_{i=0}^{1}\sum_{j=0}^{2} \mathrm{e}^{-\mathrm{i}\mathbf{K}\cdot\mathbf{R}_{ij}}(\mathbf{R}_{ij})_{\nu} = 0 , \quad \sum_{i=0}^{1}\sum_{j=0}^{2} \mathrm{e}^{-\mathrm{i}\mathbf{K}\cdot\mathbf{R}_{ij}}(\mathbf{R}_{ij})_{x}(\mathbf{R}_{ij})_{y} = 0 , \tag{C.3}$$

and one can also show that the other coefficients are real since

$$\sum_{i=0}^{1}\sum_{j=0}^{2}\mathrm{e}^{-\mathrm{i}\mathbf{K}\cdot\mathbf{R}_{ij}} \in \mathbb{R}\,, \quad \sum_{i=0}^{1}\sum_{j=0}^{2}\mathrm{e}^{-\mathrm{i}\mathbf{K}\cdot\mathbf{R}_{ij}}(\mathbf{R}_{ij})_x^2 = \sum_{i=0}^{1}\sum_{j=0}^{2}\mathrm{e}^{-\mathrm{i}\mathbf{K}\cdot\mathbf{R}_{ij}}(\mathbf{R}_{ij})_y^2 \in \mathbb{R}\,. \tag{C.4}$$

Next, we can expand the intrasublattice elements of the transverse dynamical matrix in equation (4.27) which, to quadratic order in $\mathbf{k} = \mathbf{q} - \mathbf{K}$, read

$$\begin{aligned}\mathcal{D}_{\perp+}^{\text{AA/BB}}(\mathbf{k}) \simeq \sum_{\mathbf{g}}\Bigg\{&\frac{\omega^2\xi^2}{\omega_{\mathbf{K}-\mathbf{g}}^2-\omega^2} - \mathrm{Re}[G_{\perp}^{\text{TEM}}(0,\omega)] + \frac{2\omega^2\xi^2c^2(\mathbf{K}-\mathbf{g})_\nu}{(\omega_{\mathbf{K}-\mathbf{g}}^2-\omega^2)^2}k_\nu \\ &-\frac{1}{2}\left[\frac{2c^2\omega^2\xi^2\delta_{\nu\nu'}}{(\omega_{\mathbf{K}-\mathbf{g}}^2-\omega^2)^2} - \frac{8\omega^2\xi^2c^4(\mathbf{K}-\mathbf{g})_\nu(\mathbf{K}-\mathbf{g})_{\nu'}}{(\omega_{\mathbf{K}-\mathbf{g}}^2-\omega^2)^3}\right]k_\nu k_{\nu'}\Bigg\}\,.\end{aligned} \tag{C.5}$$

Due to the symmetry of the Brillouin zone, we can find six photonic modes that are degenerate at the K point corresponding to the reciprocal lattice vectors

$$\mathbf{g}_{ij} = \mathbf{K} - (\mathcal{M}_y)^i\mathcal{R}(j2\pi/3)\cdot(\mathbf{K}-\mathbf{g})\,, \tag{C.6}$$

which are not necessarily all different. By summing the contributions from these degenerate photons one can show that the coefficients of the k_x, k_y and k_xk_y terms vanish since

$$\sum_{i=0}^{1}\sum_{j=0}^{2}(\mathbf{K}-\mathbf{g}_{ij})_\nu = 0\,, \quad \sum_{i=0}^{1}\sum_{j=0}^{2}(\mathbf{K}-\mathbf{g}_{ij})_x(\mathbf{K}-\mathbf{g}_{ij})_y = 0\,, \tag{C.7}$$

and one can also show that the other coefficients are real since

$$\sum_{i=0}^{1}\sum_{j=0}^{2}(\mathbf{K}-\mathbf{g}_{ij})_x^2 = \sum_{i=0}^{1}\sum_{j=0}^{2}(\mathbf{K}-\mathbf{g}_{ij})_y^2 \in \mathbb{R}\,, \tag{C.8}$$

Putting all this together we obtain equation (4.37), which has the expected form from the general symmetry analysis presented in section 2.2.6.

We can perform similar analysis for the intersublattice elements of the longitudinal dynamical matrix in equation (4.15) which expand as

$$\begin{aligned}\mathcal{D}_{\parallel+}^{\text{AB}}(\mathbf{k}) \simeq \sum_{\mathbf{R}}\Big[&G_{\parallel}(\mathbf{R}-\mathbf{d})\mathrm{e}^{-\mathrm{i}\mathbf{K}\cdot(\mathbf{R}-\mathbf{d})} - \mathrm{i}G_{\parallel}(\mathbf{R}-\mathbf{d})\mathrm{e}^{-\mathrm{i}\mathbf{K}\cdot\mathbf{R}}(\mathbf{R}-\mathbf{d})_\nu k_\nu \\ &-\frac{1}{2}G_{\parallel}(\mathbf{R}-\mathbf{d})\mathrm{e}^{-\mathrm{i}\mathbf{K}\cdot(\mathbf{R}-\mathbf{d})}(\mathbf{R}-\mathbf{d})_\nu(\mathbf{R}-\mathbf{d})_{\nu'}k_\nu k_{\nu'}\Big]\,.\end{aligned} \tag{C.9}$$

Again, using the symmetry of the honeycomb lattice we can find six vectors (not necessarily all different)

$$\mathbf{R}_{ij} - \mathbf{d} = (\mathcal{M}_x)^i \mathcal{R}(j2\pi/3) \cdot (\mathbf{R} - \mathbf{d}) \,, \tag{C.10}$$

which locate dipoles on the opposite sublattice that reside at the same separation distance. By summing the contributions from these dipoles one can show that the zeroth order term vanishes since

$$\sum_{i=0}^{1}\sum_{j=0}^{2} \mathrm{e}^{-\mathrm{i}\mathbf{K}\cdot(\mathbf{R}_{ij}-\mathbf{d})} = 0 \,. \tag{C.11}$$

Furthermore, one can show that the coefficient of k_x is real and the coefficient of k_y is imaginary since

$$\mathrm{i}\sum_{i=0}^{1}\sum_{j=0}^{2} \mathrm{e}^{-\mathrm{i}\mathbf{K}\cdot(\mathbf{R}_{ij}-\mathbf{d})}(\mathbf{R}_{ij}-\mathbf{d})_x = -\sum_{i=0}^{1}\sum_{j=0}^{2} \mathrm{e}^{-\mathrm{i}\mathbf{K}\cdot(\mathbf{R}_{ij}-\mathbf{d})}(\mathbf{R}_{ij}-\mathbf{d})_y \in \mathbb{R} \,, \tag{C.12}$$

and one can also show that the coefficients of k_x^2 and k_y^2 are real while the coefficient of $k_x k_y$ is imaginary since

$$\begin{aligned}\sum_{i=0}^{1}\sum_{j=0}^{2} \mathrm{e}^{-\mathrm{i}\mathbf{K}\cdot(\mathbf{R}_{ij}-\mathbf{d})}(\mathbf{R}_{ij}-\mathbf{d})_x^2 &= -\sum_{i=0}^{1}\sum_{j=0}^{2} \mathrm{e}^{-\mathrm{i}\mathbf{K}\cdot(\mathbf{R}_{ij}-\mathbf{d})}(\mathbf{R}_{ij}-\mathbf{d})_y^2 \\ &= -\mathrm{i}\sum_{i=0}^{1}\sum_{j=0}^{2} \mathrm{e}^{-\mathrm{i}\mathbf{K}\cdot(\mathbf{R}_{ij}-\mathbf{d})}(\mathbf{R}_{ij}-\mathbf{d})_x(\mathbf{R}_{ij}-\mathbf{d})_y \in \mathbb{R} \,.\end{aligned} \tag{C.13}$$

Next, we can expand the intersublattice elements of the transverse dynamical matrix in equation (4.28) which read

$$\begin{aligned}\mathcal{D}_{\perp+}^{\mathrm{AB}}(\mathbf{k}) \simeq \sum_{\mathbf{g}} \phi_{\mathbf{g}} \Bigg\{ &\frac{\omega^2\xi^2}{\omega_{\mathbf{K}-\mathbf{g}}^2 - \omega^2} + \frac{2\omega^2\xi^2c^2(\mathbf{K}-\mathbf{g})_\nu}{(\omega_{\mathbf{K}-\mathbf{g}}^2 - \omega^2)^2} k_\nu \\ -\frac{1}{2}\Bigg[&\frac{2c^2\omega^2\xi^2\delta_{\nu\nu'}}{(\omega_{\mathbf{K}-\mathbf{g}}^2 - \omega^2)^2} - \frac{8\omega^2\xi^2c^4(\mathbf{K}-\mathbf{g})_\nu(\mathbf{K}-\mathbf{g})_{\nu'}}{(\omega_{\mathbf{K}-\mathbf{g}}^2 - \omega^2)^3}\Bigg] k_\nu k_{\nu'} \Bigg\} \,.\end{aligned} \tag{C.14}$$

Using the same reciprocal lattice vectors in equation (C.6) one can show that the zeroth order term vanishes since

$$\sum_{i=0}^{1}\sum_{j=0}^{2} \phi_{\mathbf{g}_{ij}} = 0 \,. \tag{C.15}$$

Furthermore, one can show that the coefficient of k_x is real and the coefficient of k_y is imaginary since

$$\sum_{i=0}^{1}\sum_{j=0}^{2}\phi_{\mathbf{g}_{ij}}(\mathbf{K}-\mathbf{g}_{ij})_x = \mathrm{i}\sum_{i=0}^{1}\sum_{j=0}^{2}\phi_{\mathbf{g}_{ij}}(\mathbf{K}-\mathbf{g}_{ij})_y \in \mathbb{R}\,, \tag{C.16}$$

and one can also show that the coefficients of k_x^2 and k_y^2 are real while the coefficient of $k_x k_y$ is imaginary since

$$\sum_{i=0}^{1}\sum_{j=0}^{2}\phi_{\mathbf{g}_{ij}}(\mathbf{K}-\mathbf{g}_{ij})_x^2 = -\sum_{i=0}^{1}\sum_{j=0}^{2}\phi_{\mathbf{g}_{ij}}(\mathbf{K}-\mathbf{g}_{ij})_y^2 = -\mathrm{i}\sum_{i=0}^{1}\sum_{j=0}^{2}\phi_{\mathbf{g}_{ij}}(\mathbf{K}-\mathbf{g}_{ij})_x(\mathbf{K}-\mathbf{g}_{ij})_y \in \mathbb{R}\,. \tag{C.17}$$

Putting all this together we obtain equation (4.38), which has the expected form from the general symmetry analysis presented in section 2.2.6.

C.2 Expansion of the dynamical matrix near the M point

In this section we provide additional details for the expansion of the dynamical matrix near the M point which leads to the effective Hamiltonian in equation (4.59). We will begin by expanding the intrasublattice elements of the longitudinal dynamical matrix in equation (4.14) which, to quadratic order in $\mathbf{k} = \mathbf{q} - \mathbf{M}$, read

$$\mathcal{D}_{\parallel +}^{\mathrm{AA/BB}}(\mathbf{k}) \simeq \sum_{\mathbf{R}\neq 0}\left[G_{\parallel}(\mathbf{R})\mathrm{e}^{-\mathrm{i}\mathbf{M}\cdot\mathbf{R}} - \mathrm{i}G_{\parallel}(\mathbf{R})\mathrm{e}^{-\mathrm{i}\mathbf{M}\cdot\mathbf{R}}(\mathbf{R})_{\nu}k_{\nu} - \frac{1}{2}G_{\parallel}(\mathbf{R})\mathrm{e}^{-\mathrm{i}\mathbf{M}\cdot\mathbf{R}}(\mathbf{R})_{\nu}(\mathbf{R})_{\nu'}k_{\nu}k_{\nu'}\right]. \tag{C.18}$$

From the symmetry analysis that we performed in appendix A.2 we know that some of the terms in the expansion should vanish identically. Since the M point is not invariant under $\mathcal{C}_3$, it plays no role in constraining the matrix elements. However, exploiting the mirror symmetries we can find four lattice vectors (not necessarily all different)

$$\mathbf{R}_{ij} = (\mathcal{M}_x)^i(\mathcal{M}_y)^j\cdot\mathbf{R}\,, \quad i,j = 0,1\,, \tag{C.19}$$

which locate dipoles on the same sublattice that reside at the same separation distance. By summing the contributions from these dipoles one can show that the coefficients of k_x, k_y and $k_x k_y$ vanish since

$$\sum_{i,j=0}^{1}\mathrm{e}^{-\mathrm{i}\mathbf{M}\cdot\mathbf{R}_{ij}}(\mathbf{R}_{ij})_{\nu} = 0\,, \quad \sum_{i,j=0}^{1}\mathrm{e}^{-\mathrm{i}\mathbf{M}\cdot\mathbf{R}_{ij}}(\mathbf{R}_{ij})_x(\mathbf{R}_{ij})_y = 0\,, \tag{C.20}$$

while the zeroth order term and the coefficients of k_x^2 and k_y^2 are real since

$$\sum_{i,j=0}^{1} \mathrm{e}^{-\mathrm{i}\mathbf{M}\cdot\mathbf{R}_{ij}} \in \mathbb{R}\,, \quad \sum_{i,j=0}^{1} \mathrm{e}^{-\mathrm{i}\mathbf{M}\cdot\mathbf{R}_{ij}} (\mathbf{R}_{ij})_x^2 \in \mathbb{R}\,, \quad \sum_{i,j=0}^{1} \mathrm{e}^{-\mathrm{i}\mathbf{M}\cdot\mathbf{R}_{ij}} (\mathbf{R}_{ij})_y^2 \in \mathbb{R}\,. \tag{C.21}$$

Next, we can expand the intrasublattice elements of the transverse dynamical matrix in equation (4.27) which, to quadratic order in $\mathbf{k} = \mathbf{q} - \mathbf{M}$, read

$$\begin{aligned} \mathcal{D}_{\perp+}^{\mathrm{AA/BB}}(\mathbf{k}) \simeq \sum_{\mathbf{g}} \Bigg\{ & \frac{\omega^2\xi^2}{\omega_{\mathbf{M}-\mathbf{g}}^2 - \omega^2} - \mathrm{Re}[G_{\perp}^{\mathrm{TEM}}(0,\omega)] + \frac{2\omega^2\xi^2 c^2 (\mathbf{M}-\mathbf{g})_\nu}{(\omega_{\mathbf{M}-\mathbf{g}}^2 - \omega^2)^2} k_\nu \\ & - \frac{1}{2}\left[\frac{2c^2\omega^2\xi^2\delta_{\nu\nu'}}{(\omega_{\mathbf{M}-\mathbf{g}}^2 - \omega^2)^2} - \frac{8\omega^2\xi^2 c^4 (\mathbf{M}-\mathbf{g})_\nu (\mathbf{M}-\mathbf{g})_{\nu'}}{(\omega_{\mathbf{M}-\mathbf{g}}^2 - \omega^2)^3} \right] k_\nu k_{\nu'} \Bigg\}\,. \end{aligned} \tag{C.22}$$

Using the symmetry of the Brillouin zone we can find four photonic modes (not necessarily all different) that are degenerate at the M point corresponding to the reciprocal lattice vectors

$$\mathbf{g}_{ij} = \mathbf{M} - (\mathcal{I})^i (\mathcal{M}_y)^j \cdot (\mathbf{M} - \mathbf{g})\,, \quad i,j = 0,1\,. \tag{C.23}$$

By summing the contributions from these degenerate photons one can show that the coefficients of k_x, k_y and $k_x k_y$ vanish since

$$\sum_{i,j=0}^{1} (\mathbf{M} - \mathbf{g}_{ij})_\nu = 0\,, \quad \sum_{i,j=0}^{1} (\mathbf{M} - \mathbf{g}_{ij})_x (\mathbf{M} - \mathbf{g}_{ij})_y = 0\,, \tag{C.24}$$

while the zeroth order term and the coefficients of k_x^2 and k_y^2 are real since

$$\sum_{i,j=0}^{1} (\mathbf{M} - \mathbf{g}_{ij})_x^2 \in \mathbb{R}\,, \quad \sum_{i,j=0}^{1} (\mathbf{M} - \mathbf{g}_{ij})_y^2 \in \mathbb{R}\,. \tag{C.25}$$

We can perform similar analysis for the intersublattice elements of the longitudinal dynamical matrix in equation (4.15) which expand as

$$\begin{aligned} \mathcal{D}_{\parallel+}^{\mathrm{AB}}(\mathbf{k}) \simeq \sum_{\mathbf{R}} \Big[& G_{\parallel}(\mathbf{R}-\mathbf{d}) \mathrm{e}^{-\mathrm{i}\mathbf{M}\cdot(\mathbf{R}-\mathbf{d})} - \mathrm{i} G_{\parallel}(\mathbf{R}-\mathbf{d}) \mathrm{e}^{-\mathrm{i}\mathbf{M}\cdot\mathbf{R}} (\mathbf{R}-\mathbf{d})_\nu k_\nu \\ & - \frac{1}{2} G_{\parallel}(\mathbf{R}-\mathbf{d}) \mathrm{e}^{-\mathrm{i}\mathbf{M}\cdot(\mathbf{R}-\mathbf{d})} (\mathbf{R}-\mathbf{d})_\nu (\mathbf{R}-\mathbf{d})_{\nu'} k_\nu k_{\nu'} \Big]\,. \end{aligned} \tag{C.26}$$

Exploiting the mirror symmetry we can find two vectors (not necessarily different)

$$\mathbf{R}_i - \mathbf{d} = (\mathcal{M}_x)^i \cdot (\mathbf{R} - \mathbf{d})\,, \quad i = 0, 1\ , \tag{C.27}$$

which locate dipoles on the opposite sublattice that reside at the same separation distance. By summing the contributions from these dipoles one can show that the coefficients of k_x and $k_x k_y$ vanish since

$$\sum_{i=0}^{1} \mathrm{e}^{-\mathrm{i}\mathbf{M}\cdot(\mathbf{R}_i-\mathbf{d})}(\mathbf{R}_i - \mathbf{d})_x = 0\,, \quad \sum_{i=0}^{1} \mathrm{e}^{-\mathrm{i}\mathbf{M}\cdot(\mathbf{R}_i-\mathbf{d})}(\mathbf{R}_i - \mathbf{d})_x(\mathbf{R}_i - \mathbf{d})_y = 0\,. \tag{C.28}$$

Moreover, one can show that the zeroth order term is real and the coefficient of k_y is imaginary since

$$\sum_{i=0}^{1} \mathrm{e}^{-\mathrm{i}\mathbf{M}\cdot(\mathbf{R}_i-\mathbf{d})} \in \mathbb{R}\,, \quad \sum_{i=0}^{1} \mathrm{e}^{-\mathrm{i}\mathbf{M}\cdot(\mathbf{R}_i-\mathbf{d})}(\mathbf{R}_i - \mathbf{d})_y \in \mathbb{R}\,, \tag{C.29}$$

while the coefficients of k_x^2 and k_y^2 are real since

$$\sum_{i=0}^{1} \mathrm{e}^{-\mathrm{i}\mathbf{M}\cdot(\mathbf{R}_i-\mathbf{d})}(\mathbf{R}_i - \mathbf{d})_x^2 \in \mathbb{R}\,, \quad \sum_{i=0}^{1} \mathrm{e}^{-\mathrm{i}\mathbf{M}\cdot(\mathbf{R}_i-\mathbf{d})}(\mathbf{R}_i - \mathbf{d})_y^2 \in \mathbb{R}\,. \tag{C.30}$$

Next, we can expand the intersublattice elements of the transverse dynamical matrix in equation (4.28) which read

$$\begin{aligned}\mathcal{D}_{\perp+}^{\mathrm{AB}}(\mathbf{k}) \simeq \sum_{\mathbf{g}} \phi_{\mathbf{g}} \Bigg\{ & \frac{\omega^2\xi^2}{\omega_{\mathbf{M}-\mathbf{g}}^2 - \omega^2} + \frac{2\omega^2\xi^2c^2(\mathbf{M}-\mathbf{g})_\nu}{(\omega_{\mathbf{M}-\mathbf{g}}^2 - \omega^2)^2} k_\nu \\ & -\frac{1}{2}\left[\frac{2c^2\omega^2\xi^2\delta_{\nu\nu'}}{(\omega_{\mathbf{M}-\mathbf{g}}^2 - \omega^2)^2} - \frac{8\omega^2\xi^2c^4(\mathbf{M}-\mathbf{g})_\nu(\mathbf{M}-\mathbf{g})_{\nu'}}{(\omega_{\mathbf{M}-\mathbf{g}}^2 - \omega^2)^3}\right] k_\nu k_{\nu'} \Bigg\}\,.\end{aligned} \tag{C.31}$$

Using the same reciprocal lattice vectors in equation (C.23) one can show that the coefficients of k_x and $k_x k_y$ vanish since

$$\sum_{i,j=0}^{1} \phi_{\mathbf{g}_{ij}}(\mathbf{M} - \mathbf{g}_{ij})_x = 0\,, \quad \sum_{i,j=0}^{1} \phi_{\mathbf{g}_{ij}}(\mathbf{M} - \mathbf{g}_{ij})_x(\mathbf{M} - \mathbf{g}_{ij})_y = 0\,. \tag{C.32}$$

Moreover, one can show that the zeroth order term is real and the coefficient of k_y is imaginary since

$$\sum_{i,j=0}^{1} \phi_{\mathbf{g}_{ij}} \in \mathbb{R}\,, \quad \mathrm{i} \sum_{i,j=0}^{1} \phi_{\mathbf{g}_{ij}} (\mathbf{M} - \mathbf{g}_{ij})_y \in \mathbb{R}\,, \tag{C.33}$$

while the coefficients of k_x^2 and k_y^2 are real since

$$\sum_{i,j=0}^{1} \phi_{\mathbf{g}_{ij}} (\mathbf{M} - \mathbf{g}_{ij})_x^2 \in \mathbb{R}\,, \quad \sum_{i,j=0}^{1} \phi_{\mathbf{g}_{ij}} (\mathbf{M} - \mathbf{g}_{ij})_y^2 \in \mathbb{R}\,. \tag{C.34}$$

Putting all this together leads us to the effective Hamiltonian in equation (4.59), which has the expected form from the general symmetry analysis presented in appendix A.2.

D

Supplementary information for chapter 5

D.1 Wavepacket simulations beyond the linear Dirac cone approximation

In this section we present the polariton wavepacket simulations beyond the linear Dirac cone approximation. As we discussed in chapter 4, there exists a critical cavity width ($L = L_v$) where the Dirac velocity vanishes and the polariton spectrum becomes quadratic. To capture the essential physics within the vicinity of this critical cavity width, we must include second-order field gradients in the effective Hamiltonian which, for the K valley, reads

$$\begin{aligned}\mathcal{H}_+ =&\omega_\mathrm{D}(L)\mathbb{1}_2 + \mathrm{i}v_\mathrm{D}(L)\boldsymbol{\sigma}\cdot\boldsymbol{\nabla} + \mathit{\Phi}(\boldsymbol{\rho},L)\mathbb{1}_2 + \boldsymbol{\sigma}\cdot\mathbf{A}(\boldsymbol{\rho},L)\\ &- D(L)\nabla^2\mathbb{1}_2 - t(L)\boldsymbol{\sigma}\cdot\Big[\partial_x^2-\partial_y^2\,,\,-2\partial_x\partial_y\Big]\,.\end{aligned} \tag{D.1}$$

Here the trigonal warping parameter $t(L)$ is given by equation (4.43) and the band asymmetry parameter $D(L)$ is given by equation (4.44). Therefore, in this regime the pseudo-vector potential does not enter the effective Hamiltonian like a gauge field and therefore we should not expect it to generate a pseudo-magnetic field.

To investigate the effects of the quadratic terms on the effective cyclotron motion of the polariton wavepackets, we replace the operator given by equation (5.59) with

$$\mathcal{M}_k^+ = \mathrm{e}^{-\mathrm{i}(\omega_\mathrm{D}+Dk^2)\delta t}\left[\cos(U)\mathbb{1}_2 - \mathrm{i}\frac{\sin(U)}{U}\boldsymbol{\sigma}\cdot\mathbf{U}\right], \tag{D.2}$$

where we have introduced the vector

$$\mathbf{U} = \delta t\Big[-v_\mathrm{D}k_x + t(k_x^2-k_y^2)\,,\,-v_\mathrm{D}k_y - 2tk_xk_y\Big]\,. \tag{D.3}$$

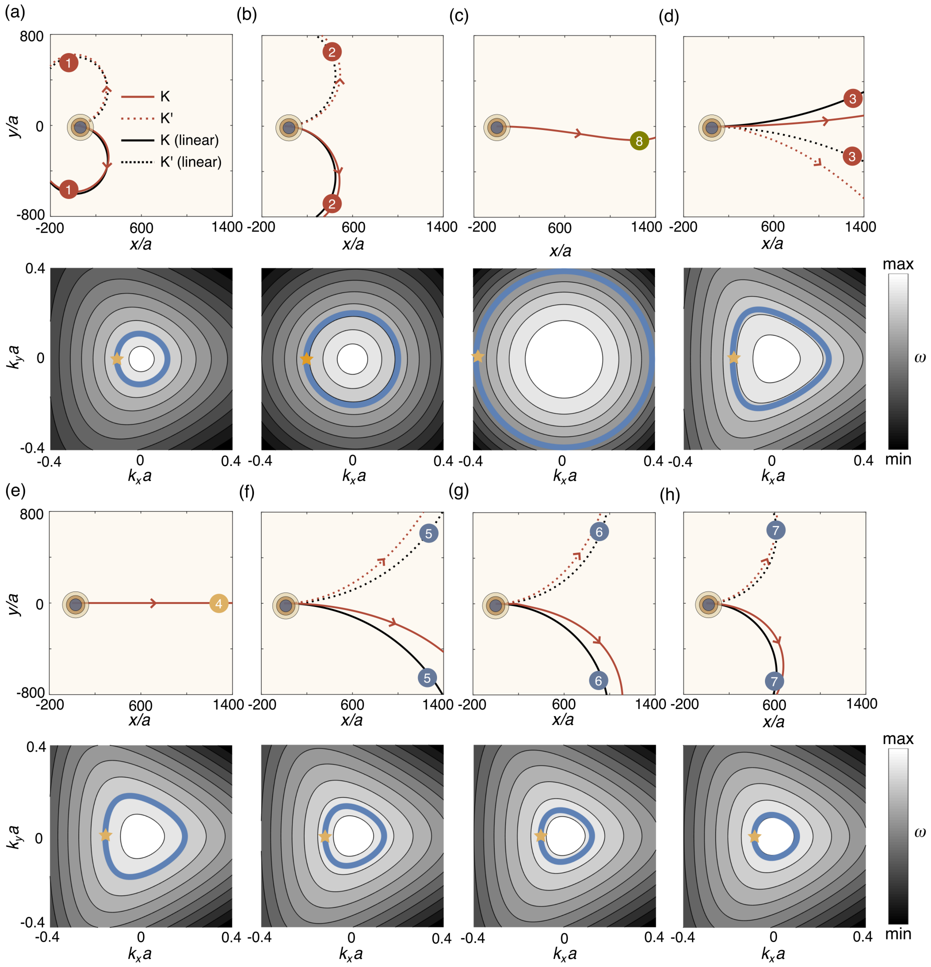

Figure D.1 | Wavepacket simulations beyond the linear Dirac cone approximation. (a)-(h) The top panels show the simulated trajectories of the Gaussian wavepackets propagating through a strained metasurface with different cavity widths. Panels (a), (b) and (d)-(h) correspond to the same parameters (and trajectory numbers) used in figure 5.5. We compare the trajectories obtained with the linear Dirac Hamiltonian (black lines) with those obtained with the effective Hamiltonian that includes the quadratic terms (red lines). The bottom panels show the isofrequency contours near the K point, where the blue lines correspond to the central frequency of the wavepackets and the orange stars represent the initial central wavevector. (c) Shows the trajectories at the critical cavity width ($L = L_v$) where the Dirac velocity vanishes and the polariton dispersion is purely quadratic. Results obtained with $\Delta = 2 \times 10^{-5}$, $\mu = 0.01\omega_0$, $\lambda_0 = 6.5a$ and $\delta\omega = -0.001\omega_0$.

The equivalent operator for the K' valley $\mathcal{M}_k^-$ is related to $\mathcal{M}_k^+$ by the replacement $\boldsymbol{\sigma} \leftrightarrow \boldsymbol{\sigma}^*$ and $\mathbf{k} \leftrightarrow -\mathbf{k}$. We initialize Gaussian wavepackets in the K and K' valleys as given by equation (5.61) and equation (5.62), respectively. However, to find the central wavevector $\mathbf{k}_0$ one has to numerically solve the dispersion

$$\omega_{\tau\lambda}(\mathbf{k}) = \omega_{\mathrm{D}} + D(L)|\mathbf{k}|^2 + \lambda \left| -\upsilon_{\mathrm{D}}(L)(\tau k_x - \mathrm{i}k_y) + t(L)(k_x^2 - k_y^2 + \tau 2\mathrm{i}k_xk_y) \right| . \quad \text{(D.4)}$$

In figures D.1(a)-(g) we plot the centre-of-mass trajectories (red lines) for a fixed strain configuration but different cavity widths (top panels), along with the isofrequency contours of the lower polariton band near the K point (bottom panels). The blue lines are the isofrequency contours corresponding to the central frequency of the wavepackets and the orange stars indicate the initial central wavevector. We compare these trajectories with those presented in figure 5.5 (black lines), which were obtained within the linear Dirac cone approximation.

For cavity widths far from the critical width L_v the isofrequency contours are essentially circular and the cyclotron orbits match very well with those obtained with the linear approximation (for example see figures D.1(a),(b),(h)). For cavity widths closer to L_v the trigonal warping of the isofrequency contours becomes more pronounced, and thus the cyclotron orbits become warped and asymmetrical for the two valleys (for example see figures D.1(d),(f),(g)). For the critical cavity width where the pseudo-vector potential vanishes $L = L_A$, there is no Lorentz-like force and therefore no cyclotron orbit (see figure D.1(e)). In figure D.1(c) we show the trajectories for the critical cavity width $L = L_v$ where the polariton dispersion is purely quadratic. At this critical width, the trajectories bear no resemblance of cyclotron orbits and the trajectories for the K/K' valleys are the same.

Finally, we note that the orbit direction depends on the signs of the Dirac velocity, cyclotron mass and pseudo-magnetic field. To highlight this, we note that for $L_A < L < L_v$ the orbit direction is reversed compared to $L > L_v$ due to the change in sign of the Dirac velocity (see figure D.1(d)). However, for $L < L_A$ the pseudo-vector potential switches sign and thus the orbit direction reverses again (see figure D.1(f))

D.2 Strain dependence of the polariton Landau levels

In this section we illustrate how the polariton Landau levels depend on the strain magnitude. In figure D.2(a) we show the evolution of the Landau level spectrum as the strain magnitude is increased, as predicted by the effective Hamiltonian within the linear Dirac cone approximation. The Landau levels display a characteristic square-root dependence on the Landau level index and the strain magnitude, which is a direct manifestation of the pseudo-relativistic nature of the massless Dirac polaritons.

In figures D.2(b)-(d) we show the local spectral function at the centre of the metasurface for a fixed cavity width but different strain magnitudes. Here we consider a large cavity width where the Coulomb interactions are dominant, and a more subwavelength lattice spacing to increase the size of the Dirac region. For the strained metasurface (see figure D.2(c)), a series of Landau level peaks emerge within the Dirac region which are not present in the

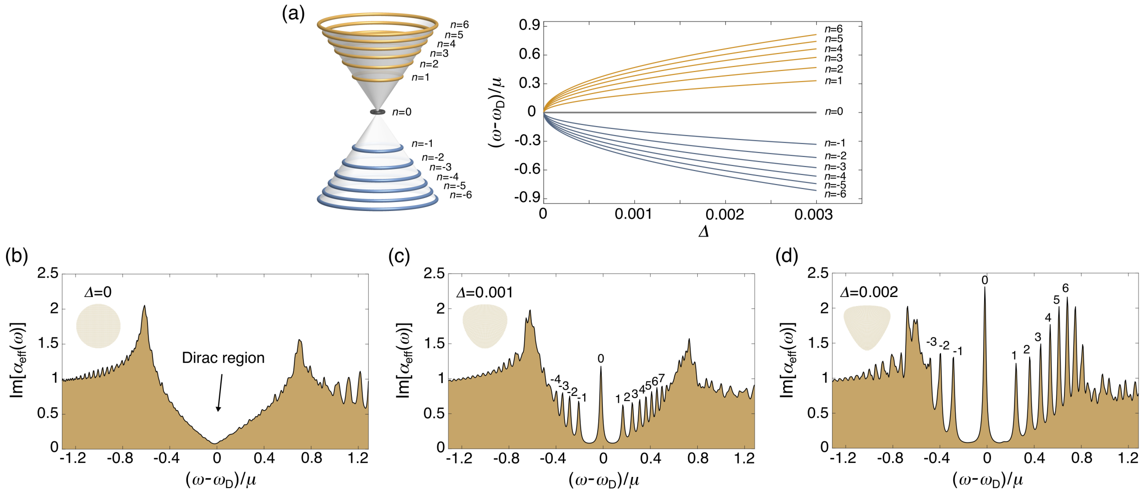

Figure D.2 | Polariton Landau levels vs strain. (a) Predicted evolution of the polariton Landau levels as the strain magnitude is increased with a fixed cavity width. In analogy with the electrons in graphene, the polaritons in the honeycomb metasurface exhibit a square-root dependence on the pseudo-magnetic field and Landau index. (b)-(d) Evolution of the local spectral function at the centre of the metasurface on the B sublattice with a fixed cavity width but different strain magnitudes of $\Delta = 0$, $\Delta = 0.001$ and $\Delta = 0.002$, respectively. The resonant peaks corresponding to the Landau levels are labeled according to their Landau index. Results obtained with $a/L = 0.2$, $\Omega = 0.01\omega_0$, $\lambda_0 = 9.1a$ and $\gamma_{\text{nr}} = 0.025\mu$.

corresponding unstrained case (see figure D.2(b)). As the magnitude of the strain is increased (see figure D.2(d)), the spacing between the Landau levels increases in accordance with the analytical predictions. Moreover, we also note that the total number of Landau levels reduce as the higher-order ones are forced beyond the Dirac region.

D.3 Cavity dependence of the polariton Landau levels

In this section we present additional local spectral function plots for different cavity widths, including those where the linear Dirac cone approximation breaks down. We stress that the analytical spectrum of the Landau levels in equation (5.64) is only valid within the approximations of the effective Dirac Hamiltonian. This breaks down for cavity widths close to L_v where one should not expect the applied strain to generate a clear sequence of Landau levels.

In figures D.3(a)-(c) we show the evolution of the local spectral function at the centre of the metasurface as the cavity width is reduced within the subcritical regime $L > L_A$. As predicted, the Landau level spacing decreases as the cavity width is reduced (see figures D.3(a)-(b)). In addition, the number of Landau level peaks reduce as the higher-order ones are forced beyond the Dirac region which reduces in size as the cavity width is decreased.

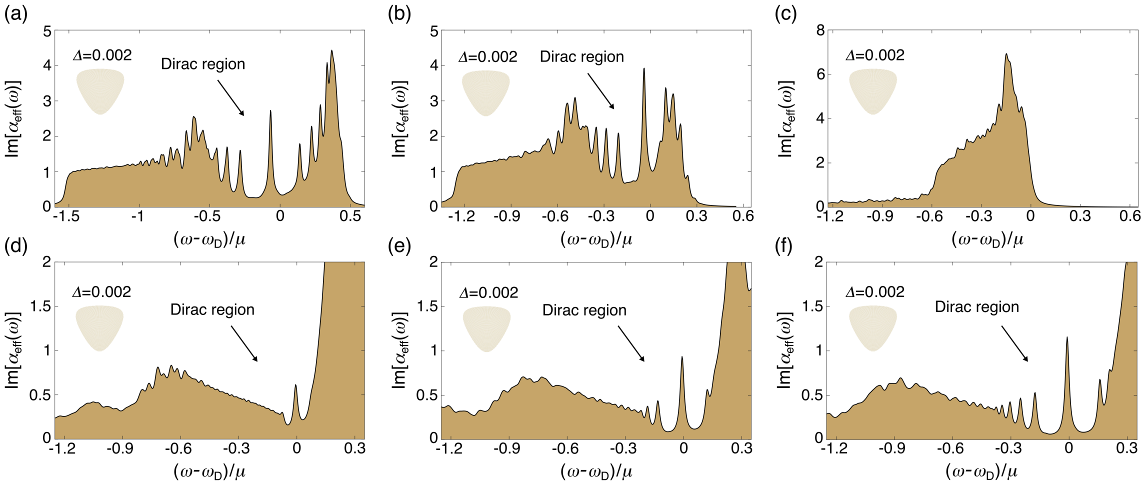

Figure D.3 | Polariton Landau levels vs cavity width. (a)-(c) Evolution of the local spectral function at the centre of the strained metasurface on the B sublattice for different cavity widths within the subcritical regime given by $a/L = 0.3$, $a/L = 0.45$ and $a/L = 0.63$, respectively. The resonant peaks corresponding to the Landau levels are labeled according to their Landau index. (d)-(f) Evolution of the local spectral function for different cavity widths within the supercritical regime given by $a/L = 0.9$, $a/L = 1$ and $a/L = 1.1$, respectively. Results obtained with $\Delta = 0.002$, $\mu = 0.01\omega_0$, $\lambda_0 = 6.5a$ and $\gamma_{\rm nr} = 0.025\mu$.

For cavity widths close to L_v (see figure D.3(c)), the strain does not produce a clear sequence of Landau levels and the Dirac region vanishes. At the critical cavity width $L = L_A$, the pseudo-magnetic field is switched off and, as a result, the applied strain does not generate Landau levels within the Dirac region (see see figure 5.7(d)).

To further elucidate the revival of the polariton Landau levels, in figures D.3(d)-(f) we show the evolution of the local spectral function at the centre of the metasurface as the cavity width is reduced within the supercritical regime $L < L_A$. For cavity widths just beyond the critical value, we start to observe the revival of the Landau levels within the Dirac region (see figure D.3(d)). As the cavity width is progressively decreased, more Landau level peaks emerge and the Landau level spacing increases in direct accordance with the analytical predictions (see figures D.3(e)-(f)).

D.4 Subradiant polariton Landau level states

In this section we briefly discuss the properties of the Landau level states. In figure 3.3 we saw that the width of the single dipole resonant peak increased as the cavity width is reduced; this is because the radiative losses increase as the light-matter coupling strength increases. However, when comparing figure 5.7(b) and figure 5.7(f) one observes that the Landau level

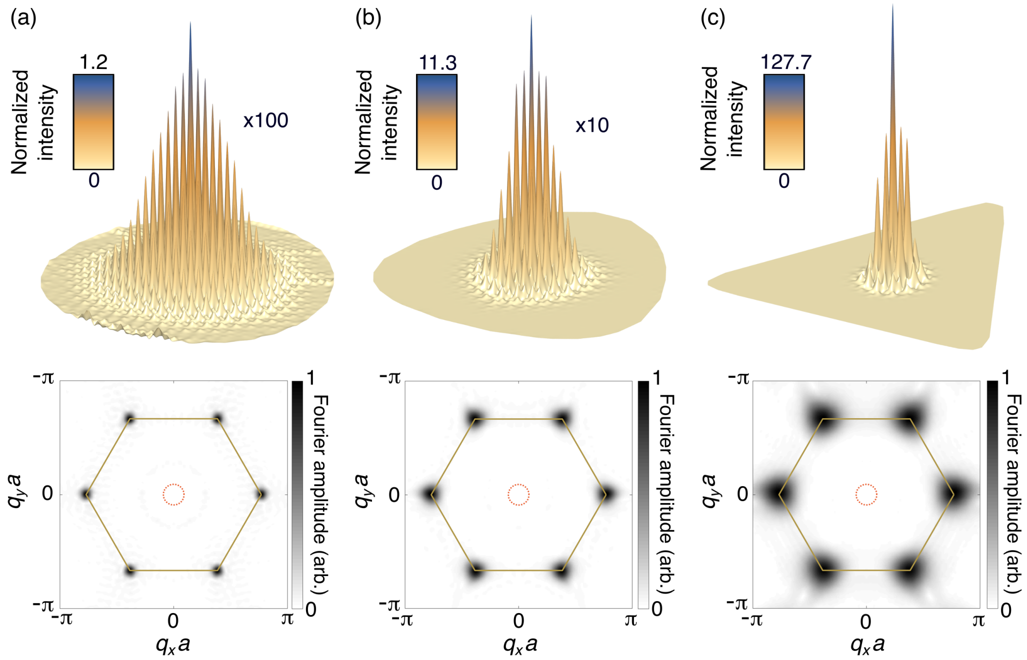

Figure D.4 | Subradiant Landau level states. (a)-(c) Top panels show the normalized dipole field intensity for a fixed cavity width but different strain magnitudes of $\varDelta = 0.001$, $\varDelta = 0.003$ and $\varDelta = 0.01$, respectively. Here, a dipole located at the centre of the metasurface on the B sublattice is driven at a frequency corresponding to the zeroth Landau level. Bottom panels show the corresponding Fourier transform of the induced dipole field, where the gold hexagon represents the first Brillouin zone and the red circle represents the isofrequency contour of the light-line. Results obtained with $L = 5a$, $\lambda_0 = 9.1a$, $\mu = 0.01\omega_0$ and $\gamma_{\mathrm{nr}} = 0.025\mu$.

peaks are very sharp and their width does not significantly vary for different cavity widths – the width is limited only by the non-radiative losses.

To see why this is the case, in figure D.4(a) we plot the normalized dipole field intensity for a large cavity width (top panel), where the strained metasurface is driven at the centre with a driving frequency that corresponds to the zeroth Landau level. We can see that the field is strongly localized near the excitation source, and therefore this state does not radiate at the edges of the metasurface. Moreover, we also plot the Fourier transform of the dipole field (bottom panel). The Fourier components lie outside the light-line near the K/K' points in the Brillouin zone, resulting in a rapidly varying phase of the dipole moments over subwavelength regions. Even in the absence of a cavity waveguide this would suppress any resonant coupling to free space photons, rendering the polariton Landau level states optically dark. In figures D.4(b)-(c) we show the same plots but for larger strain magnitudes. As the strain increases the pseudo-magnetic field increases and, as a result, the dipole field become increasingly localized near the source and the spread of the Fourier components increases.

E

Supplementary information for chapter 6

E.1 Coulomb and photon-mediated interactions

In this section we show that the essential physics for large cavity widths is dominated by the Coulomb interactions. In figure 6.3(a) and figure 6.7(b) we neglected the weak photon-mediated interactions for clarity. In figure E.1(a) we show the polariton dispersion for the shrunken metasurface ($\delta = 0.05$) with a large cavity width where we include the full dipole-dipole interactions (solid blue line). For comparison, we also plot the linear dispersion of the TEM cavity mode (dashed red line) and the approximate quasistatic dispersion where we include only the dominant Coulomb interactions (dashed orange line). The light-matter interaction results in a characteristic anticrossing between the bright quasistatic mode and the TEM cavity mode, but there is very little effect from the weak photon-mediated interactions near the K/K' points which is where our focus is. However, the hybridization results in polariton states that cross the quasistatic band gap which are predominantly of photonic character.

In figure E.1(b) we show the polariton dispersion for the interface with a large cavity width where we include the full dipole-dipole interactions, and we compare this with the quasistatic dispersion in figure E.1(c) where we include only the dominant Coulomb interactions. The color of the bands represents the inverse participation ratio $\mathrm{IPR} = \sum_j |p_j|^4/(\sum_j |p_j|)^2$, where the blue/yellow color represents localized/extended states. Note, because we apply periodic boundary conditions in the y-direction the dispersion plots also contain the valley-Hall edge states located on the B/A interface as well as the A/B interface.

Due to the absence of a complete band gap, the bulk photon-like states overlap part of the edge state spectrum (blue bands). However, one observes that the edge states only couple weakly to these bulk states (as evidenced by the very small anticrossings), and thus the weak photon-mediated interactions have very little effect on the dispersion of the valley-Hall edge states for this regime of parameters. We should emphasize that the numerical simulations in

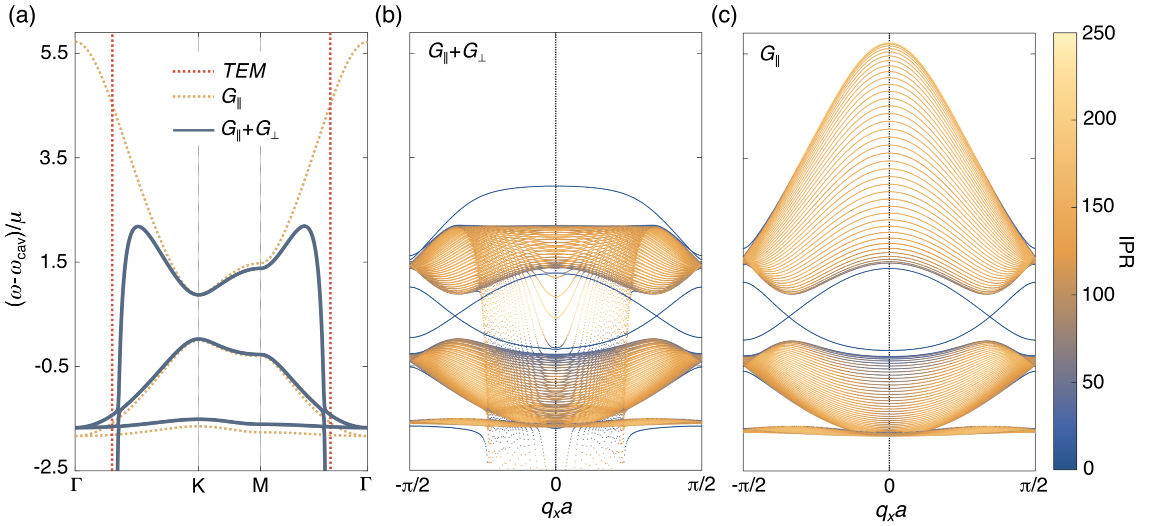

Figure E.1 | Polariton dispersion with the full dipole-dipole interactions. (a) Polariton dispersion for the shrunken metasurface ($\delta = 0.05$) with a large cavity width ($L = 5a$) where we include the full dipole-dipole interactions (solid blue line). We also show the linear dispersion of the TEM cavity mode (dashed red line) and the approximate quasistatic dispersion where we include only the Coulomb interactions (dashed orange line). (b) Polariton dispersion for the interface with a large cavity width ($L = 5a$) where we include the full dipole-dipole interactions. The color of the bands represents the IPR, where blue/yellow bands correspond to localized/extended states. (c) Same as panel (b) but including only the Coulomb interactions. One observes that the dispersion of the valley-Hall edge states is only slightly modified by the weak photon-mediated interactions. Results obtained with $\lambda_0 = 10a$ and $\mu = 0.001\omega_0$.

figure 6.8(a) do include the weak photon-mediated interactions; this demonstrates that the valley-Hall edge states can be routed around sharp corners without any significant scattering into the bulk, despite the absence of a complete band gap.

E.2 Berry curvature near the K/K' valleys

In this section we show that the effective Berry curvature in equation (6.41) captures the essential physics near the K/K' valleys in the two limiting interaction regimes. To show this, we calculate the full Berry curvature from the dynamical matrix which, for the n^{th} band, reads

$$\mathcal{F}_n(\mathbf{q}) = \mathrm{i} \sum_{m\neq n} \frac{\langle\varphi_n(\mathbf{q})|\,\frac{\partial}{\partial q_x}\mathcal{D}(\mathbf{q})\,|\varphi_m(\mathbf{q})\rangle\,\langle\varphi_m(\mathbf{q})|\,\frac{\partial}{\partial q_y}\mathcal{D}(\mathbf{q})\,|\varphi_n(\mathbf{q})\rangle}{[\breve{\alpha}_m^{-1}(\mathbf{q}) - \breve{\alpha}_n^{-1}(\mathbf{q})]^2} + \text{c.c.}\ . \tag{E.1}$$

Here $|\varphi_m\rangle$ and $\breve{\alpha}_m^{-1}$ are the eigenvectors and eigenvalues of the dynamical matrix for the m^{th} band, respectively, where we evaluate the dynamical matrix and polarizability correction at

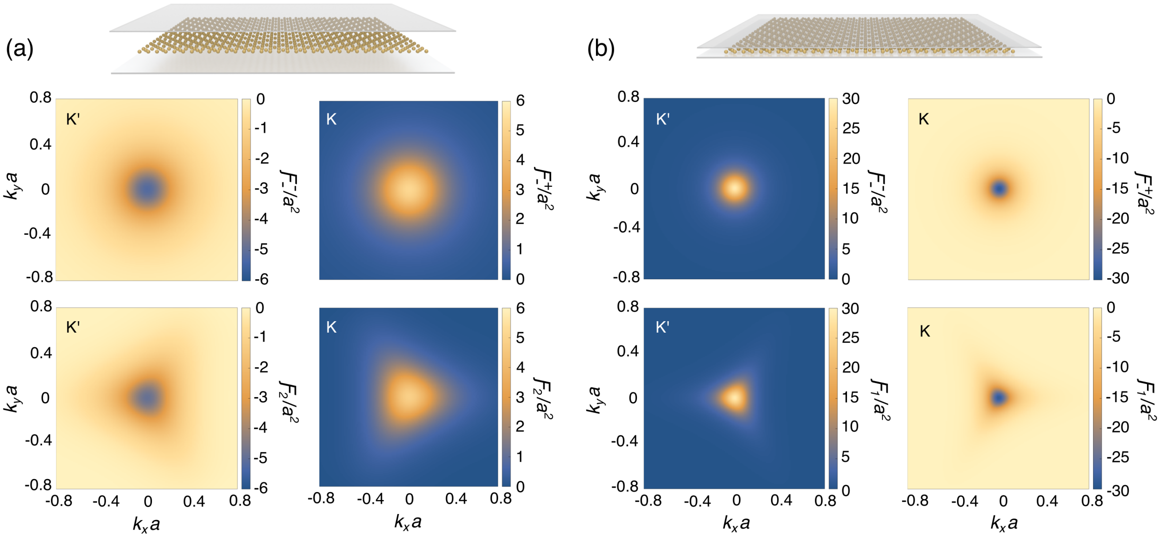

Figure E.2 | Full Berry curvature near the K/K′ points. (a) Berry curvature corresponding to the lower effective polariton band near the K/K′ points (right/left panel) for the shrunken metasurface ($\delta = 0.05$) with a large cavity width ($L = 5a$). The top panels are obtained from the effective Dirac Hamiltonian and the bottom panels are obtained from the dynamical matrix. (b) Same as panel (a) but for a small cavity width ($L = 0.5a$). The full Berry curvature is trigonally warped and exhibits $\mathcal{C}_3$ symmetry about the K/K′ points, while the effective Berry curvature from the Dirac Hamiltonian is isotropic. Apart from this small difference, the Dirac Hamiltonian captures the essential Berry curvature near the K/K′ valleys. Results obtained with $\lambda_0 = 10a$ and $\mu = 0.001\omega_0$.

the cavity resonant frequency. Note, while the effective Berry curvature within the two-band model is only accurate when the other band is well separated in frequency, equation (E.1) applies to any band and is valid for all cavity widths. Furthermore, equation (E.1) is valid for any perturbation while equation (6.41) is only accurate for small perturbations.

In figure E.2(a) we compare the Berry curvature (corresponding to the lower effective polariton band) calculated from the effective Hamiltonian (top panels) and the dynamical matrix (bottom panels) for the shrunken metasurface ($\delta = 0.05$) with a large cavity width. Figure E.2(b) is the same as figure E.2(a) but for a small cavity width. The full Berry curvature is trigonally warped and exhibits $\mathcal{C}_3$ symmetry about the K/K′ points; this feature is missed by the effective Dirac Hamiltonian where the corresponding Berry curvature is isotropic. However, apart from this slight difference, the Berry curvature peaks have very similar magnitudes and therefore the effective Dirac Hamiltonian evidently captures the essential Berry curvature near the K/K′ points in both limiting interaction regimes for small perturbations.

References

[1] Dirac, P. A. M. The quantum theory of the electron. *Proc. R. Soc. Lond. A* **117**, 610–624 (1928).

[2] Dirac, P. A. M. A theory of electrons and protons. *Proc. R. Soc. Lond. A* **126**, 360–365 (1930).

[3] Dirac, P. A. M. Quantised singularities in the electromagnetic field. *Proc. R. Soc. Lond. A* **133**, 60–72 (1931).

[4] Wehling, T. O., Black-Schaffer, A. M. & Balatsky, A. V. Dirac materials. *Adv. Phys.* **63**, 1–76 (2014).

[5] Castro Neto, A. H., Peres, N. M. R., Novoselov, K. S., Geim, A. K. & Guinea, F. The electronic properties of graphene. *Rev. Mod. Phys.* **81**, 109-162 (2009).

[6] Wallace, P. R. The band theory of graphite. *Phys. Rev.* **71**, 622–634 (1947).

[7] Semenoff, G. W. Condensed-matter simulation of a three-dimensional anomaly. *Phys. Rev. Lett.* **53**, 2449-2452 (1984).

[8] Geim, A. K. & Novoselov, K. S. The rise of graphene. *Nat. Mater.* **6**, 183–191 (2007).

[9] Fradkin, E. Critical behavior of disordered degenerate semiconductors. I. Models, symmetries, and formalism. *Phys. Rev. B* **33**, 3257–3262 (1986).

[10] Novoselov, K. S. et al. Electric field effect in atomically thin carbon films. *Science* **306**, 666-669 (2004).

[11] Klein, O. Die Reflexion von Elektronen an einem Potentialsprung nach der relativistischen Dynamik von Dirac. *Z. Phys.* **53**, 157–165 (1929).

[12] Sauter, F. Über das Verhalten eines Elektrons im homogenen elektrischen Feld nach der relativistischen Theorie Diracs. *Z. Phys.* **69**, 742-764 (1931).

[13] Dombey, N. & Calogeracos, A. Seventy years of the Klein paradox. *Phys. Rep.* **315**, 41-58 (1999).

[14] Calogeracos, A. & Dombey, N. History and physics of the Klein paradox. *Contemp. Phys.* **40**, 313-321 (1999).

[15] Greiner, W., Mueller, B. & Rafelski, J. *Quantum Electrodynamics of Strong Fields* (Springer, Berlin, 1985).

[16] Grib, A. A., Mamayev, S. G. & Mostepanenko, V. M. *Vacuum Effects in Strong Fields* (Friedmann, St-Petersburg, 1994).

[17] Page, D. N. Hawking radiation and black hole thermodynamics. *New J. Phys.* **7**, 203 (2005).

[18] Katsnelson, M. I., Novoselov, K. S. & Geim, A. K. Chiral tunnelling and the Klein paradox in graphene. *Nat. Phys.* **2**, 620-625 (2006).

[19] Kane, C. L. & Mele, E. J. Size, shape, and low energy electronic structure of carbon nanotubes. *Phys. Rev. Lett.* **78**, 1932–1935 (1997).

[20] Suzuura, H. & Ando, T. Phonons and electron–phonon scattering in carbon nanotubes. *Phys. Rev. B* **65**, 235412 (2002).

[21] Mañes, J. L. Symmetry based approach to electron–phonon interactions in graphene. *Phys. Rev. B* **76**, 045430 (2007).

[22] Guinea, F., Katsnelson, M. I. & Geim, A. K. Energy gaps and a zero-field quantum Hall effect in graphene by strain engineering. *Nat. Phys.* **6**, 30-33 (2010).

[23] Guinea, F., Geim, A. K., Katsnelson, M. I. & Novoselov, K. S. Generating quantizing pseudomagnetic fields by bending graphene ribbons. *Phys. Rev. B* **81**, 035408 (2010).

[24] Low, T. & Guinea, F. Strain-induced pseudo-magnetic field for novel graphene electronics. *Nano Lett.* **10**, 3551–3554 (2010).

[25] Chaves, A., Covaci, L., Rakhimov, K. U., Farias, G. A. & Peeters, F. M. Wave-packet dynamics and valley filter in strained graphene. *Phys. Rev. B* **82**, 205430 (2010).

[26] de Juan, F., Cortijo, A., Vozmediano, M. A. H. & Cano, A. Aharonov-Bohm interferences from local deformations in graphene. *Nat. Phys.* **7**, 810–815 (2011).

[27] Levy, N. et al. Strain-induced pseudo-magnetic fields greater than 300 Tesla in graphene nanobubbles. *Science* **329**, 544–547 (2010).

[28] Hasan, M. Z. & Kane, C. L. Colloquium: Topological insulators. *Rev. Mod. Phys.* **82**, 3045-3067 (2010).

[29] von Klitzing, K., Dorda, G. & Pepper, M. New method for high-accuracy determination of the fine-structure constant based on quantized Hall resistance. *Phys. Rev. Lett.* **45**, 494-497 (1980).

[30] Haldane, F. D. M. Model for a quantum Hall effect without landau levels: Condensed-matter realization of the 'parity anomaly'. *Phys. Rev. Lett.* **61**, 2015-2018 (1988).

[31] Kane, C. L. & Mele, E. J. Quantum spin Hall effect in graphene. *Phys. Rev. Lett.* **95**, 226801 (2005).

[32] Kane, C. L. & Mele, E. J. Z2 topological order and the quantum spin hall effect. *Phys. Rev. Lett.* **95**, 146802 (2005).

[33] Xiao, D., Yao, W. & Niu, Q. Valley-contrasting physics in graphene: magnetic moment and topological transport. *Phys. Rev. Lett.* **99**, 236809 (2007).

[34] Yao, W., Xiao, D. & Niu, Q. Valley-dependent optoelectronics from inversion symmetry breaking. *Phys. Rev. B* **77**, 235406 (2008).

[35] Gorbachev, R. V. et al. Detecting topological currents in graphene superlattices. *Science* **346**, 448-451 (2014).

[36] Martin, I., Blanter, Ya. M. & Morpurgo, A. F. Topological confinement in bilayer graphene. *Phys. Rev. Lett.* **100**, 036804 (2008).

[37] Semenoff, G. V., Semenoff, V. & Zhou, F. Domain walls in gapped graphene. *Phys. Rev. Lett.* **101**, 087204 (2008).

[38] Li, J., Morpurgo, A. F., Buttiker, M. & Martin, I. Marginality of bulk-edge correspondence for single-valley Hamiltonians. *Phys. Rev. B* **82**, 245404 (2010).

[39] Jung, J., Zhang, F., Qiao, Z. & MacDonald, A. H. Valley-Hall kink and edge states in multilayer graphene. *Phys. Rev. B* **84**, 075418 (2011).

[40] Zhang, F., MacDonald, A. H. & Mele, E. J. Valley Chern numbers and boundary modes in gapped bilayer graphene. *Proc. Natl. Acad. Sci. USA* **110**, 10546–10551 (2013).

[41] Vaezi, A., Liang, Y., Ngai, D. H., Yang, L. & Kim, E.-A. Topological edge states at a tilt boundary in gated multilayer graphene. *Phys. Rev. X* **3**, 021018 (2013).

[42] Ju, L. et al. Topological valley transport at bilayer graphene domain walls. *Nature* **520**, 650–655 (2015).

[43] Li, J. et al. Gate-controlled topological conducting channels in bilayer graphene. *Nat. Nanotech.* **11**, 1060–1065 (2016).

[44] Polini, M., Guinea, F., Lewenstein, M., Manoharan, H. C. & Pellegrini, V. Artificial honeycomb lattices for electrons, atoms and photons. *Nat. Nanotech.* **8**, 625-633 (2013).

[45] Peleg, O. et al. Conical diffraction and gap solitons in honeycomb photonic lattices. *Phys. Rev. Lett.* **98**, 103901 (2007).

[46] Sepkhanov, R. A., Bazaliy, Ya. B. & Beenakker, C. W. J. Extremal transmission at the Dirac point of a photonic band structure. *Phys. Rev. A* **75**, 063813 (2007).

[47] Zhu, S.-L., Wang, B. & Duan, L.-M. Simulation and detection of Dirac fermions with cold atoms in an optical lattice. *Phys. Rev. Lett.* **98**, 260402 (2007).

[48] Gibertini, M. et al. Engineering artificial graphene in a two-dimensional electron gas. *Phys. Rev. B* **79**, 241406(R) (2009).

[49] Torrent, D. & Sánchez-Dehesa, J. Acoustic analogue of graphene: Observation of Dirac cones in acoustic surface waves. *Phys. Rev. Lett.* **108**, 174301 (2012).

[50] Han, D., Lai, Y., Zi, J., Zhang, Z. Q. & Chan, C. T. Dirac spectra and edge states in honeycomb plasmonic lattices. *Phys. Rev. Lett.* **102**, 123904 (2009).

[51] Weick, G., Woollacott, C., Barnes, W. L., Hess, O. & Mariani, E. Dirac-like plasmons in honeycomb lattices of metallic nanoparticles. *Phys. Rev. Lett.* **110**, 106801 (2013).

[52] Kariyado, T. & Hatsugai, Y. Manipulation of Dirac cones in mechanical graphene. *Sci. Rep.* **5**, 18107 (2015).

[53] Yu, S. et al. Surface phononic graphene. *Nat. Mater.* **15**, 1243–1247 (2016).

[54] Zhang, X. & Liu, Z. Extremal transmission and beating effect of acoustic waves in two-dimensional sonic crystals. *Phys. Rev. Lett.* **101**, 264303 (2008).

[55] Bittner, S. et al. Observation of a Dirac point in microwave experiments with a photonic crystal modeling graphene. *Phys. Rev. B* **82**, 014301 (2010).

[56] Gomes, K. K., Mar, W., Ko, W., Guinea, F. & Manoharan, H. C. Designer Dirac fermions and topological phases in molecular graphene. *Nature* **483**, 306-310 (2012).

[57] Tarruell, L., Greif, D., Uehlinger, T., Jotzu, G. & Esslinger, T. Creating, moving and merging Dirac points with a Fermi gas in a tunable honeycomb lattice. *Nature* **483**, 302-305 (2012).

[58] Bellec, M., Kuhl, U., Montambaux, G. & Mortessagne, F. Tight-binding couplings in microwave artificial graphene. *Phys. Rev. B* **88**, 115437 (2013).

[59] Jacqmin, T. et al. Direct observation of Dirac cones and a flatband in a honeycomb lattice for polaritons. *Phys. Rev. Lett.* **112**, 116402 (2014).

[60] Plotnik, Y. et al. Observation of unconventional edge states in ‘photonic graphene’. *Nat. Mater.* **13**, 57–62 (2014).

[61] Hasegawa, Y., Konno, R., Nakano, H. & Kohmoto, M. Zero modes of tight-binding electrons on the honeycomb lattice. *Phys. Rev. B* **74**, 033413 (2006).

[62] Pereira, V. M., Castro Neto, A. H. & Peres, N. M. R. Tight-binding approach to uniaxial strain in graphene. *Phys. Rev. B* **80**, 045401 (2009).

[63] Montambaux, G., Piéchon, F., Fuchs, J.-N. & Goerbig, M. O. Merging of Dirac points in a two-dimensional crystal. *Phys. Rev. B* **80**, 153412 (2009).

[64] Montambaux, G., Piéchon, F., Fuchs, J.-N. & Goerbig, M. O. A universal Hamiltonian for motion and merging of Dirac points in a two-dimensional crystal. *Eur. Phys. J. B* **72**, 509-520 (2009).

[65] Bellec, M., Kuhl, U., Montambaux, G. & Mortessagne, F. Topological transition of Dirac points in a microwave experiment. *Phys. Rev. Lett.* **110**, 033902 (2013).

[66] Rechtsman, M. C. et al. Topological creation and destruction of edge states in photonic graphene. *Phys. Rev. Lett.* **111**, 103901 (2013).

[67] Real, B. et al. Semi-Dirac transport and anisotropic localization in polariton honeycomb lattices. *Phys. Rev. Lett.* **125**, 186601 (2020).

[68] Rechtsman, M. C. et al. Strain-induced pseudomagnetic field and photonic Landau levels in dielectric structures. *Nat. Photon.* **7**, 153-158 (2013).

[69] Jamadi, O. et al. Direct observation of photonic Landau levels and helical edge states in strained honeycomb lattices. *Light Sci. Appl.* **9**, 144 (2020).

[70] Bellec, M. et al. Observation of supersymmetric pseudo-Landau levels in strained microwave graphene. *Light Sci. Appl.* **9**, 146 (2020).

[71] Haldane, F. D. M. & Raghu, S. Possible realization of directional optical waveguides in photonic crystals with broken time-reversal symmetry. *Phys. Rev. Lett.* **100**, 013904 (2008).

[72] Raghu, S. & Haldane, F. D. M. Analogs of quantum-Hall-effect edge states in photonic crystals. *Phys. Rev. A* **78**, 033834 (2008).

[73] Lu, L., Joannopoulos, J. D. & Soljaćič, M. Topological photonics. *Nat. Photon.* **8**, 821–829 (2014).

[74] Khanikaev, A. B. & Shvets, G. Two-dimensional topological photonics. *Nat. Photon.* **11**, 763–773 (2017).

[75] Ozawa, T. et al. Topological photonics. *Rev. Mod. Phys.* **91**, 015006 (2019).

[76] Wang, Z., Chong, Y., Joannopoulos, J. & Soljaćič, M. Observation of unidirectional backscattering-immune topological electromagnetic states. *Nature* **461**, 772–775 (2009).

[77] Hafezi, M., Demler, E. A., Lukin, M. D. & Taylor, J. M. Robust optical delay lines with topological protection. *Nat. Phys.* **7**, 907–912 (2011).

[78] Hafezi, M., Mittal, S., Fan, J., Migdall, A. & Taylor, J. M. Imaging topological edge states in silicon photonics. *Nat. Photon.* **7**, 1001–1005 (2013).

[79] Khanikaev, A. B. et al. Photonic topological insulators. *Nat. Mater.* **12**, 233–239 (2013).

[80] Wu, L.-H. & Hu, X. Scheme for achieving a topological photonic crystal by using dielectric material. *Phys. Rev. Lett.* **114**, 223901 (2015).

[81] Cheng, X., Jouvaud, C., Ni, X., Mousavi, S. H., Genack, A. Z. & Khanikaev, A. B. Robust reconfigurable electromagnetic pathways within a photonic topological insulator. *Nat. Mater.* **15**, 542-548 (2016).

[82] Ma, T. & Shvets, G. All-Si valley-Hall photonic topological insulator. *New J. Phys.* **18**, 025012 (2016).

[83] Wu, X. et al. Direct observation of valley-polarized topological edge states in designer surface plasmon crystals. *Nat. Commun.* **8**, 1304 (2017).

[84] Gao, Z. et al. Valley surface-wave photonic crystal and its bulk/edge transport. *Phys. Rev. B* **96**, 201402 (2017).

[85] Gao, F. et al. Topologically-protected refraction of robust kink states in valley photonic crystals. *Nat. Phys.* **14**, 140–144 (2018).

[86] Zeng, Y. et al. Electrically pumped topological laser with valley edge modes. *Nature* **578**, 246–250 (2020).

[87] Yang, Y. H. et al. Terahertz topological photonics for on-chip communication. *Nat. Photon.* **14**, 446–451 (2020).

[88] Noh, J., Huang, S., Chen, K. P. & Rechtsman, M. C. Observation of photonic topological valley Hall edge states. *Phys. Rev. Lett.* **120**, 063902 (2018).

[89] Shalaev, M. I., Walasik, W., Tsukernik, A., Xu, Y. & Litchinitser, N. M. Robust topologically protected transport in photonic crystals at telecommunication wavelengths. *Nat. Nanotech.* **14**, 31–34 (2019).

[90] He, X.-T. et al. A silicon-on-insulator slab for topological valley transport. *Nat. Commun.* **10**, 872 (2019).

[91] Mehrabad, M. J. et al. Chiral topological photonics with an embedded quantum emitter. *Optica* **7**, 1690-1696 (2020).

[92] Barik, S., Karasahin, A., Mittal, S., Waks, E. & Hafezi, M. Chiral quantum optics using a topological resonator. *Phys. Rev. B* **101**, 205303 (2020).

[93] Mãnes, J. L., Guinea, F. & Vozmediano, A. H. Existence and topological stability of Fermi points in multilayered graphene. *Phys. Rev. B* **75**, 155424 (2007).

[94] Purcell, E. M. Spontaneous emission probabilities at radio frequencies. *Phys. Rev.* **69**, 681 (1946).

[95] Kleppner, D. Inhibited spontaneous emission. *Phys. Rev. Lett.* **47**, 233–236 (1981).

[96] Goy, P., Raimond, J. M., Cross, M. M. & Haroche, S. Observation of cavity-enhanced single-atom spontaneous emission. *Phys. Rev. Lett.* **50**, 1903–1906 (1983)

[97] Hulet, R. G., Hilfer, E. S. & Kleppner, D. Inhibited spontaneous emission by a Rydberg atom. *Phys. Rev. Lett.* **55**, 2137-2140 (1985).

[98] Jhe, W. et al. Suppression of spontaneous decay at optical frequencies: Test of vacuum-field anisotropy in confined space. *Phys. Rev. Lett.* **58**, 666–669 (1987).

[99] Heinzen, D. J., Childs, J. J., Thomas, J. F. & Feld, M. S. Enhanced and inhibited visible spontaneous emission by atoms in a confocal resonator. *Phys. Rev. Lett.* **58**, 1320–1323 (1987).

[100] Mann, C.-R., Sturges, T. J., Weick, G., Barnes, W. L. & Mariani, E. Manipulating type-I and type-II Dirac polaritons in cavity-embedded honeycomb metasurfaces. *Nat. Commun.* **9**, 2194 (2018).

[101] Mann, C.-R., Horsley, S. A. H. & Mariani, E. Tunable pseudo-magnetic fields for polaritons in strained metasurfaces. *Nat. Photon.* **14**, 669–674 (2020).

[102] Mann, C.-R. & Mariani, E. Topological transitions induced by cavity-mediated interactions in photonic valley-Hall metasurfaces. Preprint at arXiv:2010.01636 (2020).

[103] Lamowski, S. Mann, C.-R., Hellbach, F., Mariani, E., Weick, G. & Pauly, F. Plasmon polaritons in cubic lattices of spherical metallic nanoparticles. *Phys. Rev. B* **97**, 125409 (2018).

[104] The Nobel Foundation archive. https://www.nobelprize.org/prizes/physics/1933/dirac/facts/.

[105] The Nobel Foundation. https://www.nobelprize.org/prizes/physics/2010/geim/facts/. Photo: U. Montan.

[106] The Nobel Foundation. https://www.nobelprize.org/prizes/physics/2010/novoselov/facts/. Photo: U. Montan.

[107] Schrödinger, E. Quantisierung als Eigenwertproblem (Erste Mitteilung). *Ann. Phys.* **79**, 361-376 (1926).

[108] Schrödinger, E. Quantisierung als Eigenwertproblem (Zweite Mitteilung). *Ann. Phys.* **79**, 489-527 (1926).

[109] Schrödinger, E. Über das Verhältnis der Heisenberg-Born-Jordanschen Quantenmechanik zu der meinen. *Ann. Phys.* **79**, 734-756 (1926).

[110] Schrödinger, E. Quantisierung als Eigenwertproblem (Dritte Mitteilung: Störungstheorie, mit Anwendung auf den Starkeffekt der Balmerlinien). *Ann. Phys.* **80**, 437-490 (1926).

[111] Schrödinger, E. Quantisierung als Eigenwertproblem (Vierte Mitteilung). *Ann. Phys.* **81**, 109-139 (1926).

[112] Schrödinger, E. An undulatory theory of the mechanics of atoms and molecules. *Phys. Rev.* **28**, 1049-1070 (1926).

[113] Klein, O. Quantentheorie und fünfdimensionale Relativitätstheorie. *Z. Phys.* **37**, 895-906 (1926).

[114] Gordon, W. Der Comptoneffekt nach der Schrödingerschen Theorie. *Z. Phys.* **40**, 117-133 (1926).

[115] Pauli, W. Zur Quantenmechanik des magnetischen Elektrons. *Z. Phys.* **43**, 601-623 (1927).

[116] Anderson, C. D. The positive electron. *Phys. Rev.* **43**, 491–494 (1933).

[117] Gamow, G. Zur quantentheorie des atomkernes. *Z. Phys.* **51**, 204–212 (1928).

[118] Gurney, R. W. & Condon, E.U. *Nature* **122**, 439 (1928).

[119] Gurney, R. W. & Condon, E.U. *Phys. Rev.* **33**, 127 (1929).

[120] Cheianov, V. V. & Fal'ko, V. I. Selective transmission of Dirac electrons and ballistic magnetoresistance of n-p junctions in graphene. *Phys. Rev. B* **74**, 041403 (2006).

[121] Allain, P. E., & Fuchs, J. N. Klein tunneling in graphene: optics with massless electrons. *Eur. Phys. J. B* **83**, 301–317 (2011).

[122] Ando, T., Nakanishi, T. & Saito, R. Berry's phase and absence of back scattering in carbon nanotubes. J. *Phys. Soc. Jpn.* **67**, 2857–2862 (1998).

[123] Gorbachev, R. V., Mayorov, A. S., Savchenko, A. K., Horsell, D. W. & Guinea, F. Conductance of p–n–p graphene structures with air-bridge top gates. *Nano Lett.* **8**, 1995-1999 (2008).

[124] Stander, N., Huard, B. & Goldhaber-Gordon, D. Evidence for Klein tunneling in graphene p–n junctions. *Phys. Rev. Lett.* **102**, 026807 (2009).

[125] Young, A. F. & Kim, P. Quantum interference and Klein tunnelling in graphene heterojunctions. *Nat. Phys.* **5**, 222-226 (2009).

[126] Lee, G.-H., Park, G. & Lee, H. Observation of negative refraction of Dirac fermions in graphene. *Nat. Phys.* **11**, 925-929 (2015).

[127] Chen, S. et al. Electron optics with p-n junctions in ballistic graphene. *Science* **353**, 1522-1525 (2016).

[128] Cheianov, V. V., Fal'ko, V. & Altshuler, B. L. The focusing of electron flow and a Veselago lens in graphene p-n junctions. *Science* **315**, 1252-1255 (2007).

[129] Veselago, V. G. The electrodynamics of substances with simultaneously negative values of ϵ and μ. *Sov. Phys. Usp.* **10**, 509–514 (1968).

[130] Shelby, R. A., Smith, D. R. & Shultz, S. Experimental verification of a negative index of refraction. *Science* **292**, 77–79 (2001).

[131] von Klitzing, K. Developments in the quantum Hall effect. *Philos. Trans. R. Soc. Lond. A* **363**, 1834–3974 (2005).

[132] Quantum Hall effect intro (by Ady Stern). URL at *https://www.youtube.com/watch?v=QC3tQT7MD00* (2015).

[133] Landau, L. Diamagnetismus der Metalle. *Z. Phys.* **64**, 629–637 (1930).

[134] Laughlin, R. Quantized Hall conductivity in two dimensions. *Phys. Rev. B* **23**, 5632-5633 (1981).

[135] Halperin, B. Quantized Hall conductance, current-carrying edge states, and the existence of extended states in a two-dimensional disordered potential. *Phys. Rev. B* **25**, 2185-2190 (1982).

[136] Thouless, D. J., Kohmoto, M., Nightingale, M. P. & den Nijs, M. Quantized Hall conductance in a two-dimensional periodic potential. *Phys. Rev. Lett.* **49**, 405-408 (1982).

[137] Avron, J. E., Seiler, R. & Simon, B. Homotopy and quantization in condensed matter physics. *Phys. Rev. Lett.* **51**, 51–53 (1983).

[138] Berry, M. V. Quantal phase factor accompanying adiabatic change. *Proc. R. Soc. Lond. A* **392**, 45-57 (1984).

[139] Simon, B. Holonomy, the quantum adiabatic theorem, and Berry phase. *Phys. Rev. Lett.* **51**, 2167-2170 (1983).

[140] Kohmoto, M. Topological invariant and the quantization of the Hall conductance. *Ann. Phys.* **160**, 343-354 (1985).

[141] Hatsugai, Y. Chern number and edge states in the integer quantum Hall effect. *Phys. Rev. Lett.* **71**, 3697-3700 (1993).

[142] Hatsugai, Y. Edge states in the integer quantum Hall effect and the Riemann surface of the Bloch function. *Phys. Rev. B* **48**, 11851 (1993).

[143] McClure, J. W. Diamagnetism of graphite. *Phys. Rev.* **104**, 666-671 (1956).

[144] Zheng, Y. & Ando, T. Hall conductivity of a two-dimensional graphite system. *Phys. Rev. B* **65**, 245420 (2002).

[145] Sadowski, M. L., Martinez, G., Potemski, M., Berger, C. & de Heer, W. A. Landau level spectroscopy of ultrathin graphite layers. *Phys. Rev. Lett.* **97**, 266405 (2006).

[146] Jiang, Z. et al. Infrared spectroscopy of Landau levels of graphene. *Phys. Rev. Lett.* **98**, 197403 (2007).

[147] Li, G. & Andrei, E. Y. Observation of Landau levels of Dirac fermions in graphite. *Nat. Phys.* **3**, 623–627 (2007).

[148] Miller, D. L. et al. Observing the quantization of zero mass carriers in graphene. *Science* **324**, 924–927 (2009).

[149] Gusynin, V. P. & Sharapov, S. G. Unconventional integer quantum Hall effect in graphene. *Phys. Rev. Lett.* **95**, 146801 (2005).

[150] Novoselov, K. S. et al. Two-dimensional gas of massless Dirac fermions in graphene. *Nature* **438**, 197-200 (2005).

[151] Zhang, Y. B., Tan, Y. W., Stormer, H. L. & Kim, P. Experimental observation of the quantum Hall effect and Berry's phase in graphene. *Nature* **438**, 201-204 (2005).

[152] von Neuman, J. & Wigner, E. Uber das Verhalten von Eigenwerten bei adiabatischen Prozessen. *Phys. Z.* **30**, 467-470 (1929).

[153] McCann, E. & Fal'ko, V. I. Landau-level degeneracy and quantum Hall effect in a graphite bilayer. *Phys. Rev. Lett.* **96**, 086805 (2006).

[154] McCann, E. & Koshino, M. The electronic properties of bilayer graphene. *Reports Prog. Phys.* **76**, 056503 (2013).

[155] Novoselov, K. S. et al. Unconventional quantum Hall effect and Berry's phase of 2π in bilayer graphene. *Nat. Phys.* **2**, 177-180 (2006).

[156] Pereira, V. M. & Castro-Neto, A. H. Strain engineering of graphene's electronic structure. *Phys. Rev. Lett.* **103**, 046801 (2009).

[157] de Juan, F., Mañes, J.L. & Vozmediano, M. A. H. Gauge fields from strain in graphene. *Phys. Rev. B* **87**, 165131 (2013).

[158] Vozmediano, M. A. H., Katsnelson, M. I. & Guinea, F. Gauge fields in graphene. *Phys. Rep.* **496**, 109-148 (2010).

[159] Zhu, S., Stroscio, J. A. & Li, T. Programmable extreme pseudomagnetic fields in graphene by a uniaxial stretch. *Phys. Rev. Lett.* **115**, 245501 (2015).

[160] de Juan, F., Sturla, M. & Vozmediano, M. A. H. Space dependent Fermi velocity in strained graphene. *Phys. Rev. Lett.* **108**, 227205 (2012).

[161] Yan, H., Sun, Y., He, L., Nie, J.-C. & Chan, M. H. W. Observation of Landau-level-like quantization at 77K along a strained-induced graphene ridge. *Phys. Rev. B* **85**, 035422 (2012).

[162] Guo, D. et al. Observation of Landau levels in potassium-intercalated graphite under a zero magnetic field. *Nat. Commun.* **3**, 1068 (2012).

[163] Georgi, A. et al. Tuning the pseudospin polarization of graphene by a pseudomagnetic field. *Nano Lett.* **17**, 2240-2245 (2017).

[164] Jiang, Y. et al. Visualizing strain-induced pseudomagnetic fields in graphene through an hBN magnifying glass. *Nano Lett.* **17**, 2839-2843 (2017).

[165] Wen, X. et al. Acoustic Landau quantization and quantum-Hall-like edge states. *Nat. Phys.* **15**, 352–356 (2019).

[166] Schomerus, H. & Halpern, N. Y. Parity anomaly and Landau-level lasing in strained photonic honeycomb lattices. *Phys. Rev. Lett.* **110**, 013903 (2013).

[167] Abbaszadeh, H., Souslov, A., Paulose, J., Schomerus, H. & Vitelli, V. Sonic Landau levels and synthetic gauge fields in mechanical metamaterials. *Phys. Rev. Lett.* **119**, 195502 (2017).

[168] Brendel, C., Peano, V., Painter, O. J. & Marquardt, F. Pseudo-magnetic fields for sound at the nanoscale. *Proc. Natl. Acad. Sci.* U.S.A. **114**, 3390–3395 (2017).

[169] Yang, Z., Gao, F., Yang, Y., & Baile, Z. Strain-induced gauge field and Landau levels in acoustic structures. *Phys. Rev. Lett.* **118**, 194301 (2017).

[170] Salerno, G., Ozawa, T., Price, H. M. & Carusotto, I. How to directly observe Landau levels in driven-dissipative strained honeycomb lattices. *2D Mater.* **2**, 034015 (2015).

[171] Salerno, G., Ozawa, T., Price, H. M. & Carusotto, I. Propagating edge states in strained honeycomb lattices. *Phys. Rev. B* **95**, 245418 (2017).

[172] Guglielmon, J., Rechtsman, M. C. & Weinstein, M. I. Landau levels in strained two-dimensional photonic crystals. *Phys. Rev. A* **103**, 013505 (2021).

[173] Banerjee, S., Singh, R. R. P., Pardo, V. & Pickett, W. E. Tight-binding modeling and low-energy behavior of the semi-dirac point. *Phys. Rev. Lett.* **103**, 016402 (2009).

[174] Bernevig, B. A. & Hughes, T. L. *Topological Insulators and Topological Superconductors* (Princeton Univ. Press, Princeton, 2013).

[175] Jackiw, R. & Rebbi, C. Solitons with fermion number 1/2. *Phys. Rev. D* **13**, 3398–3409 (1976).

[176] Chang, C.-Z. et al. Experimental observation of the quantum anomalous Hall effect in a magnetic topological insulator. *Science* **340**, 167–170 (2013).

[177] Deng, Y. et al. Quantum anomalous Hall effect in intrinsic magnetic topological insulator. *Science* **367**, 895–900 (2020).

[178] Serlin, M. et al. Intrinsic quantized anomalous Hall effect in a moiré heterostructure. *Science* **367**, 900–903 (2020).

[179] Klembt, S. et al. Exciton-polariton topological insulator. *Nature* **562**, 552–556 (2018).

[180] Oka, T. & Aoki, H. Photovoltaic Hall effect in graphene. *Phys. Rev. B* **79**, 081406 (2009).

[181] Kitagawa, T., Berg, E., Rudner, M. & Demler, E. Topological characterization of periodically driven quantum systems. *Phys. Rev. B* **82**, 235114 (2010).

[182] Lindner, N. H., Refael, G. & Galitski, V. Floquet topological insulator in semiconductor quantum wells. *Nat. Phys.* **7**, 490–495 (2011).

[183] Jotzu, G. et al. Experimental realization of the topological Haldane model with ultracold fermions. *Nature* **515**, 237–240 (2014).

[184] Rechtsman, M. C. et al. Photonic Floquet topological insulators. *Nature* **496**, 196–200 (2013).

[185] Xiao, D., Liu, G.-B., Feng, W., Xu, X. & Yao, W. Coupled spin and valley physics in monolayers of MoS2 and other Group-VI dichalcogenides. *Phys. Rev. Lett.* **108**, 196802 (2012).

[186] Xu, X., Yao, W., Xiao, D. & Heinz, T. F. Spin and pseudospins in layered transition metal dichalcogenides. *Nat. Phys.* **10**, 343–350 (2014).

[187] Mak, K. F., McGill, K. L., Park, J. & McEuen, P. L. The valley Hall effect in MoS2 transistors. *Science* **344**, 1489–1492 (2014).

[188] Lu, J. et al. Observation of topological valley transport of sound in sonic crystals. *Nat. Phys.* **13**, 369–374 (2016).

[189] Zhang, Z. et al. Directional acoustic antennas based on valley-Hall topological insulators. *Adv. Mater.* **30**, 1803229 (2018).

[190] Lu, J. et al. Valley topological phases in bilayer sonic crystals. *Phys. Rev. Lett.* **120**, 116802 (2018).

[191] Vila, J., Pal, R. K. & Ruzzene, M. Observation of topological valley modes in an elastic hexagonal lattice. *Phys. Rev. B* **96**, 134307 (2017).

[192] Yan, M. et al. On-chip valley topological materials for elastic wave manipulation. *Nat. Mater.* **17**, 993–998 (2018).

[193] Drexhage, K. H. Influence of a dielectric interface on fluorescence decay time. *J. Lumin.* **1-2**, 693–701 (1970).

[194] Amos, R. M. & Barnes, W. L. Modification of the spontaneous emission rate of Eu^{3+} ions close to a thin metal mirror. *Phys. Rev. B* **55**, 7249-7254 (1997).

[195] Barnes, W. L. Fluorescence near interfaces: the role of photonic mode density. *J. Mod. Opt.* **45**, 661–699 (1998).

[196] Eschner, J., Raab, C., Schmidt-Kaler, F. & Blatt, R. Light interference from single atoms and their mirror images. *Nature* **413**, 495–498 (2001).

[197] Yablonovitch, E. Inhibited spontaneous emission in solid-state physics and electronics. *Phys. Rev. Lett.* **58**, 2059–2062 (1987).

[198] Ogawa, S., Imada, M., Yoshimoto, S., Okano, M. & Noda, S. Control of light emission by 3D photonic crystals. *Science* **305**, 227–229 (2004).

[199] Lodahl, P. et al. Controlling the dynamics of spontaneous emission from quantum dots by photonic crystal. *Nature* **430**, 654–657 (2004).

[200] Fujita, M., Takahashi, S., Tanaka, Y., Asano, T. & Noda, S. Simultaneous inhibition and redistribution of spontaneous light emission in photonic crystals. *Science* **308**, 1296–1298 (2005).

[201] Noda, S., Fujita, M. & Asano, T. Spontaneous-emission control by photonic crystals and nanocavities. *Nat. Photon.* **1**, 449–458 (2009).

[202] Dicke, R. H. Coherence in spontaneous radiation processes. *Phys. Rev.* **93**, 99–110 (1954).

[203] DeVoe, R. G. & Brewer, R. G. Observation of superradiant and subradiant spontaneous emission of two trapped ions. *Phys. Rev. Lett.* **76**, 2049–2052 (1996).

[204] Barredo, D. et al. Coherent excitation transfer in a spin chain of three Rydberg atoms. *Phys. Rev. Lett.* **114**, 113002 (2015).

[205] Nordlander, P., Oubre, C., Prodan, E., Li, K. & Stockman, M. I. Plasmon hybridization in nanoparticle dimers. *Nano Lett.* **4**, 899–903 (2004).

[206] Koh, A. L. et al. Electron energy-loss spectroscopy (EELS) of surface plasmons in single silver nanoparticles and dimers: influence of beam damage and mapping of dark modes. *ACS Nano* **3**, 3015–3022 (2009).

[207] Hentschel, M. et al. Transition from isolated to collective modes in plasmonic oligomers. *Nano Lett.* **10**, 2721–2726 (2010).

[208] Quinten, M., Leitner, A., Krenn, J. R. & Aussenegg, F. R. Electromagnetic energy transport via linear chains of silver nanoparticles. *Opt. Lett.* **23**, 1331–1333 (1998).

[209] Maier, S. A. et al. Local detection of electromagnetic energy transport below the diffraction limit in metal nanoparticle plasmon waveguides. *Nat. Mater.* **2**, 229–232 (2003).

[210] Downing, C. A. & Weick, G. Topological collective plasmons in bipartite chains of metallic nanoparticles. *Phys. Rev. B* **95**, 125426 (2017).

[211] Auguié, B. & Barnes, W. L. Collective resonances in gold nanoparticle arrays. *Phys. Rev. Lett.* **101**, 143902 (2008).

[212] Zhang, S., Genov, D. A., Wang, Y., Liu, M. & Zhang, X. Plasmon-induced transparency in metamaterials. *Phys. Rev. Lett.* **101**, 047401 (2008).

[213] Zhou, W. et al. Lasing action in strongly coupled plasmonic nanocavity arrays. *Nat. Nanotech.* **8**, 506–511 (2013).

[214] García de Abajo, F. J. Colloquium: light scattering by particle and hole arrays. *Rev. Mod. Phys.* **79**, 1267–1290 (2007).

[215] Meinzer, N., Barnes, W. L. & Hooper, I. R. Plasmonic meta-atoms and metasurfaces. *Nat. Photon.* **8**, 889–898 (2014).

[216] Yu, N. & Capasso, F. Flat optics with designer metasurfaces. *Nat. Mater.* **13**, 139–150 (2014).

[217] Bettles, R. J., Gardiner, S. A. & Adams, C. S. Enhanced optical cross section via collective coupling of atomic dipoles in a 2D array. *Phys. Rev. Lett.* **116**, 103602 (2016).

[218] Shahmoon, E., Wild, D. S., Lukin, M. D. & Yelin, S. F. Cooperative resonances in light scattering from two-dimensional atomic arrays. *Phys. Rev. Lett.* **118**, 113601 (2017).

[219] Perczel, J. et al. Photonic band structure of two-dimensional atomic lattices. *Phys. Rev. A* **96**, 063801 (2017).

[220] Bettles, R. J., Minář, J., Adams, C. S., Lesanovsky, I. & Olmos, B. Topological properties of a dense atomic lattice gas. *Phys. Rev. A* **96**, 041603 (2017).

[221] Perczel, J. et al. Topological quantum optics in two-dimensional atomic arrays. *Phys. Rev. Lett.* **119**, 023603 (2017).

[222] Asenjo-Garcia, A., Moreno-Cardoner, M., Albrecht, A., Kimble, H. J. & Chang, D. E. Exponential improvement in photon storage fidelities using subradiance and selective radiance in atomic arrays. *Phys. Rev. X* **7**, 031024 (2017).

[223] Barredo, D., de Léséleuc, S., Lienhard, V., Lahaye, T. & Browaeys, A. An atom-by-atom assembler of defect-free arbitrary two-dimensional atomic arrays. *Science* **354**, 1021–1023 (2016).

[224] de Léséleuc, S. et al. Observation of a symmetry-protected topological phase of interacting bosons with Rydberg atoms. *Science* **365**, 775–780 (2019).

[225] Rui, J. et al. A subradiant optical mirror formed by a single structured atomic layer. *Nature* **583**, 369–374 (2020).

[226] Bekenstein, R. et al. Quantum metasurfaces with atom arrays. *Nat. Phys.* **16**, 676–681 (2020).

[227] Gonzalez-Tudela, A. et al. Entanglement of two qubits mediated by one-dimensional plasmonic waveguides. *Phys. Rev. Lett.* **106**, 020501 (2011).

[228] Douglas, J. S. et al. Quantum many-body models with cold atoms coupled to photonic crystals. *Nat. Photon.* **9**, 326–331 (2015).

[229] González-Tudela, A., Hung, C.-L., Chang, D. E., Cirac, J. I. & Kimble, H. J. Subwavelength vacuum lattices and atom–atom interactions in two-dimensional photonic crystals. *Nat. Photon.* **9**, 320–325 (2015).

[230] Hood, J. D. et al. Atom-atom interactions around the band edge of a photonic crystal waveguide. *Proc. Natl. Acad. Sci. USA* **113**, 10507–10512 (2016).

[231] Perczel, J., Borregaard, J., Chang, D. E., Yelin, S. F. & Lukin, M. D. Topological quantum optics using atom-like emitter arrays coupled to photonic crystals. *Phys. Rev. Lett.* **124**, 083603 (2020).

[232] Chang, D. E., Douglas, J. S., González-Tudela, A., Hung, C.-L. & Kimble, H. J. Quantum matter built from nanoscopic lattices of atoms and photons. *Rev. Mod. Phys.* **90**, 031002 (2018).

[233] Svidzinsky, A. A., Chang, J.-T. & Scully, M. O. Cooperative spontaneous emission of N atoms: Many-body eigenstates, the effect of virtual Lamb shift processes and analogy with radiation of N classical oscillators. *Phys. Rev. A* **81**, 053821 (2010).

[234] Maxwell, J. C. A dynamical theory of the electromagnetic field. *Phil. Trans. R. Soc. Lond.* **155**, 459–512 (1865).

[235] Jackson, J. D. *Classical Electrodynamics* (Wiley, New York, 1999).

[236] Craig, D. P. & Thirunamachandran, T. *Molecular Quantum Electrodynamics: An Introduction to Radiation-Molecule Interactions.* (Academic Press, London, 1984).

[237] Jackson, J. D. From Lorenz to Coulomb and other explicit gauge transformations. *Am. J. Phys.* **70**, 917-928 (2002).

[238] Novotny, L. & Hecht, B. *Principles of Nano-Optics.* (Cambridge Univ. Press, Cambridge, 2006).

[239] Morse, P. M. & Feshbach, H. *Methods of Theoretical Physics Part 1* (McGraw-Hill, New York, 1953).

[240] Tai, C.-T. *Dyadic Green Functions in Electromagnetic Theory* (IEEE Press, New York, 1993).

[241] Abramowitz, M. & Stegun, I.A. *Handbook of Mathematical Functions* (Dover, New York, 1965).

[242] Cohen-Tannoudji, C., Dupont-Roc, J. & Grynberg, G. *Photons and Atoms: Introduction to Quantum Electrodynamics* (Wiley, New York, 1989).

[243] Wokaun, A., Gordon, J. P. & Liao, P. F. Radiation Damping in Surface-Enhanced Raman Scattering. *Phys. Rev. Lett.* **48**, 957-960 (1982).

[244] Hopfield, J. J. Theory of the contribution of excitons to the complex dielectric constant of crystals. *Phys. Rev. Lett.* **112**, 1555-1567 (1958).

[245] Antezza, M. & Castin, Y. Fano-Hopfield model and photonic band gaps for an arbitrary atomic lattice. *Phys. Rev. A* **80**, 013816 (2009).

[246] Soluyanov, A. A. et al. Type-II Weyl semimetals. *Nature* **527**, 495–498 (2015).

[247] Huang, L. et al. Spectroscopic evidence for a type II Weyl semimetallic state in $MoTe_2$. *Nat. Mater.* **15**, 1155-1160 (2016).

[248] Huang, H., Zhou, S. & Duan, W. Type-II Dirac fermions in the $PtSe_2$ class of transition metal dichalcogenides. *Phys. Rev. B* **94**, 121117(R) (2016).

[249] Deng, K. et al. Experimental observation of topological Fermi arcs in type-II Weyl semimetal $MoTe_2$. *Nat. Phys.* **12**, 1105–1110 (2016).

[250] Yan, M. et al. Lorentz-violating type-II Dirac fermions in transition metal dichalcogenide $PtTe_2$. *Nat. Commun.* **8**, 257 (2017).

[251] Pyrialakos, G. G., Nye, N. S., Kantartzis, N. V & Christodoulides, D. N. Emergence of type-II Dirac points in graphynelike photonic lattices. *Phys. Rev. Lett.* **119**, 113901 (2017).

[252] Lin, J. Y., Hu, N. C., Chen, Y. J., Lee, C. H. & Zhang, X. Line nodes, Dirac points, and Lifshitz transition in two-dimensional nonsymmorphic photonic crystals. *Phys. Rev. B* **96**, 075438 (2017).

[253] Bena, C. & Simon, L. Dirac point metamorphosis from third-neighbor couplings in graphene and related materials. *Phys. Rev. B* **83**, 115404 (2011).

[254] Umucalılar, R. O. & Carusotto, I. Artificial gauge field for photons in coupled cavity arrays. *Phys. Rev. A* **84**, 043804 (2011).

[255] Fang, K., Yu, Z. & Fan, S. Realizing effective magnetic field for photons by controlling the phase of dynamic modulation. *Nat. Photon.* **6**, 782–787 (2012).

[256] Fang, K., Yu, Z. & Fan, S. Photonic Aharonov–Bohm effect based on dynamic modulation. *Phys. Rev. Lett.* **108**, 153901 (2012).

[257] Fang, K. & Fan, S. Controlling the flow of light using the inhomogeneous effective gauge field that emerges from dynamic modulation. *Phys. Rev. Lett.* **111**, 203901 (2013).

[258] Lin, Q. & Fan, S. Light guiding by effective gauge field for photons. *Phys. Rev. X* **4**, 031031 (2014).

[259] Tzuang, L. D., Fang, K., Nussenzveig, P., Fan, S. & Lipson, M. Non-reciprocal phase shift induced by an effective magnetic flux for light. *Nat. Photon.* **8**, 701–705 (2014).

[260] Liu, F. & Li, J. Gauge field optics with anisotropic media. *Phys. Rev. Lett.* **114**, 103902 (2015).

[261] Schine, N., Ryou, A., Gromov, A., Sommer, A. & Simon, J. Synthetic Landau levels for photons. *Nature* **534**, 671–675 (2016).

[262] Jia, H. et al. Observation of chiral zero mode in inhomogeneous three-dimensional Weyl metamaterials. *Science* **363**, 148–151 (2019).

[263] Peri, V., Serra-Garcia, M., Ilan, R. & Huber, S. D. Axial-field-induced chiral channels in an acoustic Weyl system. *Nat. Phys.* **15**, 357–361 (2019).

[264] Ashcroft, N. W. & Mermin, N. D. Solid State Physics (Brooks Cole, Belmont, 1976)

[265] Lu, J. et al. Dirac cones in two-dimensional artificial crystals for classical waves. *Phys. Rev. B* **89**, 134302 (2014).

[266] Ni, X., Gorlach, M. A., Alù, A. & Khanikaev, A. B. Topological edge states in acoustic Kagome lattices. *New J. Phys.* **19**, 055002 (2017).

[267] Xue, H., Yang, Y., Gao, F., Chong, Y. & Zhang, B. Acoustic higher-order topological insulator on a kagome lattice. *Nat. Mater.* **18**, 108-112 (2019).

[268] Ni, X., Weiner, M., Alù, A. & Khanikaev, A. B. Observation of higher-order topological acoustic states protected by generalized chiral symmetry. *Nat. Mater.* **18**, 113-120 (2019).

[269] Lera, N., Torrent, D., San-Jose, P., Christensen, J. & Alvarez, J. V. Valley Hall phases in kagome lattices. *Phys. Rev. B* **99**, 134102 (2019).

[270] Wong, S., Saba M., Hess O. & Oh S. S. Gapless unidirectional photonic transport using all-dielectric kagome lattices. *Phys. Rev. Res.* **2**, 012011(R) (2020).

[271] Mengyao, L. et al. Higher-order topological states in photonic kagome crystals with long-range interactions. *Nat. Photon.* **14**, 89–94 (2020).

[272] Nakada, K., Fujita, M., Dresselhaus, G. & Dresselhaus, M. S. Edge state in graphene ribbons: Nanometer size effect and edge shape dependence. *Phys. Rev. B* **54**, 17954–17961 (1996).

[273] Kohmoto, M. & Hasegawa, Y. Zero modes and edge states of the honeycomb lattice. *Phys. Rev. B* **76**, 205402 (2007).

[274] Delplace, P., Ullmo, D. & Montambaux, G. Zak phase and the existence of edge states in graphene. *Phys. Rev. B* **84**, 195452 (2011).

[275] Kobayashi, Y., Fukui, K., Enoki, T., Kusakabe, K. & Kaburagi, Y. Observation of zigzag and armchair edges of graphite using scanning tunneling microscopy and spectroscopy. *Phys. Rev. B* **71**, 193406 (2005).

[276] Tao, C. et al. Spatially resolving edge states of chiral graphene nanoribbons. *Nat. Phys.* **7**, 616–620 (2011).

[277] Noh, J. et al. Topological protection of photonic mid-gap defect modes. *Nat. Photon.* **12**, 408–415 (2018).

[278] Nikitin, A. Y., Guinea, F., García-Vidal, F. J. & Martín-Moreno, L. Fields radiated by a nanoemitter in a graphene sheet. *Phys. Rev. B* **84**, 195446 (2011).

[279] Gradshteyn, I. S. & Ryzhik, I. M. *Table of Integrals, Series, and Products.* (Academic Press, New York, 2007).